MASARYK UNIVERSITY
FACULTY OF SCIENCE

Effective Quantum Models of Spin-Orbit Entangled Transition Metal Oxides

Doctoral thesis

BRNO 2024 JURAJ RUSNAČKO

MASARYK UNIVERSITY
FACULTY OF SCIENCE
DEPARTMENT OF CONDENSED MATTER PHYSICS

Effective Quantum Models of Spin-Orbit Entangled Transition Metal Oxides

Doctoral thesis

Juraj Rusnačko

Supervisor: doc. Mgr. Jiří Chaloupka, Ph.D. **Brno 2024**

Bibliografický záznam

Autor:	Mgr. Juraj Rusnačko Přírodovědecká fakulta, Masarykova univerzita Ústav kondenzovaných látek
Název práce:	Efektivní kvantové modely spin-orbitálně provázaných oxidů přechodových kovů
Studijní program:	Pokročilé materiály a nanovědy
Studijní obor:	Pokročilé nanotechnologie a mikrotechnologie
Školitel:	doc. Mgr. Jiří Chaloupka, Ph.D.
Akademický rok:	2023/2024
Počet stran:	xiv + 149
Klíčová slova:	oxidy přechodových kovů, spin-orbitální vazba, rozšířený Kitaevův-Heisenbergův model, Na_2IrO_3, Ca_2RuO_4, exaktní diagonalizace, kvantové Monte Carlo, harmonická aproximace, bosonická kondenzace

Bibliographic Entry

Author:	Mgr. Juraj Rusnačko Faculty of Science, Masaryk University Department of Condensed Matter Physics
Title of Thesis:	Effective Quantum Models of Spin-Orbit Entangled Transition Metal Oxides
Degree Programme:	Advanced Materials and Nanosciences
Field of Study:	Advanced Nanotechnologies and Microtechnologies
Supervisor:	doc. Mgr. Jiří Chaloupka, Ph.D.
Academic Year:	2023/2024
Number of Pages:	xiv + 149
Keywords:	transition metal oxides, spin-orbit coupling, extended Kitaev-Heisenberg model, Na_2IrO_3, Ca_2RuO_4, exact diagonalization, quantum Monte Carlo, harmonic approximation, bosonic condensation

Abstrakt

Tato dizertační práce představuje dvě teoretické studie magnetismu ve vybraných sloučeninách přechodových kovů se silnou spin-orbitální vazbou. V některých z těchto materiálů působí neobvyklé anizotropní magnetické interakce, které vznikají, když se prostorová symetrie orbitalů uplatněných při přeskocích mezi ionty promítne do pseudospinových interakcí v důsledku propletení lokálních spinových a orbitálních momentů hybnosti. Jiná situace může nastat v některých d^4 materiálech, kde spin-orbitální interakce přeuspořádá nízkoenergiové multipletové stavy, což vede k neobvyklé lokální bázi složené z kvazidegenerovaných singletních a tripletních hladin dynamicky promíchaných výměnnou interakcí. Práce se zabývá dvěma konkrétními příklady takových jevů: i) anizotropními interakcemi na vazbách v Kitaevových magnetech a ii) měkkým spinovým magnetismem v d^4 ruthenátech. V první polovině práce se zabýváme rozšířeným Kitaevovým-Heisenbergovým modelem, který představuje efektivní kvantový spinový model pro kvazi-2D voštinové materiály, jako jsou Na_2IrO_3 a α-$RuCl_3$. Kombinací analytického rozboru založeného na symetriích s numerickými metodami konstruujeme globální popis fázového diagramu modelu a nacházíme některé jeho překvapivé rysy, jako je existence souvislých oblastí v prostoru parametrů, v nichž je základní stav prostý kvantových fluktuací. Druhá polovina práce je věnována studiu hard-core bosonového modelu popisujícího excitonový magnetismus v Ca_2RuO_4. Zde rozšiřujeme harmonickou aproximaci o korekce v rámci metody středního pole, která částečně zohledňuje hard-core povahu příslušných pomocných bosonů. Srovnání s numerickými výpočty na bázi kvantové metody Monte Carlo ukázalo, že metoda středního pole poskytuje přesné výsledky jak pro statické veličiny, tak pro disperze magnetických excitací.

Abstract

The thesis presents two theoretical studies of magnetism in selected transition metal compounds with strong spin-orbit coupling. Some of these materials feature unusual anisotropic magnetic interactions that arise when the spatial symmetry of orbitals entering inter-site hopping is imprinted onto the pseudospin interactions by an entanglement of local spin and orbital momenta. A different situation may occur in some d^4 materials, where the spin-orbit interaction reorganizes the low-lying multiplet states, leading to an unusual local basis composed of quasi-degenerate singlet and triplet levels dynamically mixed by exchange interactions. The thesis covers two specific examples of such phenomena: i) bond-selective interactions in Kitaev magnets, and ii) soft-spin magnetism in d^4 ruthenates. In the first half of the work, we address the extended Kitaev-Heisenberg model, which is an effective quantum spin model for quasi-2D honeycomb compounds such as Na_2IrO_3 and α-$RuCl_3$. By combining analytical symmetry-based analysis with numerical methods, we provide a global description of the model's phase diagram, revealing surprising features such as fluctuation-free manifolds in parameter space. The second half of the thesis is devoted to the study of a hard-core bosonic model describing excitonic magnetism in Ca_2RuO_4. We develop a mean-field method which partly incorporates the hard-core properties of bosons, thus extending the harmonic approximation. A comparison with Quantum Monte Carlo calculations revealed that the mean-field method yields accurate results for both static quantities and dispersions of magnetic excitations.

Acknowledgements

First and foremost, I want to thank my supervisor, doc. Mgr. Jiří Chaloupka, Ph.D. for guiding me in research, teaching me a lot about physics and academia, and dedicating so much time and effort for the benefit of his students. I am also grateful to prof. Mgr. Dominik Munzar, Dr., the head of the Department of Condensed Matter Physics, for his continuous all-round support throughout my studies. I want to express my thanks to Dr. Dorota Gotfryd, Assoc. Prof. Krzysztof Wohlfeld, Prof. Andrzej Oleś and Prof. Kurt Hingerl for their hospitality during my short stays at the Jagiellonian University Kraków, University of Warsaw and Johannes Kepler University Linz. Finally, I want to thank Jiří, Ondřej, and Karel of room 2008 for thoroughly broadening my horizons with trivia on Jewish culture, Czechoslovak naval battles, academia politics, and much more.

Declaration

I declare that I have composed this dissertation independently with the use of information sources that are properly cited and listed in the thesis.

Brno 16. June 2024 . . . . . .

Juraj Rusnačko

Contents

Introduction **1**

1 Effective model description of relativistic transition metal oxides **3**
1.1 Formulation of an effective model 3
1.1.1 Transition metal oxides 3
1.1.2 Multiplet structure of a single magnetic ion 4
1.1.3 Superexchange interactions and formulation of an effective model 12
1.2 Kitaev physics in relativistic $J = 1/2$ Mott insulators 15
1.2.1 Kitaev model and quantum spin liquid 15
1.2.2 Kitaev coupling in $J = 1/2$ oxides: the Jackeli-Khaliullin mechanism 17
1.2.3 Signatures of Kitaev physics in real materials 19
1.3 Van-Vleck magnetism in d^4 transition metal oxides 23
1.3.1 Soft spins and Higgs mode 23
1.3.2 Effective singlet-triplet model 26
1.3.3 Higgs mode in Ca_2RuO_4 28

2 Extended Kitaev-Heisenberg model **31**
2.1 Analytical exploration of the phase diagram 31
2.1.1 Definition of the model and used reference frames 32
2.1.2 Symmetry analysis of the interaction Hamiltonian 35
2.1.3 The case of a single interaction axis: Ising-Kitaev-compass model 39
2.1.4 Spin states without quantum fluctuations 43
2.1.5 Symmetry-based view of the phase diagram 49
2.2 Numerical exploration of the phase diagram 54
2.2.1 Exact diagonalization on finite clusters 55
2.2.2 The method of spin-$\frac{1}{2}$ coherent states 58
2.2.3 Classical phase diagram of the extended Kitaev-Heisenberg model 66
2.2.4 Global phase diagram obtained by the spin-$\frac{1}{2}$ coherent states method 70

3 Soft spins in d^4 ruthenates **81**
3.1 Singlet-doublet model in the harmonic approximation 82
3.1.1 Definition of the model and used reference frames 82
3.1.2 Variational magnetic ground state 84
3.1.3 Harmonic excitations 86

3.2 Beyond the harmonic approximation: mean-field and quantum Monte Carlo 92
3.2.1 Quantum Monte Carlo: Stochastic Series Expansion (SSE) method 92
3.2.2 Mean-field treatment of the hard-core bosonic Hamiltonian 95
3.2.3 Quantitative analysis of the effects beyond the harmonic approximation . . . 98

Conclusion **109**

A Derivation of the Kitaev-Heisenberg model **111**

B The method of spin-$\frac{1}{2}$ coherent states **115**

C Stochastic Series Expansion **119**

D Bogoliubov transformation by numerical diagonalization **127**

E Self-consistent solution of the mean-field bosonic Hamiltonian **131**

Published articles **137**

Bibliography **139**

Introduction

In condensed matter physics, we try to provide an accurate description of real materials and the various physical phenomena they exhibit. Working towards a theoretical description, one big challenge is to sort out the large number of effects that all play some role in producing an experimental outcome. With a goal of fundamental understanding, we try to omit those details of specific materials that are not key to the physical phenomena of interest and rather produce simplified models. One such case is represented by effective lattice spin models, which can capture the low-energy magnetic behavior of a given material, producing a qualitative description of the magnetic ground state and low-lying spin excitations.

In terms of materials, one class of materials that have been intensively studied in recent years is transition metal compounds with strong spin-orbit coupling. These compounds include heavy magnetically active elements belonging to the $4d$ and $5d$ series. In some of these elements, a strong spin-orbit coupling is manifested by entangling the local orbital and spin degrees of freedom, creating local pseudospin moments. This relativistic entanglement can lead to exotic magnetic phenomena, such as spin liquid behavior [1], or soft spin excitations [2].

The topic of this thesis is the application of effective quantum spin models to certain transition metal oxides with strong spin-orbit coupling. The thesis is comprised of two separate parts discussing two different topics, together with a common theoretical introduction. The general structure of the text is the following:

(i) We begin with an introductory chapter which serves both as a theoretical overview of microscopic physics underlying effective spin models and as a motivational introduction to the two topics representing the main body of the thesis. First, we discuss the formation of an effective spin model, which is a relatively high abstraction above the microscopic details of a given material. The first section includes a qualitative description of the effective model's ingredients: starting from the multiplet structure of the transition metal ion, including the effects of the lattice, spin-orbit interaction, Coulomb interactions, and electronic hopping. The aim is to provide the reader with a relatively simple and brief overview; an example of a more thorough derivation of an effective spin model is given in Appendix A. Next, we include a short introduction to each of the two effective spin systems studied in this thesis: the honeycomb Kitaev materials and soft-spin systems in d^4 ruthenates. These are short pieces of text that contain experimental overviews of materials manifesting unconventional magnetic properties, serving as motivation for the study of the corresponding spin systems.

(ii) The second chapter is devoted to the study of the so-called Kitaev materials: these are Ir^{4+} and Ru^{3+} compounds (and, more recently also Co^{2+} compounds [3]) which host local pseudospin-$\frac{1}{2}$ moments. Due to the specific orbital arrangement, the effective interactions between the entangled spin-orbital moments are highly anisotropic, with one part having the form of the Kitaev bond-selective interaction [4]. The complete effective spin model describing the

discussed Kitaev materials is the extended Kitaev-Heisenberg (EKH) model, which is the main protagonist of Chapter 2. Our focus is on the phase diagram of the model. Although specific parts of the diagram have been published before [5, 6, 7, 8, 9], these focused only on small parts of the parameter space guided mainly by ab initio estimates. Our goal was to provide a detailed description of the global phase diagram of the model, without having specific parameter values in mind. The original contribution of this part of the thesis is two-fold. First, we provide numerical solutions of the model in a broad parameter range, including the analysis of several incommensurate phases that were not studied before. To this end, we use the spin-$\frac{1}{2}$ coherent state method by Chaloupka and Khaliullin [10] to analyze the cluster ground states obtained by exact diagonalization. We extend this method to general noncollinear states. Further, we provide an efficient implementation of the method in the form of two algorithms: one suited to a general case and the other tailored to collinear phases. Second, we provide an analytical treatment of the phase diagram based on its hidden symmetries. Building on previous work [11], we uncover sets of fluctuation-free states covering a whole manifold in the model's parameter space. Moreover, we find new mappings that provide a connection between a parameter subspace of the EKH model and a model that features a single bond-dependent interaction axis [12]. In this way, a whole group of models – Ising, Kitaev, and compass – can emerge from the richness of the EKH model.

(iii) The third and final chapter contains a study of Mott-insulating transition metal oxides in the d^4 valence shell configuration subject to strong spin-orbit coupling, where the ground state is a nonmagnetic singlet, and the magnetism is mainly of Van Vleck type. This type of magnetism features the magnetic moments lying mainly on the transition between the singlet ground state and triplet excited levels. In contrast with magnons, the excitations corresponding to transitions between spinless and spinful states can vary the length of the spin: the spins are "soft". The effective model describing such magnetic systems is formulated in terms of hard-core bosons and allows us to study the condensation of triplet excitations into a condensate establishing long-range magnetic order. We study the magnetic ground state and low-energy spin excitations by solving the model in different degrees of approximation. We start with the harmonic approximation, which provides a qualitative understanding of the main features of the model. The original contributions of the thesis lie in applied approaches that go beyond the harmonic level. One of these is numerical: we use the Quantum Monte Carlo - Stochastic Series Expansion (QMC-SSE) algorithm to obtain numerical solutions of ground-state properties and dynamical susceptibilities on much larger clusters than what is possible using exact diagonalization. Further, we investigate an analytical mean-field method to solve the model, gaining original results in the form of mean-field-corrected spin excitation spectra. We show that even a simple incorporation of two crucial effects stemming from the hard-core nature of bosons – renormalization of local triplet excitation energy and interaction screening due to hopping being blocked by the presence of another boson – can be sufficient to obtain a very good quantitative agreement with numerical data.

Chapter 1

Effective model description of relativistic transition metal oxides

1.1 Formulation of an effective model

The topic of this thesis are effective models describing relativistic transition metal oxides. The relativistic properties arise in heavier transition metal atoms in the form of spin-orbit coupling, which acts as a binding force and combines the spin and orbital degrees of freedom into a single effective object. The interactions of these pseudospins inherit the anisotropic nature of orbitals and give rise to unconventional magnetic phenomena.

The following chapter aims to introduce and motivate the use of effective quantum models to describe such materials. The first section contains an overview of the most prominent ingredients contributing to the formulation of an effective model. Some of these include the effects of the oxygen ligands on the electronic levels, spin-orbit entanglement, Coulomb interactions, and electronic hopping between the neighboring ions in a solid. We also try to illustrate how those ingredients are combined to produce an effective model in the context of perturbation theory.

Afterwards, we move to the motivation behind introducing effective models, namely the need to describe correlated materials theoretically. We mention two examples of real materials behind the specific effective models we study in this thesis. The first example concerns the honeycomb iridate Na_2IrO_3 which hosts anisotropic compass-like interactions that depend on the bond direction, and a connection to the topological Kitaev model. The second topic concerns the physics of Ca_2RuO_4, where a specific hierarchy of energy scales leads to a type of excitonic Van Vleck magnetism.

1.1.1 Transition metal oxides

Transition metal oxides (TMOs) represent a prominent class of materials that are well-known not only to physicists but also to engineers, chemists, and members of other technology areas due to their wide-ranging real-life applications. More than 50 years of research in TMOs has produced many fascinating discoveries, initiated by the discovery of high Tc superconductivity of cuprates in the 1980s [13]. Later successes include colossal magnetoresistance and various exotic spin-orbital phenomena [14]. In recent years, more research has been focused on TMOs featuring heavier $4d$ and $5d$ elements, where relativistic spin-orbit coupling plays a prominent

role. A wide variety of spin-orbit entangled states may arise, as evidenced by the surprising connection to spin liquids [15], the discovery of correlated topological semimetals, or excitonic magnetism [2].

The d valence shells of transition metal ions provide an interesting balance between two opposing tendencies: electron delocalization through orbital wave-function overlap and Coulomb repulsion preventing electron motion. The spatial extent of d orbitals varies, rising steadily from the relatively localized $3d$ shells to quite extended $5d$ orbitals. Depending on which of these tendencies dominates for a given material, either a Fermi metal or a Mott insulator emerges. Such competition is not captured by the conventional single-particle approaches based on band theory since it does not handle the many-body nature of local correlations. The metal-insulator transition was successfully described by the prototype Hubbard model [16], which embodies the two main conflicting forces: electronic hopping t and local Coulomb repulsion U. The success of the Hubbard model inspires the use of effective model approaches for the description of correlated phenomena in transition-metal compounds. This is also the way we take in this thesis, devoting the later two chapters to particular effective models describing real compounds Na_2IrO_3 and Ca_2RuO_4.

In this section, we describe the aspects one needs to consider when building an effective model for a particular TMO. The strategy is to start from a local perspective and identify the local low-energy degrees of freedom. To achieve this, we consider how the hydrogen-like d orbitals of the magnetic ions are affected by the local environment created by the ligand atoms, most often arranged in an octahedron. In addition, we include intraionic correlations between electrons in the d shell, which reorganize wave functions into eigenstates of total spin S and orbital angular momentum L. Finally, the important relativistic effect of spin-orbit coupling is included, binding the spins and orbitals into a total angular momentum J. If the spin-orbit coupling is strong enough, the local degrees of freedom are in the form of a particular type of J eigenstate. These moments then interact with their neighbors on the crystal lattice through hopping. Treating these in a perturbative manner, we finally obtain an effective superexchange model.

1.1.2 Multiplet structure of a single magnetic ion

Crystal field splitting

The orbitals of a free-standing magnetic ion are given by spherical harmonics, which capture the the spherical symmetry of the Coulomb potential of the nucleus and closed electron shells. However, when the ion is placed in a crystal, the interaction with surrounding ligands and neighboring ions changes the electronic levels. Here, we will consider only one effect of the lattice environment, namely the static repulsion of valence electrons with the surrounding ligand charges. In general, the presence of the lattice has additional consequences, such as hybridization of d orbitals with the p orbitals of the ligands or interaction-induced crystal distortions known as the Jahn-Teller effect [17].

In many transition metal oxides, the transition metal ion is surrounded by an octahedral cage of oxygen atoms. This prominent example is also relevant for compounds considered in this thesis, namely Na_2IrO_3 and Ca_2RuO_4, as shown in Figure 1.1. In such a regular octahedron complex MO_6, the valence d-electrons of the magnetic ion M are subject to Coulomb repulsion of the negatively charged oxygen ligands. Representing each oxygen as a point charge of

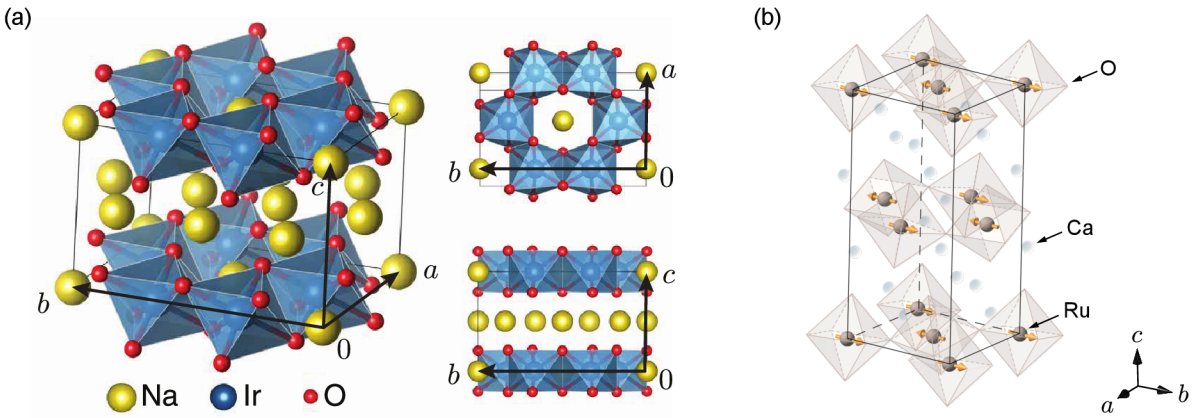

Figure 1.1: (a) Different views of the layered crystal structure of Na_2IrO_3. It consists of weakly bound $NaIr_2O_6$ planes, resulting in a quasi-two-dimensional structure. Magnetic Ir^{4+} ions shown in blue are arranged in a planar honeycomb lattice and surrounded by edge-shared oxygen octahedra. Na atoms fill the gaps in the lattice and do not contribute significantly to the magnetic properties. Adapted from [5]. (b) Perovskite structure of Ca_2RuO_4, showing weakly bound planes of Ru^{4+} ions with Ca atoms in-between. The magnetic ruthenium ions form a square lattice arrangement and are surrounded by corner-shared oxygen octahedra. The octahedral cages are significantly distorted: they are tetragonally compressed along the c direction and are further rotated and tilted. Reproduced from [18].

magnitude $-2e$, we may write the repulsive potential of the octahedral crystal field:

$$V_{MO_6}(\mathbf{r}) = \frac{+2e^2}{4\pi\varepsilon_0}\sum_{i=1}^{6}\frac{1}{|\mathbf{r}-\mathbf{R}_i|}, \tag{1.1}$$

where $\mathbf{R}_i$ are positions of the oxygen charges in the corners of the octahedral cage. Writing out the sum explicitly, we obtain an expansion in powers of (r/R):

$$\begin{aligned} V_{MO_6} &= \frac{e^2}{2\pi\varepsilon_0}\left[\frac{1}{\sqrt{(x-R)^2+y^2+z^2}}+\frac{1}{\sqrt{(x+R)^2+y^2+z^2}}+\dots\right] \\ &= \frac{e^2}{2\pi\varepsilon_0 R}\left[6+\frac{35}{4R^4}\left(x^4+y^4+z^4-\frac{3}{5}r^4\right)+O\left(\left(\frac{r}{R}\right)^5\right)\right]. \end{aligned} \tag{1.2}$$

Since the valence d orbitals are relatively localized, we can keep only terms up to fourth order $(r/R)^4$. The first constant term only leads to an overall energy shift, which means that the interesting part of the potential has the form $(x^4+y^4+z^4-3/5r^4)/R^4$. The restructuring of electronic levels by this crystal field can be obtained most directly by a first-order perturbation theory. Concretely, the matrix of the perturbed potential on the original basis of hydrogen-like orbitals $\langle d_m|V_{MO_6}|d_{m'}\rangle$ should be diagonalized, yielding energy shifts as eigenvalues and reshaped orbitals as eigenstates.

The perturbing potential splits the original 5-fold degenerate d-manifold into a three-fold degenerate subspace with eigenvalue $-\frac{2}{5}\Delta_{\mathrm{CF}}$ and a two-times degenerate subspace with eigenvalue $\frac{3}{5}\Delta_{\mathrm{CF}}$, where

$$\Delta_{\mathrm{CF}} = \frac{5e^2}{6\pi\varepsilon_0 R}\frac{\langle r^4\rangle}{R^4}. \tag{1.3}$$

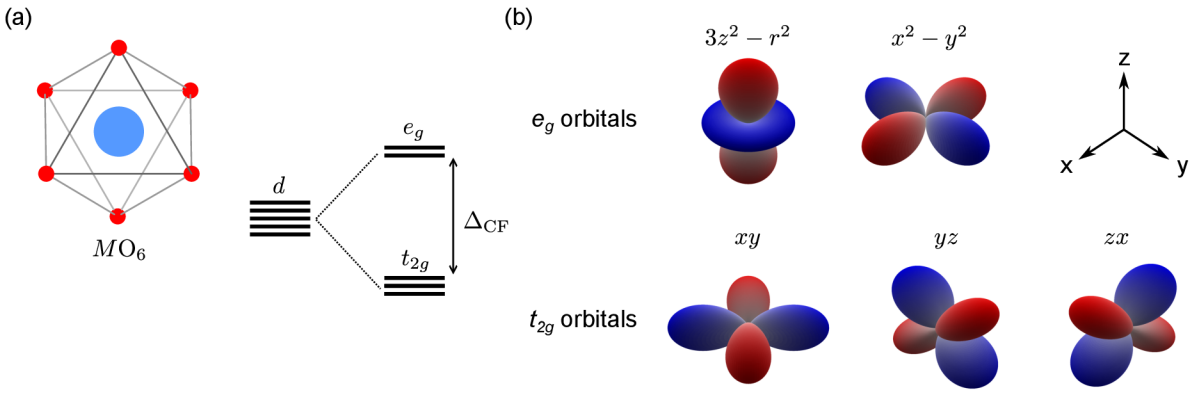

Figure 1.2: (a) Octahedral complex MO_6 consisting of a magnetic ion M in the center (blue) surrounded by a regular octahedron with oxygens (red) placed in the vertices. The octahedral electrostatic field of oxygens splits the five-fold degenerate d shell of the magnetic ion into e_g and t_{2g} subspaces separated by crystal field splitting energy Δ_{CF}. (b) Shapes of e_g and t_{2g} orbitals derived from linear combinations of spherical harmonics. The shapes are given by the absolute value of the wavefunction, and color encodes the sign. Partially adapted from [20].

For historical reasons, the crystal field splitting Δ_{CF} energy is sometimes notated as 10Dq. Restructured electronic orbitals are referred to as three-fold degenerate t_{2g} and two-fold degenerate e_g states. Explicitly written as linear combinations of the d-shell L_z eigenstates $|d_m\rangle$, the low-energy t_{2g} states are [19]

$$\begin{aligned} |xy\rangle &= -\tfrac{i}{\sqrt{2}}(|d_{+2}\rangle - |d_{-2}\rangle), \\ |yz\rangle &= \tfrac{i}{\sqrt{2}}(|d_{+1}\rangle + |d_{-1}\rangle), \\ |zx\rangle &= -\tfrac{1}{\sqrt{2}}(|d_{+1}\rangle - |d_{-1}\rangle), \end{aligned} \tag{1.4}$$

and the high-energy e_g states

$$\begin{aligned} \left|3z^2 - r^2\right\rangle &= \quad |d_0\rangle\,, \\ \left|x^2 - y^2\right\rangle &= \tfrac{1}{\sqrt{2}}(|d_{+2}\rangle + |d_{-2}\rangle). \end{aligned} \tag{1.5}$$

We may gain an intuitive understanding of the crystal field splitting by inspecting the shapes of the above orbitals, depicted in Fig. 1.2 panel (b), placed in the octahedral oxygen cage. The highest electron density in the e_g orbitals is in the directions pointing towards the oxygen atoms, which is why the repulsion lifts up the corresponding energy levels. In contrast, in the t_{2g} orbitals, the electron density peaks between the neighboring oxygens, thus having lower energies.

In transition-metal oxides with oxygen octahedral cages, the value of crystal field splitting is typically expressed as units of electronvolts. It is therefore a relatively strong effect and, as we will comment on later, may take precedence over the nominal filling expressed by the first Hund's rule. Also, real materials often show various distortions, such as the oxygen octahedra being uniaxially squashed/elongated. For example, in Na_2IrO_3 the octahedral cages are distorted along an axis perpendicular to one of the octahedral faces, the so-called trigonal distortion. This further lowering of the symmetry splits the three-fold degenerate t_{2g} levels into a singlet and a doublet and can be captured by a term $\propto L_z^2$ in the case of a z-axis distortion [21].

The lowering of orbital symmetry by the crystal field and the accompanying restructuring of electronic states have a profound effect on the orbital angular momentum of the valence electrons. Whereas hydrogen-like orbitals $|d_m\rangle$ are eigenstates of operators $\mathbf{L}^2$ and L_z with $l = 2, m = -2, \ldots, 2$, the new t_{2g} and e_g orbitals are no longer L_z eigenstates. This is evident from the expressions (1.4) and (1.5), as they contain linear combinations of $|d_m\rangle$ states with different m's. Expressing the angular momentum operators in the new basis respecting the octahedral crystal symmetry, one finds that the angular momentum in the e_g subspace is zero, that is, it is fully quenched. In the t_{2g} subspace, the angular momentum operators expressed in the basis (1.4) have the same matrix elements as an $\mathbf{L}$ operator for p states (namely $|p_x\rangle, |p_y\rangle, |p_z\rangle$) with $l = 1$, apart from an additional minus sign. The minus sign is often absorbed into a definition of effective angular momentum $\mathbf{L}^{\text{eff}} = -\mathbf{L}$; the t_{2g} states then carry a quantum number $l^{\text{eff}} = 1$. Quenching of angular momentum has a direct impact on how the low-energy basis for the effective spin model is formed, as we will see already in the next paragraph, where we couple the orbital motion with spin via spin-orbit coupling.

Relativistic electron motion: spin-orbit coupling

The canonical atomic orbitals which we worked with in the previous section are the solution to the non-relativistic Schrödinger equation. The spin of the electron is only added post hoc, doubling the degeneracy of atomic orbitals. Such an approximation works well for lighter atoms, and full relativistic treatment gives only the fine structure of the energy levels. However, the electrons in heavier ions move faster – rough approximation ignoring screening gives a root mean square of electron velocity

$$v_{\text{rms}} \approx Z\alpha c, \tag{1.6}$$

where Z is the proton number of the considered ion and $\alpha \doteq 1/137.036$ is the fine structure constant. Applying the formula on $4d$ and $5d$ transition metals with proton numbers between 40 and 80, we estimate the electron speed to be around half the speed of light. Even though this is only an order-of-magnitude estimate, it is clear that relativistic effects may play a prominent role in some heavier transition metals.

We consider the effect of *spin-orbit coupling* (SOC), which is the quantum interaction of spin and orbital quantum momenta. An intuitive picture of how it arises may be gained by considering the rest frame of the electron, with the atomic nucleus orbiting around it. The magnetic field due to the orbital motion of the nucleus interacts with the electron's spin, giving rise to the spin-orbit interaction. More precise derivation using Dirac's equation leads to the expression for the interaction

$$\mathcal{H}_{\text{SOC}} = \frac{\hbar^2}{2m^2c^2}\frac{1}{r}\frac{\mathrm{d}V}{\mathrm{d}r}\mathbf{s}\cdot\mathbf{l} = \xi(r)\mathbf{s}\cdot\mathbf{l}, \tag{1.7}$$

where the angular momenta $\mathbf{l}, \mathbf{s}$ are measured in units of $\hbar$. The above formula holds for centro-symmetric binding potential V of the atom and a single-electron interaction. The SOC strength ξ is positive, thus the interaction is isotropic and favors antiparallel alignment of spin and orbital moments.

Atomic wave functions in a spherical environment are eigenstates of angular momentum operators $\mathbf{l}^2, l_z, \mathbf{s}^2, s_z$. Including the spin-orbit coupling term $\mathbf{s}\cdot\mathbf{l}$, l_z and s_z are no longer good

quantum numbers. To see this explicitly, we first form the total angular momentum operator $\mathbf{j}$

$$\mathbf{j} = \mathbf{l} + \mathbf{s}, \tag{1.8}$$

and rewrite the $\mathbf{s} \cdot \mathbf{l}$ term as

$$\mathbf{s} \cdot \mathbf{l} = \frac{1}{2}\left(\mathbf{j}^2 - \mathbf{l}^2 - \mathbf{s}^2\right). \tag{1.9}$$

When considering only $t_{2g} - e_g$ splitting without additional lattice distortions, the angular momentum operator $\mathbf{j}^2$ does not commute with l_z and s_z, and the atomic wave functions are not eigenstates of the Hamiltonian that includes SOC. The set of four commuting operators $\{\mathbf{j}^2, \mathbf{l}^2, \mathbf{s}^2, j_z\}$ forms a natural basis for the description of the system; the new eigenstates can then be labeled $|l, s, j, j_z\rangle$. Specific examples of the formation of such states in the d^4 and d^5 systems will be given later in this section.

What is the relative importance of spin-orbit coupling in a solid? We already estimated that electrons in transition metal ions reach relativistic speeds comparable with the speed of light. A simple approximation for the SOC strength ξ considering a hydrogen-like atom gives a $\propto Z^4$ dependence, which is lowered due to screening to $\propto Z^2$ [22]. For the ruthenium ion in d^4 configuration and the d^5 iridium ion, we may look for experimental studies determining SOC strength. The results given by the resonant inelastic x-ray scattering (RIXS) and electron paramagnetic resonance methods give approximately 80 meV for the $4d$ Ru^{4+} ion [23] and roughly 400 meV for the Ir^{4+} ion [24]. Although an order of magnitude lower than crystal field splitting values for ions in oxygen octahedral cages, spin-orbit interaction in $4d$ and $5d$ transition metals is still energetically strong enough to affect the structure of localized states and, as we will describe in later chapters, can lead to strongly anisotropic, bond-selective interactions.

Electron correlations in an isolated ion

In the previous discussions, we worked with single-particle hydrogen-like orbitals as a starting point. However, if the valence shell of the d atom contains more than one electron, Coulomb repulsion between the electrons cannot be ignored, as it reshapes the single-particle orbitals into their many-body counterparts. The full Coulomb interaction can be systematically expanded into a series and truncated, leaving only the most essential contributions; one then obtains the Hubbard-Kanamori Hamiltonian for the purely t_{2g} system [25]:

$$\mathcal{H}_{\mathrm{HK}} = U \sum_{\alpha} n_{\alpha\uparrow} n_{\alpha\downarrow} + \sum_{\alpha<\beta} \left(U - \frac{J_H}{2}\right) n_\alpha n_\beta - 2J_H \sum_{\alpha<\beta} \mathbf{S}_\alpha \cdot \mathbf{S}_\beta + J_H \sum_{\alpha\neq\beta} \alpha_\uparrow^\dagger \alpha_\downarrow^\dagger \beta_\downarrow \beta_\uparrow. \tag{1.10}$$

The first term in the sum is the Hubbard interaction between electrons occupying the same orbital. Energetically, it is the most significant contribution. The second term represents the repulsion of electrons in different orbitals. The third term is the so-called *Hund's coupling*, which tends to align spins in different orbitals ferromagnetically and is the main driver behind the first Hund's rule. The last term of the Kanamori Hamiltonian is a pair-hopping interaction term: it means that energy may be gained kinetically by the hopping of singlet electron pairs between orbitals.

Having introduced a brief description of intraionic Coulomb interactions, we are now ready to bring together all the pieces we have discussed so far: crystal field splitting, spin-orbit coupling, Coulomb repulsion, and deduce the multiplet structure of a transition metal ion with a valence t_{2g} shell.

Low-energy basis states of t_{2g}^4 and t_{2g}^5 configuration

The filling of electronic levels in a free-standing ion is described by Hund's rules, which express the agency of Hubbard intra-orbital repulsion and Hund's coupling. First, electrons try to fill different orbitals to minimize the dominant Hubbard repulsion U. These are aligned ferromagnetically by the Hund's coupling J_H, maximizing the total spin, which is the content of the first Hund's rule. In a crystal environment, the situation is changed since Δ_{CF} splitting between t_{2g} and e_g manifolds is quite large. This means that in ions with ≤ 6 valence electrons, it may be energetically favorable to fill the whole set of t_{2g} levels first. This is the case we consider in this thesis; in the following, we stay exclusively in the t_{2g} subspace.

Let us discuss two configurations in more detail: t_{2g}^5 configuration relevant for Ir^{4+} ions in Na_2IrO_3 and t_{2g}^4 configuration motivated by the case of Ru^{4+} ions in Ca_2RuO_4. In a t_{2g}-only system, the Hubbard-Kanamori Hamiltonian commutes with $\mathbf{S}^2$ and $(\mathbf{L}^{\mathrm{eff}})^2$ and can be written as [26]

$$\mathcal{H}_{t_{2g}} = \frac{1}{2}(U-3J_H)N(N-1) + \frac{5}{2}J_H N - 2J_H\mathbf{S}^2 - \frac{1}{2}J_H(\mathbf{L}^{\mathrm{eff}})^2. \tag{1.11}$$

Eigenstates of t_{2g}^5 and t_{2g}^4 configurations can thus be labeled using four quantum numbers $\left|L^{\mathrm{eff}}, L_z^{\mathrm{eff}}, S, S_z\right\rangle$. In the case of t_{2g}^5 configuration, five electrons in the six-fold degenerate t_{2g} subspace is equivalent to placing a single hole in a full t_{2g}^6 manifold. There are six energetically equivalent solutions that describe a hole with $L^{\mathrm{eff}} = 1, S = \frac{1}{2}$:

$$\left|1,0,\frac{1}{2},+\frac{1}{2}\right\rangle, \left|1,0,\frac{1}{2},-\frac{1}{2}\right\rangle, \left|1,1,\frac{1}{2},+\frac{1}{2}\right\rangle, \left|1,1,\frac{1}{2},-\frac{1}{2}\right\rangle, \left|1,-1,\frac{1}{2},+\frac{1}{2}\right\rangle, \left|1,-1,\frac{1}{2},-\frac{1}{2}\right\rangle. \tag{1.12}$$

The t_{2g}^4 configuration is more complex since we now have two holes. There are two types of states that can arise: (i) the two holes occupy two different orbitals, and the third one is filled; (ii) two orbitals are filled by 4 electrons, and one is unoccupied. In the first case (i), there are 12 possibilities in total: 3 ways to place the orbitals and four ways to arrange the spins. However, these are not energetically equivalent since Hund's coupling J_H prefers ferromagnetically aligned spins in singly occupied orbitals. Regarding total spin, such states may be singlets ($S = 0$) or triplets ($S = 1$). In the second case (ii), the Hubbard repulsion is paid for twice, Hund's coupling is inactive, and the pair-hopping term is also active since there are two completely filled orbitals. These states are spin singlets. In terms of orbital angular momentum, the combination of two L^{eff} holes can result in total $L^{\mathrm{eff}} = 0,1,2$. Combined with either a spin singlet or a triplet, we arrive at the following classification:

- The highest-energy state is a non-degenerate singlet with $L^{\mathrm{eff}} = 0, S = 0$: $|0,0,0,0\rangle$.
- Lower in energy, $L^{\mathrm{eff}} = 2$ is combined with $S = 0$ (symmetric orbital part of the wave-function comes together with antisymmetric spin part so that the electron wave-function is always antisymmetric) into five states:

$$|2,+2,0,0\rangle, |2,+1,0,0\rangle, |2,0,0,0\rangle, |2,-1,0,0\rangle, |2,-2,0,0\rangle. \tag{1.13}$$

- Last, the $L^{\mathrm{eff}} = 1$ and $S = 1$ sector encompassing 9 states:

$$|1,\pm1,1,\pm1\rangle\,(4\times), |1,\pm1,1,0\rangle\,(2\times), |1,0,1,\pm1\rangle\,(2\times), |1,0,1,0\rangle. \tag{1.14}$$

So far, we have included crystal field splitting and local Coulomb repulsion in the analysis of electronic filling. The last important piece missing in the proper identification of low-energy basis states is to incorporate the spin-orbit coupling. There are two approaches to achieve this: *j-j coupling* and *LS coupling* (also sometimes dubbed Russel-Saunders coupling) schemes. The j-j coupling scheme works by first forming $\mathbf{j} = \mathbf{l} + \mathbf{s}$ individual moments for each electron, which are eigenstates of SOC. These are subsequently combined to diagonalize the Coulomb repulsion. Such an approach is appropriate when SOC dominates, which is the case of heavy transition metals due to approximate $\propto Z^2$ scaling. The second approach of LS coupling works in the reversed order. First, total $\mathbf{L}$ and $\mathbf{S}$ moments are formed, diagonalizing the Coulomb interaction part of the Hamiltonian. Then, $\mathbf{L}$ and $\mathbf{S}$ moments are mixed by spin-orbit coupling. In this case, SOC has the form

$$\mathcal{H}_{\mathrm{SOC}} = \lambda \mathbf{S} \cdot \mathbf{L}, \tag{1.15}$$

where $|\lambda| = \frac{\xi}{2S}$, with λ positive for less than half-filled shell and negative for more than half-filled shell. As we saw previously, the $\mathbf{S} \cdot \mathbf{L}$ form of interaction leads to the formation of total moments $\mathbf{J} = \mathbf{L} + \mathbf{S}$. In the t_{2g} subspace, the diagonalized SOC can be written

$$\mathcal{H}_{\mathrm{SOC}} = \lambda \mathbf{S} \cdot \mathbf{L}^{\mathrm{eff}} = \frac{\lambda}{2} \left[\mathbf{J}^2 - (\mathbf{L}^{\mathrm{eff}})^2 - \mathbf{S}^2 \right]. \tag{1.16}$$

In the above expression, we incorporated an extra minus sign coming from $\mathbf{L}^{\mathrm{eff}} = -\mathbf{L}$ into λ, so for our case of t_{2g} shell with four or five electrons λ is positive. With this slight modification, the above equation grounds the second Hund's rule: for electronic shells with $\lambda > 0$, the levels with the lowest value of total angular momentum J lie lowest in energy.

Let us now build the SOC eigenstates for the t_{2g}^5 configuration using the LS scheme. We combine the momenta $L^{\mathrm{eff}} = 1$ and $S = \frac{1}{2}$, hence the resulting total angular momentum will have two values, representing a $J = \frac{1}{2}$ doublet and $J = \frac{3}{2}$ quartet – see Fig. 1.3 panel (a). The energy splitting is $\frac{3}{2}\lambda$, with the doublet lying lower in energy. The two $J = \frac{1}{2}$ states are also called the Kramers doublet, which relates to Kramers theorem. It states that whenever the Hamiltonian commutes with the time-reversal operator, odd-numbered electron systems will possess a ground state consisting of a doubly-degenerate pair – a Kramers doublet – of states related by time reversal. The action of the time reversal operator on the spin is to flip it from $\uparrow$ to $\downarrow$ and vice versa. The $J = \frac{1}{2}$ doublet is the final low-energy basis, which can be used to form an effective spin model.

We previously obtained three sets of states in the case of the t_{2g}^4 configuration. Two of these are unaffected by spin-orbit coupling since the total spin is a singlet: these are $L^{\mathrm{eff}} = 2, S = 0$ and $L^{\mathrm{eff}} = 2, S = 0$ states. The nine $L^{\mathrm{eff}} = 1, S = 1$ states respond to spin-orbit interaction and, as a result, combine into $J = 0, 1, 2$ states. The lowest-energy state is the singlet $J = 0$, energy λ above it lies the triplet $J = 1$, and finally, another 2λ higher in energy there is the $J = 2$ quintuplet; see the energy scheme depicted in Fig. 1.3 panel (b). Even though the low-lying singlet is nonmagnetic, we will see in later chapters that the t_{2g}^4 systems may host a Van Vleck type of magnetism, where the magnetic moment lies on the transition between the $J = 0$ singlet and $J = 1$ triplet.

An essential consequence of spin-orbit coupling is the non-uniform spin polarization of the resulting $\mathbf{J}^2$ eigenstates. SOC tries to contra-align $\mathbf{L}^{\mathrm{eff}}$ with $\mathbf{S}$, which happens differently for individual L_z^{eff}-components of original wave functions. When these get mixed to $\mathbf{J}^2$ eigenstates,

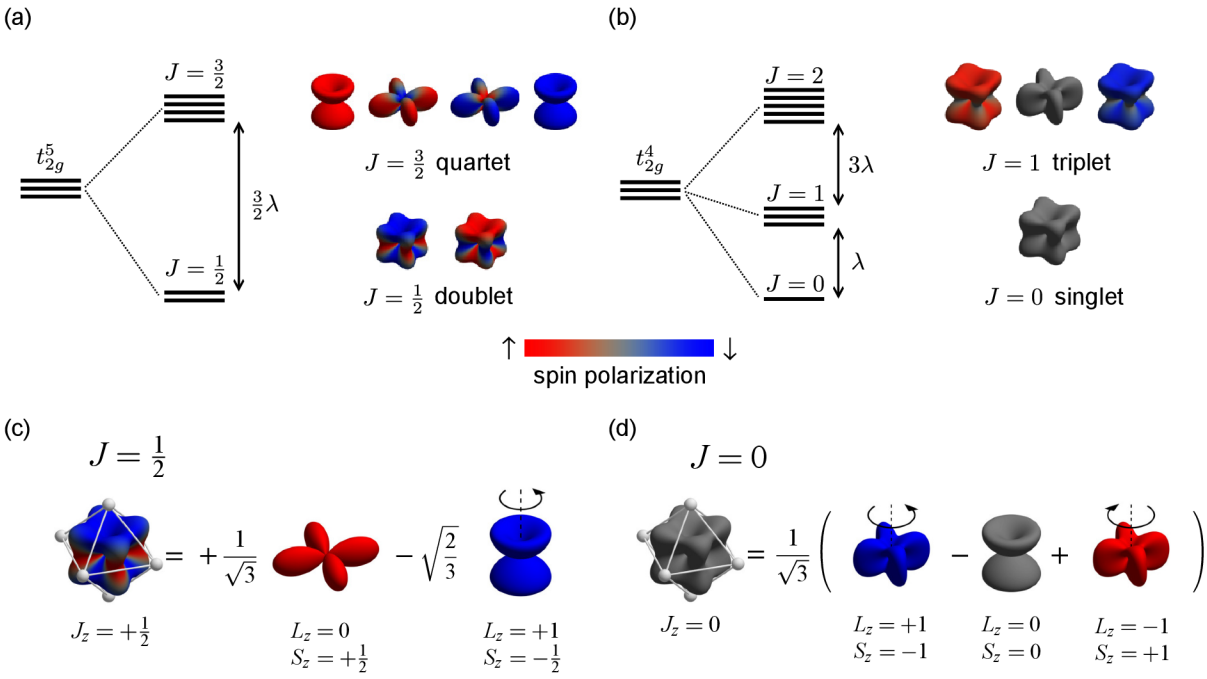

Figure 1.3: (a) Low-energy states of the t_{2g}^5 configuration split by spin-orbit coupling. The low-lying $J=\frac{1}{2}$ doublet is Kramers-degenerate and separated from the $J=\frac{3}{2}$ quartet by energy $\frac{3}{2}\lambda$. The figure also shows the shapes and spin polarization of the J moments inherited from the spin and orbital momenta comprising them. (b) Splitting of the t_{2g}^4 shell by SOC into singlet, triplet, and quintuplet levels. The ground-state is a nonmagnetic singlet, the magnetic moment is carried by higher energy $J=1$ and $J=2$ states. (c) Constituents of the $J=\frac{1}{2}$ Kramers doublet in the form of L^z, S^z eigenstates of a single hole. A non-homogeneous spin polarization of the composite state results from binding states of different spin and orbital shapes by SOC. (d) Decomposition of a $J=0$ state into two-hole states of d^4. Opposing angular momenta L and S cancel out, resulting in a fully symmetric $J=0$ state. Reproduced from [2].

a non-homogeneous spin polarization in real space arises, as can be seen in panels (c) and (d) of Figure 1.3. This effect can have far-reaching consequences: the entanglement of spin and orbital degrees of freedom translates in some cases into anisotropic effective interactions that depend on the direction of bonds – such a situation will be a content of our discussion in the future text pertaining to Kitaev interactions.

Having identified the low-energy eigenstates of both t_{2g}^4 and t_{2g}^5 electron configurations, we conclude the discussion of multiplet structure. As we have seen, the transition metal oxides contain several distinct effects reorganizing the electronic states. The energy scales of these effects are pretty similar, and their competition can lead to different behavior depending on the studied transition metal compound. In addition to the impacts discussed above, distortions of crystal field from ideal octahedral symmetry also play a non-negligible role in real materials. In the following section, we will look at the cross-talk between multiple magnetic ions in the lattice and the formation of an effective exchange model.

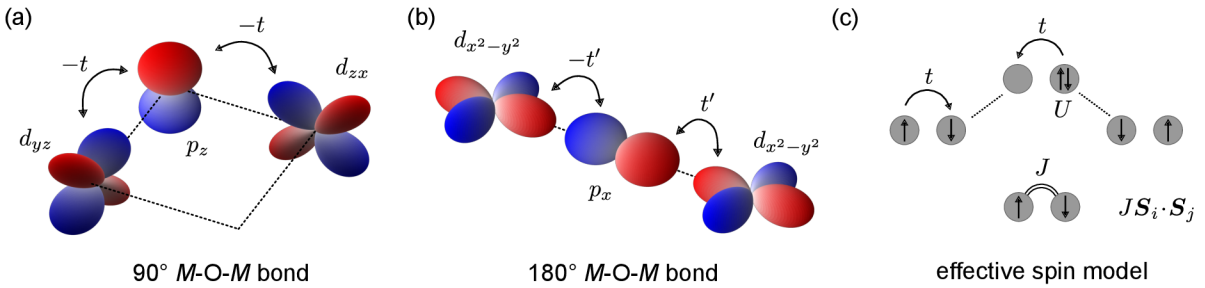

Figure 1.4: (a) 90° bonding geometry on a square plaquette, arising when neighboring oxygen octahedra share an edge. The electronic connection between two d-orbitals is mediated by an oxygen p-orbital. In this geometry, only orbitals of different species are connected by hopping. Direct hopping that does not involve oxygen states (not shown) is also possible. (b) 180° bonding geometry, which arises when MO_6 octahedra share a corner. The oxygen-mediated hopping connects two d orbitals of the same flavor. (c) Virtual hopping process between two half-filled orbitals with opposing spins. The hopping t creates an intermediate excited state with excitation energy U, relaxed by a second hopping. The associated kinetic energy gain and consequent preference of singlet is effectively captured by the Heisenberg interaction between spins. Inspired by [21].

1.1.3 Superexchange interactions and formulation of an effective model

Electronic hopping between transition metal ions

The previous discussion of the multiplet structure considered isolated transition-metal atoms, in contact only with octahedral cages of surrounding ligand atoms. When such an ion is placed into a crystal, the valence orbitals of neighboring atoms overlap, leading to a cross-talk between ions. The amount of the overlap depends on the ions and the type of valence orbitals. In d-elements, the spatial extent of d orbitals is increasing in the direction towards heavier elements, so that $5d$ electronic wave-functions are more delocalized than $3d$ wave-functions. In the limit of weakly coupled atoms, the tight-binding approximation is a well-known tool for describing electronic hopping between localized valence shells. In second quantization formalism, a simple tight-binding Hamiltonian connecting on a bond $\langle ij \rangle$ can be written as

$$\mathcal{H}_{\mathrm{TB}} = -t \sum_{\langle ij \rangle, \sigma} (c^{\dagger}_{i,\sigma} c_{j,\sigma} + \mathrm{h.c.}), \tag{1.17}$$

where t is the hopping amplitude. This simple approximation is very useful for describing how dispersing bands arise from localized states when moving the atoms closer to each other, thus increasing the overlap of electronic wave functions.

The tight-binding approach has its merit not only as a toy model but also as a fitting model for single-particle bands in *ab initio* methods for calculating electronic band structure such as density functional theory. A practical method for calculating the hopping integrals t was introduced by Slater and Koster [27]. Using the Slater-Koster integrals for the various pairs of neighboring orbitals, we can construct hopping Hamiltonians for a bonding geometry applicable in the transition metal compound of interest.

The most prominent examples of bonding geometry in transition metal oxides are 90° metal-oxygen-metal bonds and 180° bonding geometry. Figure 1.4 panel (a) shows the case of 90° M-O-M bonding, which is relevant for Na_2IrO_3. Considering a square plaquette of $d-p-d-p$

atoms, two hopping processes are applicable: (i) direct hopping between neighboring d orbitals and (ii) oxygen-mediated hopping between d orbitals. In both cases, the symmetry of orbitals and geometry of the bond dictates which hopping channels are active. As an example shown in the Figure 1.4 panel (a), a non-zero hopping amplitude arises between d_{yz} and d_{zx} orbitals, mediated by an oxygen p_z orbital. There is no hopping between d-orbitals of the same flavor, i.e., d_{xy} does not connect to d_{xy}, etc. In contrast, in the case of 180°-bond shown in panel (b), d-orbitals of the same species are active in hopping: as an example, we show the $d_{x^2-y^2} - p_x - d_{x^2-y^2}$ channel.

The $d-d$ hopping mediated by oxygen p-orbitals can be described as a multi-step process. Starting with a full valence shell of an oxygen O^{2-} ion, the initial configuration is $d^n - p^6 - d^n$. First, an electron hops from the oxygen p orbital to a metal ion, creating an intermediate state $d^{n+1} - p^5 - d^n$. The excited state is higher in energy and may be relaxed by a second hopping process, which restores the p^6 shell. Depending on the hierarchy of energy scales [28, 29], the result may either be the restored original $d^n - p^6 - d^n$ state (charge-transfer regime) or an excited $d^{n+1} - p^6 - d^{n-1}$ state (Mott-Hubbard regime), where two more electron hoppings are needed to restore the original $d^n - p^6 - d^n$ state. Such processes comprising multiple hoppings can be described by second-order perturbation theory, producing effective couplings between localized transition metal ions, often referred to as *superexchange* interactions [30, 31]. In the following paragraphs, we will describe such a perturbative treatment using a canonical example of a two-site Hubbard model.

Hubbard model and Heisenberg superexchange

With the inclusion of electronic contact between magnetic ions, we can assemble a total Hamiltonian for a transition metal oxide system:

$$\mathcal{H}_{\text{total}} = \mathcal{H}_{\text{ionic}} + \mathcal{H}_{\text{hopping}}. \tag{1.18}$$

The ionic term includes contributions of crystal field, Coulomb interactions, and spin-orbit coupling, whereas the second term brings hopping between individual ions. The problem we face is generally not solvable due to the many-body nature of Coulomb interactions. If these are relatively weak, standard band theory can be applied to obtain the electronic band structure. However, strong Coulomb interactions in localized d orbitals invalidate such one-electron approaches, as is evidenced by the case of Mott insulators [32] – whereas band theory predicts a metallic state for a material with an odd number of electrons in a valence shell, local Coulomb repulsion can render the system insulating.

Dealing with strongly correlated compounds calls for a different approach. In this thesis, we use the method of effective spin-orbital models, where the transition-metal ions have fixed valence and thus charge excitations are suppressed, leaving only interactions between localized spin and orbital degrees of freedom. To show how such an effective model can arise, we now focus on a canonical example of the single-orbital Hubbard model [16]. It encompasses the chief opposing tendencies of the electrons in a crystal: delocalization through hopping and localization due to electrostatic repulsion. The model captures the metal-insulator transition in correlated materials; depending on the energetic balance of the two tendencies, either a metal or a Mott insulator emerges.

Specifically, the Hubbard model for two sites with one orbital each has the following form:

$$\mathcal{H}_{\text{Hub}} = -t \sum_{\sigma=\uparrow,\downarrow} (c^{\dagger}_{1\sigma} c_{2\sigma} + c^{\dagger}_{2\sigma} c_{1\sigma}) + U \sum_{i=1}^{2} n_{i\uparrow} n_{i\downarrow}, \tag{1.19}$$

where t is the hopping amplitude between the sites $1,2$ and U is the on-site interaction energy, representing the energy cost associated with double occupation of one orbital. The Coulomb interactions between electrons on different sites are neglected.

Consider a lattice version of the model and the case of half-filling, meaning, on average, one electron per orbital (site). We are interested in a strong coupling limit, where the on-site repulsion dominates the hopping $U \gg t$, resulting in an insulating state with electrons on different sites. The charge distribution is thus wholly determined and the only degree of freedom is the electron spin. The spins interact by virtual hopping processes such as the one depicted in Fig. 1.4 panel (c), where an intermediate excited state is created and subsequently relaxed. The virtual hopping leads to a gain of kinetic energy by the system, which favors the singlet state of the two electrons over the triplet since hopping for triplet states is forbidden by the Pauli principle.

Mathematically, the effective spin interaction can be obtained using second-order perturbation theory, where hopping is treated as a perturbation. The basis states $|n\rangle$ of a two-electron system are one spin singlet and three triplet states, and the excited states $|\text{exc}\rangle$ are the ones with one doubly occupied site and one empty site. The effective Hamiltonian matrix is:

$$\langle n|\mathcal{H}_{\text{eff}}|n'\rangle = -\sum_{\text{exc}} \frac{\langle n|\Delta\mathcal{H}|\text{exc}\rangle \langle \text{exc}|\Delta\mathcal{H}|n'\rangle}{U}, \tag{1.20}$$

where $\Delta\mathcal{H}$ is the hopping part of the Hubbard model. Explicit calculation shows that the matrix separates into two blocks: the low-energy subspace corresponding to the singlet with energy $-\frac{4t^2}{U}$ and the high-energy sector spanned by the three triplet states with energy 0. Using spin operators, the effective interaction can be written in the form of Heisenberg Hamiltonian [33, 34]

$$\mathcal{H}_{\text{Heis}} = J\left(\mathbf{S}_1 \cdot \mathbf{S}_2 - \frac{1}{4}\right), \tag{1.21}$$

where $J = \frac{4t^2}{U}$ is the interaction constant.

The effective spin model succinctly captures the low-energy dynamics in the strong coupling limit in the form of superexchange interactions between spins. In real materials, the situation is more complicated than the above simple case, but the procedure of deriving the effective model is the same in principle. First, we identify the low-energy multiplet states, and then we treat the hopping in a perturbative manner (higher than second-order processes have to be considered for oxygen-mediated hopping). The result is an interaction matrix with a high-energy and a low-energy sector. Under the assumption that these are well-separated and weakly coupled, an effective spin Hamiltonian can be formulated in the low-energy subspace. In the following sections of this chapter, we will focus on specific examples of transition metal oxides, with effective models encoding rich and interesting physics.

1.2 Kitaev physics in relativistic $J = 1/2$ Mott insulators

Among the most interesting aspects of condensed matter research is investigating novel states of matter. The quantum spin liquid (QSL) is one of the exotic cases drawing particular attention from the community. Contrary to conventional materials, the QSL ground state does not spontaneously break symmetry but rather forms a long-ranged entangled state at zero temperature. In the first proposal of a QSL state [35], such a ground state was imagined as a quantum superposition of fluctuating pairs of spins (spin singlets), dubbed the resonating valence bond (RVB) state. This would constitute a constantly fluctuating state possessing short-range correlations, thus invoking the parallel with a liquid.

The state was expected to emerge as the ground state in $S = 1/2$ systems on highly frustrated lattices, such as the Heisenberg model on a triangular lattice. This specific model turned out to order magnetically, and conclusive proof of RVB ground states seemed elusive. As such, the honeycomb Kitaev model [4] constitutes a significant breakthrough: the model allows for an analytical solution featuring a spin liquid ground state. More than that, it contains other interesting features such as fractionalized spin excitations, which are accessible without resorting to numerics. For its importance, we will devote the first part of the current section to the Kitaev model, summarizing its essential features.

Apart from theoretical interest, the central issue regarding a spin model is its realization in an existing material. Several avenues have been proposed for the Kitaev model, including metal-organic frameworks [36, 37] and superconducting networks [38]. Perhaps the most intriguing is the proposal of Jackeli and Khaliullin [39], who showed that effective interactions of $J = 1/2$ moments in relativistic transition metal oxides can be described by an extended Kitaev model. Building on the notions developed in the preceding section, we combine the necessary ingredients to construct the effective spin model and discuss how additional couplings unavoidably arise in real materials.

Last, we discuss the materials for which Kitaev physics is expected. Here, we mention the effects brought about by additional "complications" such as distortions of the crystal field, multiple hopping channels and long-range interactions beyond nearest neighbors. With these in mind, we formulate the extended Kitaev-Heisenberg model and discuss a few chosen examples of Ir and Ru compounds as experimental realizations of this model.

1.2.1 Kitaev model and quantum spin liquid

The Kitaev model is formulated in terms of $S = 1/2$ spins interacting on a honeycomb lattice in an Ising-like way

$$\mathcal{H} = \sum_{\langle ij \rangle} K_\gamma S_i^\gamma S_j^\gamma, \tag{1.22}$$

where $\langle ij \rangle$ is the bond connecting neighboring sites i, j and $\gamma \in \{x, y, z\}$ depends on the direction of the bond. The coupling is bond-dependent, as only one spin component is active for a particular bond, depending on the bond direction – see Fig. 1.5 (a) for a sketch. The honeycomb lattice is bipartite and thus not frustrated, however, the frustration comes from the interactions. Thinking classically, every two out of three pairs of bonds can be "satisfied" by forming a spin pair in the direction dictated by the bond direction. There is a huge number of such energy-equivalent coverings of the lattice (one is shown in Fig. 1.5 (a)), leading to an extensive degeneracy in

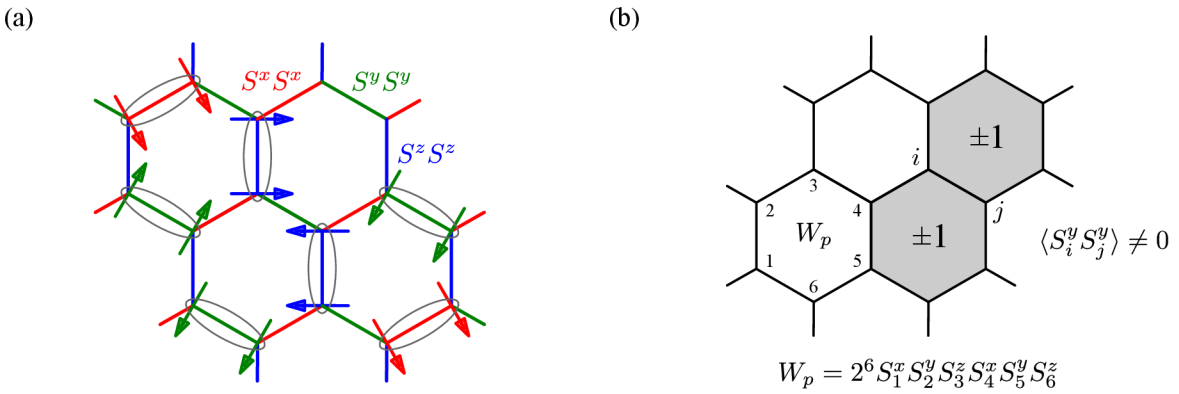

Figure 1.5: (a) Kitaev model features bond-selective interactions between nearest neighbors on a honeycomb lattice. For each one of the three possible bond directions (differentiated by color) only one spin component is interacting. The minimum of classical energy is obtained by forming spin dimers with spins pointing in the easy axis direction for the given bond type. One such configuration is sketched in the figure; the large number of degenerate coverings is a fingerprint of frustration. (b) Plaquette operator W_p is defined for each hexagon. Since it commutes with the Hamiltonian, its eigenvalues ± 1 can be used as quantum numbers (fluxes) describing the ground state. An application of local spin operator S_i^α leads to a flip of the W_p flux on two neighboring hexagons, undone by an additional S_j^α. Due to this feature, the nearest-neighbor correlator $\langle S_i^\alpha S_j^\alpha \rangle$ is non-zero, in contrast to all longer-range spin correlations.

the ground state. In the quantum case, we can represent the ground state by forming a large superposition of all such possible orderings in an RVB fashion.

Kitaev solved the model by the application of a mapping between $S = 1/2$ spins and four flavors of Majorana fermions b^x, b^y, b^z, c:

$$\sigma_\gamma = i b_\gamma c, \tag{1.23}$$

where $\sigma_\gamma = 2S_\gamma$ are Pauli spin operators. The b_γ fermions are local since bonds of a given type γ do not meet anywhere in the lattice, and thus the product $u_{ij} = i b_i^\gamma b_j^\gamma$ is a conserved quantity with eigenvalues ± 1. This insight leads to the exact solution of the model since the Hamiltonian can be diagonalized for each configuration of $\langle u_{ij} \rangle$. The over-completeness of Majorana representation is dealt with by introducing the gauge-invariant flux operator on a hexagonal plaquette:

$$W_p = \prod_{\langle ij \rangle \in p} u_{ij} = 2^6 S_1^x S_2^y S_3^z S_4^x S_5^y S_6^z, \tag{1.24}$$

see Fig. 1.5 panel (b). W_p is a conserved quantity with eigenvalues ± 1: the states can be organized into subspaces with a given plaquette configuration of W_p. The ground state is found for $W_p = 1$ at each plaquette. The fact that the ground state is specified by "flux order" described by W_p and that this operator does not commute with local spin operators S_i^α means that there is no long-range spin order and the ground state is a quantum spin liquid. The action of a spin operator S_i^α leads to a flip in W_p from $+1$ to -1 on two plaquettes connected by the α-bond, which is restored by applying S_j^α ($\langle ij \rangle$ forms the bond). Consequently, the spin-spin correlations between nearest neighbors are finite, but all longer-range correlators are zero in a true liquid fashion.

The tractability of the model by analytical methods has led to a significant understanding of the model in terms of its dynamics and excitations. For example, both spin structure factor [40]

and Raman response [41, 42] have been calculated, featuring fractionalized excitations. As a result of a specially developed numerical method, it has also been possible to obtain thermodynamical quantities over a large temperature range [43]. These exciting properties of the model have been reviewed multiple times [5, 1, 44, 45, 46]; we instead opt to proceed to the discussion of the Kitaev model in real materials.

1.2.2 Kitaev coupling in $J = 1/2$ oxides: the Jackeli-Khaliullin mechanism

However exciting the properties of the Kitaev model may be, it can be difficult at first to imagine it occurring in nature. Indeed, thinking about spin interactions arising as effective descriptions of exchange processes (see Sec. 1.1.3), we usually encounter isotropic Heisenberg-like interactions since the total spin is conserved during the electron exchange. However, orbital interactions are far more complex, displaying anisotropic behavior due to the orbital shape in real space [47]. Because of their spatial anisotropy, orbital interactions are also highly frustrated in high-symmetry crystal environments, where it is impossible to simultaneously satisfy interacting bonds from all directions. By means of strong spin-orbit coupling, it is possible to bind spin and orbital degrees of freedom, transferring the spatial anisotropy and frustrating nature of orbitals into the resulting pseudospin $\mathbf{J} = \mathbf{L} + \mathbf{S}$ [48]. This would turn out to be the critical insight in initiating the research of Kitaev materials.

In the following paragraphs, we show a brief overview of how an effective Kitaev coupling arises in relativistic $5d$ and $4d$ oxides. The complete derivation, which is relatively lengthy, can be found in Appendix A.

To obtain the Kitaev model as a result of effective pseudospin interactions, it was realized [39] that two conditions must be satisfied: (i) the balance of crystal field splitting Δ_{CF}, Hund's coupling J_H and spin-orbit coupling strength λ is such that the ionic ground state is formed by the $J = \frac{1}{2}$ pseudospin doublet, and (ii) the angle of metal-ligand-metal bond is approximately 90°. Among the first examples of materials fulfilling these conditions are layered honeycomb oxides Na_2IrO_3 and α-$RuCl_3$, whose atomic structure shows weakly coupled honeycomb planes, allowing us to treat them as quasi-two-dimensional materials. The structure of Na_2IrO_3 is shown in Fig. 1.1 (a), where $NaIr_2O_6$ honeycomb layers are stacked atop each other in a 3D structure and only weakly coupled by a layer of Na atoms. Another material α-$RuCl_3$ is very similar, the only changes are that there are no Na atoms and the magnetic ion is Ru^{3+} instead of Ir^{4+}. Around each magnetic ion are octahedral complexes formed by the halide atoms (oxygen or chlorine), sharing an edge. The edge-sharing geometry is crucial, as it leads to the formation of 90° Ir-O-Ir bonds (or, alternatively, Ru-Cl-Ru), in contrast to corner-sharing situations leading to the 180° geometry. Further, the rotational symmetry of the lattice allows us to consider only one of the three bond types (conventionally z) since the results for the other two can be obtained by suitable permutations in the orbital flavors involved.

First, consider the multiplet structure of a d^5 magnetic ion surrounded by six ligand atoms. As we have elaborated in Sec. 1.1.2, the strong crystal field of the octahedral cage defeats the first Hund's rule and separates the energy levels into low-lying t_{2g} and high-energy e_g manifolds. The five d electrons are all accommodated by the triply degenerate t_{2g} subspace, which, in the hole picture, amounts to a one-body problem. The single hole carries an unquenched orbital moment $L^{\mathrm{eff}} = -L = 1$ and spin $S = \frac{1}{2}$. The spin-orbit coupling λ can be as large as 0.5 eV for

heavy elements such as Ir, overcoming typical crystal field splittings in the t_{2g} manifold arising due to distortions in oxygen octahedra [1]. Consequently, the ionic ground state is the $J = \frac{1}{2}$ Kramers doublet. These one-half moments form a pseudospin basis, written in the $\left|J, J_z, L^{\text{eff}}, S\right\rangle$ notation as

$$|\tilde{\uparrow}\rangle = \left|\frac{1}{2}, +\frac{1}{2}, 1, \frac{1}{2}\right\rangle, \qquad |\tilde{\downarrow}\rangle = \left|\frac{1}{2}, -\frac{1}{2}, 1, \frac{1}{2}\right\rangle. \tag{1.25}$$

The tilde marks are used to emphasize that the arrows now denote $J = \frac{1}{2}$ pseudospin, as opposed to $S = \frac{1}{2}$ spins. The pseudospin states $|\tilde{\uparrow}\rangle, |\tilde{\downarrow}\rangle$ serve as our local degrees of freedom. Their electron density is cubic in shape (cf. Fig 1.3) and hosts a magnetic moment corresponding to a conventional $S = \frac{1}{2}$ state. All three orbital flavors $|xy\rangle, |yz\rangle, |zx\rangle$ are superimposed in the pseudospin states, and since the orbitals are very sensitive to the hopping geometry, relatively complex superexchange processes between pseudospins arise.

When considering hopping processes between magnetic ions, the local symmetry is crucial. In the studied example, we may single out a square plaquette containing two magnetic ions (Ir or Ru) and two ligand atoms (O or Cl). The contact between d orbitals in the valence shell of the ion and p orbitals of the ligand atoms is in the form of 90° $d-p-d$ bonds. Two hopping processes are dominant in such a situation: (i) p-mediated hopping between d orbitals and (ii) bonding between d orbitals due to direct overlap. Considering the former case, there are always two d orbitals active in the hopping processes, and the specific pair is dependent on the direction of the bond. The superexchange interactions among d^5 ions can be obtained in the framework of second-order degenerate perturbation theory, whereby hopping first creates intermediate $d^4 - d^6$ excited states, and the $d^5 - d^5$ configuration is subsequently restored by another hopping process. It turns out that the intermediate processes that arise due to p-mediated hopping are such that the typical isotropic $4t^2/U$ interaction term does not occur due to destructive interference of bonding paths. The first non-zero term is then generated by a higher-order process between excited $J = \frac{3}{2}$ states. The resulting effective coupling has an Ising-like form $S_i^z S_j^z$ on the z-bond, and due to bond dependence of orbitals active in the hopping, the coupling for perpendicular bond directions x and y is $S_i^x S_j^x$ and $S_i^y S_j^y$, respectively. This way, the Kitaev coupling emerges as the dominant interaction due to $d-p-d$ hopping processes.

The second important hopping channel we consider is the direct $d-d$ bonding. Since direct hopping conserves both spin and angular momentum, it necessarily leads to an isotropic interaction between pseudospins. Therefore, a Heisenberg interaction term $\mathbf{S}_i \cdot \mathbf{S}_j$ enters the effective model. Finally, a bond-dependent interaction term Γ arises due to the combination of p-mediated and direct $d-d$ hoppings. Altogether, the resulting effective interaction between two magnetic ions on a square plaquette perpendicular to the z direction is

$$\mathcal{H}_{ij}^z = J\mathbf{S}_i \cdot \mathbf{S}_j + K S_i^z S_j^z + \Gamma(S_i^x S_j^y + S_i^y S_j^x), \tag{1.26}$$

where S^α are pseudospin-$\frac{1}{2}$ operators. The expressions for x- and y-bonds can be obtained by cyclic permutation in the x, y, z components of pseudospin operators.

Since the interaction parameters J, K, Γ are functions of microscopic quantities – Hubbard repulsion U, Hund's coupling J_H, hopping amplitudes t ($d-p-d$ hopping) and t' (direct $d-d$ hopping) – one may try to obtain estimates for the relative strengths of J, K, Γ using *ab-initio* methods [49, 6, 50]. Unfortunately, the situation in real materials is considerably more complex. Apart from the d-d excitations that we considered, charge-transfer pd processes play

a role as well, and there are yet more exchange paths: cyclic exchange or hopping through higher-lying e_g orbitals. Due to the considerable spatial extent of $4d$ and $5d$ orbitals, long-range couplings beyond nearest neighbors also generally arise. The pseudospin wave functions can also be modified in the presence of local crystal field distortions, typically encountered as trigonal elongation or compression of the ligand octahedra. All of the mentioned effects may play some role depending on the material under consideration [5]. Because of the great difficulty in judging the relative strength of such a large number of effects, we may put aside the microscopic details and rather consider the most general nearest-neighbor Hamiltonian constrained only by the local symmetry or the bonds, which is the extended Kitaev-Heisenberg model [51, 52]:

$$\mathcal{H}^z_{ij} = J\mathbf{S}_i \cdot \mathbf{S}_j + KS^z_i S^z_j + \Gamma(S^x_i S^y_j + S^y_i S^x_j) + \Gamma'(S^x_i S^z_j + S^z_i S^x_j + S^y_i S^z_j + S^z_i S^y_j). \tag{1.27}$$

Compared to the effective model (1.26), an extra off-diagonal Γ' term emerges as a result of including further C_3-preserving distortions. Because of its generality, we can expect the model to apply to a relatively wide range of suitable materials. An exception to this would be materials in which distortions of the local octahedral field lower the symmetry further, where additional terms may be required to fully parametrize the interactions, such as Dzyalozhinskii-Moriya interactions between second neighbors [5]. We will, however, not consider such low-symmetry cases in this thesis and instead consider the model (1.27) extended by third-nearest neighbor Heisenberg coupling J_3, which seems to be the most important out of next nearest neighbor interactions [6].

1.2.3 Signatures of Kitaev physics in real materials

Kitaev coupling extended by further interaction terms can arise in relativistic $J = \frac{1}{2}$ Mott insulators with approximately 90° metal-ligand-metal bond geometry. Layered honeycomb structures were the earliest suggestions, but Kitaev physics is not limited to this single case. On the contrary, there is a relatively large number of lattice geometries where the extended Kitaev-Heisenberg model is relevant. In case of 2D structures, there are studies on triangular [48, 53, 54, 55, 56] and kagomé [57] lattices, but many three-dimensional structures are possible, too. These include experimentally realized hyperhoneycomb [58, 59, 60, 61, 62], harmonic honeycomb [63, 64, 65, 59, 61], hyperkagomé [66, 67], fcc [68, 69, 70], and pyrochlore lattices [71, 72], or hypothetical hyperoctagon lattice [73]. Concerning specific materials, the largest group of Kitaev candidate materials is represented by iridium oxides, mostly a variants of A_2IrO_3 stoichiometry. These include Na_2IrO_3 [74, 5, 75, 76, 77], Cu_2IrO_3 [78], α-Li_2IrO_3 [79, 80, 81], β-Li_2IrO_3 [58, 64, 82, 83], and γ-Li_2IrO_3 [63, 64]. The variety of Ir^{4+} candidate compounds was broadened further by starting with the α-Li_2IrO_3 structure and replacing the Li^+ ions sitting between the honeycomb layers with a different monovalent ion. The resulting materials include $H_3LiIr_2O_6$ [84], $Cu_3LiIr_2O_6$ [85] and $Ag_3LiIr_2O_6$ [86].

The key element in all mentioned compounds is the magnetic Ir^{4+} ion that belongs to the $5d$ family and thus features a large SOC necessary for the formation of $J = \frac{1}{2}$ pseudospins. From the $4d$-based compounds, ruthenium halides α-$RuCl_3$ [87, 88, 89, 90, 91] and more recently $RuBr_3$ [92] have been considered; especially α-$RuCl_3$ is an important example, as it is one of the most studied Kitaev materials. Surprisingly, even materials based on $3d$ elements with considerably weaker SOC have been suggested to host Kitaev physics [3, 93, 94]. Some examples

are cobaltates $Na_2Co_2TeO_6$ [95] or $A_3Co_2SbO_6$ (A=Na,Ag,Li) [95, 96, 97, 98] in the d^7 valence configuration with active e_g orbitals.

Most experimental efforts targeting Kitaev candidates strive to demonstrate the presence of a quantum spin liquid state in an existing material. The task is a difficult one, mainly for two reasons: (i) highly entangled states are rarely found in nature, and (ii) the lack of unambiguous smoking-gun experimental measurements [15]. Some signatures of the Kitaev mechanism can be probed separately, e.g., the formation of $J = \frac{1}{2}$ pseudospin moments, bond-directionality of interactions [99] or the degree of frustration. Better than that, it is desirable to access detailed information about the low-energy dynamics of a material, and to that end, one needs to probe the time-resolved spin excitations. The traditional method of choice for studying magnetic properties is inelastic neutron scattering (INS). However, recent advances in the energy resolution of resonant inelastic x-ray scattering (RIXS) instrumentation have also made it possible to use RIXS to study low-energy phenomena. Perhaps the most studied Kitaev candidates are Na_2IrO_3 and α-$RuCl_3$, which have been among the first materials proposed to host Kitaev physics, and in the case of Na_2IrO_3 also the quantum spin Hall effect [100]. In the next paragraphs, we provide an overview of the unconventional physics found in Na_2IrO_3 and mention some of the challenges that arise when studying Kitaev magnetism.

Na_2IrO_3

Sodium iridate Na_2IrO_3 crystallizes in a quasi-2D honeycomb structure [101] consisting of $NaIr_2O_6$ layers stacked upon each other with additional Na atoms in-between the layers, as shown in panel (a) of Figure 1.1. As part of the $NaIr_2O_6$ sheets, iridium atoms form a honeycomb lattice surrounded by edge-sharing oxygen octahedra (cf. Fig. A.1). Na_2IrO_3 exhibits insulating behavior – the charge gap inferred from the optical conductivity spectrum [102] is 340 meV. The origin of the charge gap is not completely obvious, as similar compounds are often found to be correlated metals [103]. Nevertheless, the prevailing picture is that Na_2IrO_3 features a Mott-insulating state assisted by strong spin-orbit coupling. RIXS measurements [104] of crystal field splitting of Ir $5d$ states provide evidence for this statement: observed low-energy excitations at 0.7 eV correspond to $J = \frac{1}{2} \to \frac{3}{2}$ transitions within the t_{2g} manifold requiring energy $3\lambda/2$ (hence $\lambda \approx 0.5$ eV). Moreover, the relevant RIXS peak is split, which likely originates in trigonal lattice distortions of the oxygen octahedra. The energy scales of both spin-orbit coupling strength λ and trigonal crystal field Δ_{tri} can be inferred from the spectra, leading to an estimate $\Delta_{\text{tri}}/\lambda \approx 0.1$ [105]. Because $\lambda > \Delta_{\text{tri}}$, we can expect Na_2IrO_3 to be well-described by a pseudospin-$\frac{1}{2}$ ground state, though distortions play a role as second-order effects.

Magnetic properties are often studied using temperature-dependent magnetic susceptibility $\chi(T)$. At high temperatures, the form of $\chi(T)$ can be modeled by the phenomenological Curie-Weiss law

$$\chi(T) = \chi_0 + \frac{C}{T - \Theta}, \tag{1.28}$$

where χ_0 is the temperature-independent susceptibility, C is a constant dependent on the effective magnetic moment μ_{eff} and Θ is the Weiss constant that characterizes the sign and scale of magnetic interactions. For Na_2IrO_3, measurements of magnetic susceptibility show Curie-Weiss behavior [74, 79], although strongly anisotropic. Initially, the fits gave a value of $\Theta \approx -125$ K, which was much larger than expected from the estimates provided by *ab-initio* calculations [106, 107, 6]. Recently, it has been suggested [108] that the simple Curie-Weiss

form (1.28) is inadequate for spin-orbit coupled magnets. Using a modified approach taking into account high-energy van Vleck contributions to $\chi(T)$, the Curie constant Θ was fitted to a nearly isotropic value of $\Theta \approx -75$ K [108]. At low temperatures, Na_2IrO_3 undergoes a phase transition to a long-range ordered state, as evidenced by anomalous features in specific heat and magnetic susceptibility around $T_N = 15$ K [74, 101, 76]. This may be disappointing in light of the fact that, as a Kitaev candidate, the hope was to find a spin liquid state without long-range order. On the other hand, the suppression of T_N below Θ can be interpreted as a sign of frustration, which is expected for materials close to a spin liquid regime.

The type of magnetic ordering is zigzag, in which ferromagnetic zigzag chains are stacked antiferromagnetically along a direction perpendicular to the chains [101, 76] – see Fig. 1.6 (a). Even though the zigzag order was established theoretically based on the Kitaev coupling extended by a Heisenberg interaction [109], a better theoretical grasp of the magnetic interactions would require high-quality spin excitation spectra. These are difficult to obtain in the case of Na_2IrO_3 due to the fact that iridium is a strong neutron absorber. Nevertheless, x-ray probes could provide some clues about the nature of interactions.

In diffuse magnetic x-ray scattering experiments [99], the experimental geometry was manipulated so that individual components of momentum-resolved spin-spin correlations could be accessed. As we can see on the presented momentum-dependent maps in Fig. 1.6 (b), the map corresponding to each diagonal component of the correlations contains two pairs of Bragg spots, complementary to the other two components. When combined, the result is a perfectly symmetrical pattern featuring Bragg spots corresponding to the zigzag magnetic ordering. The interpretation of this puzzling observation is based on the fact that there are three possible zigzag directions on the honeycomb lattice, each characterized by a different pair of Bragg spots, as shown in Fig. 1.6(a). Above the ordering temperature T_N, all three such patterns are mixed in the ground state, explaining the symmetrical shape of the combined correlation map. Moreover, due to the bond-dependent Kitaev interaction, the direction of the ordered magnetic moment differs for each zigzag type (shown as 1,2,3 in the picture), which in turn features distinct Bragg spots. In this way, momentum- and real-space directions are tied in the resulting $\langle S^\alpha_{-\mathbf{q}} S^\alpha_{\mathbf{q}} \rangle$ maps. Moreover, the resolution into components makes it possible to extract the direction of magnetic moment from the experiment, which, as we will refer to several times in the thesis, can be used to guide numerical calculations.

The strong anisotropy present in spin-spin correlation maps indicates the dominance of bond-directional Kitaev interaction over any possible isotropic couplings. Some non-Kitaev interactions have to be present to establish long-range order. To judge the relative strength of isotropic and anisotropic interactions, the authors of [99] performed an ED calculation of a model containing Kitaev $K < 0$ and Heisenberg $J_{1,2,3} > 0$ couplings in a proportion given by ξ. Fig. 1.6 (c) shows a progression of $\langle S^\alpha_{-\mathbf{q}} S^\alpha_{\mathbf{q}} \rangle$ maps with increasing proportion of Kitaev K. At the far left at $\xi = 0$, only Heisenberg interactions are present, resulting in a symmetric pattern of zigzag Bragg spots; J_2, J_3 terms up to third neighbors have to be included to stabilize zigzag instead of a Néel state. On the other hand, purely Kitaev coupling at $\xi = 1$ leads to a cosine-like pattern characteristic of the Kitaev spin liquid state. Between the limits, one can observe an asymmetry in the intensity of Bragg spots, with one pair being suppressed by K. By comparison with experimental data in Fig. 1.6 (b), it seems that Na_2IrO_3 is close to the Kitaev limit, and Heisenberg interactions are comparatively weak. One should, however, keep in mind that further anisotropic exchange terms Γ, Γ' are expected in the real material as well.

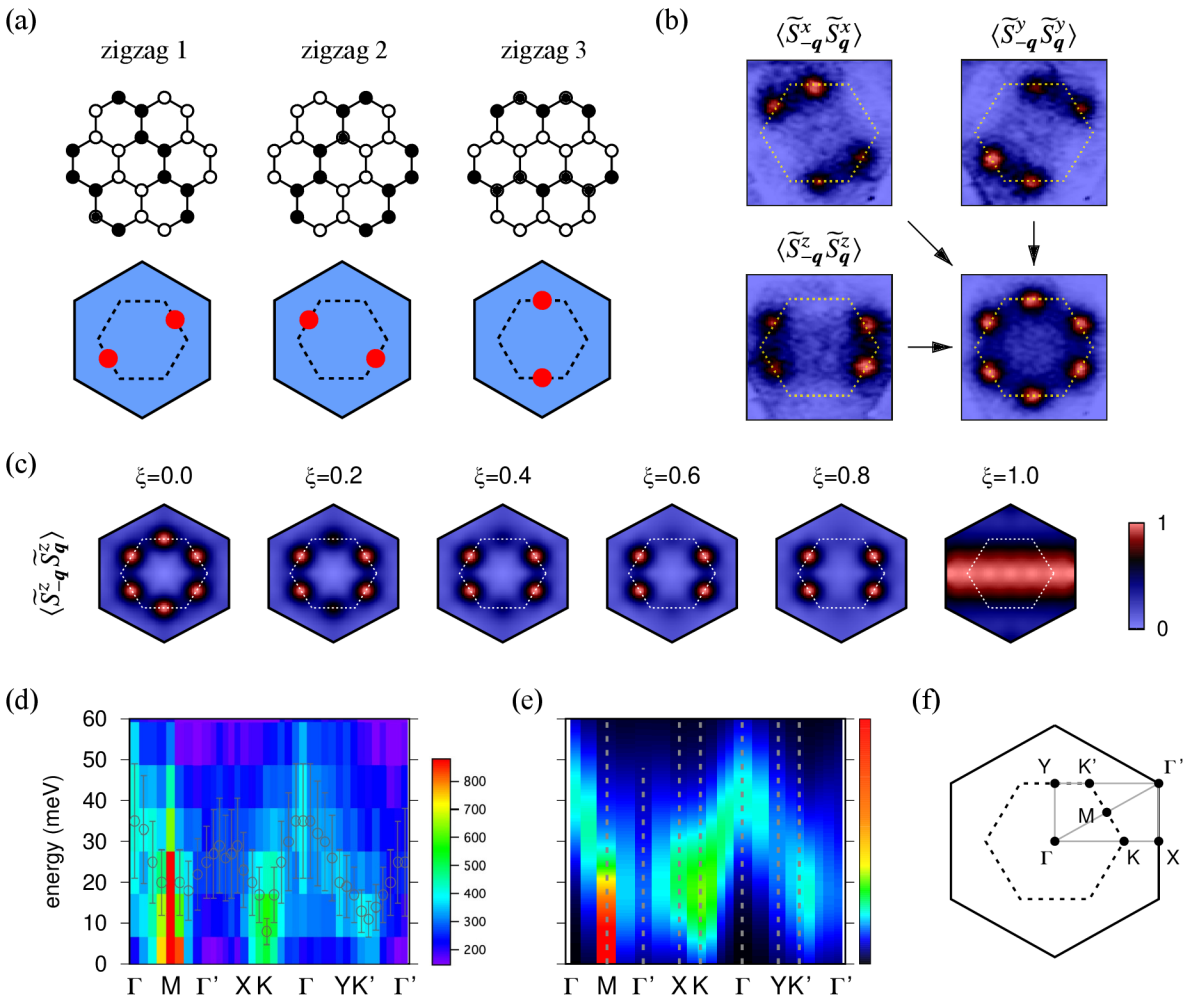

Figure 1.6: (a) Three possible zigzag orderings on the honeycomb lattice and the corresponding Bragg spots at the edges of the first Brillouin zone of the honeycomb lattice. (b) Momentum-space maps of the diagonal components of spin-spin correlation functions $\langle S^{\alpha}_{-\mathbf{q}} S^{\alpha}_{\mathbf{q}} \rangle$ as determined from the diffuse magnetic x-ray scattering measured right above T_N. The bottom right figure shows the sum of all diagonal terms $\sum_{\alpha=x,y,z} \langle S^{\alpha}_{-\mathbf{q}} S^{\alpha}_{\mathbf{q}} \rangle$. (c) Progression of $\langle S^{z}_{-\mathbf{q}} S^{z}_{\mathbf{q}} \rangle$ simulated for a model combining Kitaev coupling $K = -\xi$ and Heisenberg couplings up to third nearest neighbor $J = J_2 = J_3 = 1 - \xi$. The comparison with experimental data in (b) hints at the dominance of Kitaev coupling. (d) RIXS response measured by Kim *et al.* [77] in the ordered phase at $T = 7$ K. (e) Theoretical spectra obtained by exact diagonalization of the extended Kitaev-Heisenberg model [77] with model parameters are $J \approx 10$ meV, $K \approx -15$ meV, $\Gamma \approx 16$ meV, $\Gamma' = -2.4$ meV, $J_2 = 1.2$ meV, $J_3 = 2.4$ meV. Panels (a)-(c) reprinted from Refs. [99, 21], (d)-(f) from Ref. [77].

Recently, a thorough analysis of the excitations in Na_2IrO_3 in the framework of extended Kitaev-Heisenberg model (1.27) was made possible by enhanced-resolution RIXS measurements [77]. The experimental spectrum with a resolution of 12 meV is shown in Fig. 1.6 (d) along a Brillouin-zone path displayed in panel (f). The spectrum is gapped with maximum intensity in the M point, as is expected for the zigzag order. Despite the limited momentum-space resolution, the spectrum was successfully simulated by exact diagonalization (see panel (b) of Fig. 1.6), allowing for an interpretation. The sharp low-energy features are due to Heisenberg

interactions, whereas K and Γ terms define the shape of higher-energy features. These are significantly broadened since they are subject to strong decay processes. The best fit of the spectra was obtained for $-K \approx \Gamma > J > \Gamma', J_2, J_3$, i.e. Kitaev interaction is among the strongest. The link between momentum space correlations and pseudospin components provided by the bond-dependent K is present once again – whereas M and Y points in the Brillouin zone would be equivalent in the isotropic case, the spectra show significant intensity only in the M point. As a final point, we note that the theoretical interpretation of data was greatly aided by the use of hidden symmetries of the extended Kitaev-Heisenberg model, which, as one of the key parts of this thesis, will be discussed at length in Sec. 2.1.2.

1.3 Van-Vleck magnetism in d^4 transition metal oxides

In transition metal ions with an odd number of electrons in the valence d shell, such as the t_{2g}^5 configuration relevant for iridates, the spin of the valence states is half-integer. Together with an unquenched angular momentum, the strong spin-orbit coupling binds S and L^{eff} to half-integer total angular momentum states J. The ground state of such an ion is degenerate, as dictated by Kramers theorem, and is magnetically active. In this section, we move to a conceptually different case, where the valence shell of a transition metal ion contains an even number of electrons, more specifically, the t_{2g}^4 configuration found in $4d$ ions such as Ru^{4+} and $5d$ ions like Re^{3+} or Os^{4+}. In such cases, the integer spin and orbital momentum bound by spin-orbit coupling generate $J = 0$ nonmagnetic singlet as the ground state. The magnetism comes from the excitations to $J = 1$ triplet level and is called Van-Vleck magnetism [110].

The effective description of such systems is naturally formulated in terms of singlet-triplet transitions. The on-site superposition of spinless singlets and spinful triplet states produces a local pseudospin moment which is "soft", meaning not of fixed length, but rather undergoing length fluctuations. One example are frustrated t_{2g}^4 systems with 90° bonding geometry, which feature a singlet-triplet model which can be connected to the Kitaev model [111, 112]. Similar physics can be observed in systems with singlet-triplet states on bonds, such as various dimer systems [113, 114] or bilayer magnets [115].

In this thesis, we describe a case of t_{2g}^4 Ru^{4+} ions in Ca_2RuO_4, where the interatomic exchange interactions are close in energy to the spin-orbit energy scale separating the singlet and triplet states, allowing for the emergence of amplitude pseudospin fluctuations, also called Higgs mode.

1.3.1 Soft spins and Higgs mode

Let us study the magnetic moment of the t_{2g}^4 shell in some detail and explain the notion of Van Vleck magnetic moment. From definition, the magnetic moment operator relates to spin and orbital angular momentum

$$\mathbf{M} = -\mu_B(\mathbf{L} + g_0\mathbf{S}), \tag{1.29}$$

where $\mu_B = e\hbar/2m_e \doteq 9.27 \times 10^{-24}\ \text{JT}^{-1}$ is the Bohr magneton and $g_0 \approx 2$ is the electron g-factor. For simplicity, use a notation where $\mathbf{M} = \mathbf{L} + g_0\mathbf{S}$, leaving out the Bohr magneton with a minus sign, which has to be added to the Zeeman $-\mathbf{B}\cdot\mathbf{M}$ term to preserve the form of the interaction Hamiltonian. As we have shown in Section 1.1.2, the crystal environment quenches

the angular momentum of the d shell considerably, and only a reduced $L^{\text{eff}} = 1$ residing in t_{2g} orbitals remains, therefore we have $\mathbf{M} = 2\mathbf{S} - \mathbf{L}^{\text{eff}}$.

For the d shell in t_{2g}^4 configuration, we consider the lowest two levels split by spin-orbit coupling, the $J = 0$ singlet and $J = 1$ triplet. A convenient formal way to handle this situation is to introduce a set of singlet and triplet operators s, T_{+1}, T_0, T_{-1} which create the $J = 0$ and $J = 1$ states out of the full t_{2g}^6 shell. In terms of $|J, J_z\rangle$ states, the definition is [111]

$$\begin{aligned} s^\dagger \left| t_{2g}^6 \right\rangle &= |0,0\rangle\,, \\ T_{\pm 1}^\dagger \left| t_{2g}^6 \right\rangle &= |1,\pm 1\rangle\,, \\ T_0^\dagger \left| t_{2g}^6 \right\rangle &= |1,0\rangle\,. \end{aligned} \tag{1.30}$$

The triplet states can be rearranged to the cartesian form $\mathbf{T} = (T_x, T_y, T_z)$ using a transformation

$$\begin{aligned} T_x &= \frac{1}{i\sqrt{2}}(T_{+1} - T_{-1}), \\ T_y &= \frac{1}{\sqrt{2}}(T_{+1} + T_{-1}), \\ T_z &= iT_0. \end{aligned} \tag{1.31}$$

In this basis the matrix elements of the magnetic moment operator evaluate to a simple form. We obtain two contributions:

$$\begin{aligned} \langle T_\beta | (2\mathbf{S} - \mathbf{L}^{\text{eff}})_\alpha | T_\gamma \rangle &= -\frac{i}{2}\varepsilon_{\alpha\beta\gamma}, \\ \langle s | (2\mathbf{S} - \mathbf{L}^{\text{eff}})_\alpha | T_\beta \rangle &= -i\sqrt{6}\delta_{\alpha\beta}. \end{aligned} \tag{1.32}$$

Altogether, the magnetic moment hosted by the singlet-triplet ion can be written using the $s, \mathbf{T}$ operators as

$$\mathbf{M} = -\frac{i}{2}(\mathbf{T}^\dagger \times \mathbf{T}) - i\sqrt{6}(s^\dagger \mathbf{T} - \mathbf{T}^\dagger s). \tag{1.33}$$

The first term represents the magnetic moment residing on the $J = 1$ levels, with a quite modest g-factor of $\frac{1}{2}$. In conventional Mott insulators, this is the only type of term that contributes to the magnetic moment. In our case, however, the second term emerges, representing the van Vleck contribution of singlet-triplet excitations. For this reason, such magnetism is also sometimes called "excitonic magnetism."

Let us devote a few paragraphs to the fluctuations of the van Vleck magnetic moment. The spin-orbit coupling energy separates the triplet excitations from the ground state. However, superexchange interactions lower their energy and give them dispersion. The emergence of a long-range order of magnetic moments on the lattice depends on the balance of spin-orbit energy scale λ and superexchange energy J. In the limit where SOC dominates $\lambda \gg J$, the ground state is made of singlets with excitations to triplet states with bandwidth J. At the other extreme $J \gg \lambda$, the triplet excitations carrying the magnetic moment are condensed and form a long-range order. Somewhere between these limits, there is a point where λ and J are balanced such that the dispersion of excitations just touches zero, and a quantum phase transition is observed. Here, the ground state switches to the Bose-Einstein condensate of triplet excitations.

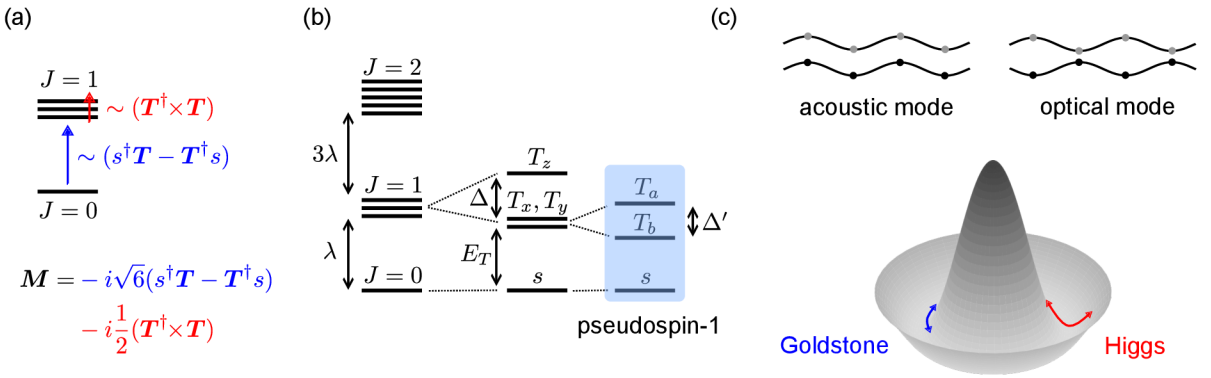

Figure 1.7: (a) Low-energy states of the spin-orbit-coupled t_{2g}^4 configuration. The lowest $J = 0$ level is nonmagnetic, and the triplet $J = 1$ level carries a magnetic moment with a rather small g-factor of $\frac{1}{2}$. The largest contribution to the magnetic moment comes from the Van Vleck part, i.e., from the transitions between $J = 0$ and $J = 1$ states. (b) Splitting of the t_{2g}^4 multiplet structure by crystal field distortions. Tetragonal crystal field Δ splits the $J = 1$ triplet into a low-energy T_x, T_y doublet, and a high-energy T_z state, effectively confining the magnetic moment to the xy plane. Further orthorhombic deformations split the doublet into distinct T_a, T_b levels, favoring the b direction. The trio of s, T_a, T_b states form a convenient basis for pseudospin-1 effective description. (c) A pictorial sketch of a massless Goldstone mode and massive Higgs mode. Goldstone modes relate to phase oscillations of the order parameter along a minimum of the mexican hat potential, whereas the Higgs mode represents symmetric amplitude oscillations. These modes may be understood in an analogy with oscillations of a diatomic linear chain featuring a gapless acoustic mode and a gapped optical mode. Panel (b) inspired by [21], panel (c) by [116].

The condensate creates order, but close to the transition, the ordered moments are still "soft" and undergo strong amplitude fluctuations. In the excitation spectra, the above fact is manifested by a splitting of a previously degenerate set of three modes (corresponding to three triplet levels) to two magnons and one amplitude mode.

The distinction between spin waves and an amplitude mode can be compared [116] to oscillating modes of a linear atomic chain with two types of atoms per primitive cell. Two oscillating modes arise: an acoustic and an optical mode. In an acoustic mode, both kinds of atoms oscillate at the same frequency, amplitude, and phase, their relative displacement staying unchanged – see Fig. 1.7 panel (c). The collective excitation that corresponds to this mode is the acoustic phonon, whose dispersion is linear with the wavevector $\mathbf{q}$ and touches zero at $\mathbf{q} = 0$; it is therefore gapless. In the optical mode, the atoms oscillate opposite each other; they are out of phase. The relative displacement of the atom species oscillates, too. The relevant elementary excitation is the optical phonon. The dispersion of an optical phonon is gapped, meaning its excitation always costs energy.

The acoustic phonon can be seen as analogous to a spin wave (magnon), and the optical phonon as an analog of the amplitude mode. Both arise from the spontaneous breaking of global continuous symmetry [117, 118], one being the phase oscillations of the order parameter and the other the amplitude oscillations. The phase oscillations – Goldstone modes – are well-known in condensed matter, mainly in the form of phonons, and in magnets as spin waves. The Higgs mode is more famous in its relativistic form in particle physics [119]. Recently,

the existence of Higgs modes in solid state systems has been shown in multiple contexts, for example, in superconductors [120], topological insulators [121], and others.

1.3.2 Effective singlet-triplet model

We will now show the basic steps needed to derive an effective model for Ca_2RuO_4, following [111, 21]. The states that form a basis for the effective model are the nonmagnetic $J = 0$ ground state, and the three $J = 1$ triplet states that arise in the multiplet structure of the t_{2g}^4 configuration. We neglect the $J = 2$ quintuplet with energy 3λ higher than the $J = 1$ triplet. The local part of the effective model is simple – it counts the excitation energy of triplets with respect to the singlet ground state, i.e.

$$\mathcal{H}_{\text{loc}} = \lambda \sum_i n_{Ti} = E_T \sum_i n_{Ti}, \tag{1.34}$$

where we use the symbol $E_T = \lambda$ to denote the triplet excitation energy henceforth. Next, we incorporate interatomic hopping, which generates an effective interaction on the bond. The bonding geometry relevant for Ca_2RuO_4 features 180° metal-ligand-metal bonds characteristic for corner-shared octahedra surrounding the metal ions. As we have discussed before, in this case, two of the three t_{2g} orbitals are active for each bond direction, and the non-zero interaction channel is between orbitals of the same type. These considerations are included in the form of hopping interaction for a z-bond:

$$\mathcal{H}_{\text{hop}} = -t(d_{yz}^\dagger d_{yz} + d_{zx}^\dagger d_{zx}). \tag{1.35}$$

In contrast, for the 90° bond geometry, we found that only orbitals of different species are coupled.

Based on the hopping Hamiltonian, it is possible to generate the virtual excited states in the singlet-triplet basis and form the superexchange model in a similar fashion as in the case of Kitaev-Heisenberg model in Sec. 1.2. An alternative route involves the formulation of a general spin-orbital Kugel-Khomskii [122] model in the $L^{\text{eff}} = 1, S = 1$ subspace. The Kugel-Khomskii spin-orbital model contains two parts, one belonging to the spins and the other to orbitals. The spin part is isotropic and has the form of the dot product $\mathbf{S}_i \cdot \mathbf{S}_j$. This is not the case for the orbital part, which depends on the bonding geometry, and thus, the specific form of the Kugel-Khomskii model for Ca_2RuO_4 is constructed according to the above geometry considerations. Finally, the spin-orbital model is projected to the $J = 0, 1$ basis by expressing the products of spin and orbital operators in the singlet-triplet basis $s, \mathbf{T}$ and neglecting parts that fall to the $J = 2$ sector. After the projection, the singlet-triplet effective Hamiltonian is obtained.

$$\mathcal{H}_{\text{eff}} = E_T \sum_i n_{Ti} + J \sum_{\langle ij \rangle} \sum_\alpha \left[(T_\alpha^\dagger s)_i (s^\dagger T_\alpha)_j - (T_\alpha^\dagger s)_i (T_\alpha^\dagger s)_j + \text{h.c.} \right], \tag{1.36}$$

where J is the superexchange interaction strength related to t and U. There are two types of superexchange processes: one involves the hopping of triplet excitations between sites I, j, and the other represents the creation/annihilation of a pair of triplet excitations. These bring kinetic energy gains and generate a dispersion of the initially flat triplet excitations.

There are further effects that alter the model form. The most important such effect that we have not mentioned yet is the tetragonal deformation of oxygen octahedra in Ca_2RuO_4. Due to

these deformations, a tetragonal crystal field brings the planar d_{xy} orbital lower in energy. In terms of **T** levels, this effect is manifested by lifting up the T_z level from T_x, T_y by a tetragonal crystal field energy Δ, as is shown in Figure 1.7 panel (b). From the point of view of the model, the T_z level is simply omitted, and a singlet-doublet model remains (the α index in the above equation (1.36) then runs only through x, y). With three degrees of freedom left, it is possible to introduce a pseudospin-1 basis. The mapping of pseudospin-1 operators S_x, S_y, S_z onto the singlet and triplet operators s, T_x, T_y reads as:

$$\begin{aligned} S_x &= -i(s^\dagger T_x - T_x^\dagger s), \\ S_y &= -i(s^\dagger T_y - T_y^\dagger s), \\ S_z &= -i(T_x^\dagger T_y - T_y^\dagger T_x). \end{aligned} \tag{1.37}$$

The effective Hamiltonian in a pseudospin-1 basis can be derived by projecting the spin-orbital Kugel-Khomskii model on the pseudospin-1 basis. For an x-bond, the Hamiltonian reads:

$$\mathcal{H}^x = E_T \sum_i (S_i^z)^2 + \sum_{\langle ij \rangle} \left[(J+A) S_i^x S_j^x + (J-A) S_i^y S_j^y + J(1-\alpha) S_i^z S_j^z \right]. \tag{1.38}$$

The isotropic part of the model $J(S_i^x S_j^x + S_i^y S_j^y)$ corresponds to the previously derived singlet-triplet model (1.36) with T_z projected out. We include some extra terms that were left out before, namely the A-term and a J_z interaction in a parametrization containing a z-anisotropy parameter α. The A-term is bond-dependent: the sign in front of the parameter A is reversed for the y-bond.

Finally, there is one more effect to consider, specifically the orthorhombic crystal field Δ'. The crystal field Δ' is related to an in-plane anisotropy favoring a direction $b = \frac{x+y}{\sqrt{2}}$ over the perpendicular direction $a = \frac{x-y}{\sqrt{2}}$. The anisotropy lifts the in-plane degeneracy and locks the magnetic moment in the long-range-ordered phase to the b-direction. The effect is captured by a Hamiltonian term

$$\mathcal{H}_{\text{ortho}} = \frac{1}{2}\Delta'(n_{Tx} - n_{Ty}) = \frac{1}{2}\Delta'(S_a^2 - S_b^2) = -\frac{1}{2}\Delta'(S_x S_y + S_y S_x). \tag{1.39}$$

In conclusion, the final form of the effective pseudospin-1 Hamiltonian for Ca_2RuO_4 which we will use throughout the third chapter, consists of a local part containing triplet excitation energy E_T and anisotropy parameter Δ' together with a bond interaction consisting of both bond-isotropic terms J, α as well as a bond-anisotropic A-term:

$$\begin{aligned} \mathcal{H}^{\text{eff}} &= \sum_i \mathcal{H}_i^{\text{loc}} + \sum_{\langle ij \rangle \in \text{NN}} \mathcal{H}_{ij}^{(\xi)}, \\ \mathcal{H}_i^{\text{loc}} &= E_T \left(S_i^z\right)^2 - \tfrac{1}{2}\Delta' \left(S^x S^y + S^y S^x\right)_i, \\ \mathcal{H}_{ij}^{(\xi)} &= (J + A_\xi) S_i^x S_j^x + (J - A_\xi) S_i^y S_j^y + J(1-\alpha) S_i^z S_j^z, \end{aligned} \tag{1.40}$$

where

$$A_\xi = \begin{cases} +A & \text{if } \xi \parallel x \\ -A & \text{if } \xi \parallel y \end{cases}. \tag{1.41}$$

1.3.3 Higgs mode in Ca_2RuO_4

Among the real materials, calcium ruthenate Ca_2RuO_4 has emerged as a prime candidate for a realization of the excitonic singlet-triplet magnetism assisted by spin-orbit coupling. It crystallizes in a distorted perovskite structure [123] with relatively low symmetry – see panel (b) of Figure 1.1. Experimentally, it was identified as a Mott insulator [123, 124], showing a metal-insulator transition around 360 K [125]. At temperatures below $T_N \approx 110$ K it develops antiferromagnetic order [123, 126, 127]. Because of the relatively low local symmetry around the Ru^{4+} ion, it was suspected that the orbital momentum is fully quenched [128, 129], producing an exclusively spin-related isotropic magnetic moment. However, early experiments showed [130] that spin-orbit coupling is strong enough to induce a substantial angular momentum, producing a $J = 0, J = 1$ hierarchy of spin-orbit momentum states. More recently, resonant inelastic x-ray scattering (RIXS) experiments [131] quantified the crucial energy scales λ (SOC strength), Δ (tetragonal distortion), and J_H (Hund's coupling strength), showing unequivocally that their balance places Ca_2RuO_4 in the regime of excitonic magnetism.

Questions about the origin of magnetic states are often answered by accessing dynamical magnetic susceptibility through scattering probes. Such an experiment was performed for Ca_2RuO_4 using spin-polarized inelastic neutron scattering (INS) [18]. The measured magnetic spectra shown in Fig. 1.8 panel (a) have an unusual shape, with a global maximum at $\mathbf{q} = (0,0)$, which is very different from isotropic Heisenberg-like magnets, which have a minimum at zero momentum (and at the ordering wavevector). This proves that orbital momentum is unquenched, and its anisotropic nature alters the magnetic interactions. The experimental spectrum is similar to the one obtained for the XY-model, which is explained by the $\approx 2\%$ tetragonal compression of oxygen octahedra, which lifts one member of the $J = 1$ triplet up in energy, confining the moment into an $a - b$ plane. The ordered moment is found to be locked to the crystallographic b direction as a result of orthorhombic distortions. The shapes of measured spectra agree exceptionally well with spectra derived from the effective soft-spin model as given in the previous section, with parameter values $E_T = 25$ meV$, J = 5.8$ meV$, \alpha = 0.15, A = 2.3$ meV$, \Delta' = 4.0$ meV. The inelastic neutron spectra show a well-defined dispersive Higgs mode [18]. Its visibility is, however, not guaranteed in general – it depends heavily on the symmetry of the probe and dimensionality [133, 134]. In the specific polarization corresponding to the Higgs mode, INS probes longitudinal magnetic susceptibility. Unfortunately, observation of the Higgs mode in this channel is hindered by a simultaneous excitation and a decay into a 2-magnon continuum. For this reason, the spectra at ordering wavevector $\mathbf{Q} = (\pi, \pi)$ feature a broad dispersive 2-magnon peak, see Fig. 1.8 panel (c). Nevertheless, the Higgs mode is well-visible at different points in the Brillouin zone, such as $\mathbf{q} = (0,0)$ shown in panel (b).

A somewhat surprising contribution to the Higgs mode "hunt" is provided by Raman scattering, which probes the vibrational states of the material using coherent laser light. In a recent work [132], Ca_2RuO_4 modes were studied using Raman scattering in two polarization geometries. The so-called A_g channel is scalar and does typically not couple to magnetic excitations. In the present system, however, it couples the $E_T n_T$ part of the interaction, probing the n_T susceptibility. Since n_T measures the balance of singlets and triplets in the ground state, it is directly connected to condensate density. By shaking up the condensate density, the amplitude mode is excited, with an additional advantage that no other spin-wave contribution is present, therefore a 2-magnon continuum does not obscure the Higgs mode. The experiment supports this hypothesis, showing a unique spectral feature (labeled A in Fig. 1.8 panel (d)) at 40 meV

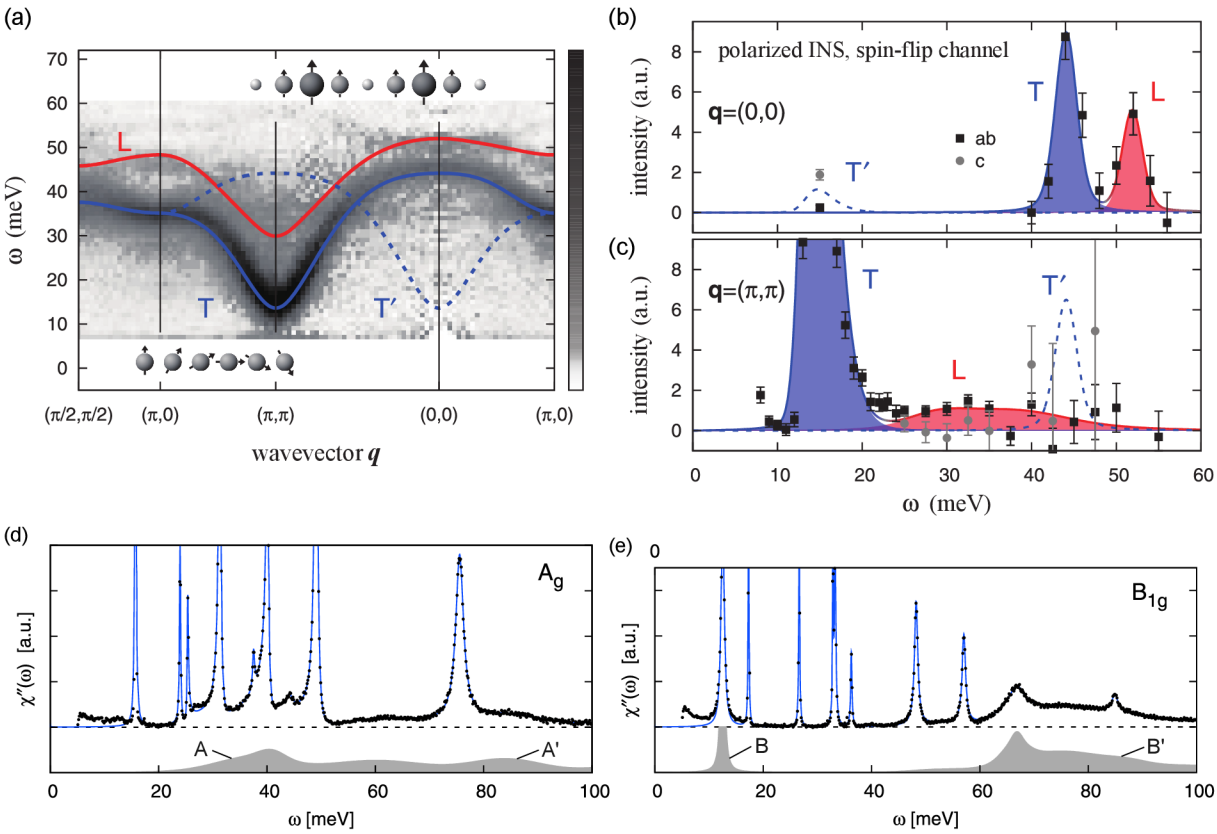

Figure 1.8: (a) INS excitation spectra of Ca_2RuO_4, together with theoretical dispersions obtained using the effective singlet-doublet model, shown as lines. The red line denotes a longitudinal amplitude mode L, the solid blue line corresponds to in-plane transversal magnon T, and the dashed blue line labels out-of-plane magnon T'. Insets show a pictorial representation of the modes: magnon as magnetic moment rotation at the bottom and magnetic moment length modulations of the Higgs mode at the top. (b) INS spectra at zero momentum, showing clearly defined in-plane magnon T and Higgs mode L. (c) INS spectra at ordering wavevector $\mathbf{Q} = (\pi, \pi)$, showing a 2-magnon continuum masking the longitudinal Higgs mode. (d) Raman spectra in the scalar A_g channel with a well-resolved Higgs peak around 40 meV. (e) Raman spectra in the magnetic B_{1g} channel, featuring a combination of high-energy 2-magnon continuous spectra and a single-magnon peak around 12.5 meV. Panels (a)-(c) reproduced from [2], (d)-(e) adapted from [132].

arising below $T_N = 110$ K. Further, B_{1g} channel was probed, which is connected to the exchange part of the Hamiltonian J and the bond-anisotropic part A. In agreement with expectations, a high-energy 2-magnon continuum above 60 meV emerges due to exchange J, along with a single-magnon peak at 12.5 meV produced by the A interaction term. Finally, we mention that the Raman magnetic spectra feature modulations due to Jahn-Teller coupling with magnetic phonon background, creating asymmetrical Fano-shapes of peaks shown in Figure 1.8 (d),(e).

Chapter 2

Extended Kitaev-Heisenberg model

The upcoming chapter is dedicated to a study of the extended Kitaev-Heisenberg model as an effective spin model for layered honeycomb compounds, which we have motivated in Sec. 1.2. The chapter consists of two main parts. First, we introduce the model and perform an analytical analysis of its hidden symmetry points, following the approach presented in Ref. [11]. The sublattice rotations that connect isolated parameter points with points of SU(2) symmetry enable us to also find the magnetically ordered phases present in the model's phase diagram. We present two original findings: a link to a class of models with a single interaction axis and a mapping uncovering a continuous phase-space manifold of fluctuation-free ground states.

The second part of the chapter contains a numerical exploration of the phase diagram by exact diagonalization (ED) on finite clusters. Apart from the standard analysis of ED ground states using spin-spin correlations, we also employ the spin-$\frac{1}{2}$ coherent states method, for which we provide a thorough description. Along with the spin patterns, it allows us to extract from the ED ground states also the direction of ordered magnetic moment, which can be compared to experimental data for Na_2IrO_3. Finally, combining both the symmetry-aided analysis and the numerics, we present a comprehensive view of the model's phase diagram featuring positions of high-symmetry points, probability maps of magnetic orderings, and maps of the direction of ordered magnetic moment.

2.1 Analytical exploration of the phase diagram

Finding a solution to a quantum spin model describing correlated electron phenomena typically requires the usage of approximate methods (mean-field theory, perturbation theory) and/or numerical methods (exact diagonalization, tensor networks, density matrix renormalization group, quantum Monte Carlo and others). The reason for this is that only a very limited number of spin models can be solved exactly [135]. Exact solutions are of course highly desired, especially since many approximate/numerical methods cannot make definite claims about e.g. long-range order. A few examples of exactly solvable models would be: the Ising model in 1D [136] and in 2D on the square [137] and triangular lattice [138], 1D Heisenberg [139] and 1D XY [140] models, and the relatively recently discovered honeycomb Kitaev model [4].

Even though there is no hope of solving such a complex model as the extended Kitaev-Heisenberg model exactly, this does not mean, as we will attempt to show in the present section, that no analytical treatment is possible. After establishing some definitions, we describe the

model's hidden symmetries represented by dual mappings between the exact limits of the model (Heisenberg, Kitaev) and other phase diagram points. Such mappings enable us to find several ground state configurations leading us to a basic understanding of the phase diagram.

Next, we present our original contribution to the topic in the form of a link between the extended Kitaev-Heisenberg model and a continuum of single-interaction-axis Hamiltonians, dubbed as Ising-Kitaev-compass model. Such a link provides us with additional exact points in the phase diagram (corresponding to Ising interaction) and with connections to models already studied in the literature (120° honeycomb compass model).

In the third part of this section, continuing with our original findings, we describe the surprising disappearance of quantum fluctuations in extended regions of the phase diagram. In such regions, the classical ferromagnetic (parallel) and Neél (antiparallel) spin configurations persist as eigenstates of the model due to an exact cancellation of the quantum-fluctuation-related terms at each lattice site.

Finally, we collect all previous findings and provide a symmetry-based view of the model's phase diagram. Although one cannot expect to gain a complete and detailed understanding of the phase diagram based on a limited number of isolated phase points (e.g., the positions of phase boundaries would be missing), we show that it is possible to obtain many of the model's main features without resorting to approximations or numerical methods.

2.1.1 Definition of the model and used reference frames

The full extended Kitaev-Heisenberg model on a 2D honeycomb lattice, as considered in this thesis, consists of two parts: the nearest neighbor bond-dependent interaction and the third-nearest neighbor isotropic Heisenberg interaction:

$$\mathcal{H} = \sum_{\langle ij\rangle \in \mathrm{NN}} \mathcal{H}_{ij}^{(\xi)} + \sum_{\langle ij\rangle \in 3^{\mathrm{rd}}\mathrm{NN}} J_3 \mathbf{S}_i \cdot \mathbf{S}_j \,. \tag{2.1}$$

The third nearest neighbor Heisenberg part will be discussed mostly in the context of comparison with real materials. Until that point, the term extended Kitaev-Heisenberg model (abbreviated as *EKH*) will refer to the nearest neighbor interaction (unless explicitly stated otherwise). Such interaction denoted by $\mathcal{H}_{ij}^{(\xi)}$ has a bond-dependent form

$$\mathcal{H}_{ij}^{(\xi)} = J\mathbf{S}_i \cdot \mathbf{S}_j + K S_i^\gamma S_j^\gamma + \Gamma(S_i^\alpha S_j^\beta + S_i^\beta S_j^\alpha) + \Gamma'(S_i^\alpha S_j^\gamma + S_i^\gamma S_j^\alpha + S_i^\beta S_j^\gamma + S_i^\gamma S_j^\beta), \tag{2.2}$$

where i, j denote the sites of the particular bond and the superscripts $\{\alpha, \beta, \gamma\}$ stand for the spin components x, y, z in the order corresponding to the bond direction ξ:

$$\alpha, \beta, \gamma = \begin{cases} y, z, x & \text{if } \xi = a, \\ z, x, y & \text{if } \xi = b, \\ x, y, z & \text{if } \xi = c. \end{cases} \tag{2.3}$$

The bond directions a, b, c and the cubic axes x, y, z are shown in the sketch of the honeycomb lattice for Na_2IrO_3 in Fig. 2.1 (a). The cubic axes point from a site of the honeycomb lattice (occupied by magnetic iridium atoms in Na_2IrO_3) to corners of the octahedron surrounding the

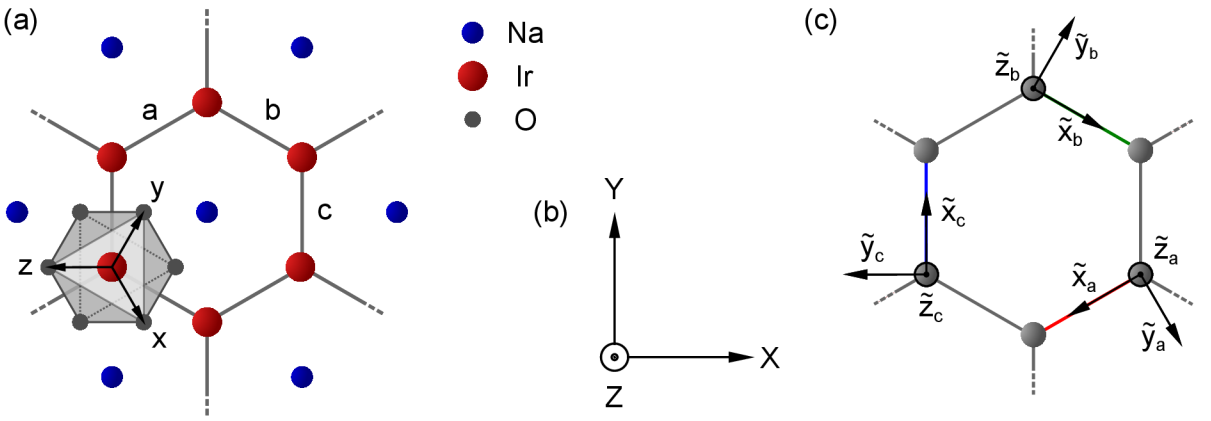

Figure 2.1: (a) Sketch of the planar honeycomb lattice in Na_2IrO_3. The three bond directions are labeled a, b, c and the cubic axes x, y, z point from the honeycomb site containing the magnetic atom to the corner of the octahedral cage (occupied by oxygen atoms). (b) Global set of axes XYZ. Z is pointing out of the plane perpendicular to it, Y is in the direction of the c bond and X is lying in the plane and is perpendicular to Y. (c) Rotating set of axes $\tilde{x}\tilde{y}\tilde{z}$ capturing the C_3 symmetry of the lattice. The unit vector $\tilde{x}$ follows the bond direction, $\tilde{z}$ is perpendicular to the honeycomb plane and $\tilde{y}$ completes the right-handed coordinate system.

site (occupied by oxygen atoms in Na_2IrO_3). The set of cubic axes is the most natural one when considering the microscopic electronic interaction paths between the magnetic atoms that give rise to the effective model, as we elaborated in the previous section 1.1.

Aside from the cubic axes, it is very useful to express the Hamiltonian also in the XYZ reference frame. The Z-axis is chosen perpendicular to the honeycomb plane and the Y-axis parallel to the bond direction c (see Fig. 2.1). Because of this choice, this reference frame is well-suited to capture the overall symmetry of the honeycomb lattice, and for this reason, is referred to as "global" [11] or "crystallographic" [141] set of axes in the literature. As we will show later, this reference frame is useful for capturing the symmetry of some spin configurations of the model under consideration.

The relation between the cubic x, y, z and global X, Y, Z unit vectors is:

$$\begin{pmatrix} x \\ y \\ z \end{pmatrix} = \begin{pmatrix} \frac{1}{\sqrt{6}} & -\frac{1}{\sqrt{2}} & \frac{1}{\sqrt{3}} \\ \frac{1}{\sqrt{6}} & \frac{1}{\sqrt{2}} & \frac{1}{\sqrt{3}} \\ -\sqrt{\frac{2}{3}} & 0 & \frac{1}{\sqrt{3}} \end{pmatrix} \begin{pmatrix} X \\ Y \\ Z \end{pmatrix} . \tag{2.4}$$

The bond dependence of the EKH Hamiltonian $\mathcal{H}_{ij}^{(\xi)}$ is realized by a simultaneous cyclic permutation of bond directions $\{a, b, c\}$ and spin axes $\{x, y, z\}$. In terms of the global XYZ reference frame this permutation corresponds to the rotation around the Z-direction by $0, \frac{2\pi}{3}$ and $\frac{4\pi}{3}$, respectively. We denote the corresponding angles by ϕ_ξ:

$$\phi_\xi = \begin{cases} 0 & \text{if } \xi = c, \\ \frac{2\pi}{3} & \text{if } \xi = a, \\ \frac{4\pi}{3} & \text{if } \xi = b. \end{cases} \tag{2.5}$$

Performing such a rotation and the reference frame transformation of Eq. (2.4) at the same time, we get

$$\begin{pmatrix} S^x \\ S^y \\ S^z \end{pmatrix} = \begin{pmatrix} \frac{1}{\sqrt{6}} & -\frac{1}{\sqrt{2}} & \frac{1}{\sqrt{3}} \\ \frac{1}{\sqrt{6}} & \frac{1}{\sqrt{2}} & \frac{1}{\sqrt{3}} \\ -\sqrt{\frac{2}{3}} & 0 & \frac{1}{\sqrt{3}} \end{pmatrix} \begin{pmatrix} \cos\phi_\xi & \sin\phi_\xi & 0 \\ -\sin\phi_\xi & \cos\phi_\xi & 0 \\ 0 & 0 & 1 \end{pmatrix} \begin{pmatrix} S^X \\ S^Y \\ S^Z \end{pmatrix} . \tag{2.6}$$

Using these relations together with Eq. (2.2) we can rewrite the nearest-neighbor Hamiltonian to the global XYZ reference frame [11]

$$\begin{aligned} \mathcal{H}_{ij}^{(\xi)} = {} & J_{XY}(S_i^X S_j^X + S_i^Y S_j^Y) + J_Z S_i^Z S_j^Z + \\ & + A\left[(S_i^X S_j^X - S_i^Y S_j^Y)\cos\phi_\xi - (S_i^X S_j^Y + S_i^Y S_j^X)\sin\phi_\xi\right] - \\ & - B\left[(S_i^X S_j^Z + S_i^Z S_j^X)\cos\phi_\xi + (S_i^Y S_j^Z + S_i^Z S_j^Y)\sin\phi_\xi\right] . \end{aligned} \tag{2.7}$$

The interaction parameters in (2.7) expressed in terms of the original J, K, Γ, and Γ' read as

$$\begin{pmatrix} J_{XY} \\ J_Z \\ A \\ B \end{pmatrix} = \begin{pmatrix} 1 & \frac{1}{3} & -\frac{1}{3} & -\frac{2}{3} \\ 1 & \frac{1}{3} & \frac{2}{3} & \frac{4}{3} \\ 0 & \frac{1}{3} & \frac{2}{3} & -\frac{2}{3} \\ 0 & \frac{\sqrt{2}}{3} & -\frac{\sqrt{2}}{3} & \frac{\sqrt{2}}{3} \end{pmatrix} \begin{pmatrix} J \\ K \\ \Gamma \\ \Gamma' \end{pmatrix} . \tag{2.8}$$

We will often switch back and forth between cubic and global axes as needed. Hence such a transformation will be useful to have at hand.

Motivated by the form of (2.7), we may also incorporate the ϕ_ξ-rotations into the axes themselves, i.e., use a rotating reference frame (see Fig. 2.1 panel (c)):

$$\begin{aligned} \tilde{x}_\xi &= -X\sin\phi_\xi + Y\cos\phi_\xi , \\ \tilde{y}_\xi &= -X\cos\phi_\xi - Y\sin\phi_\xi , \\ \tilde{z}_\xi &= Z \end{aligned} \tag{2.9}$$

in which the Hamiltonian has a compact form

$$\mathcal{H}_{ij}^{(\xi)} = (J_{XY} - A) S_i^{\tilde{x}_\xi} S_j^{\tilde{x}_\xi} + (J_{XY} + A) S_i^{\tilde{y}_\xi} S_j^{\tilde{y}_\xi} + J_Z S_i^{\tilde{z}_\xi} S_j^{\tilde{z}_\xi} + B(S_i^{\tilde{y}_\xi} S_j^{\tilde{z}_\xi} + S_i^{\tilde{z}_\xi} S_j^{\tilde{y}_\xi}) \tag{2.10}$$

with the same J_{XY}, J_Z, A, B parameters as for the global axes. The advantage of using such a rotating reference frame is that, because the rotations are chosen to "fit" the bond directions, the Hamiltonian expression is common for all bond directions. We can take advantage of this property when considering local effects happening on a single bond, whereas the global set of axes XYZ is more suitable when multiple bond directions come into play at once.

For the convenience of the reader, we will be repeating the necessary definitions at various places in the thesis. Even though a single reference frame is, in principle, sufficient to fully capture the model, the various model properties are sometimes best appreciated in a particular reference frame from the above set. We will be demonstrating this fact already in the following section in which we explore several real-space and spin-space symmetries of the EKH model.

2.1.2 Symmetry analysis of the interaction Hamiltonian

Facing a complex anisotropic spin model, it can be very helpful to understand its underlying symmetries. On top of lattice symmetries, such models may also possess various spin space symmetries. A simple example is the full rotational symmetry of the Heisenberg magnet (called $SU(2)$ symmetry for spin-$1/2$ systems) – the scalar product of spin operators $\mathbf{S}_i \cdot \mathbf{S}_j$ is rotationally invariant which leads to infinite degeneracy of the ground state manifested by the occurrence of gapless Goldstone modes [142].

In general, effective models describing Mott insulators with strong spin-orbit coupling feature more peculiar symmetries [48, 14] which have roots in the bond-directional nature of electronic orbitals. Relevant to our model under consideration, we now first illustrate an example of such a symmetry which is realized in the original Kitaev-Heisenberg model

$$\mathcal{H}_{\mathrm{KH}} = \sum_{\langle ij \rangle \| \xi} J\mathbf{S}_i \cdot \mathbf{S}_j + K S_i^{\xi} S_j^{\xi}. \tag{2.11}$$

The authors of [143, 109] showed that upon application of a specific four-sublattice spin rotation $\mathbf{S} \to \tilde{\mathbf{S}}$ the Hamiltonian of the model $\tilde{\mathcal{H}}_{\mathrm{KH}}$ retains the same analytical form but with effective couplings $\tilde{K} = 2J + K$ and $\tilde{J} = -J$ replacing the original K and J:

$$\tilde{\mathcal{H}}_{\mathrm{KH}} = \sum_{\langle ij \rangle \| \xi} \tilde{J}\tilde{\mathbf{S}}_i \cdot \tilde{\mathbf{S}}_j + \tilde{K}\tilde{S}_i^{\xi}\tilde{S}_j^{\xi} = \sum_{\langle ij \rangle \| \xi} -J\tilde{\mathbf{S}}_i \cdot \tilde{\mathbf{S}}_j + (2J+K)\tilde{S}_i^{\xi}\tilde{S}_j^{\xi}. \tag{2.12}$$

Because these sublattice rotations preserve the spin commutation relations and correspond merely to a change of the local coordinate system, the physical properties of the spin system remain the same. The transformation thus provides a link between two parameter-space points featuring a common physical state. This way, two "hidden" $SU(2)$ points are found by mapping the AF ($J > 0, K = 0$) and FM ($J < 0, K = 0$) Heisenberg points to the rotated pair $\tilde{J} = -J, \tilde{K} = 2J$. Performing the sublattice spin rotations also gives us the ground-state spin configurations for the hidden $SU(2)$ points – collinear FM configuration is mapped to an AF-type stripy order, whereas anti-collinear Neél configuration maps to a zigzag state.

These configurations obtained from the ordered Heisenberg FM/AF with moments along the z axis are displayed in Fig. 2.2 panel (f) along with the sketch of sublattice-dependent spin rotations in panel (d). The stripes of spins in the stripy pattern are stacked antiferromagnetically, yet the nature of the state is ferromagnetic. This shows that the spin configurations themselves do not constitute sufficient knowledge about the ground state. Perhaps the best insight into the nature of the ground state is provided by the spectrum of spin excitations, often used also in comparison with experiments. The spectrum of a hidden $SU(2)$ point is obtained by a $\mathbf{q}$-space shift of the original $SU(2)$ point's spectrum by a vector $\mathbf{Q}$ characteristic of the transformation. This way, the gapless Goldstone mode of the Heisenberg ferromagnet appearing at the Γ point moves to the Y point of the first Brillouin zone (see Fig. 2.2 panel (c)). For completeness, the Bragg spots of the mapped zigzag and stripy patterns are shown in panel (f) of Fig. 2.2.

Hidden symmetries of the extended Kitaev-Heisenberg model

After the above exposition, we may now consider the extended Kitaev Heisenberg model, whose symmetries were analyzed in [11]. It, of course, inherits the $SU(2)$ points of the original Kitaev-Heisenberg model and additionally contains several new ones. These were identified by dual

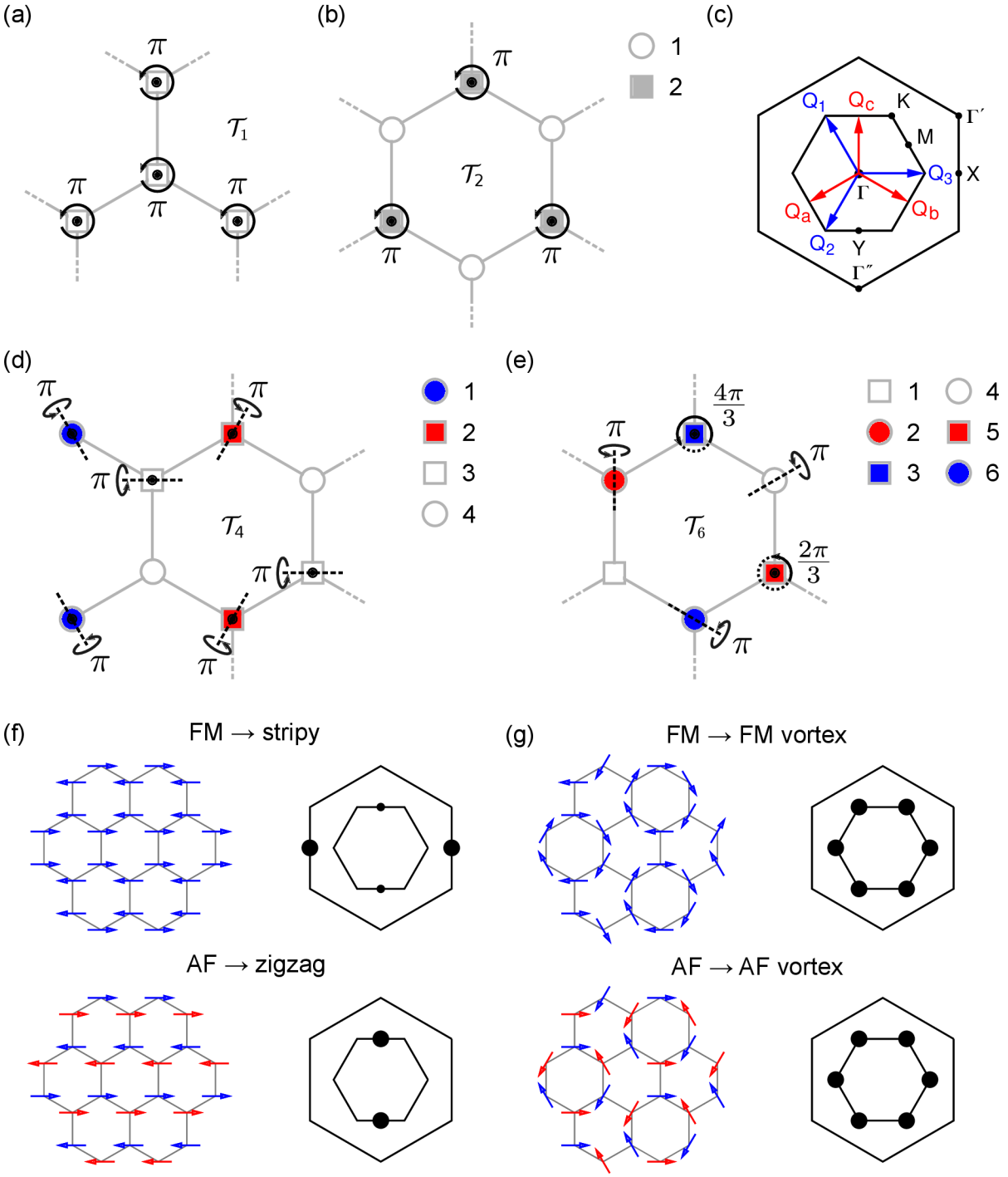

Figure 2.2: (a) $\mathcal{T}_1$ is a global π-rotation around the Z axis. (b) Definition of two-sublattice transformation $\mathcal{T}_2$. It maps the in-plane FM pattern into in-plane AF and vice versa. (c) First Brillouin zone of the honeycomb lattice (inner hexagon) and of the complementary triangular lattice (outer hexagon). Red vectors $\mathbf{Q}_a, \mathbf{Q}_b, \mathbf{Q}_c$ indicate $\mathbf{q}$-space shifts brought by the $\mathcal{T}_4$ transformation and blue vectors $\mathbf{Q}_1, \mathbf{Q}_2, \mathbf{Q}_3$ correspond to $\mathcal{T}_6$. (d) Spin rotations of the $\mathcal{T}_4$ transformation. (e) Spin rotations of the $\mathcal{T}_6$ transformation. (f) $\mathcal{T}_4$ maps FM to a stripy pattern shown at the top in all blue, together with the corresponding Bragg spots. Similarly, AF is mapped to a zigzag pattern. (g) Vortex FM and AF spin configurations in which (most) neighboring spins point at 120° angles. Panels (c),(f),(g) are re-created from Ref. [11].

transformations of the type $J_0 \leftrightarrow JK\Gamma\Gamma'$, i.e. the Heisenberg magnet described by the single coupling strength parameter J_0 is mapped to the EKH Hamiltonian with specific values of parameters J, K, Γ, Γ'. Three such transformations were found in total, denoted by $\mathcal{T}_n$, corresponding to n-sublattice spin rotations with $n = 2, 4, 6$. We will now describe them one by one.

The four-sublattice rotation discussed above is denoted as $\mathcal{T}_4$, and its definition in cubic coordinates reads as

$$\mathcal{T}_4: \quad x', y', z' = \begin{cases} x, -y, -z & \text{at sublattice 1,} \\ -x, \ \ y, -z & \text{at sublattice 2,} \\ -x, -y, \ \ z & \text{at sublattice 3,} \\ x, \ \ y, \ \ z & \text{at sublattice 4.} \end{cases} \tag{2.13}$$

As we can see, on three sublattices $1, 2, 3$ the transformation amounts to a π-rotation around one of the cubic x, y, z axes while keeping the spin axes unchanged on the fourth sublattice (see Fig. 2.2 panel (d)). It converts the FM/AF patterns with moments pointing in z-direction to stripy/zigzag orderings.

The simplest transformation $\mathcal{T}_2$ is π-rotation about the Z axis perpendicular to the honeycomb plane which is applied on one of the two sublattices of the honeycomb lattice:

$$\mathcal{T}_2: \quad X', Y', Z' = \begin{cases} X, \ \ Y, \ \ Z & \text{at sublattice 1,} \\ -X, -Y, \ \ Z & \text{at sublattice 2.} \end{cases} \tag{2.14}$$

Clearly, the transformation does not affect the collinear orderings with ordered moments along the Z-direction. Curiously, if we rather consider an FM in-plane pattern, we observe that $\mathcal{T}_2$ maps it to an in-plane AF pattern. One may, therefore, have a paradoxical situation where the spin pattern is antiferromagnetic, but the nature of the state (shown, e.g., in the spin dynamics) is ferromagnetic. This happens for a hidden $SU(2)$ point found for the parameters given in Table 2.1.

Arguably, the most interesting transformation is a six-sublattice rotation $\mathcal{T}_6$ consisting of rotations around axes $Z, Y, \frac{\sqrt{3}}{2}X + \frac{1}{2}Y$ and $\frac{\sqrt{3}}{2}X - \frac{1}{2}Y$, depicted in panel (e) of Fig. 2.1.2. A convenient way to capture these is in cubic coordinates:

$$\mathcal{T}_6: \quad x', y', z' = \begin{cases} x, \ \ y, \ \ z & \text{at sublattice 1,} \\ -y, -x, -z & \text{at sublattice 2,} \\ y, \ \ z, \ \ x & \text{at sublattice 3,} \\ -x, -z, -y & \text{at sublattice 4,} \\ z, \ \ x, \ \ y & \text{at sublattice 5,} \\ -z, -y, -x & \text{at sublattice 6,} \end{cases} \tag{2.15}$$

where the rotations correspond to cyclic permutations among x, y, z or anticyclic permutations followed by a spin inversion. These rotations lead to a hidden $SU(2)$ point for $K = \Gamma, J = \Gamma' = 0$ with the spins lying in the plane and at 120° angles, forming an unusual "vortex" pattern. The

Table 2.1: List of all $SU(2)$ points of the extended Kitaev-Heisenberg model obtained by mapping the pure Heisenberg model using listed symmetry transformations. The table is taken from ref. [11].

	$\widetilde{J}/J_0$	$\widetilde{K}/J_0$	$\widetilde{\Gamma}/J_0$	$\widetilde{\Gamma}'/J_0$
$\mathcal{T}_2$	$-1/3$	0	$2/3$	$2/3$
$\mathcal{T}_4$	-1	2	0	0
$\mathcal{T}_6$	0	-1	-1	0
$\mathcal{T}_1\mathcal{T}_4$	$-1/9$	$-2/3$	$8/9$	$-4/9$
$\mathcal{T}_2\mathcal{T}_6$	$-2/3$	1	$1/3$	$-2/3$

vortex configurations displayed in Fig. 2.2 panel (g) are obtained by rotating FM/AF Heisenberg patterns with ordered moments pointing in the z direction. We note that the ground state degeneracy is inherited by the hidden $SU(2)$ point, and thus there are infinitely many possible spin configurations of equal energy. Here we arrive at a fascinating situation, where the interactions are exclusively anisotropic (K and Γ terms are non-zero), the spins are non-collinear, and yet the nature of the states as observed in the spin excitation spectra is AF/FM (shifted to the K point in the first Brillouin zone) including e.g. the presence of gapless Goldstone modes. The $\mathcal{T}_6$ mapping has the unique feature of connecting the EKH model with the Kekulé-Kitaev model [144], which we will discuss in more detail in the section dedicated to fluctuation-free phase diagram manifolds 2.1.4.

Table 2.1 contains all $SU(2)$ points of the extended Kitaev-Heisenberg model – three connected to $\mathcal{T}_2, \mathcal{T}_4, \mathcal{T}_6$ transformations and two more obtained by composite $\mathcal{T}_2\mathcal{T}_6$ and $\mathcal{T}_1\mathcal{T}_4$ transformations. $\mathcal{T}_1$ is the final transformation yet to be discussed. It is the simplest, corresponding to a global π-rotation around the Z axis:

$$\mathcal{T}_1: \quad X', Y', Z' = -X, -Y, Z. \tag{2.16}$$

It is, however, exceptional since in contrast to $\mathcal{T}_2, \mathcal{T}_4, \mathcal{T}_6$ that map the EKH Hamiltonian to the Heisenberg model, it is the only self-dual transformation of the EKH model, linking every $JK\Gamma\Gamma'$ point to a rotated $\tilde{J}\tilde{K}\tilde{\Gamma}\tilde{\Gamma}'$ partner. Considering the rather simple form (2.16), it is perhaps a little surprising that the duality transformation linking parameters of the model expressed in cubic coordinates is rather convolved:

$$\begin{pmatrix} \tilde{J} \\ \tilde{K} \\ \tilde{\Gamma} \\ \tilde{\Gamma}' \end{pmatrix} = \begin{pmatrix} 1 & +\frac{4}{9} & -\frac{4}{9} & +\frac{4}{9} \\ 0 & -\frac{1}{3} & +\frac{4}{3} & -\frac{4}{3} \\ 0 & +\frac{4}{9} & +\frac{5}{9} & +\frac{4}{9} \\ 0 & -\frac{2}{9} & +\frac{2}{9} & +\frac{7}{9} \end{pmatrix} \begin{pmatrix} J \\ K \\ \Gamma \\ \Gamma' \end{pmatrix}. \tag{2.17}$$

The relative complexity of this expression can be understood as an artifact of the parametrization of the exchange matrix 2.2 in the cubic xyz axes. Indeed, choosing the global/crystallographic

XYZ axes, the $\mathcal{T}_1$ transformation corresponds to a benign sign change in one of the parameters:

$$\begin{pmatrix} \tilde{J}_{XY} \\ \tilde{J}_Z \\ \tilde{A} \\ \tilde{B} \end{pmatrix} = \begin{pmatrix} +1 & 0 & 0 & 0 \\ 0 & +1 & 0 & 0 \\ 0 & 0 & +1 & 0 \\ 0 & 0 & 0 & -1 \end{pmatrix} \begin{pmatrix} J_{XY} \\ J_Z \\ A \\ B \end{pmatrix}. \tag{2.18}$$

More important than the formal matters are the implications brought by the self-dual mapping. The duality provides us with a hidden "copy" of any parameter point in phase space. Although it does not by itself bring about new $SU(2)$ points (Heisenberg AF/FM points are mapped onto themselves by $\mathcal{T}_1$), we do obtain two (AF and FM) hidden Kitaev points by performing a transformation $K \leftrightarrow \tilde{J}\tilde{K}\tilde{\Gamma}\tilde{\Gamma}'$. We can read out the parameter values of these hidden points from (2.17) in units of K as:

$$\tilde{J} = \tfrac{4}{9},\ \tilde{K} = -\tfrac{1}{3},\ \tilde{\Gamma} = \tfrac{4}{9},\ \tilde{\Gamma}' = -\tfrac{2}{9}. \tag{2.19}$$

Remarkably, the dual mapping has provided us with two additional points with exactly known ground states, featuring all the unique properties of Kitaev spin liquid. This observation is important both theoretically and experimentally since it provides an additional parameter window where Kitaev spin liquid can be found.

To summarize, the extended Kitaev-Heisenberg model features various sublattice-dependent spin transformations that uncover hidden $SU(2)$ points of the model. We have shown that such transformations are more general and apply to Kitaev-like models in different geometries and dimensions. In addition, the model possesses a single self-dual transformation that reveals dual Kitaev spin liquids in the phase diagram. In practice, hidden symmetries can aid in the interpretation of spin dynamics spectra and, in general, are useful when trying to pinpoint a parameter window for the studied material by comparison with experimental data. In the following text, we will present an original finding of further hidden symmetries in the form of a link to single-axis compass models.

2.1.3 The case of a single interaction axis: Ising-Kitaev-compass model

In the preceding text, we have seen that it is possible to design sublattice-dependent rotations of spin axes in such a way that the rather complicated anisotropic interaction reduces to an exactly solvable spin Hamiltonian. We were able to find multiple images of $SU(2)$-symmetric Heisenberg points and also one $\mathcal{T}_1$-image for each of the two (AF and FM) Kitaev points.

At this point we may wonder whether this model could perhaps also harbor a hidden Ising point. Ising interaction is distinct from Kitaev interaction as it is not bond-dependent, but its interaction axis is common to all bonds. The square lattice Ising model is exactly solvable, as shown by Onsager in his seminal 1944 paper [137]. It is perhaps lesser known that the Ising model is exactly solvable also on the honeycomb lattice (see Wannier [138] and Houtappel [145]). We would, therefore, possess complete information about the ground state of such a phase space point.

It turns out that the answer is yes and, moreover, the process illuminates a previously unknown connection between the EKH model and the whole family of single-axis interactions.

It is useful to write the EKH interaction expressed in the rotating reference frame (2.9) as a matrix, i.e. $\mathcal{H}_{ij}^{(\xi)} = \mathbf{S}_i^{\xi T} H_{ij} \mathbf{S}_j^{\xi}$, where:

$$H_{ij} = \begin{pmatrix} J_{XY} - A & 0 & 0 \\ 0 & J_{XY} + A & B \\ 0 & B & J_Z \end{pmatrix}. \tag{2.20}$$

The $\tilde{x}$ and $\tilde{y}$ axes rotate in sync with the bonds a, b, c, but the $\tilde{z}$ axis does not; this means that it is eligible to represent an Ising axis. Therefore, if the only nonzero component in the interaction is J_Z, the Ising case is realized. We have thus found two (AF for positive J_Z and FM for negative J_Z) Ising points in our model:

$$J_{XY} = A = B = 0,\ J_Z \neq 0. \tag{2.21}$$

The usefulness of casting the Hamiltonian in the rotating reference frame is showing now – it is not at all obvious to discover the hidden Ising points using the cubic representation of EKH (2.2) – in cubic coordinates, the Ising points are at

$$J = \Gamma = \Gamma',\ K = 0. \tag{2.22}$$

At these parameter points, the ground state is a classical ferromagnet (for negative interaction constant J_Z) or a Néel state of contra-aligned spins (for positive interaction constant). The mapping to the Ising model works only for this exact combination of J, K, Γ, Γ' parameters, so when they are changed slightly (moving away from the Ising point in the phase diagram), presumably the quantum fluctuations will kick in and change the character of the spin state. We will come back to this issue in part 2.1.4 and show that surprisingly, the non-fluctuating state is more robust and is realized on a whole manifold of parameter-space points.

We can continue our analysis of (2.20) by inspecting more limiting cases. If the only nonzero component of the interaction is in the $\tilde{x}$-direction, which is in the direction of the bond, we get the so-called 120° honeycomb compass model [146, 147, 148]

$$\mathcal{H}_{120} = \sum_{\langle ij \rangle \in NN} (J_{XY} - A) S_i^{\tilde{x}} S_j^{\tilde{x}}, \tag{2.23}$$

which is a member of a broader class of compass models [149]. It is frustrated by the bond directionality of interactions, the same as the Kitaev model, but an exact solution for its ground state is not known. We will comment on the ground state later in the thesis when describing the numerical analysis of the EKH model 2.2.4. The link between the 120° honeycomb compass and the EKH model was not known before, although in principle it is expected since the EKH Hamiltonian represents the most general symmetry-allowed interaction on the honeycomb lattice and thus encompasses any possible valid spin interaction. In terms of model parameters, we have

$$J_{XY} = -A,\ B = J_Z = 0 \quad \Leftrightarrow \quad J = -K = -\Gamma,\ \Gamma' = 0. \tag{2.24}$$

Yet there are more links to be established. Having found already two cases of a single interaction axis hidden in the EKH Hamiltonian (one bond-independent and one fully bond-dependent), we can generalize and postulate the Hamiltonian of the single-axis model hidden in the EKH model as

$$\mathcal{H}_{IKc} = \sum_{\langle ij \rangle \in NN} \tilde{K} (\mathbf{n}_\xi \cdot \mathbf{S}_i)(\mathbf{n}_\xi \cdot \mathbf{S}_j), \tag{2.25}$$

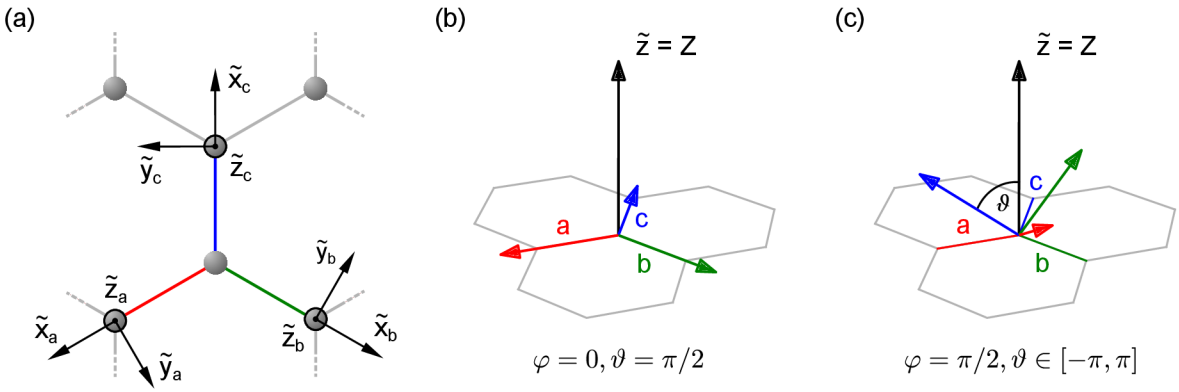

Figure 2.3: (a) Rotating-axes reference frame used in the text. The $\tilde{x}$ unit vector is in the direction of the bond, $\tilde{z}$ is perpendicular to the honeycomb plane, and $\tilde{y}$ lies in the plane and is perpendicular to the bond direction. The color coding of bond types is consistent with the panels to the right. (b) Position of the single interaction axis in the singular case of 120° compass model. The interaction axis lies in the bond direction, corresponding to $\vartheta = \pi/2, \varphi = 0$. The arrow color corresponds to the active bond direction. (c) The situation shown describes the continuous case, which includes Ising, Kitaev, and "compass" models for $\varphi = \pi/2$ and varying values of angle ϑ – angle that the interaction axis strikes with the $\tilde{z}$ direction.

where the bond-dependent interaction axis is represented by a unit vector $\mathbf{n}_\xi$. The direction of the single axis can be encoded naturally by a polar angle ϑ from the global Z axis (perpendicular to the honeycomb plane) and by an azimuthal angle φ measured from the bond, see Figure 2.3. This way, in the rotating reference frame $\tilde{x}\tilde{y}\tilde{z}$ we have

$$\mathbf{n}_\xi = (\sin\vartheta\cos\varphi, \sin\vartheta\sin\varphi, \cos\vartheta). \tag{2.26}$$

The two cases that we have already seen are the Ising model, corresponding to $\vartheta = 0$, and the compass model at $\vartheta = \pi/2, \varphi = 0$. Between these two limits, we also encounter the Kitaev model ($\vartheta = \arccos\left(1/\sqrt{3}\right), \varphi = \pi/2$). Therefore we call such a single-axis Hamiltonian the Ising-Kitaev-compass (IKc) model (one other study refers to it as the tripod model [148]).

The mapping between the EKH and IKc models is established by simply comparing their forms (2.25), (2.20) expressed in the same coordinates. First, we find the singular case:

$$\tilde{K} = J_{XY} - A, \quad \vartheta = \pi/2, \varphi = 0 \tag{2.27}$$

corresponding to the previously discussed 120° compass model. Here the model parameters are constrained by

$$\begin{aligned} J_{XY} + A &= 0, \\ J_Z &= 0, \\ B &= 0. \end{aligned} \tag{2.28}$$

Second, the single interaction axis can lie in the whole plane perpendicular to the bond direction, spanned by $\vartheta \in [-\pi, \pi], \varphi = \pi/2$. Such a continuum corresponds to the bottom right block of

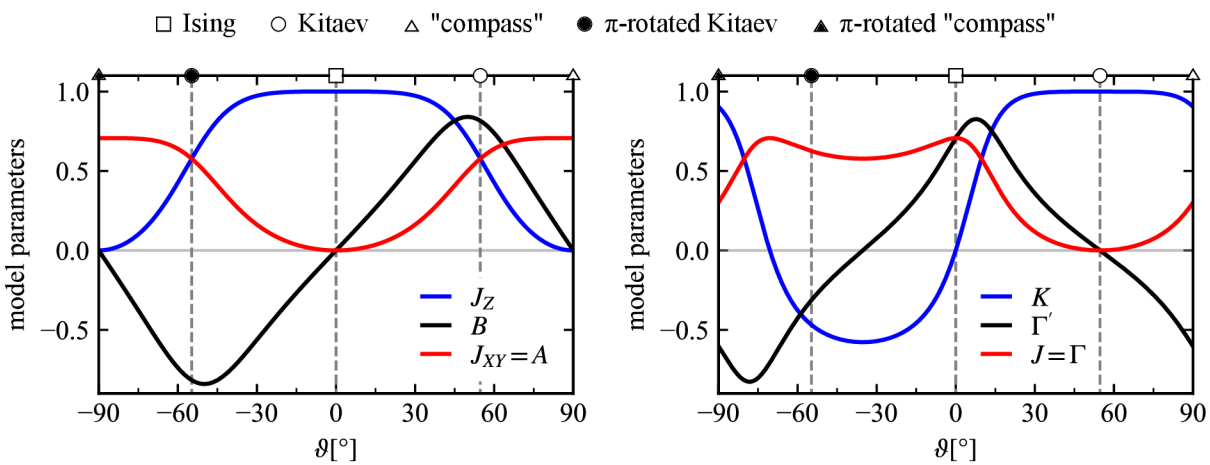

Figure 2.4: Values of model's parameters with respect to the angle ϑ between the single interaction axis with the $\tilde{z}$ direction. Notable positions are pictorially designated by symbols at the top. The left panel shows parameters J_{XY}, J_Z, A, B corresponding to the model formulation in $XYZ/\tilde{x}\tilde{y}\tilde{z}$ coordinates whereas the right panel contains J, K, Γ, Γ' parameters used in the standard description of the model using cubic xyz coordinates. The interaction strength $\tilde{K}$ is fixed and equals $2J_{XY} + J_Z = 3J + K$ and is chosen positive, i.e., the displayed figure corresponds to the AF case. With one degree of freedom left, we chose a parametrization such that $J_{XY}^2 + J_Z^2 + A^2 = J^2 + K^2 + \Gamma^2 = 1$.

(2.20) and is therefore realized for $J_{XY} = A \Leftrightarrow J = \Gamma$. Writing the mapping explicitly, we have

$$\begin{aligned} \varphi &= \pi/2, \\ J_{XY} &= A, \\ J_{XY} + A &= \tilde{K}\sin^2\vartheta, \\ B &= \tilde{K}\sin\vartheta\cos\vartheta, \\ J_Z &= \tilde{K}\cos^2\vartheta. \end{aligned} \tag{2.29}$$

From this set of equations we can express ϑ in terms of model parameters:

$$\tan 2\vartheta = \frac{2B}{J_Z - 2J_{XY}} \,. \tag{2.30}$$

Figure 2.4 shows the evolution of model parameters J_{XY}, A, B, J_Z and J, K, Γ, Γ' with respect to polar angle ϑ within the $\varphi = \pi/2$ plane (also see Figure 2.3 (b)). We see the aforementioned Ising and Kitaev cases with $\vartheta = 0$ and $\vartheta = \arccos\left(1/\sqrt{3}\right)$ respectively. When the interaction axis lies in the honeycomb plane, we call this the "compass" case – it differs from the 120° compass model by a trivial π rotation in the honeycomb plane. Notably, the $\mathcal{T}_1$ global rotation discussed in section 2.1.2 comes into play again – here it corresponds to the exchange $\vartheta \leftrightarrow -\vartheta$. By applying it, we uncover the $\mathcal{T}_1$-rotated partner of Kitaev and "compass" points, displayed in Figure 2.4 by full symbols. The π-rotated Kitaev point is especially interesting since it represents another phase diagram region containing the experimentally desired Kitaev spin liquid state.

Table 2.2 shows parameter values for the aforementioned notable cases. Same as in Fig. 2.4, we show the AF case of positive interaction strength $\tilde{K}$. The $\mathcal{T}_1$ global rotation connecting

Table 2.2: Parameters for specific cases in the Ising-Kitaev-compass continuum of single-axis Hamiltonians. Normalization of parameters is the same as in Fig. 2.4.

	global				cubic				axis direction	
	J_{XY}	J_Z	A	B	J	K	Γ	Γ'	ϑ	φ
Ising	0	1	0	0	$\frac{1}{\sqrt{2}}$	0	$\frac{1}{\sqrt{2}}$	$\frac{1}{\sqrt{2}}$	$0, \pi$	-
Kitaev	$\frac{1}{\sqrt{3}}$	$\frac{1}{\sqrt{3}}$	$\frac{1}{\sqrt{3}}$	$\frac{\sqrt{2}}{3}$	0	1	0	0	$\arccos\left(\frac{1}{\sqrt{3}}\right)$	$\pi/2$
"compass"	$\frac{1}{\sqrt{2}}$	0	$\frac{1}{\sqrt{2}}$	0	$\frac{1}{\sqrt{11}}$	$\frac{3}{\sqrt{11}}$	$\frac{1}{\sqrt{11}}$	$-\frac{2}{\sqrt{11}}$	$\pi/2$	$\pi/2$
π-Kitaev	$\frac{1}{\sqrt{3}}$	$\frac{1}{\sqrt{3}}$	$\frac{1}{\sqrt{3}}$	$-\frac{\sqrt{2}}{3}$	$\frac{4}{\sqrt{41}}$	$-\frac{3}{\sqrt{41}}$	$\frac{4}{\sqrt{41}}$	$-\frac{2}{\sqrt{41}}$	$-\arccos\left(\frac{1}{\sqrt{3}}\right)$	$\pi/2$
π-"compass"	$\frac{1}{\sqrt{2}}$	0	$\frac{1}{\sqrt{2}}$	0	$\frac{1}{\sqrt{11}}$	$\frac{3}{\sqrt{11}}$	$\frac{1}{\sqrt{11}}$	$-\frac{2}{\sqrt{11}}$	$-\pi/2$	$\pi/2$
compass	$\frac{1}{\sqrt{2}}$	0	$-\frac{1}{\sqrt{2}}$	0	$\frac{1}{\sqrt{3}}$	$-\frac{1}{\sqrt{3}}$	$-\frac{1}{\sqrt{3}}$	0	$\pi/2$	0

Kitaev and "compass" points with their rotated variants is realized simply by $\vartheta \leftrightarrow -\vartheta$ and $B \leftrightarrow -B$, although the transformation is more complex in cubic coordinates. Note that the parameters corresponding to the "compass" case are mapped to themselves by $\mathcal{T}_1$ – in other words, the vector of these parameters is the eigenvector of the $\mathcal{T}_1$ matrix.

To summarize, we found a broad class of models characterized by a single interaction axis. By choosing the interaction strength $\tilde{K}$ positive or negative, we realize an antiferromagnetic or ferromagnetic class of interactions. The link between such a class of models and the extended Kitaev-Heisenberg model provide us with additional intuitions about the character of spin states in certain regions of the parameter space. As a last comment, we add that the full derivation of the mapping between IKc and EKH models using cubic coordinates was performed in our paper [12], but we choose not to include it here as the choice of cubic reference frame makes it more involved.

2.1.4 Spin states without quantum fluctuations

Thus far, we have been mostly focusing our analysis of the EKH model on specific points that are exactly solvable or possess a special symmetry. In the pure Kitaev case, the spin state is highly degenerate, but in other cases, we found a classical ground state, namely, FM Heisenberg point and FM/AF Ising points. Such classical states can be pretty straightforward to deal with, but because of the relative abundance of various anisotropic interaction channels, we would not expect them to occur in a phase diagram on a larger scale than those few isolated points mentioned before.

In this section, we will show that, surprisingly, due to some nontrivial on-site cancellation of interaction terms, the model's phase diagram hosts whole manifolds of classical spin states without quantum fluctuations. We will show such cancellation for both FM and Neél spin configurations by utilizing one of the sublattice transformations introduced in section 2.1.2. Finally, we address how the states are affected by the third-nearest neighbor Heisenberg coupling.

Ferromagnetic Z-polarized state

We start by considering the hidden FM Ising point located at $J_{XY} = A = B = 0, J_Z < 0$ and consider how the state changes by switching on the J_{XY}, A, B interaction terms. As a reminder, the ground state of the hidden Ising point is a classical ferromagnetic spin state polarized in the Z-direction, i.e., perpendicular to the honeycomb plane. The EKH interaction expressed in global XYZ axes reads as:

$$\begin{aligned}\mathcal{H}_{ij}^{(\xi)} = & J_{XY}(S_i^X S_j^X + S_i^Y S_j^Y) + J_Z S_i^Z S_j^Z + \\ & + A\left[(S_i^X S_j^X - S_i^Y S_j^Y)\cos\phi_\xi - (S_i^X S_j^Y + S_i^Y S_j^X)\sin\phi_\xi\right] - \\ & - B\left[(S_i^X S_j^Z + S_i^Z S_j^X)\cos\phi_\xi + (S_i^Y S_j^Z + S_i^Z S_j^Y)\sin\phi_\xi\right], \end{aligned} \tag{2.31}$$

with the bond-dependent factors

$$\phi_\xi = \begin{cases} 0 & \text{if } \xi = c, \\ \frac{2\pi}{3} & \text{if } \xi = a, \\ \frac{4\pi}{3} & \text{if } \xi = b. \end{cases} \tag{2.32}$$

To see the effect of quantum fluctuations, it is advantageous to use the $S^\pm, S^Z$ operator set, where the $S^\pm$ operators are related to the Cartesian S^X, S^Y operators by

$$S^\pm = S^X \pm i S^Y. \tag{2.33}$$

Using this standard definition, we can analyze the action of Hamiltonian terms one by one. Starting with the J_{XY} term, we get

$$\frac{J_{XY}}{2}(S_i^+ S_j^- + S_i^- S_j^+), \tag{2.34}$$

from which it is clear that the XY-interaction does not affect Z-collinear states such as the one under consideration. This is an unsurprising and familiar situation since by switching on J_{XY} in addition to already present J_Z, we obtain the XY spin model (which reduces to the isotropic Heisenberg model for $J_{XY} = J_Z$). More interesting are the bond-dependent terms; starting with the A-term, we obtain

$$\frac{A}{2}\left[(S_i^+ S_j^+ + S_i^- S_j^-)\cos\phi_\xi - (S_i^+ S_j^+ - S_i^- S_j^-)\sin\phi_\xi\right]. \tag{2.35}$$

The S^+S^+ and S^-S^- terms affect the classical FM state, hence in the presence of the A interaction term it is no longer the ground state. Lastly, and perhaps most interestingly, we consider the action of B-type coupling terms:

$$-\frac{B}{2}\left[(S_i^+ S_j^Z + S_i^- S_j^Z + S_i^Z S_j^+ + S_i^Z S_j^-)\cos\phi_\xi - i(S_i^+ S_j^Z - S_i^- S_j^Z + S_i^Z S_j^+ - S_i^Z S_j^-)\sin\phi_\xi\right]. \tag{2.36}$$

At first sight, these terms individually also disrupt the FM Z-state. However, to see how a single site is affected by the whole term, we rewrite it as a sum over sites (as opposed to the standard way of summing over nearest-neighbor bonds):

$$-B\sum_{\text{sites } i}\left[S_i^X \sum_{\xi=a,b,c} S_{i+\xi}^Z \cos\phi_\xi + S_i^Y \sum_{\xi=a,b,c} S_{i+\xi}^Z \sin\phi_\xi\right], \tag{2.37}$$

where $S^Z_{i+\xi}$ denotes a spin S^Z operator at such i's nearest-neighbor site that the bond $\langle i, i+\xi\rangle$ is of type ξ. Because we deal with an eigenstate of S^Z, the expression becomes

$$-B\langle S^Z\rangle \sum_{\text{sites } i} \left[S_i^X \sum_{\xi=a,b,c} \cos\phi_\xi + S_i^Y \sum_{\xi=a,b,c} \sin\phi_\xi \right]. \tag{2.38}$$

The sums of bond-dependent factors over the three bond types can be calculated explicitly:

$$\sum_{\xi=a,b,c} \cos\phi_\xi = \sum_{\xi=a,b,c} \sin\phi_\xi = 0. \tag{2.39}$$

Remarkably, the contributions of B interaction terms from the three bond types cancel out exactly at each site, having no net effect. This situation is depicted in Fig. 2.5, where we evaluate the bond-dependent trigonometric factors to see the summation to zero more clearly. This cancellation means that the only term that creates quantum fluctuations in the Z-polarized FM state is the A-term. The phase diagram of the spin model, therefore, contains a whole manifold of phase points for which classical FM states are possible. This manifold is simply given by

$$A = 0 \Leftrightarrow K + 2\Gamma - 2\Gamma' = 0. \tag{2.40}$$

It is important to note that there is no guarantee that such Z-polarized FM state is also a ground state at each phase point of this manifold, as different states might have lower energy. We do know, however, that there are at least two points where the Z-FM state is the ground state, namely, the FM Heisenberg point and the FM Ising point which both lie on the above-mentioned manifold of classical states. The manifold also contains phase points where certainly different spin states will be realized as ground states, for example, in regions with positive J_Z.

Néel Z-polarized state

We can perform an analogous analysis for a Neél Z-polarized state, beginning in the Ising AF point $J_{XY} = A = B = 0, J_Z > 0$. Switching on the interaction channels, we observe that the role of A- and J_{XY}-terms is now reversed: the A-term does not affect the Z-polarized anticollinear state, whereas the J_{XY}-term contains S^+S^-/S^-S^+ operators that are active in the Neél state and introduce quantum fluctuations. Again, this is a well-known situation that occurs in the XY/Heisenberg models, where the Neél state is not the ground state.

The situation with on-site cancellation of fluctuation terms coming from the B interaction term is analogous as well. The only difference is that the value of $\langle S^Z\rangle$ on the i's neighboring sites depends on the AF sublattice to which the site i belongs. The cancellation, however, is still present individually on all lattice sites as all the neighbors of a given site belong to the same sublattice. This means that the manifold

$$J_{XY} = 0 \Leftrightarrow 3J + K - \Gamma - 2\Gamma' = 0 \tag{2.41}$$

may indeed host fluctuation-free Neél spin states.

There is another way to reach this conclusion by mapping the AF state to the previously discussed FM state using the $\mathcal{T}_6$ transformation introduced in section 2.1.2. The result is the

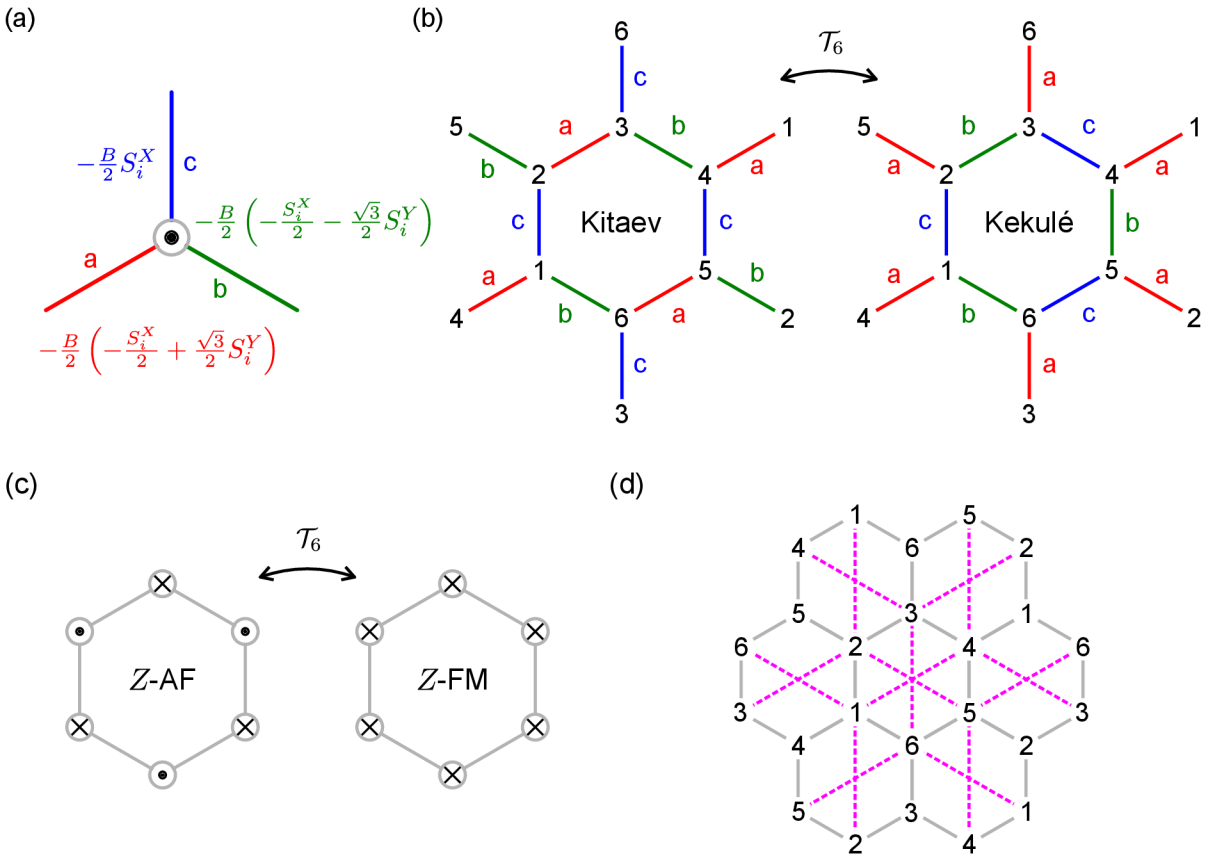

Figure 2.5: (a) On-site cancellation of quantum fluctuations coming from the B-term for a Z-polarized (anti)collinear spin state. Each of the three bonds contributes a different term, but their total sum is zero. (b) $\mathcal{T}_1$ transformation maps the EKH model to an extended Kitaev-Kekulé model which features a benzene-like bond structure. (c) $\mathcal{T}_6$ maps a Z-polarized Neél state to a Z-polarized collinear FM state and vice versa. (d) Third-nearest neighbor bonds of the six central hexagon sites are shown in magenta. The sublattice distribution is identical to the nearest neighbor situation.

same, but we will show it nonetheless – first, for historical reasons (it is the way we obtained the form of fluctuation-free phase-space manifolds for the first time, and as such it is shown in our paper [12]) and second because it is an opportunity to illustrate how $\mathcal{T}_6$ subtly transforms the bond structure of Kitaev honeycomb model.

$\mathcal{T}_6$ is a 6-sublattice mapping represented by sublattice-dependent spin rotations. The position of sublattices 1-6 is shown in Fig. 2.5 panel (b) and (c). We can represent these rotations as matrices $\mathcal{T}_6^i$ that multiply the vector of spin operators $\mathbf{S}_i$ on a lattice i:

$$\tilde{\mathbf{S}}_i = \mathcal{T}_6^i \mathbf{S}_i. \tag{2.42}$$

In such a notation, the matrices and the geometric rotations they represent are (using the global

XYZ reference frame):

$$\mathcal{T}_6^1 = \overbrace{\begin{pmatrix} 1 & 0 & 0 \\ 0 & 1 & 0 \\ 0 & 0 & 1 \end{pmatrix}}^{\text{identity}}, \quad \mathcal{T}_6^2 = \overbrace{\begin{pmatrix} -1 & 0 & 0 \\ 0 & 1 & 0 \\ 0 & 0 & -1 \end{pmatrix}}^{\pi\text{-rot. around } Y}, \quad \mathcal{T}_6^3 = \overbrace{\begin{pmatrix} -\frac{1}{2} & -\frac{\sqrt{3}}{2} & 0 \\ \frac{\sqrt{3}}{2} & -\frac{1}{2} & 0 \\ 0 & 0 & 1 \end{pmatrix}}^{\frac{4}{3}\pi\text{-rot. around } Z},$$

$$\mathcal{T}_6^4 = \underbrace{\begin{pmatrix} \frac{1}{2} & \frac{\sqrt{3}}{2} & 0 \\ \frac{\sqrt{3}}{2} & -\frac{1}{2} & 0 \\ 0 & 0 & -1 \end{pmatrix}}_{\pi\text{-rot. around } \frac{\sqrt{3}}{2}X+\frac{1}{2}Y}, \quad \mathcal{T}_6^5 = \underbrace{\begin{pmatrix} -\frac{1}{2} & \frac{\sqrt{3}}{2} & 0 \\ -\frac{\sqrt{3}}{2} & -\frac{1}{2} & 0 \\ 0 & 0 & 1 \end{pmatrix}}_{\frac{2}{3}\pi\text{-rot. around } Z}, \quad \mathcal{T}_6^6 = \underbrace{\begin{pmatrix} \frac{1}{2} & -\frac{\sqrt{3}}{2} & 0 \\ -\frac{\sqrt{3}}{2} & -\frac{1}{2} & 0 \\ 0 & 0 & -1 \end{pmatrix}}_{\pi\text{-rot. around } \frac{\sqrt{3}}{2}X-\frac{1}{2}Y}. \tag{2.43}$$

The first thing to notice is the ZZ-components of the matrices – we get two groups of sublattices, half of them with a $+1$ component and the other half with -1. As it turns out, sites that are nearest neighbors always belong to sublattices that fall into different groups, which means that the $\mathcal{T}_6$ mapping flips one spin in each bond of a Z-polarized spin state, connecting thereby FM and Neél states, as shown in panel c) of Fig. 2.5. It remains to show what happens to the interaction under the $\mathcal{T}_6$ transformation.

Applying the mapping, we obtain the interaction matrices $\tilde{H}_{ij}$ for each bond type ij as

$$\tilde{H}_{ij} = \mathcal{T}_6^i H_{ij} \mathcal{T}_6^{jT}, \tag{2.44}$$

where we need to consider all unique combinations of neighboring pairs ij with i, j each belonging to one of the 6 sublattices $\{1,2,3,4,5,6\}$. There are 9 such combinations, three for each bond direction a, b, c. The respective Hamiltonian matrices are (again using the XYZ reference frame):

$$\begin{aligned} H_{14} = H_{23} = H_{56} &= \begin{pmatrix} J_{XY} - \frac{A}{2} & -\frac{\sqrt{3}}{2}A & \frac{B}{2} \\ -\frac{\sqrt{3}}{2}A & J_{XY} + \frac{A}{2} & -\frac{\sqrt{3}}{2}B \\ \frac{B}{2} & -\frac{\sqrt{3}}{2}B & J_Z \end{pmatrix} = H_a, \\ H_{16} = H_{25} = H_{34} &= \begin{pmatrix} J_{XY} - \frac{A}{2} & \frac{\sqrt{3}}{2}A & \frac{B}{2} \\ \frac{\sqrt{3}}{2}A & J_{XY} + \frac{A}{2} & \frac{\sqrt{3}}{2}B \\ \frac{B}{2} & \frac{\sqrt{3}}{2}B & J_Z \end{pmatrix} = H_b, \\ H_{12} = H_{36} = H_{45} &= \begin{pmatrix} A + J_{XY} & 0 & -B \\ 0 & -A + J_{XY} & 0 \\ -B & 0 & J_Z \end{pmatrix} = H_c. \end{aligned} \tag{2.45}$$

Compare this with the group of interaction matrices after applying the transformation (2.44):

$$\tilde{H}_{14} = \tilde{H}_{25} = \tilde{H}_{36} = \begin{pmatrix} -A + \frac{J_{XY}}{2} & \frac{\sqrt{3}}{2}J_{XY} & -\frac{B}{2} \\ \frac{\sqrt{3}}{2}J_{XY} & -A - \frac{J_{XY}}{2} & \frac{\sqrt{3}}{2}B \\ -\frac{B}{2} & \frac{\sqrt{3}}{2}B & -J_Z \end{pmatrix} = \tilde{H}_a,$$

$$\tilde{H}_{16} = \tilde{H}_{23} = \tilde{H}_{45} = \begin{pmatrix} -A + \frac{J_{XY}}{2} & -\frac{\sqrt{3}}{2}J_{XY} & -\frac{B}{2} \\ -\frac{\sqrt{3}}{2}J_{XY} & -A - \frac{J_{XY}}{2} & -\frac{\sqrt{3}}{2}B \\ -\frac{B}{2} & -\frac{\sqrt{3}}{2}B & -J_Z \end{pmatrix} = \tilde{H}_b, \tag{2.46}$$

$$\tilde{H}_{12} = \tilde{H}_{34} = \tilde{H}_{56} = \begin{pmatrix} -A - J_{XY} & 0 & B \\ 0 & -A + J_{XY} & 0 \\ B & 0 & -J_Z \end{pmatrix} = \tilde{H}_c.$$

Again, we obtain three groups of matrices corresponding to three bond types, but the matrices now fall into different groups, meaning that the bond-type distribution has been altered by $\mathcal{T}_6$. Each site is still connected to its neighbors by three distinct bond types, but their distribution on the lattice is now reminiscent of benzene-like rings of two alternating bond types, with the rings connected by the bonds of the third type. This bond structure is depicted in Fig. 2.5 panel (b), where a center ring of alternating b, c bonds is connected to the rest of the lattice by a-type bonds. Such a bond distribution is characteristic for Kekulé spin models, we can therefore say that the $\mathcal{T}_6$ transformation maps the EKH model to an extended variant of Kekulé-Kitaev model [144].

Secondly, looking at the matrix elements, we see that they have the same form as the original EKH interaction matrices, just with different values of interaction parameters. These are related to the original EKH parameters via

$$(J_{XY}, J_Z, A, B)_{\text{Kekulé}} = (-A, -J_Z, -J_{XY}, -B)_{\text{EKH}}, \tag{2.47}$$

i.e., J_{XY} and A are interchanged, and all parameters acquire a minus sign. In this way, FM and AF Ising points can be mapped onto each other. Since after the transformation, the interaction form is unchanged and only the bond distribution is altered, the on-site cancellation of B-type fluctuation terms applies in the same way, and the FM fluctuation-free manifold represented by $A = 0$ is thus mapped onto the AF manifold with $J_{XY} = 0$.

Effects of J_3

As a final note, we discuss how are the conclusions of the preceding paragraphs affected by the addition of third-nearest neighbor Heisenberg coupling

$$\mathcal{H}_3 = \sum_{\langle ij \rangle \in 3^{\text{rd}}\text{NN}} J_3 \mathbf{S}_i \cdot \mathbf{S}_j. \tag{2.48}$$

Panel (d) of Fig. 2.5 shows the third-nearest neighbors of the six central hexagon sites. Interestingly, the bond distribution with respect to the six sublattices is the same as for the next-nearest neighbor situation – e.g., a site belonging to sublattice 1 forms a c-bond with a site from sublattice 2, an a-bond with a site from sublattice 4 and a b-bond with a site from sublattice 6. As such, the addition of J_3 interaction has the same effect as J_{XY} and J_Z interaction terms of the same magnitude. Because of that, the ferromagnetic classical states are preserved, since J_{XY} does not couple to them. It does couple to AF Z-polarized states though, and these are consequently no longer eigenstates of the Hamiltonian after the addition of $\mathcal{H}_3$.

2.1.5 Symmetry-based view of the phase diagram

In this section we show how the analytical calculations based on symmetry arguments can be used to partially construct the phase diagram of the model. We can understand the hidden $SU(2)$ points as "centers" in the phase space and the respective ordered phases as "emanating" from them. In other cases, the exact points are found to delimit borders/meeting points of neighboring phases, hosting a degeneracy. The $\mathcal{T}_1$ transformation serves as a guide to two additional Kitaev spin liquid windows that might otherwise be overlooked. Additionally, the symmetry analysis provides us with information about the ordered moment direction and the strength of quantum fluctuations which helps with the interpretation of numerical data shown in the next chapter of this thesis 2.2.

Parametrization

Because of the relatively high number of free parameters of our model, we must make a compromise in how to display the phase diagram. Guided by the choices made in earlier publications [109, 51], we parametrize J, K, Γ by angles θ, φ

$$\begin{aligned} J &= \sin\theta\cos\varphi, \\ K &= \sin\theta\sin\varphi, \\ \Gamma &= \cos\theta, \end{aligned} \tag{2.49}$$

and make sections through the parameter space corresponding to constant Γ', J_3. The parametrization fixes the overall energy scale $\sqrt{J^2+K^2+\Gamma^2} = 1$ which has no effect on the phase characteristics of the states. We can aid our intuition by using a geometric interpretation (see Fig. 2.6) – angles θ, φ represent latitude and longitude, whereas the setting of absolute energy scale means moving on the surface of a sphere. On the equator of the sphere ($\theta = \pi/2$) we have the original Kitaev-Heisenberg $J-K$ model, with the Heisenberg limits at $\varphi = 0, \pi$ and Kitaev points at $\varphi = \pi/2, 3\pi/2$. The parameter Γ is tied to the latitude θ, being maximal $\Gamma = 1$ at the north pole and minimal $\Gamma = -1$ at the south pole.

This parametrization choice is mostly guided by historical developments. Jackeli and Khaliullin [39] derived a two-parameter $J-K$ model as a minimal description of Na_2IrO_3 low-energy physics, which led the authors of [109] to represent its phase diagram by a single angle (corresponding to φ in (2.49)). It was further realized [51] that the model was incomplete and a bond-dependent symmetric off-diagonal exchange Γ must be added. The above two-angle "spherical" parametrization was therefore chosen, being completely appropriate for such a three-parameter model. In our case, adding Γ' and J_3 complicates things, and because it is not clear whether J, K, Γ are dominant with respect to Γ', J_3, the parametrization may not be the most natural. Nevertheless, given these limitations and the lack of a better alternative, we opt to retain it to enable an easier comparison with the existing literature.

One feature of parametrization 2.49 is that a planar map shows a region of only positive Γ or only negative Γ, not both at the same time. Geometrically speaking, we are projecting one hemisphere at a time – northern or southern (see Fig. 2.6). The situation can be helped by observing a classical symmetry of our model, namely the $\Gamma \leftrightarrow -\Gamma$ symmetry. The connection can be found by dividing the honeycomb lattice into two hexagonal sublattices such that neighboring spins belong to a different sublattice, and flipping the spin coordinates $\mathbf{S}_i \to -\mathbf{S}_i$ on one

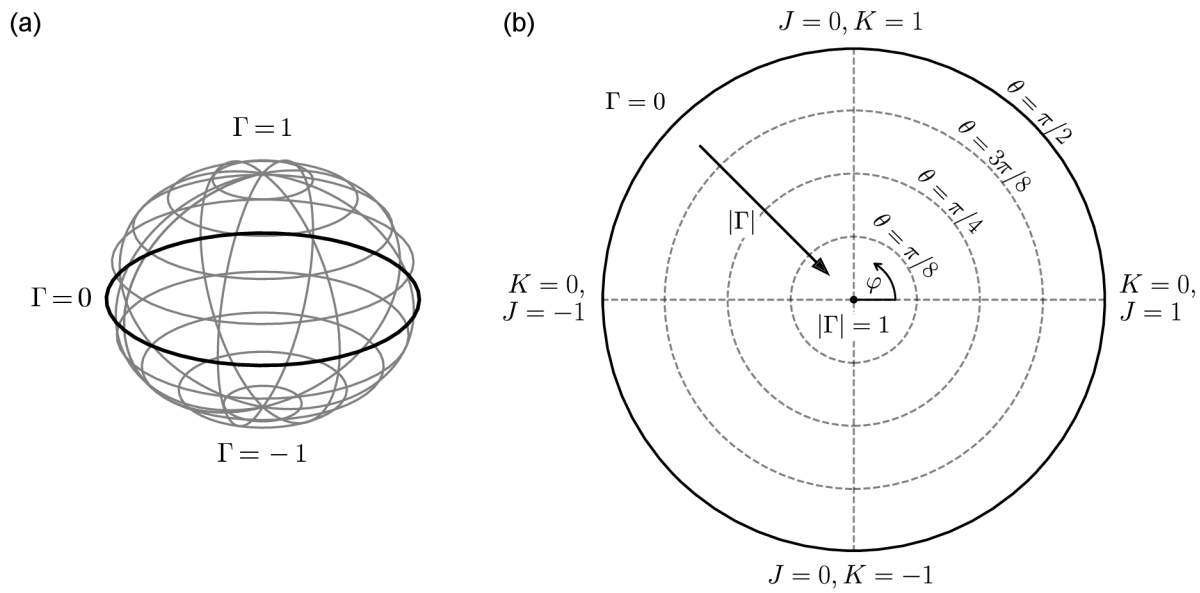

Figure 2.6: A visual guide to the model's spherical parametrization. (a) Lines of constant θ, φ representing latitude and longitude. Parameter Γ is given by the latitude $\theta \in [0, \pi]$ – it is maximum at the poles and zero at the equator (shown in black). (b) 2D projection of the sphere that is used to plot phase diagrams. Parameters J, K vary with longitude $\varphi \in [0, 2\pi]$. Parameters Γ' and J_3 vary independently.

sublattice. After such a mapping, the form of the Hamiltonian is unchanged, but with mapped parameters

$$J \to -J, \quad K \to -K, \quad \Gamma \to -\Gamma, \quad \Gamma' \to -\Gamma', \quad J_3 \to -J_3. \tag{2.50}$$

This translates to the change in angular parameters $\theta \to \pi - \theta, \varphi \to \varphi - \pi$, or in other words, to mirroring around the center of the phase diagram. Because the $\Gamma > 0$ and $\Gamma < 0$ regions are tied together in this way, some authors choose to focus on the positive case only [51]. It is necessary to keep in mind that this symmetry works only on a classical level, since it violates spin commutation relations, and thus cannot be applied to obtain $\Gamma < 0$ ground states from $\Gamma > 0$ and vice versa. Nevertheless, the symmetry can be seen in several features of the phase diagram, such as the positions of hidden $SU(2)$ points, which we illustrate in the following paragraphs.

Exact points in the quantum phase diagram

Let us now start building a picture of the model's phase diagram by considering its symmetries. We focus on the $\Gamma > 0$ region and let the reader observe the $\Gamma \leftrightarrow -\Gamma$ connection displayed in the following figure 2.7. We also let $J_3 = 0$ throughout.

We begin with the $SU(2)$ points, shown in Fig. 2.7 panels (a)-(d) as blue/red circles, depending on whether they originate in FM or AF Heisenberg point. In general, these points do not lie in a single Γ' parameter slice, hence the figure shows projections of a group of points into a single parameter circle. Each hidden $SU(2)$ point in the figure is labeled by the transformation that connects it to a Heisenberg $SU(2)$ point. Looking at the phase diagram, we can expect it to contain FM and AF phases, located around their respective Heisenberg points. Similarly, a zigzag and a stripy phase will be found around the hidden $SU(2)$ points located on the circumference of the phase diagram which we obtained by the $\mathcal{T}_4$ transformation. Ad-

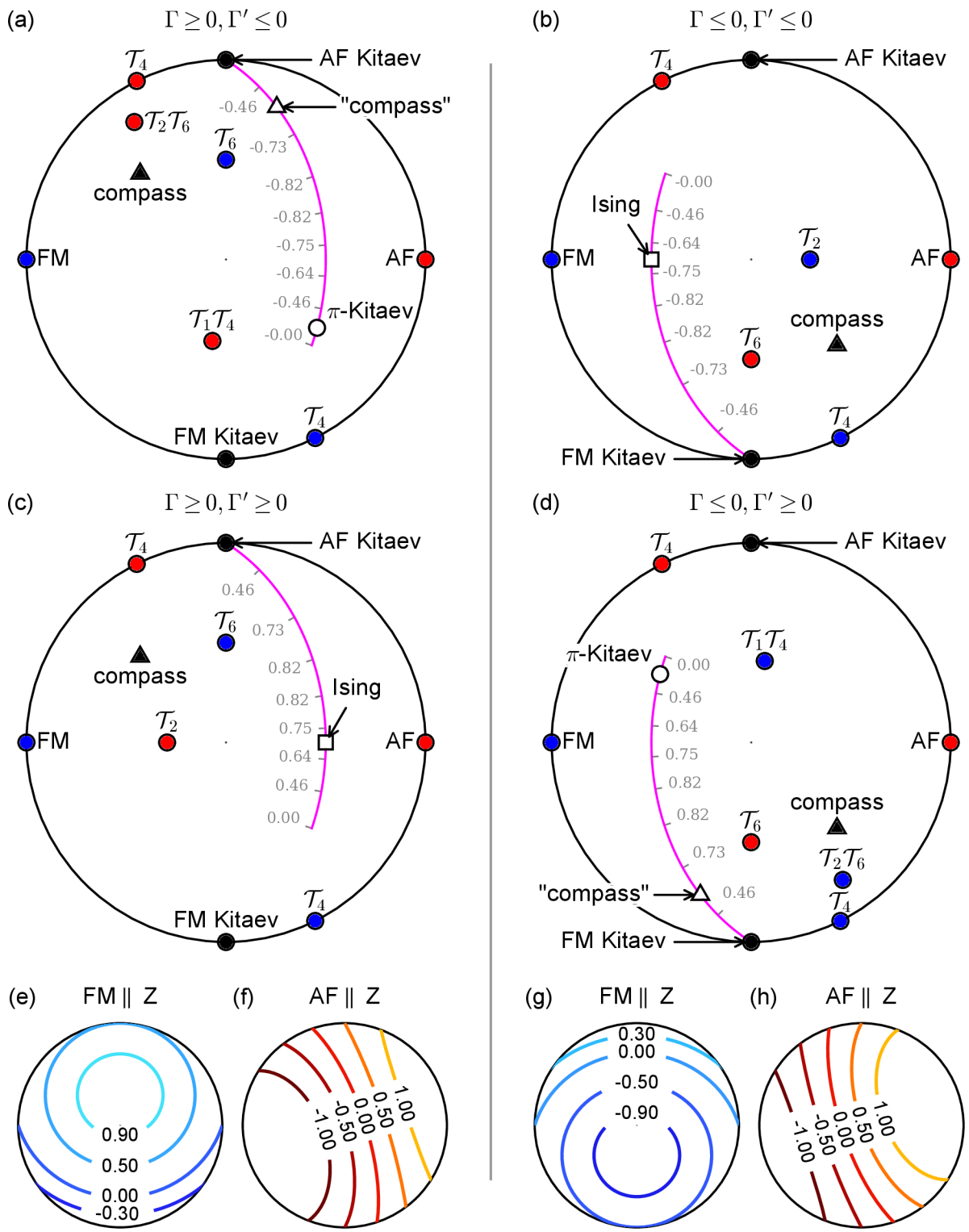

Figure 2.7: (a)-(d) Phase diagram for $\Gamma \geq 0$ (left part of the figure) and $\Gamma \leq 0$ (right part of the figure). Blue (red) circles mark $SU(2)$ points of FM (AF) nature, labeled by the transformations that map them to Heisenberg points. The Ising-Kitaev-compass line is drawn in magenta, with values of Γ' alongside it. Symbols for other notable points are consistent with part 2.1.3. (e),(g) Contours show constant Γ' slices for which classical, non-fluctuating Z-polarized FM states are eigenstates of the Hamiltonian. (f),(h) Same for Z-polarized Neél states. Positions of multiple features in the $\Gamma > 0$ and $\Gamma < 0$ diagrams are connected by mirroring around the center, flipping the sign of Γ' and exchange of FM/AF character.

ditionally, the $\mathcal{T}_6$ transformation maps the FM $SU(2)$ point to a vortex point with parameters $K = \Gamma > 0, J = \Gamma' = 0$.

New hidden $SU(2)$ points uncovered by $\mathcal{T}_2, \mathcal{T}_1\mathcal{T}_4$ and $\mathcal{T}_2\mathcal{T}_6$ transformations help us pinpoint additional ordered phases, as well as say something about the direction of the ordered moment in them. For instance, the $\mathcal{T}_1\mathcal{T}_4$ mapping uncovers an $SU(2)$ point located at the bottom of the diagram's center – see Fig. 2.7 panel (a). This point is a dual partner of the $\mathcal{T}_4$ zigzag point, as they are connected by the dual $\mathcal{T}_1$ mapping. We know from the structure of $\mathcal{T}_1$ that it rotates the magnetic moment by π around the Z-axis. Therefore, the whole zigzag phase centered around the $\mathcal{T}_4$-zigzag point will have a dual partner – another zigzag phase around the $\mathcal{T}_1\mathcal{T}_4$-$SU(2)$ point with spins rotated in the aforementioned way. A completely analogous situation occurs for the stripy phase in the $\Gamma < 0$ region, as one can observe on panel (d). No separate images of FM and AF phases are produced by $\mathcal{T}_1$, as it maps the Heisenberg points onto themselves.

Last, we comment on the $\mathcal{T}_2$ transformation that produces two pairs (one FM, one AF) of $SU(2)$ points from the $\mathcal{T}_6$-vortex and Heisenberg $SU(2)$ points, respectively. The AF $\mathcal{T}_2$-point can be seen near the center of Fig. 2.7 panel (b). We see that it occurs for negative J which favors ferromagnetic spin configurations, but we know that its ground state is identical to a Heisenberg antiferromagnet. Indeed, as we have observed before, $\mathcal{T}_2$ can map FM and AF spin patterns onto each other, effectively "concealing" an AF state behind an FM spin pattern and vice versa. The true nature of the state can be recognized, for example, in the shape of the spin excitation spectra.

Alongside $SU(2)$ points, Kitaev points are the next exactly solvable parameter points featured in the phase diagram. They are shown as full black circles at the top and bottom of the circle in Fig. 2.7 panels (a),(b). As we will see, the spin liquid states persist in a finite parameter window around these points. Using the $\mathcal{T}_1$ transformation, we find two hidden Kitaev points, which are in fact parts of the Ising-Kitaev-compass manifold discussed in section 2.1.3 (shown in the figure as open circles). Since $\mathcal{T}_1$ is the (only) self-dual transformation of the model, finite liquid windows centered around Kitaev points are mapped to finite liquid windows around the hidden Kitaev points. This is especially striking since the hidden AF Kitaev point (panel (a) of Fig. 2.7) is quite near the parameter windows expected for real materials [6].

Uncovering the connection with the Ising-Kitaev-compass continuum of models brought us a hidden Ising point of the EKH model, shown as an open square in panel (b). It occurs for a relatively large positive Γ' in the $J > 0$ part of the phase diagram, serving as another anchor for the AF phase. We also obtain the direction of the ordered moment in the Ising point, which is along Z, i.e. perpendicular to the honeycomb plane. Later we will see that this direction is stable for a larger region around the Ising point.

For completeness, the figure also shows the Ising-Kitaev-compass manifold as a magenta line (the ticks indicate Γ' values) as well as the compass points as triangles. These are not analytically solvable points, but we will address them later on as a part of our numerical study of the phase diagram.

Spin states without quantum fluctuations

As discussed in Sec. 2.1.4, there is an on-site cancellation of quantum fluctuations for manifolds of phase space, where Z-polarized classical FM and Neél states are eigenstates. These manifolds are plotted separately for FM- (blue) and AF-compatible (red) cases as contours of constant Γ' in Fig. 2.7 panels (e)-(h). We showed these to be eigenstates of the Hamiltonian, but it is not

a priori clear whether they are also the lowest ones in energy and thus enter the ground-state phase diagram. However, equipped with insights based on hidden symmetries, we may try to at least speculate for now.

First, let us consider the AF case pictured in panel (f). We expect the AF phase to be located in the right part of the phase diagram with dominant $J > 0$, near the AF Heisenberg point. For positive Γ' the red curves move towards this region, and thus it seems possible that the classical Z-polarized Néel state could form the ground state there. To proceed further, it could be useful to calculate the classical energy based on the ordered moment direction and observe whether the Z-direction is a minimum for finite $\Gamma, \Gamma' > 0$. If this is the case, it would be a strong hint towards the stability of such fluctuation-free spin states as the lowest energy states. We will do this later in Sec. 2.2.3, but for now we note that the presence of the Ising point in the relevant region guarantees that the Z-polarized classical state is the ground state at least at that point, and most likely also in a finite region around it. As we can see from the figure, negative Γ' shifts the fluctuation-free manifold to the left, most likely pushing it out of the AF phase.

The FM case is quite similar – the classical state may realize in regions of dominant negative J near the FM Heisenberg point, for small-to-moderate $|\Gamma'|$. Again, the ground state is certainly classical at the FM Ising point, which occurs for $\Gamma < 0$ and $\Gamma' < 0$. Inversely to the AF case, we can expect the FM classical states to occur mostly for negative Γ'.

All these speculations will be put on stronger ground in the numerical part of this chapter where we will be able to directly see the fluctuation-free ground states as they emerge in the exact diagonalization calculations.

Applications: methodology and interpretation of experimental data

We conclude the current section by discussing the usefulness of the presented symmetry analysis in studying different models and their connection to experiments. We see two different ways in which it can be useful: as a methodological advancement for studying new quantum models, and as a valuable tool helping to connect theoretical and experimental findings. Methodology-wise, we already presented how the hidden $SU(2)$ points assist in constructing the phase diagram for the extended Kitaev-Heisenberg model, but dual transformations can be found for other models and various geometries as well.

For example, Kimchi and Vishwanath [72] have found a way to generalize the concept of four-sublattice transformations for Kitaev-Heisenberg models, uncovering an underlying Klein four-group structure, and dubbing such mappings Klein dualities. Such dualities are applicable for honeycomb, triangular, and kagome lattices in 2D, and even for 3D FCC, pyrochlore, and hyperkagome lattices. The 3D lattices offer even more complex symmetries – for example, a 3D hyperhoneycomb lattice studied in the context of counter-rotating spiral order in β-Li_2IrO_3 [150] affords a 12-site transformation uncovering a hidden $SU(2)$ point of the considered model.

Second, properties of dual transformations can be practically useful for the analysis of spin excitation spectra. Let us mention a few examples: the authors of [151] considered Kitaev-Heisenberg model on the triangular lattice. Using the four-sublattice rotations described above, they were able to relate the quasi-Goldstone mode found in the stripe phase to an accidental degeneracy in the dual ferromagnetic phase. Considering real materials, the spectrum of honeycomb α-$RuCl_3$ contains pseudo-Goldstone modes at the M points of the first Brillouin zone, complementary to the ordering vector of the zigzag phase [152, 153] which suggests proximity to an accidental degeneracy of the ground state. Using the dual transformation of the extended

Kitaev-Heisenberg model together with the four-sublattice rotation, the authors of [141] traced this feature back to a classical degeneracy of the Neél state persisting under the influence of an antisymmetric Dzyaloshinskii-Moriya-type interaction.

Finally, the $\mathcal{T}_1$ mapping uncovering a hidden zigzag $SU(2)$ point was key in resolving a disparity between expected and measured ordered moment direction in Na_2IrO_3 [99, 11], which is the first materials expected to realize the Jackeli-Khaliullin mechanism. In Ref. [109] the available experimental data were fitted by a two-parameter Kitaev-Heisenberg model, which was believed to be a minimal model for Na_2IrO_3 at the time, predicting an ordered zigzag phase. On one hand, later experimental RIXS data [104, 99] confirmed the agreement of theory with experiment on the spin dynamics front. However, the resonant magnetic x-ray diffraction data [99] on ordered moment direction was impossible to reconcile with the predictions of the original Kitaev-Heisenberg model. This apparent conflict can be resolved by applying the $\mathcal{T}_1$ transformation to the predicted parameter point of the original Kitaev-Heisenberg model: the agreement in spin excitation spectra is preserved since the ground state is unchanged, while at the same time, the rotation of the magnetic ordered moment by π around the Z axis produces a very good agreement with the magnetic moment data of [99].

2.2 Numerical exploration of the phase diagram

Numerical calculations are often a key component in the study of a quantum spin model, as they can provide unbiased information regarding quantum effects. Incorporating numerics becomes especially valuable in the presence of "complications" that limit the application of traditional approaches such as linear spin waves – an example would be frustration by bond-dependent interactions in the case of the EKH model. The utility of numerics is also indisputable in connection with real materials: access to physical quantities such as the direction of magnetic moment or spin excitation spectra can enable detailed comparison with experiments and contributes to our understanding of the material.

For these reasons, a thorough numerical investigation of the EKH Hamiltonian is desired. Several studies have reported portions of the EKH model's phase diagram, both classically [51, 154, 155] and on the quantum level [5, 6, 7, 8, 9]. Our approach is a little bit different – we take a global view of the phase diagram, not focusing on a specific subset of parameters. This way, we are able to map out trends dictated by the interplay of anisotropic interactions and understand them in the context of the model's symmetries discussed in the previous section. Moreover, we paid special attention to the direction of ordered moment in the collinear phases.

We begin by describing the numerical methods used in this work. After a brief exposition of exact diagonalization on finite clusters, we discuss the spin-$\frac{1}{2}$ coherent states method, introduced previously in [10], and extend it to the general case of non-collinear states. The method enables us to determine both the spin orderings as well as the direction of the ordered moment, providing also an estimate of quantum fluctuations present in the ground state. The discussion of the quantum phase diagram is preceded by a short classical analysis, which is found especially useful for the interpretation of effects regarding the direction of ordered moment. Finally, we present the global phase diagram, including the unpublished $\Gamma < 0$ region, incorporating features such as hidden symmetries, fluctuation-free ground states, and mapping to a single-axis model.

2.2.1 Exact diagonalization on finite clusters

Our numerical method of choice is exact diagonalization on finite clusters (henceforth abbreviated as ED). Since the method is well-known and many good references are available [156, 157, 158, 159], it is not our ambition to give a full description here. Instead, we focus on a few specific aspects of the method that are relevant to the following parts of the thesis.

To apply ED to a specific Hamiltonian, one first chooses a finite cluster of sites and a basis of the Hilbert space associated with that cluster. Using this basis, the Hamiltonian is expressed as a (often sparse) matrix and diagonalized. The specific diagonalization procedure is chosen depending on whether the full spectrum is necessary or only a few lowest energy states are sufficient. The lowest eigenvector represents the ground state and can be used to calculate ground state properties such as energy, correlation functions, length/direction of ordered moment, etc. Access to excited states provides the possibility to calculate dynamical quantities, e.g., retarded Green's function, dynamical susceptibilities, and other response functions.

The main advantages of this approach are flexibility, accuracy, and simplicity. Large classes of quantum systems can be treated by ED and expectation values of many observables are easily calculated. Moreover, no approximations are made, and the results are therefore exact. The simplicity of the scheme, direct access to the Hamiltonian and its eigenvectors, and the general transparency of the ED approach are also valuable elements, especially in comparison with the more advanced methods such as DMRG or QMC. On the other hand, the cluster size in ED is severely limited due to the exponential scaling of Hilbert space, making it difficult to draw conclusions about the thermodynamic limit. The finite size of the cluster also means that continuous symmetries cannot be spontaneously broken (see Mermin-Wagner theorem [160, 161, 162]). Thus, the onset of order can be detected only indirectly.

Choice of the cluster

The cluster is normally chosen as large as possible given the available computational resources. Size, however, is not the only criterion – it is also important to consider the symmetry of the cluster and the ratio of the number of boundary sites to bulk sites. Since it is standard practice to use periodic boundary conditions, the cluster should be compatible with spin orderings of the specific model in the sense that it is possible to cover the infinite lattice with these spin patterns by periodically repeating their cluster sub-patterns [1]. For this work, we chose a honeycomb cluster with $N = 24$ sites shown in Fig. 2.8 panel (a). We are dealing with a spin-$\frac{1}{2}$ model, thus the size of a state vector is $2^N = 2^{24} = 16777216$, comfortably fitting into the memory of a standard desktop PC without needing to employ Hilbert space reductions using symmetries [157]. It is compatible with spin orderings of the EKH model, as can be seen in Fig. 2.2, with the sole exception of spiral phases, whose unit cell is larger than the cluster itself. There are also 32-site compatible honeycomb clusters we could use, but, although the dimension of Hilbert space is not entirely prohibitive [77], the additional computational cost makes it difficult to produce phase diagrams of the EKH model, considering the large number of parameters it involves.

As a direct consequence of the finite size of the cluster, there is a limited number of available wavevectors $\mathbf{q}$ compatible with the periodic boundary conditions. The relationship is simple –

[1] The simplest example is a 1D spin chain cluster, which must have an even number of sites to be able to support AF order.

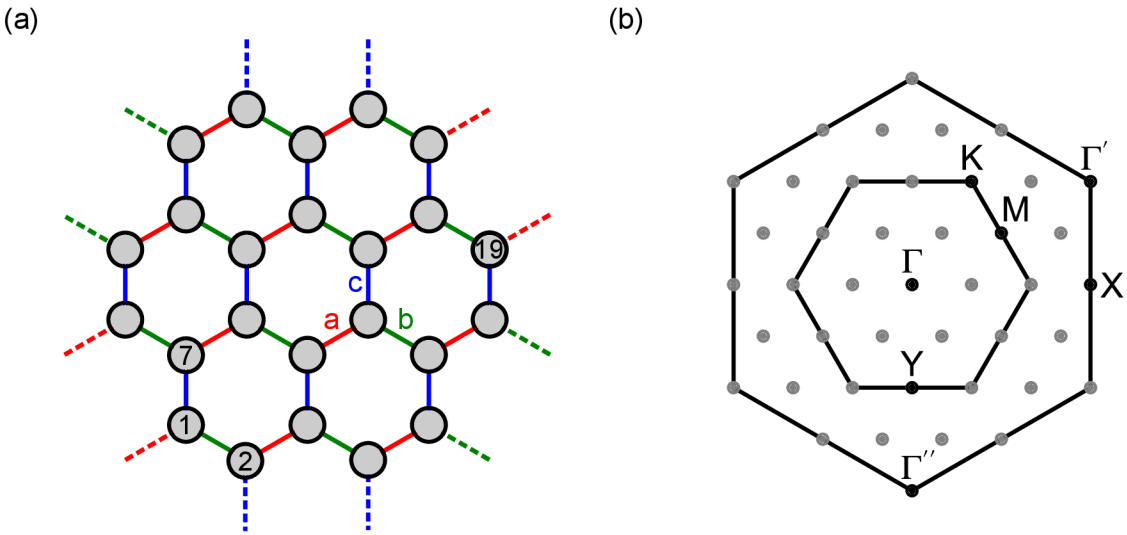

Figure 2.8: (a) 24-site honeycomb cluster used for exact diagonalization calculations. Nearest-neighbor bond directions a, b, c are distinguished by color. We employ periodic boundary conditions – boundary bonds are shown by dashed lines. In this way, each site has exactly three nearest neighbors, one for each bond direction. For example, site 1 is connected to site 19 by an a-bond, to site 2 by a b-bond, and to site 7 by a c-bond. (b) First Brillouin zones of the honeycomb (inner hexagon) and completed triangular (outer hexagon) lattice with labels for distinguishing $\mathbf{q}$-points. The triangular lattice is obtained by filling the hexagonal voids in the honeycomb lattice with extra sites to form a triangular lattice with the same lattice parameter as that of the honeycomb one. The dots show all accessible $\mathbf{q}$-vectors corresponding to the 24-site cluster.

the larger the cluster, the better the $\mathbf{q}$-resolution. Panel (b) of Fig. 2.8 shows the accessible $\mathbf{q}$-points in the case of the 24-site cluster shown in (a). A small complication arises because the honeycomb lattice is not a Bravais lattice, which means we need to show the first Brillouin zone of both the honeycomb (inner hexagon) and the completed triangular lattice (outer hexagon). The point we made earlier about the compatibility of the cluster with certain spin orderings can be reformulated in reciprocal space: the location of Bragg spots of relevant spin patterns (see Fig. 2.11) must coincide with the accessible $\mathbf{q}$-points corresponding to the chosen cluster. As a last remark, we note that one should keep in mind the limited $\mathbf{q}$-resolution especially when encountering various reciprocal-space maps (for example correlation functions $\left\langle S^{\alpha}_{-\mathbf{q}} S^{\beta}_{\mathbf{q}} \right\rangle$): even though continuous maps are often shown (we also do this in Sec. 2.2.4), these are a result of interpolation.

Diagonalization procedure: the Lanczos algorithm

Standard procedures for full diagonalization of Hermitian matrices suffer from an unfavorable quadratic $\mathcal{O}(N^2)$ scaling of the memory requirements with the linear system size N and even worse, cubic $\mathcal{O}(N^3)$ scaling of the computational time with N [163]. In case only a few extremal eigenvalues and eigenvectors are needed, for example, the ground state and a few low-lying excited states, the Lanczos algorithm [164] provides a significantly faster alternative to full diagonalization, with $\mathcal{O}(N)$ scaling for both storage and computational time.

The algorithm starts with a random vector $|\psi_0\rangle$ and by repeatingly applying the Hamiltonian matrix $\mathcal{H}$ the so-called Krylov space is formed:

$$\mathcal{K}_M = \{|\psi_0\rangle, \mathcal{H}|\psi_0\rangle, \mathcal{H}^2|\psi_0\rangle, \ldots, \mathcal{H}^M|\psi_0\rangle\}. \tag{2.51}$$

Orthogonalizing these states against each other yields the Krylov basis in which the Hamiltonian matrix has a tridiagonal form. This matrix can then be diagonalized using one of the standard algorithms suitable for tridiagonal matrices [165]. Such a procedure is, in principle, exact in the limit $M \to \infty$, though in practice, one has to introduce a cutoff at some finite M. One of the main advantages of the Lanczos procedure is the fact that the convergence is usually very quick and often it is enough to use $M \approx 100$ to reach machine precision, even though N is many orders of magnitude larger.

Drawing from practical experience with the algorithm, we find that only very rarely it is necessary to iterate for more than 200 iterations, and we always reach sufficient precision with $M < 1000$. The larger values of M are typically needed to sufficiently resolve quasi-degenerate states. Obtaining the tridiagonal Hamiltonian matrix is generally very quick since the matrix multiplication can be well parallelized. The algorithm's most often cited shortcomings stem from the loss of orthogonality due to numerical round-off errors, leading to artificial degeneracies such as excited states "falling down" in energy onto lower states. In our experience this is not a problem when only the ground state is needed, one only has to keep in mind that the degeneracies of resulting eigenstates are meaningless.

The exact point when the Krylov recursion is truncated has to be determined by an ad-hoc criterion. One can follow the change in the few lowest eigenvalues during the iterations, but the precision of the ground state vector does not follow the precision of the ground state energy and usually comes later. Instead, we have observed that the minimum error of the ground state vector determined by $\mathcal{H}|\mathrm{GS}\rangle - E_{\mathrm{GS}}|\mathrm{GS}\rangle$ correlates with oscillations of the overlap between the first and last Lanczos vector, signifying a change of regime regarding the orthogonality of the Krylov basis. We have successfully applied this heuristic to various spin models, and it has proven to be quite reliable.

Ordered magnetic moment in ED

Apart from the identification of phases, one of the main numerical tasks of this work is the calculation of ordered magnetic moment. As already noted, the ED cluster ground state does not spontaneously break symmetry and corresponds to a superposition of all possible degenerate orderings. For this reason, the resolution of ordered moment using ED is an intricate task, which is accomplished more easily using different variants of the method, such as self-consistent cluster mean-field theory [166]. The standard way of approaching this problem is to evaluate the 3×3 correlation matrix $\langle S^{\alpha}_{-\mathbf{Q}} S^{\beta}_{\mathbf{Q}} \rangle$ $(\alpha, \beta = x, y, z)$ at the ordering wavevector $\mathbf{Q}$ and identify the direction of ordered moment with the eigenvector corresponding to the largest eigenvalue. Similarly, the Bragg spots in the static structure factor $\mathrm{Tr}\left\langle S^{\alpha}_{-\mathbf{q}} S^{\beta}_{\mathbf{q}} \right\rangle$ are often used to identify the spin ordering of the ED ground state.

This standard method using correlation matrices has several deficiencies [10]. The most problematic is the case when the ground state contains several degenerate easy axis directions. These are represented by identical eigenvalues of the correlation matrix evaluated at ordering wavevector $\mathbf{Q}$, and therefore cannot be resolved. Such situations are present also for the EKH

model, as investigated in [10]. In the most severe case, when three cubic axes x, y, z are equivalent, all eigenvalues of the correlation matrix are the same, and thus, the matrix is isotropic. Other problems may arise when probing orderings such as zigzag or stripy, where several equivalent spin patterns (running along the three bond directions) exist in a superposition. These equivalent patterns correspond to distinct ordering wavevectors $\mathbf{Q}$, whose separation is imperfect because of the limited range of spin correlations caused by the finite size of the cluster. This phenomenon can cause slight shifts of the ordered moment direction inferred from the correlation matrix at ordering $\mathbf{Q}$.

In light of these facts, we instead use an alternative method of obtaining the moment direction that does not suffer from the flaws mentioned above. It consists of measuring the presence of particular classical product states in the ground state. This approach was introduced by Chaloupka and Khaliullin in [10], but more detailed expositions are not available. Using this opportunity, we dedicate the whole next section to a thorough description of the algorithm, including a discussion of practical implementation with examples. We extensively use the method in the construction of the global phase diagram of the EKH model in Sec. 2.2.

2.2.2 The method of spin-$\frac{1}{2}$ coherent states

Consider the FM Ising point of the EKH model: the ground state is a classical ferromagnetic state polarized along the Z axis. We can obtain the ground state numerically using exact diagonalization and the result is in general a linear combination of two cluster basis states:

$$|\mathrm{FM}\rangle = c_{\uparrow}|\uparrow\uparrow\ldots\uparrow\rangle + c_{\downarrow}|\downarrow\downarrow\ldots\downarrow\rangle\,, \tag{2.52}$$

where the quantization axis is chosen parallel with the moment direction. If we calculate overlaps with all cluster basis states, we get

$$\begin{aligned}\langle\uparrow\uparrow\ldots\uparrow|\mathrm{FM}\rangle &= c_{\uparrow},\\ \langle\downarrow\downarrow\ldots\downarrow|\mathrm{FM}\rangle &= c_{\downarrow},\end{aligned} \tag{2.53}$$

and all other overlaps are zero. This is very clear, however, departing from the Ising point, the anisotropic interactions rotate the magnetic moment and dress the classical ground state with quantum fluctuations. In that case, the exact diagonalization ground state is no longer transparent but is a complex superposition of a large number of states since ED ground states do not spontaneously break the symmetry. The standard way of analyzing such states is to compute auxiliary physical quantities such as spin structure factor. Possible problems with this approach were mentioned at the end of the last section.

To mitigate these problems and disentangle the ground state in another way, we propose the following method. First, we construct a set of cluster states rotated such that the spins point into a direction $\mathbf{n}$ given by spherical angles θ, ϕ:

$$\begin{aligned}|\uparrow\uparrow\ldots\uparrow\rangle_{\theta\phi} &= |\uparrow\rangle_{\theta\phi}\otimes|\uparrow\rangle_{\theta\phi}\otimes\cdots\otimes|\uparrow\rangle_{\theta\phi}\,,\\ |\downarrow\downarrow\ldots\downarrow\rangle_{\theta\phi} &= |\downarrow\rangle_{\theta\phi}\otimes|\downarrow\rangle_{\theta\phi}\otimes\cdots\otimes|\downarrow\rangle_{\theta\phi}\,.\end{aligned} \tag{2.54}$$

Each such product state is constituted by eigenstates of the local $\mathbf{n}\cdot\mathbf{S}$ operator: $|\uparrow\rangle_{\theta\phi}, |\downarrow\rangle_{\theta\phi}$. Then, calculating $\langle\uparrow\uparrow\ldots\uparrow_{\theta\phi}|\mathrm{GS}\rangle$ we get, in analogy with (2.53), a large overlap for only a

handful of states whose moment direction matches those contained in the cluster ground state. Therefore, the direction of the ordered magnetic moment in the ground state corresponds to the direction **n** for which the overlap (squared) is maximal:

$$\max\{P(\theta,\phi) = \left|\langle\uparrow\uparrow\ldots\uparrow_{\theta\phi}|\mathrm{GS}\rangle\right|^2\}. \tag{2.55}$$

The proposed method enables us to obtain the direction of magnetic moment provided that the ground state is a ferromagnet. In addition, it also makes it possible to quantify the strength of quantum fluctuations in the ground state since we directly access the probability of a given classical state $\left|\langle\uparrow\uparrow\ldots\uparrow_{\theta\phi}|\mathrm{GS}\rangle\right|^2$. For example, in the case of the Ising ferromagnet, it holds that

$$\left|\langle\uparrow\uparrow\ldots\uparrow_{\theta\phi}|\mathrm{FM}\rangle\right|^2 + \left|\langle\downarrow\downarrow\ldots\downarrow_{\theta\phi}|\mathrm{FM}\rangle\right|^2 = 1 \tag{2.56}$$

and all overlaps with different basis states are zero. Quantum fluctuations transfer probability from the two FM states (though they remain the most probable) to the other basis states, meaning we can estimate their strength by the quantity

$$1 - \left|\langle\uparrow\uparrow\ldots\uparrow_{\theta\phi}|\mathrm{GS}\rangle\right|^2 - \left|\langle\downarrow\downarrow\ldots\downarrow_{\theta\phi}|\mathrm{GS}\rangle\right|^2. \tag{2.57}$$

The method can be generalized to spin states other than just FM, but before we discuss that, let us first describe in more detail how to obtain the rotated cluster basis states.

Construction of rotated cluster basis states

The basic constituents of the rotated cluster states $|\uparrow\rangle_{\theta\phi}, |\downarrow\rangle_{\theta\phi}$ are referred to as spin-$\frac{1}{2}$ coherent states [167]. We construct them using the spin rotation operator $\mathcal{R}$ (for brevity, we show only the formulas for $\uparrow$):

$$|\uparrow\rangle_{\theta\phi} = \mathcal{R}_Z(\phi)\mathcal{R}_Y(\theta)|\uparrow\rangle. \tag{2.58}$$

The spin-$\frac{1}{2}$ rotation operator $\mathcal{R}_{\mathbf{n}}(\varphi)$ of angle φ about axis **n** is

$$\mathcal{R}_{\mathbf{n}}(\varphi) = e^{-i\mathbf{n}\cdot\boldsymbol{\sigma}\frac{\varphi}{2}}, \tag{2.59}$$

where $\boldsymbol{\sigma}$ denotes the vector of Pauli matrices. Next, we express $\mathcal{R}$ in the standard spin basis of S^Z eigenstates $\{|\uparrow\rangle, |\downarrow\rangle\}$. Since σ_Z is diagonal in this basis, obtaining $\mathcal{R}_Z(\phi)$ is trivial:

$$\mathcal{R}_Z(\phi) = \begin{pmatrix} e^{-i\frac{\phi}{2}} & 0 \\ 0 & e^{i\frac{\phi}{2}} \end{pmatrix}. \tag{2.60}$$

$\mathcal{R}_Y(\theta)$ requires rewriting (2.59) to a form in which the Pauli matrices are not exponentiated. The standard calculation [22] shows that $\mathcal{R}$ is linear in $\boldsymbol{\sigma}$:

$$\mathcal{R}_{\mathbf{n}}(\varphi) = \begin{pmatrix} 1 & 0 \\ 0 & 1 \end{pmatrix}\cos\frac{\varphi}{2} - i(\mathbf{n}\cdot\boldsymbol{\sigma})\sin\frac{\varphi}{2}. \tag{2.61}$$

Inserting $\mathbf{n} = Y, \varphi = \theta$ we get the second desired rotation matrix

$$\mathcal{R}_Y(\theta) = \begin{pmatrix} \cos\frac{\theta}{2} & -\sin\frac{\theta}{2} \\ \sin\frac{\theta}{2} & \cos\frac{\theta}{2} \end{pmatrix}. \tag{2.62}$$

Assembling the pieces, the spin-$\frac{1}{2}$ coherent state $|\uparrow\rangle_{\theta\phi}$ equals

$$|\uparrow\rangle_{\theta\phi} = \begin{pmatrix} e^{-i\frac{\phi}{2}} & 0 \\ 0 & e^{i\frac{\phi}{2}} \end{pmatrix} \begin{pmatrix} \cos\frac{\theta}{2} & -\sin\frac{\theta}{2} \\ \sin\frac{\theta}{2} & \cos\frac{\theta}{2} \end{pmatrix} \begin{pmatrix} 1 \\ 0 \end{pmatrix} = \underbrace{e^{-i\frac{\phi}{2}}\cos\frac{\theta}{2}}_{\equiv\alpha^{\uparrow\uparrow}}|\uparrow\rangle + \underbrace{e^{i\frac{\phi}{2}}\sin\frac{\theta}{2}}_{\equiv\alpha^{\uparrow\downarrow}}|\downarrow\rangle \tag{2.63}$$

and $|\downarrow\rangle_{\theta\phi}$ is

$$|\downarrow\rangle_{\theta\phi} = \begin{pmatrix} e^{-i\frac{\phi}{2}} & 0 \\ 0 & e^{i\frac{\phi}{2}} \end{pmatrix} \begin{pmatrix} \cos\frac{\theta}{2} & -\sin\frac{\theta}{2} \\ \sin\frac{\theta}{2} & \cos\frac{\theta}{2} \end{pmatrix} \begin{pmatrix} 0 \\ 1 \end{pmatrix} = \underbrace{-e^{-i\frac{\phi}{2}}\sin\frac{\theta}{2}}_{\equiv\alpha^{\downarrow\uparrow}}|\uparrow\rangle + \underbrace{e^{i\frac{\phi}{2}}\cos\frac{\theta}{2}}_{\equiv\alpha^{\downarrow\downarrow}}|\downarrow\rangle\,. \tag{2.64}$$

To make latter formulas more concise, we introduce a notation $\alpha^{\chi\xi}$ for the coefficients: $\chi \in \{\uparrow,\downarrow\}$ designates the spin-$\frac{1}{2}$ coherent state on the left-hand side of the equation, $\xi \in \{\uparrow,\downarrow\}$ denotes the S^z-basis state on the right-hand side. This being established, we begin with a cluster state of choice $|\Psi\rangle_{00}$:

$$|\Psi\rangle_{00} = |\chi_1\rangle \otimes |\chi_2\rangle \otimes \ldots \otimes |\chi_N\rangle = |\chi_1\chi_2\ldots\chi_N\rangle\,, \tag{2.65}$$

where N is the number of cluster sites. We choose $|\Psi\rangle_{00}$ as a classical spin pattern corresponding to the studied magnetic ordering (e.g. in the AF phase $|\Psi\rangle_{00}$ is a Neél state). From it, we construct the cluster product state polarized in the (θ,ϕ) direction:

$$|\Psi\rangle_{\theta\phi} = |\chi_1\rangle_{\theta\phi} \otimes |\chi_2\rangle_{\theta\phi} \otimes \ldots \otimes |\chi_N\rangle_{\theta\phi} = |\chi_1\chi_2\ldots\chi_N\rangle_{\theta\phi}\,. \tag{2.66}$$

Inserting the above relations for the on-site spin-$\frac{1}{2}$ coherent states, we obtain

$$|\Psi\rangle_{\theta\phi} = \left[\alpha^{\chi_1\uparrow}|\uparrow_1\rangle + \alpha^{\chi_1\downarrow}|\downarrow_1\rangle\right] \otimes \left[\alpha^{\chi_2\uparrow}|\uparrow_2\rangle + \alpha^{\chi_2\downarrow}|\downarrow_2\rangle\right] \otimes \ldots \otimes \left[\alpha^{\chi_N\uparrow}|\uparrow_N\rangle + \alpha^{\chi_N\downarrow}|\downarrow_N\rangle\right]. \tag{2.67}$$

The (θ,ϕ)-dependence is now wholly in the coefficients α. It remains to multiply the terms in the brackets and identify the products of on-site spin states with the cluster basis states $|i\rangle$:

$$|\Psi\rangle_{\theta\phi} = \sum_{i=0}^{2^N-1}\prod_{j=1}^{N}\alpha^{\chi_j\xi_i}(\theta,\phi)\,|i\rangle = \sum_{i=0}^{2^N-1}\Lambda_i(\theta,\phi)\,|i\rangle\,. \tag{2.68}$$

At this point, we are almost done. We have constructed the cluster state $|\Psi\rangle_{\theta\phi}$ polarized in the (θ,ϕ) direction as a linear combination of standard cluster states $|i\rangle$ with the coefficients $\Lambda_i(\theta,\phi)$ which are themselves products of coefficients α defined by (2.63), (2.64). It remains to construct squared overlaps with the ground state $|\mathrm{GS}\rangle$ and thus measure the weight $P(\theta,\phi)$ of the state $|\Psi\rangle_{\theta\phi}$ in $|\mathrm{GS}\rangle$:

$$P(\theta,\phi) = \left|\langle\Psi_{\theta,\phi}|\mathrm{GS}\rangle\right|^2 = \left|\sum_{i=0}^{2^N-1}\Lambda_i^*(\theta,\phi)\,\langle i|\mathrm{GS}\rangle\right|^2 = \left|\sum_{i=0}^{2^N-1}c_i\Lambda_i^*(\theta,\phi)\right|^2, \tag{2.69}$$

where

$$|\mathrm{GS}\rangle = \sum_{i=0}^{2^N-1}c_i\,|i\rangle \tag{2.70}$$

is the cluster basis representation of the ground state on the N-site cluster. Finding the maximum of $P(\theta,\phi)$ gives us the desired moment direction along with the estimate of the strength of quantum fluctuations in the ground state.

The peak of $P(\theta,\phi)$ has some intrinsic broadness; if it is too flat, it could hinder the accuracy of locating the maximum. The width is given by the overlap of cluster product states differing by the directions of polarization. Consider two such states $|\Psi\rangle, |\Psi'\rangle$ with common $|\Psi\rangle_{00}$, where one is polarized in the Z direction and the other in some other direction given by (θ,ϕ). Then, the overlap is easily computed:

$$\left|\langle\Psi|\Psi'\rangle\right|^2 = |\alpha^{\chi\chi}(\theta,\phi)|^{2N} = \cos^{2N}\left(\frac{\theta}{2}\right), \tag{2.71}$$

This result is general: it holds for any polarization directions $(\theta,\phi),(\theta',\phi')$, one only needs to replace the cosine argument θ with the relative angle between the two directions. We express the width of the peak by the full width at half maximum, which is in this case

$$\mathrm{FWHM} = 4\arccos\left(\frac{1}{2}\right)^{\frac{1}{2N}} \approx 2\sqrt{2/N}. \tag{2.72}$$

Although the width is sizeable and decreases slowly with cluster size, the maximum has the shape of a parabola and thus can be found accurately. We will show an example towards the end of this section where we apply the method to a few ground states of the EKH model.

The above derivation of the method assumed a non-degenerate collinear cluster ground state. In case the ground state is degenerate, the calculation of $P(\theta,\phi)$ from $\left|\langle\Psi_{\theta\phi}|\mathrm{GS}\rangle\right|^2$ is not as simple as (2.69) and has to be adjusted accordingly. This is merely a technical point, which we address in Appendix B. What is more interesting is the situation where the ground state belongs to a phase that is characterized by a non-collinear spin pattern (e.g. vortex, spiral), or if one has no prior information about the phase. In such cases, one must use a generalized form of the procedure with a higher number of angular parameters θ_j,ϕ_j. We continue with the formulation of such a generalized method.

General non-collinear spin patterns

So far, we have presented the method of spin-$\frac{1}{2}$ coherent states with a couple of assumptions that restrict its applicability. The most important of these assumptions are:

- we know the phase of the ground state which we are probing in advance,
- the subspace of cluster states that we are interested in can be described by a single rotating vector such as (2.66), i.e. using only one pair of angles θ,ϕ.

Both of these assumptions have to hold in order to apply the method in the way that we have described it. We have to know the phase of the ground state in advance, since we need to make a choice of the initial cluster state $|\Psi\rangle_{00}$ which we then rotate to obtain $|\Psi\rangle_{\theta\phi}$. Moreover, by choosing just a single pair of angles, in constructing $|\Psi\rangle_{\theta\phi}$ we reach only a subspace of cluster states that can be obtained in this way. We will encounter a counterexample soon, where we will see that the vortex phase of the EKH model contains two subphases that are characterized by spin patterns that cannot be interpolated by a simple rotation.

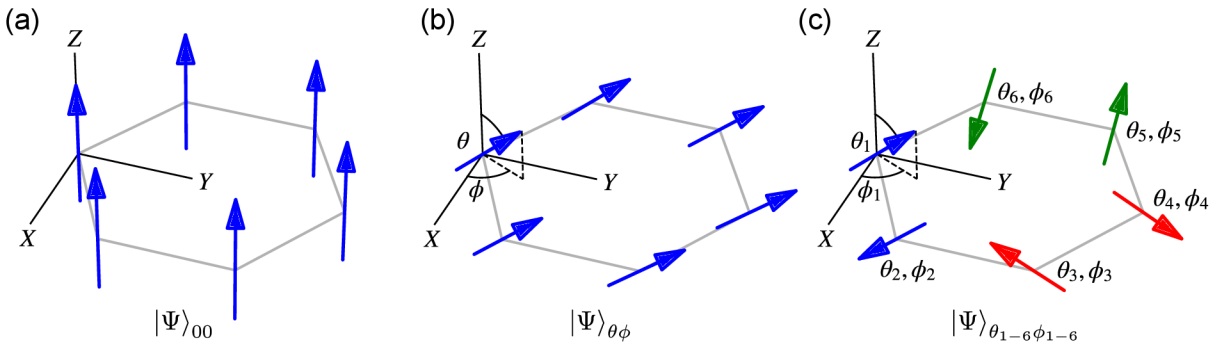

Figure 2.9: Geometrical representation of rotated cluster states $|\Psi\rangle$ on a six-site honeycomb cluster. (a) Cluster basis state $|\Psi\rangle_{00}$ (chosen as FM) polarized in the z direction. (b) FM cluster state $|\Psi\rangle_{\theta\phi}$ polarized in the (θ, ϕ) direction common for all sites. (c) General non-collinear state $|\Psi\rangle$ with one pair of angular variables (θ_i, ϕ_i) per site.

The purpose of these paragraphs is to relax both of these assumptions and consider the most general situation, where we have no prior knowledge about the ground state, and we want to include the whole space of possible product cluster states $|\Psi\rangle$. As before, we start with an initial cluster state $|\Psi\rangle_{00}$:

$$|\Psi\rangle_{00} = |\chi_1\rangle \otimes |\chi_2\rangle \otimes \ldots \otimes |\chi_N\rangle = |\chi_1 \chi_2 \ldots \chi_N\rangle \,. \tag{2.73}$$

This state can be chosen arbitrarily, but it is natural to choose FM for a convenient measurement of rotation angles from a single direction. Next, we construct the rotated cluster state $|\Psi\rangle$ by on-site rotations

$$|\Psi\rangle = |\chi_1\rangle_{\theta_1\phi_1} \otimes |\chi_2\rangle_{\theta_2\phi_2} \otimes \ldots \otimes |\chi_N\rangle_{\theta_N\phi_N} \,. \tag{2.74}$$

The generalization we have made is clear – instead of a single pair of angles (θ, ϕ), the rotation on each site is independent, hence creating a general product cluster spin state. We can imagine it as the state where each spin points in an individually prescribed direction [2] - see Figure 2.9 panel (c). The following relation describes the coordinate representation of this state in the standard cluster basis $|i\rangle$:

$$|\Psi\rangle = \sum_{i=0}^{2^N-1} \prod_{j=1}^{N} \alpha^{\chi_j \xi_i}(\theta_j, \phi_j)\, |i\rangle = \sum_{i=0}^{2^N-1} \Lambda_i(\theta_1, \phi_1, \theta_2, \phi_2, \ldots, \theta_N, \phi_N)\, |i\rangle \,. \tag{2.75}$$

As before, the probability of finding this state in the ground state is given by the squared magnitude of the overlap of $|\Psi\rangle$ with $|\mathrm{GS}\rangle$:

$$P(\theta_1, \phi_1, \theta_2, \phi_2, \ldots, \theta_N, \phi_N) = |\langle \Psi | \mathrm{GS} \rangle|^2 \,. \tag{2.76}$$

The maximum of P gives the most probable 3D spin pattern encoded by the θ_j, ϕ_j angles. This concludes the specification of the most general form of the spin-$\frac{1}{2}$ coherent states method.

In general, the rotated product cluster state $|\Phi\rangle$, which has the maximum overlap with the ground state, is not unique due to a complex phase factor. As a simple example, consider a classical Néel ground state polarized in the z-direction:

$$|\mathrm{GS}\rangle = |\uparrow_1\rangle \otimes |\downarrow_2\rangle \otimes \ldots |\downarrow_N\rangle = |\uparrow_1 \downarrow_2 \ldots \downarrow_N\rangle \,. \tag{2.77}$$

[2] We are using a classical representation of spin as a vector for the sake of creating an intuitive image

The obvious choice for $|\Psi\rangle_{00}$ is the Néel state itself – the maximum of P then occurs for $\theta_j = 0$. However, since we are not aware of this in advance, we begin arbitrarily with an FM state:

$$|\Psi\rangle_{00} = |\downarrow_1\rangle \otimes |\downarrow_2\rangle \otimes \ldots \otimes |\downarrow_N\rangle = |\downarrow_1\downarrow_2 \ldots \downarrow_N\rangle \,. \tag{2.78}$$

Intuitively, we expect our method to yield the maximum weight for

$$\theta_1 = \pi, \theta_2 = 0, \theta_3 = \pi, \ldots, \theta_N = 0,$$

meaning that a state $|\uparrow\rangle$ can be thought of as $|\downarrow\rangle$ rotated around y by an angle π. However, each π-rotation generates a phase (-1):

$$\mathcal{R}_Y(\pi)\,|\downarrow\rangle = e^{-i\sigma_Y \frac{\pi}{2}}\,|\downarrow\rangle = \begin{pmatrix} \cos\frac{\pi}{2} & -\sin\frac{\pi}{2} \\ \sin\frac{\pi}{2} & \cos\frac{\pi}{2} \end{pmatrix} |\downarrow\rangle = -\,|\uparrow\rangle \,. \tag{2.79}$$

Since we identify the direction of the ordered moment by the probability P, which is calculated as the squared magnitude of the $|\Psi\rangle$'s overlap with $|\mathrm{GS}\rangle$, the phase factor disappears and does not affect P. Thus, even though $|\Psi\rangle$ is only unique up to a phase, the non-uniqueness has no effect and the geometrically intuitive approach leads to the correct result.

Efficient implementation of the spin-$\frac{1}{2}$ coherent states method

After establishing the theory, we move to practical aspects of the method. Our starting point is a ground state vector $|\mathrm{GS}\rangle$ obtained numerically by exact diagonalization on a finite cluster containing N sites. We also assume no prior knowledge about the ground state, meaning that we are going to use the fully general formulation of the method. This is typical when one constructs a numerical phase diagram of an unexplored spin model.

Technically, the identification of the most probable spin configuration amounts to finding a global maximum of the function $P(\theta_1, \phi_1, \ldots, \theta_N, \phi_N)$ of $2N$ variables. In general, this poses a difficult computational problem, especially if N is large, which is desirable in our case since we want to minimize the finite-size effects of the cluster. Specifically, we used a 24-site cluster for the exact diagonalization of the EKH model, meaning the function P has 48 arguments.

On the other hand, we can also take advantage of several favorable circumstances. First, the domain $\mathcal{D}$ of the function is constrained and highly regular, since each $\theta_j \in [0, \pi]$ and $\phi_j \in [0, 2\pi]$, and therefore:

$$\mathcal{D}(P) = \underbrace{[0,\pi] \times [0,2\pi] \times [0,\pi] \times \ldots \times [0,2\pi]}_{2N \text{ terms}} . \tag{2.80}$$

Moreover, the function P is "well-behaved": it is a sum of products of simple sines and cosines, so it is continuous, infinitely differentiable, and generally smooth. The function also has a known internal structure, since we constructed it analytically. Therefore we can, for example, access its gradient analytically:

$$\mathbf{x} \equiv \{\theta_1, \phi_1, \ldots, \theta_N, \phi_N\}, \tag{2.81}$$

$$P(\mathbf{x}) = |\langle\Psi|\mathrm{GS}\rangle|^2, \tag{2.82}$$

$$\nabla P = \langle \mathrm{GS}|\Psi\rangle \nabla \langle \Psi|\mathrm{GS}\rangle + \langle \Psi|\mathrm{GS}\rangle \nabla \langle \mathrm{GS}|\Psi\rangle = 2\,\mathrm{Re}\left(\langle \mathrm{GS}|\Psi\rangle \nabla \langle \Psi|\mathrm{GS}\rangle\right). \tag{2.83}$$

$$\nabla \langle \Psi|\mathrm{GS}\rangle = \nabla \left(\sum_{i=0}^{2^N-1} c_i \Lambda_i^*(\mathbf{x}) \right) = \sum_{i=0}^{2^N-1} c_i \nabla \Lambda_i^*(\mathbf{x}) = \sum_{i=0}^{2^N-1} c_i \nabla \prod_{j=1}^{N} \alpha^{\chi_i \xi_j}(\theta_j, \phi_j), \tag{2.84}$$

$$\frac{\partial \langle \Psi|\mathrm{GS}\rangle}{\partial \theta_k} = \sum_{i=0}^{2^N-1} c_i \frac{\partial \alpha^{\chi_i \xi_k}(\theta_k, \phi_k)}{\partial \theta_k} \prod_{\substack{j=1 \\ j\neq k}}^{N} \alpha^{\chi_i \xi_j}(\theta_j, \phi_j), \tag{2.85}$$

$$\frac{\partial \langle \Psi|\mathrm{GS}\rangle}{\partial \phi_k} = \sum_{i=0}^{2^N-1} c_i \frac{\partial \alpha^{\chi_i \xi_k}(\theta_k, \phi_k)}{\partial \phi_k} \prod_{\substack{j=1 \\ j\neq k}}^{N} \alpha^{\chi_i \xi_j}(\theta_j, \phi_j). \tag{2.86}$$

$$\frac{\partial \alpha^{\uparrow\uparrow}}{\partial \theta} = -e^{-i\frac{\phi}{2}} \sin\frac{\theta}{2}, \qquad \frac{\partial \alpha^{\uparrow\uparrow}}{\partial \phi} = -i\frac{\phi}{2} e^{-i\frac{\phi}{2}} \cos\frac{\theta}{2}, \tag{2.87}$$

$$\frac{\partial \alpha^{\uparrow\downarrow}}{\partial \theta} = e^{i\frac{\phi}{2}} \cos\frac{\theta}{2}, \qquad \frac{\partial \alpha^{\uparrow\downarrow}}{\partial \phi} = i\frac{\phi}{2} e^{i\frac{\phi}{2}} \sin\frac{\theta}{2}, \tag{2.88}$$

$$\frac{\partial \alpha^{\downarrow\uparrow}}{\partial \theta} = -e^{-i\frac{\phi}{2}} \cos\frac{\theta}{2}, \qquad \frac{\partial \alpha^{\downarrow\uparrow}}{\partial \phi} = i\frac{\phi}{2} e^{-i\frac{\phi}{2}} \sin\frac{\theta}{2}, \tag{2.89}$$

$$\frac{\partial \alpha^{\downarrow\downarrow}}{\partial \theta} = -e^{i\frac{\phi}{2}} \sin\frac{\theta}{2}, \qquad \frac{\partial \alpha^{\downarrow\downarrow}}{\partial \phi} = i\frac{\phi}{2} e^{i\frac{\phi}{2}} \cos\frac{\theta}{2}. \tag{2.90}$$

This allows for the use of gradient-based optimization methods, widening the pool of possible algorithms that can be applied. Similarly, the Hessian matrix of second derivatives can be computed for a closer analysis of the function's maximum (as we will see in the next section, it can be useful for pinpointing phase boundaries).

The problematic part is, of course, that the function P contains a large number of local maxima corresponding to quasi-stable spin configurations that differ slightly from the most probable configuration (for example, with one or a couple of spins flipped). The goal of global optimization methods is to overcome the local maxima and find the global one. Numerous global optimization algorithms are available (e.g. simulated annealing [168], genetic algorithms [169], stochastic methods [170], etc.) that can be applied to this problem and work well. However, we found a quicker optimization method, tailor-made for the problem of optimization on spin clusters. It involves updates of only a subset of spins at a single step, which significantly speeds up the calculation, while quite reliably leading to global maxima.

Due to increased speed and sufficient accuracy, we consider the custom optimization method suitable for a first rough sweep of the phase diagram. Afterward, for a more precise and refined treatment, we use a separate efficient implementation of the spin-$\frac{1}{2}$ coherent states method targeted specifically at collinear phases (and some other ordered phases such as vortex). This efficient implementation leads to a gain in speed by a factor 10^3 (using the 24-site honeycomb cluster) with respect to a naive implementation, enabling the calculation of a full probability profile $P(\theta, \phi)$ in a few seconds. We include the specification of both methods – the custom global optimization, as well as the efficient method targeting collinear phases – in the Appendix B.

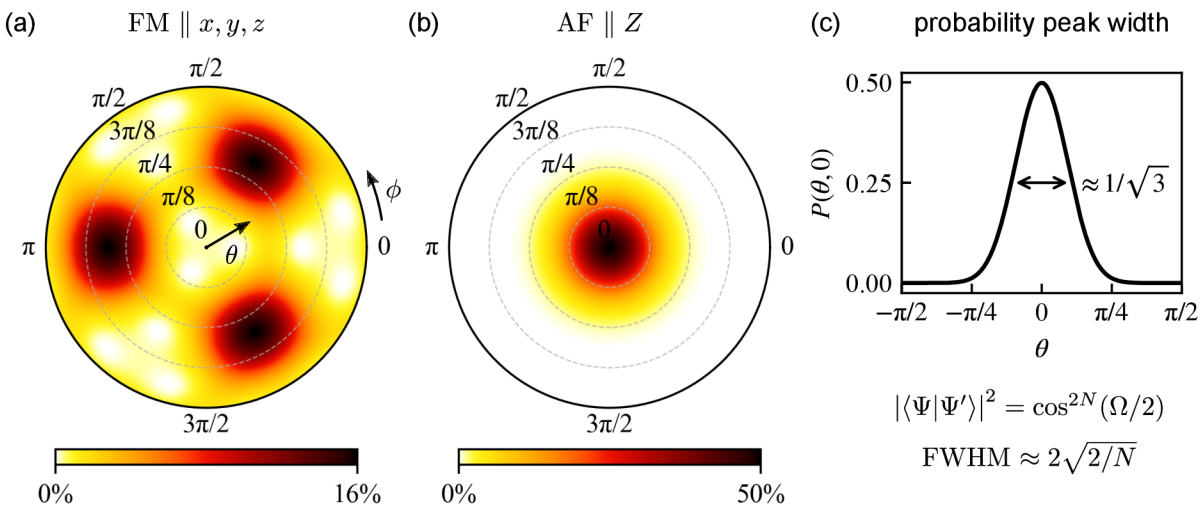

Figure 2.10: Polar probability maps $P(\theta,\phi)$ with θ plotted as the radial coordinate and ϕ as the polar angle. (a) $P(\theta,\phi)$ for a case of a FM ground state with parameters $J=-1, K=-0.2, \Gamma=0$. The maximum probability has a value of 1/6 and occurs for three directions corresponding to cubic axes x,y,z. (b) $P(\theta,\phi)$ for the case of an AF ground state in the Ising point of the model. The probability maximum 50% corresponds to a classical Néel state polarized perpendicular to the honeycomb plane. (c) The cut of the probability map of the panel (b) with $\phi=0$. The relatively large width of the probability peak occurs because cluster states polarized in different directions have non-zero overlap given by the relative angle Ω between the directions of polarization and the cluster size N. For our 24-site cluster, the full width at half maximum is $\approx 2\sqrt{2/24} = 1/\sqrt{3} \doteq 33°$.

We conclude the present section with a few examples illustrating the practical use of the spin-$\frac{1}{2}$ coherent states method. Figure 2.10 shows probability maps obtained using the method as polar plots with θ as the radial and ϕ as the angular coordinate. Panel (a) shows the probability profile for a dominant Heisenberg interaction $J=-1$ and negative Kitaev $K=-0.2$. The quantum fluctuations brought by the Kitaev term partly lift the degeneracy of the Heisenberg FM state and force the moment into one of the cubic x,y,z directions: $P(\theta,\phi)$ contains three equivalent maxima. Compare the transparency of this situation with the correlation matrix method, which, in this case, gives an isotropic matrix with three identical eigenvalues. The ED ground state contains a superposition of six classical spin configurations and a small amount of quantum fluctuations, confirmed by the value of $P \approx 16\%$ in the maxima, which is slightly lower than $\frac{1}{6}$.

The central panel (b) displays the probability profile $P(\theta,\phi)$ for the case of AF Ising point. Here, the quantum fluctuation terms in the Hamiltonian are inactive (see part 2.1.3) and the doubly-degenerate ground state is a superposition of two classical Néel states polarized in the Z-direction, perpendicular to the honeycomb plane. Numerical calculation confirms this, showing a maximum of exactly 50% for $\theta=0$. Knowing the maximum probability values can be very helpful in practice, since it can signalize the lack of quantum fluctuations, strongly hinting at the presence of a hidden symmetry.

The rightmost panel shows a cut of the probability distribution of panel (b) through $\phi=0$, mirrored to show a symmetric peak around $\theta=0$. We can see that the peak is relatively wide for reasons already discussed at the beginning of the section. The full width at half maximum

is $4\arccos\left(\frac{1}{2}\right)^{2N}$ which can be roughly approximated to $2\sqrt{2/N}$, amounting to cca 33° for the 24-site cluster. However, because of the parabolic shape of the peak near the apex, the position of the maximum can be pinpointed with basically unlimited accuracy and the wideness of the peak does not pose a problem for the method.

To summarize: in our experience, the presented procedure is generally faster and more transparent than the traditional way of calculating the ordered moment direction by diagonalizing the correlation matrix $\langle S^{\mu}_{-\mathbf{q}} S^{\nu}_{\mathbf{q}} \rangle$. Because of the efficiency of the described method, it is often advantageous to find the maximum of $P(\theta,\phi)$ for all considered collinear states $|\Psi\rangle_{00}$ – e.g., for the EKH model, these would be FM, AF, stripy and zigzag – and construct the phase by comparing them. The advantage of this approach is accuracy since we are not performing any numerical optimizations, which can be very useful for accurately pinpointing the phase transitions. On the other hand, one cannot directly handle non-collinear (spiral, vortex) and disordered (Kitaev spin liquid) phases this way. In the following text, we provide a thorough inspection of the EKH model's phase diagram, where these issues are discussed at length.

2.2.3 Classical phase diagram of the extended Kitaev-Heisenberg model

Before addressing the quantum case, we construct the classical phase diagram of the extended Kitaev-Heisenberg model obtained by the method of Luttinger & Tisza [171, 172]. In the Luttinger-Tisza algorithm, one relaxes the constraint of fixed spin length at each site $\left|\mathbf{S}^2_{\mathbf{R}}\right| = \frac{1}{4}$ and only requires it to be correct on average, i.e. $\sum_{\mathbf{R}} \left|\mathbf{S}^2_{\mathbf{R}}\right| = \frac{1}{4}N$, where N is the number of spins. The lowest-energy spin configuration can be then found by Fourier-transforming the spin Hamiltonian and diagonalizing the resulting matrix in reciprocal space.

More specifically, we represent the honeycomb lattice as a hexagonal lattice with a two-site basis labeled A,B. We perform the Fourier transformation separately for both sublattices:

$$\mathbf{S}_{\alpha\mathbf{q}} = \frac{1}{N}\sum_{\mathbf{R}} e^{i\mathbf{q}\cdot\mathbf{R}}\mathbf{S}_{\alpha\mathbf{R}}, \qquad \alpha \in \{A,B\}, \tag{2.91}$$

and cast the Hamiltonian to a form of a 6×6 matrix $H_{\mathbf{q}}$:

$$\mathcal{H}_{\text{class}} = \sum_{\mathbf{q}} \mathbf{S}^{\dagger}_{\mathbf{q}} H_{\mathbf{q}} \mathbf{S}_{\mathbf{q}}, \qquad \text{where} \quad \mathbf{S}_{\mathbf{q}} = \begin{pmatrix} \mathbf{S}_{A\mathbf{q}} \\ \mathbf{S}_{B\mathbf{q}} \end{pmatrix}. \tag{2.92}$$

The calculation of $H_{\mathbf{q}}$ is straightforward, and the resulting matrices can be found e.g. in the Appendix of Ref. [11]. We sample the lowest eigenvalue of $H_{\mathbf{q}}$ throughout the first Brillouin zone and find the minimum, which is realized for the ordering $\mathbf{Q}$-vector. Finally, a backward Fourier transformation yields the spin ordering $\mathbf{S}_{\alpha\mathbf{R}}$:

$$\mathbf{S}_{\alpha\mathbf{R}} = e^{-i\mathbf{Q}\cdot\mathbf{R}}\mathbf{S}_{\alpha\mathbf{Q}}, \qquad \alpha \in \{A,B\}, \tag{2.93}$$

where $\mathbf{S}_{\alpha\mathbf{Q}}$ comes from the eigenvector corresponding to the lowest eigenvalue at $\mathbf{Q}$. As a final step of the algorithm, one checks if the spin length constraint is satisfied for each site $\mathbf{R}$; if not, the method fails, and one must resort to a different approach (e.g. classical Monte Carlo).

Before discussing the classical phase diagram, we reiterate that on the classical level, it is enough to inspect the region $\theta \in [0,\pi/2]$, i.e. $\Gamma \geq 0$ due to a classical symmetry detailed in

Section 2.1.2. For compactness, we do not show the $\Gamma \leq 0$ diagrams in the following paragraphs – if needed, they can be obtained from the $\Gamma \geq 0$ partners by mirroring about the center, inverting the sign of Γ', J_3 and flipping the spins on one of the sublattices (the spin-flip connects AF↔FM and zigzag↔stripy spin patterns).

Figure 2.11 shows the classical phase diagram of the EKH Hamiltonian for several chosen values of Γ' and J_3. First, we focus on the $\Gamma' = J_3 = 0$ diagram in panel (b), which contains also the $SU(2)$ points of the model as well as the compass point. We find the same five types of ordered phases as from the previous analysis of exact points, and no extra phase. The two most dominant phases are antiferromagnet (green) and ferromagnet (blue), centered around the Heisenberg $SU(2)$ points. Apart from the zigzag phase around the $\mathcal{T}_4$-$SU(2)$ point, we also see a second zigzag region in the center of the diagram, which is related to the hidden $\mathcal{T}_1\mathcal{T}_4$-point that occurs for large negative Γ'. Curiously, the compass point (shown in the Fig. 2.11 as a gray triangle) lies at the intersection of four distinct ordered regions, hinting at the presence of a degeneracy. The spin length constraint is not fulfilled for this point, but we will tackle this point later with exact diagonalization.

Panels (a)-(f) show the phase diagram for various values of parameters Γ', J_3. We observe that negative Γ' supports mainly vortex and middle-zigzag orderings – this is consistent with the fact that we are approaching the hidden zigzag $SU(2)$ point. Contrary to this trend, positive Γ' works against these phases, supporting AF and FM. Regarding the J_3 parameter, by far the most pronounced is its effect on the zigzag phase. Positive J_3 provides strong support for the zigzag phase, so much so that the two zigzag regions merge in panel (f); negative J_3 completely eliminates the middle zigzag region. Such an effect is pretty intuitive – looking at the spin patterns in panel (g) one sees immediately that positive J_3 brings an energy gain of $\frac{1}{4}J_3$ for each of the three bonds connecting a spin to its neighbors, whereas in the case of J and K terms two bonds lower the energy and one increases it, or vice versa. The regime of negative Γ' and positive J_3 depicted in panel (f) is expected to be relevant for Na_2IrO_3 [6].

Each phase diagram cut contains a gray region where the Luttinger-Tisza algorithm failed to provide a spin ordering that satisfied the constraint of constant spin length. Other authors [51] performed additional analyses and came to the conclusion that the model contains a spiral phase with Bragg peaks at multiple $\mathbf{Q}$-points that are incommensurate with the lattice reciprocal vectors. Multiple such spiral patterns are possible [51, 154], with the ordering $\mathbf{Q}$ varying smoothly between the stripy, zigzag, and vortex positions. In addition to these, the analysis also failed for some isolated points such as compass and Kitaev points – this is because the Kitaev spin liquid is classically unstable against any perturbation caused by the other terms.

Previously, we have studied fluctuation-free manifolds of the model and found classical FM and AF patterns with spins oriented parallel with the Z axis, i.e. perpendicular to the honeycomb plane. We may study the classical energy dependence on the moment direction to see whether such states are likely to occur as ground states of the quantum model. We study the effects of K, Γ, and Γ', since J and J_3 only add isotropic terms to the energy. Starting with the FM phase in the regime of dominant $|J| > K$, a second-order perturbation analysis [10, 173] shows that the spins point to one of the cubic directions x, y, z. Further, adding $\Gamma > 0$ pushes the moment to the honeycomb plane, but this tendency is in conflict with $\Gamma' < 0$ which in turn tries to align the spins with the Z direction. Evaluating the classical energy illuminates these effects: $E_{\text{class}} \propto 3J + K - \Gamma + (\Gamma + 2\Gamma')(n_x + n_y + n_z)^2$. As a result, for finite $\Gamma' < 0$ there is a critical value Γ_c under which the classical moments are in the Z direction – in such a region, whose

shape is a strip along the left-most edge of the circular phase diagram, we may expect to find fluctuation-free states even in the quantum regime.

The nature of the AF $J > K$ case is quite different due to strong fluctuations present already in the Heisenberg case, but the result is again moments pointing to one of the cubic x, y, z directions. Finite $\Gamma > 0$ aligns the moments with the Z axis, minimizing the classical energy $E_{\text{class}} \propto -3J - K + \Gamma - (\Gamma + 2\Gamma')(n_x + n_y + n_z)^2$, just opposite to the action of Γ for the FM phase. We thus expect to find classical Néel states in the quantum phase diagram already for $\Gamma' = 0$, since the range of the AF phase seems to be sufficient to include the fluctuation-free manifold (cf. Fig. 2.7). Negative Γ' can overcome positive Γ and push the moments to the honeycomb plane, creating an analogous situation to the FM case – a critical Γ_c separates the in-plane from the out-of-plane regimes.

The zigzag phase is the one experimentally detected in Na_2IrO_3 and α-$RuCl_3$ and is therefore also the most thoroughly studied one [10]. The anisotropic part of the classical energy is $E_{\text{class}} \propto \mathbf{m}^T M \mathbf{m}$, where $\mathbf{m}$ is a unit vector and M is the matrix

$$M = \begin{pmatrix} 2K & -\Gamma + 2\Gamma' & \Gamma \\ -\Gamma + 2\Gamma' & 2K & \Gamma \\ \Gamma & \Gamma & 0 \end{pmatrix}. \tag{2.94}$$

The eigenvector that corresponds to the lowest eigenvalue of M specifies the ordered moment direction. Clearly, the Kitaev interaction on the diagonal is the dominant factor, preferring either the cubic z axis for $K > 0$ or the xy plane for negative K. Parameters Γ and Γ' lead to smaller shifts from these preferred directions. Specifically, the moment direction in the top zigzag phase around the $\mathcal{T}_4$-point is close to the z-direction, while in the other zigzag region stabilized by $K < 0, \Gamma' < 0, J_3 > 0$ it is in the xy-plane. This means that if the zigzag phases merge, as in panel (f) of Fig. 2.11, the moment direction has to somehow travel between z and xy. Careful analysis [10] shows that this happens gradually through the XZ- and XY-planes.

Finally, we are left with stripy and vortex phases. Similar to the top zigzag phase, the ordered moment of the stripy ordering is tied to the proximity of the cubic axes, lifting a bit away from the honeycomb plane with positive Γ. We find that the vortex ordering lies within the honeycomb plane, in agreement with a previous work [51], without pronounced effects of Γ'.

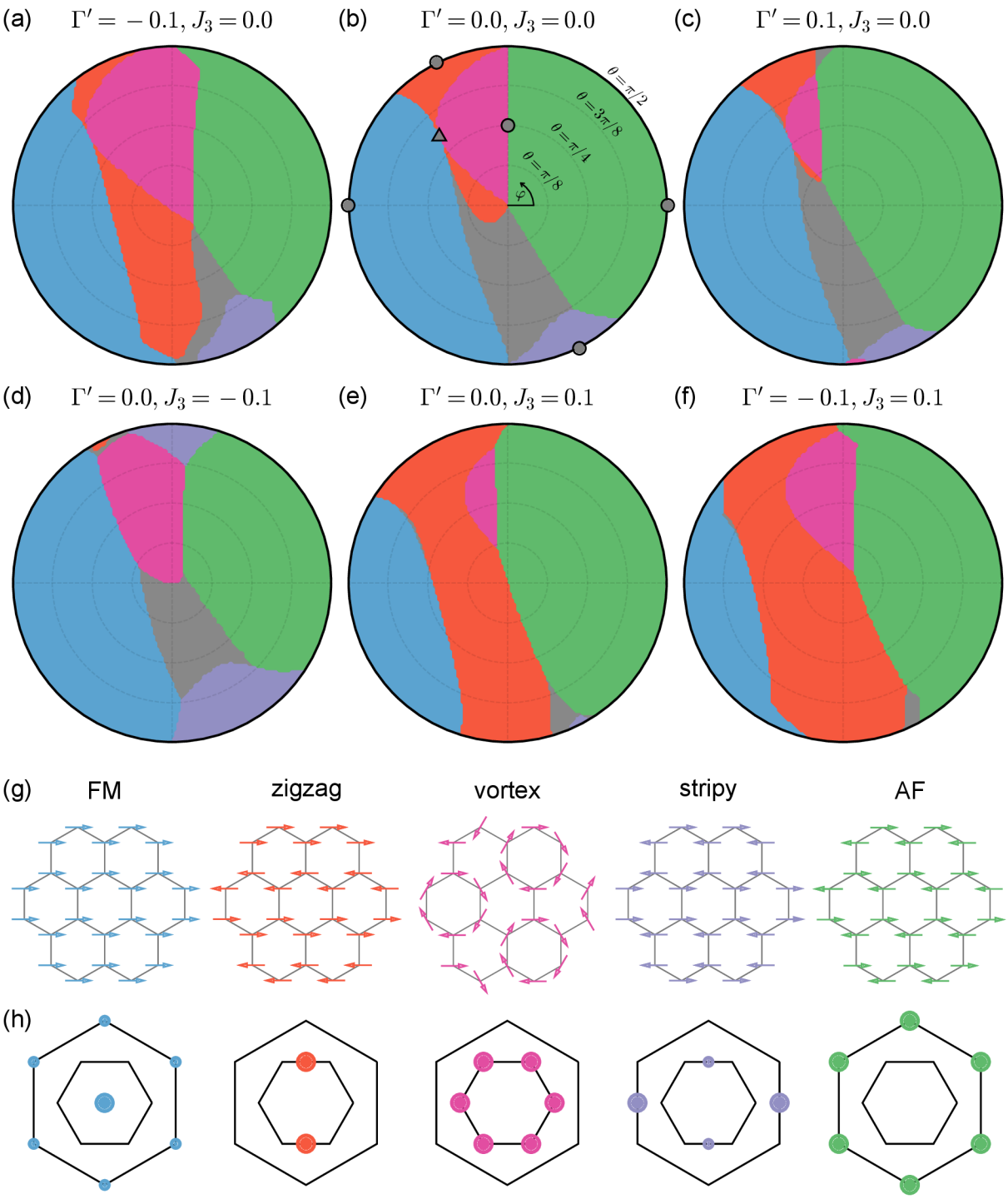

Figure 2.11: Classical phase diagram for $\Gamma \geq 0$ computed using the Luttinger-Tisza method. Circular maps in panels (a)-(c) represent phase diagrams for three values of parameter Γ', whereas the next row (d)-(f) adds J_3-dependence. Points of hidden symmetry are indicated with gray symbols in panel (b). Each region in the phase diagram painted in one color comprises a specific phase – a representative spin configuration for each ordered phase is in panel (g), together with Bragg spots for that phase placed in the first Brillouin zone of the honeycomb (inner hexagon) and triangular (outer hexagon) lattice – panel (h). Phase diagram sections where the Luttinger-Tisza method failed are shown in gray.

2.2.4 Global phase diagram obtained by the spin-$\frac{1}{2}$ coherent states method

We continue our investigation of the EKH model by constructing the quantum phase diagram with the use of exact diagonalization on a 24-site cluster (see Sec. 2.2.1) and subsequent analysis of the ground state by the spin-$\frac{1}{2}$ coherent states method (see Sec. 2.2.2). Apart from the most general optimization in a 48-dimensional parameter space, we also employ the efficient implementation of the coherent states method suitable for collinear states. After finding the most probable collinear configuration, we calculate the Hessian matrix of second derivatives with respect to all 48 angular parameters. By inspecting the eigenvalues of this matrix, we can find a potential instability of the collinear configuration. We found that such an approach is generally quicker and more reliable than the full optimization performed by a global optimization algorithm.

Ordered states of the model in the $\Gamma \geq 0$ subspace

Let us start by considering the $\Gamma \geq 0$ subspace first. Fig. 2.12 panel (a) shows the $\Gamma' = J_3 = 0$ cut of the phase diagram as probability contours for each ordered phase. Broadly speaking, it is similar to the classical phase diagram (cf. Fig. 2.11 panel (b)), but closer inspection shows multiple new effects. The probability in the FM phase approaches $\frac{1}{6}$ near the Heisenberg point – because the ordered moment lies in one of the cubic directions x, y, z, probability $\frac{1}{6}$ is the maximum corresponding to zero quantum fluctuations. In accord with intuition, the quantum fluctuations intensify away from the Heisenberg point, leading to lower probabilities. The ordered moment is pushed to the honeycomb plane by positive Γ, which we understood well already on the classical level. Additionally, we find two separate regions inside the FM phase, with the moments pointing either in the bond direction or perpendicular to it. These regions, including the corresponding patterns, are depicted in the bottom left of Fig. 2.12 panel (a),(b). The origin of such regions is of a quantum nature since classically all in-plane directions are degenerate.

The $\mathcal{T}_4$ transformation links the FM phase to the stripy phase, and this link can be seen also in the probabilities – they peak at $\frac{1}{6}$, same as in the ferromagnet. The moment direction behaves as predicted by the classical analysis, i.e. stays around the cubic x, y, z directions. The probabilities in the vortex phase peak at $\frac{1}{6}$ too, since its origin is also in a hidden $SU(2)$ point of FM nature, this time uncovered by the $\mathcal{T}_6$ transformation. The vortex phase comprises two regions with different most probable spin configurations, which we call vortex-a and vortex-b. Their spin patterns can be captured by a single in-plane deviation angle β, see panel (b) of the figure. The out-of-plane behavior is, however, distinct: vortex-b is always planar, while in the vortex-a region the spins start to tilt out of plane in a staggered AF way. This is most pronounced in the regions near the boundary with zigzag and AF phases and thus can be explained as a proximity effect.

We may gain a deeper understanding of the structure of the vortex phase with the use of symmetries. The $\mathcal{T}_6$-point of FM nature visible in the $\Gamma' = 0$ cut is one of the "sources" for the phase, another being the $\mathcal{T}_2\mathcal{T}_6$-point of AF nature occurring for $\Gamma' \approx 0.5$. In both these points, patterns vortex-a and vortex-b are supported equally, along with a continuous range of configurations stemming from the $SU(2)$ symmetry of the original Heisenberg points. Because of the different nature of FM/AF, quantum fluctuations will differ in strength throughout the phase, depending on the proximity of either hidden $SU(2)$ points. The choice between vortex-

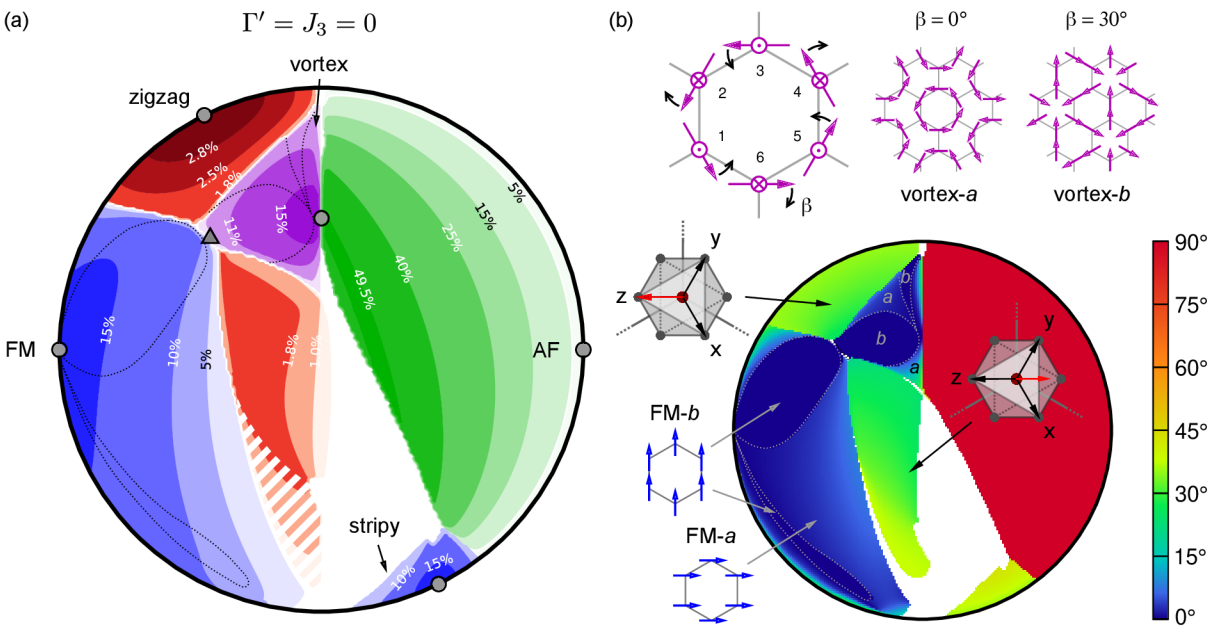

Figure 2.12: (a) Probability contours for the ordered phases in the $\Gamma' = J_3 = 0$ phase diagram slice. Dashed black lines separate distinct regions within one phase. White areas represent regions where no long-range order was found. The hatched part of the middle zigzag phase contains points with a considerable probability of zigzag ordering but also shows a tendency to form noncollinear spin arrangements. Gray circles indicate positions of (hidden) $SU(2)$ points, and the gray triangle labels the FM compass point. (b) The angle of the ordered moment with the honeycomb plane. Included schematics give further information about the direction of spins in ferromagnetic, zigzag and vortex phases. Figure adapted from Ref. [12].

a and vortex-*b* is in turn decided by the vicinity to the two degenerate compass-like points discussed in Sec. 2.1.3. One of them, placed at the meeting point of phases at $K = \Gamma = -J > 0$ and visible in the $\Gamma' = 0$ slice in panel (a), corresponds to the FM compass model and prefers the vortex-*b* configuration. The other is AF compass point with $J = \Gamma > 0, K > 0, \Gamma' < 0$ (see panel (a) of Fig. 2.7) and supports vortex-*a*.

The moments in the AF phase are aligned with the Z-direction, i.e. perpendicular to the honeycomb plane, except when $\Gamma = 0$. Again, such behavior is in accord with what follows from the classical energy. The quantum fluctuations are very strong in the JK limit, leading to small probabilities of the Néel ordering around 2%. The probabilities increase with Γ, peaking at 1/2 on a line that intersects the hidden $\mathcal{T}_6$-point. The 50% probability corresponds to two possible Néel patterns with spins aligned $\parallel Z$, and such states are thus the Ising-like fluctuation-free states that we introduced in Sec. 2.1.4.

Finally, we find two zigzag regions, the same as was the case classically. The direction of ordered moments in these regions are also the same as in the classical phase diagram – near the cubic z axis for the top zigzag region and between x and y for the middle zigzag – but the extent of the middle zigzag region seems to be considerably larger.

To better illuminate the phase boundaries, we plot $\log_{10}|\min(\lambda_H)|$ in Fig. 2.13(i), where $\min(\lambda_H)$ is the lowest eigenvalue of the Hessian matrix. Contrary to the probability map which shows mostly a steady progression, the Hessian uncovers separate regions inside FM and vortex phases, that we labeled using suffixes *a* and *b*. Moreover, we can see that the middle zigzag

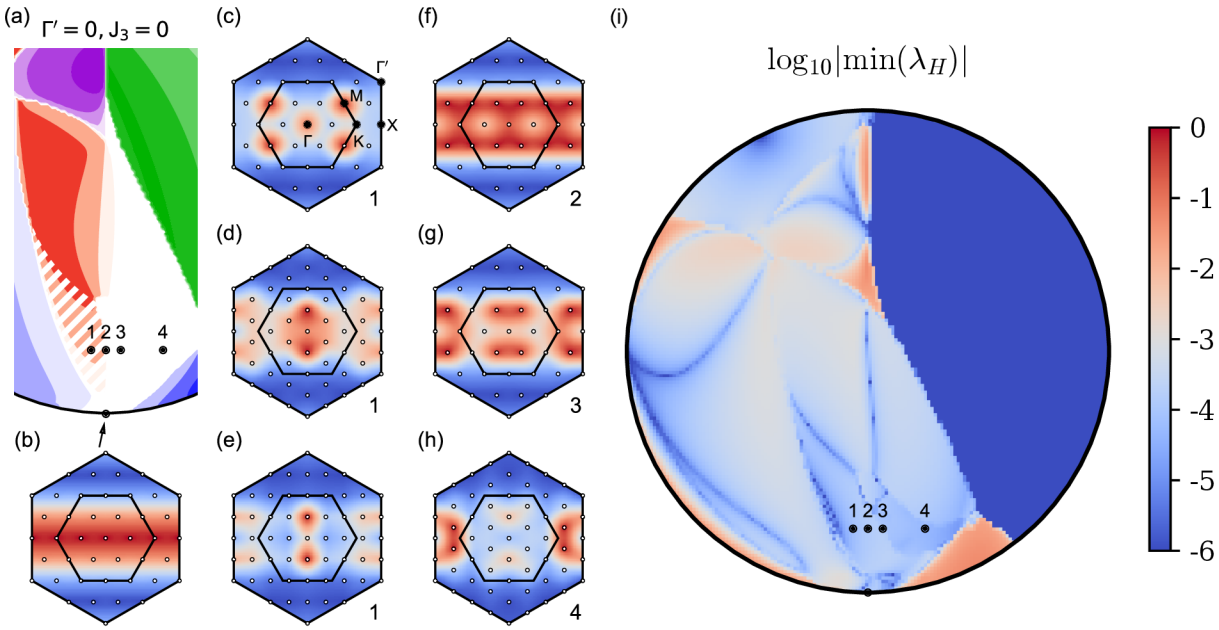

Figure 2.13: (a) Part of the $\Gamma' = J_3 = 0$ phase diagram slice, showing the positions of four parameter points chosen for comparison. (b)-(h) Maps of $\langle S^z_{-\mathbf{q}} S^z_{\mathbf{q}} \rangle$ computed in different parameter points and using clusters of different sizes: (d),(h) 32-site hexagonal cluster, (e) 32-site rectangular and 24-site hexagonal cluster for the rest. Panel (c) also shows positions of high-symmetry reciprocal points. Each map includes the available $\mathbf{q}$-resolution for the used cluster. (i) Logarithmic map of the Hessian matrix' lowest eigenvalue, displayed for the $\Gamma' = J_3 = 0$ phase diagram cut. Small values correspond to shallow minima, indicating instabilities of the calculated optimal spin arrangements.

region also contains a separate area, which we indicate in Fig. 2.12(a) with white hatches. The hatched area is neighboring the white region where Luttinger-Tisza analysis failed to find the minimum-energy configuration, and incommensurate spiral states are expected [51, 8]. It is possible that we are running here into limitations connected with small cluster size, rendering us unable to resolve orderings with large unit cells. In the following, we focus our attention on the white parts of the phase diagram cut.

Incommensurate and spin liquid-like phases

To further investigate the aforementioned region, we performed an analysis based on equal-time spin-spin correlation functions $\langle S^z_{-\mathbf{q}} S^z_{\mathbf{q}} \rangle$: the Fig. 2.13 shows their $\mathbf{q}$-space maps. There are two caveats connected with the correlation maps: first, one should keep in mind that the cluster ground state does not spontaneously break symmetry, but rather contains linear combinations of several possible ordering patterns differing by the moment direction. By focusing on a specific component of the momentum-space correlation function, we are able to access various components of such a combination. The 24-site cluster that we use the most is C_3 symmetric, and therefore in that case the components $\langle S^x_{-\mathbf{q}} S^x_{\mathbf{q}} \rangle, \langle S^y_{-\mathbf{q}} S^y_{\mathbf{q}} \rangle, \langle S^z_{-\mathbf{q}} S^z_{\mathbf{q}} \rangle$ are just $\pm 2\pi/3$-rotated copies of each other. Second, the finite cluster size implies limited $\mathbf{q}$ resolution, and thus continuous maps are always formed by an interpolation between available $\mathbf{q}$ vectors.

Figure 2.13 (a) shows four parameter points that we chose for comparison: 1 in the hatched

(unstable) zigzag region, 2 on the $J = 0$ line, 3 in the expected spiral phase close to the boundary and 4 deeper into the expected spiral phase. Panels (c)-(h) contain maps of equal-time spin-spin correlation functions $\langle S^z_{-\mathbf{q}} S^z_{\mathbf{q}} \rangle$ for points, 1-4, and panel (b) contains the same for the FM Kitaev point (used as a reference). In addition to our default 24-site cluster, we also employed two 32-site clusters, one hexagonal (panel (d) and (h)) and one rectangular (panel (e)). Together, the correlation maps allow us to spot multiple trends regarding the zigzag-spiral boundary.

First, we focus on correlation maps of point 1, where we found a substantial probability of a zigzag ordering. Utilizing three types of clusters – see panels (c),(d), and (e) – we demonstrate that this parameter point is instead part of an incommensurate phase. While the 24-site cluster calculation still shows zigzag-like correlations with peaks at the M momenta (panel (c)), the larger 32-site clusters uncover the instability of zigzag order, showing peaks corresponding to an incommensurate phase. The difference occurs because a more spacious cluster provides denser $\mathbf{q}$-space covering, thus allowing for the preferred state to develop. The difference between two 32-site clusters in panels (d), and (e) is caused by their shapes: while the C_3 symmetric cluster supports all three degenerate moment directions superposed in the ground state, the rectangular-shaped cluster selects only one of those directions.

Next, we investigate how the incommensurate correlations evolve as we move from point 1 to point 3, in the vicinity of the $J = 0$ boundary. Panels (c),(f), and (g) show correlation maps calculated at these points, illustrating how correlations peaked at the M momenta (point 1, panel (c)) and moved partly outside of the first Brillouin zone (point 3, panel (g)). In-between at the boundary point 2 with $J = 0$, we see a level crossing of the corresponding states, resulting in an average pattern resembling the one for the FM Kitaev point (panel (b)). Deeper into the expected spiral phase (point 4, panel (h)), we observe that the Bragg peaks move completely out of the first Brillouin zone, which is a behavior that was predicted also classically using Monte Carlo techniques [52]. Observing the Hessian map in Fig. 2.13(i), we confirm that point 4 seems to be a part of a distinct, L-shaped region, presumably corresponding to an incommensurate spiral phase with ordering wavevectors outside of the first Brillouin zone. On the other hand, points 1-3 lie in a separate area where we found competing zigzag and incommensurate correlations.

Last, the cosine-like shape of the momentum-represented nearest-neighbor correlations of the Kitaev spin liquid (see panel (b)) is present as a background at all points 1-4, although less apparently for maps dominated by Bragg peaks. This suggests that apart from the tendencies towards various incommensurate orderings, the studied region also features liquid behavior, which could be interpreted as a proximity effect of the spin liquid states found on the $J = 0$ line [174, 150]. A variational Monte Carlo study [175] found in this region a proximate Kitaev spin liquid phase that differs from the Kitaev spin liquid phases centered around $|K| = 1$ points in its low-energy spin response.

Apart from the incommensurate regions, the phase diagram also contains disordered regions, most notably those occupied by Kitaev spin liquid states. It is known that both AF and FM Kitaev liquids span a finite parameter window, although the phase transition is of a different nature [176]. Understandably, highly entangled spin liquid states cannot be naturally captured by a spin-$\frac{1}{2}$ coherent state, which is a product state with no entanglement. Despite this fact, we find that the spin liquid ground state still features significant overlaps with configurations found in the classical $S \to \infty$ limit of the Kitaev model. The most probable configurations found by the applied method are shown in Figure 2.14(a),(b) for AF and FM liquids respectively. In such states, spins form aligned (FM) or contra-aligned (AF) pairs on nearest neighbor sites. Each

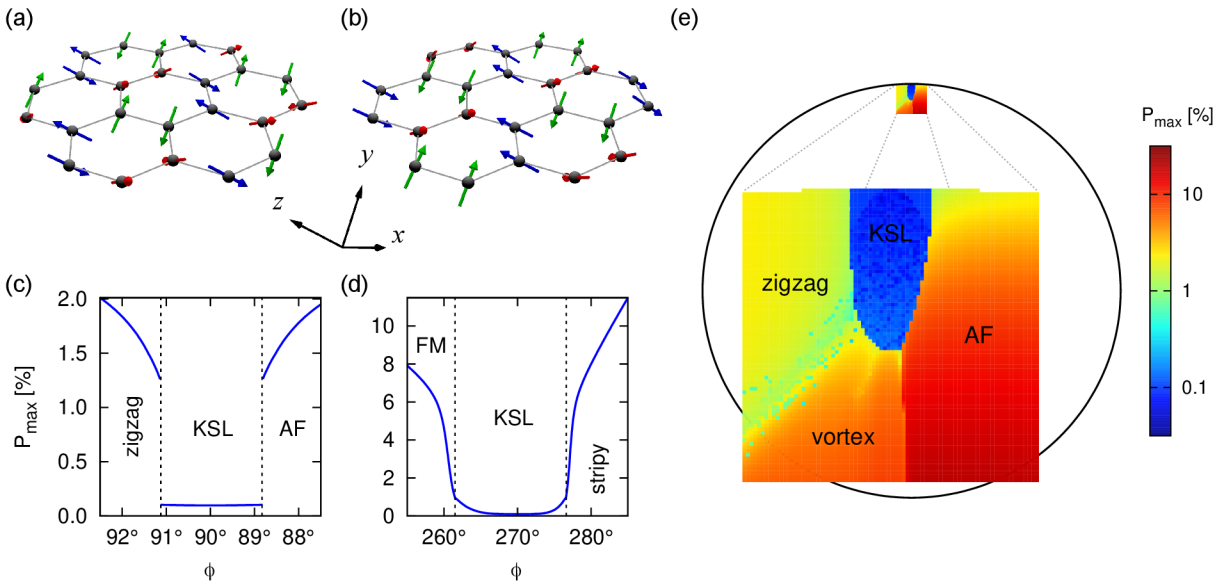

Figure 2.14: Most probable spin configurations near the AF (a) and FM (b) Kitaev points. Spins on nearest neighbor bonds form pairs pointing in the x, y or z cubic directions according to the the active component of Kitaev interaction. (c) Probability of the optimal configuration $P_{\max}$ around the AF Kitaev point, perturbed by the Heisenberg interaction. Dashed vertical lines indicate phase boundaries, where $P_{\max}$ shows a discontinuity. (d) $P_{\max}$ around the FM point – this time, the probability curve is continuous, and the phase boundaries occur at the discontinuity in the first derivative. (e) Map of the AF Kitaev spin liquid in the $\Gamma > 0, \Gamma' = J_3 = 0$ phase diagram slice. Figure adapted from Ref. [12].

pair is polarized in a direction corresponding to one of the cubic axes x, y, z, dictated by the active component of Kitaev interaction.

The boundaries between liquid and ordered regions can be pinpointed using the present method too, as one can see in Fig. 2.14 panel (e), which shows a clear dip in the maximum probability corresponding to the spin liquid region. Naturally, such identification is easiest when there is a clear, order of magnitude separation in probability between the ordered and liquid regions. Otherwise, the difficulties of the global 48-parameter optimization may arise, and the risk of getting trapped in a local maximum increases. In such cases, the Hessian can be helpful in finding the boundaries (cf. Fig. 2.13 panel (i)).

The nature of the liquid-ordered phase boundary is significantly different for AF and FM Kitaev spin liquids, which can be demonstrated by following the evolution of maximum probability $P_{\max}$ across the liquid regions. Panels (c),(d) of Fig. 2.14 show such evolution for both AF and FM Kitaev liquids, with the only perturbation coming from the Heisenberg interaction. While in the AF case we see a sharp step in the maximum probability on the liquid-ordered phase boundary, the FM Kitaev liquid states are continuously connected with the neighboring FM and stripy phases (a discontinuity appears in the derivative with respect to the model's parameters). Further calculations of spin excitations show that this symmetry can be traced to the different magnitude of quantum fluctuations in AF and FM Kitaev spin-liquid regions [176].

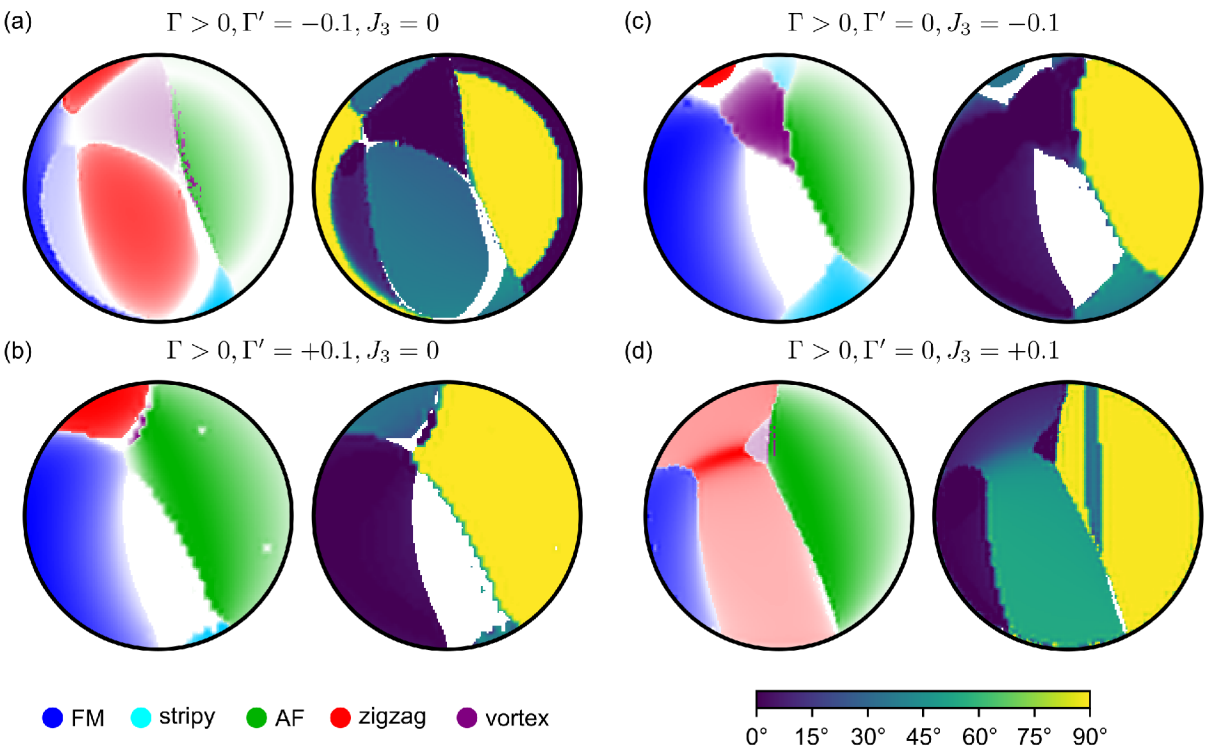

Figure 2.15: Evolution of the quantum phase diagram with [(a),(b)] $\Gamma' \neq 0$ and [(c),(d)] $J_3 \neq 0$. Each panel shows a pair of circular maps: on the left is the probability of optimal spin configuration, and on the right, we plot the angle of the ordered moment with the honeycomb plane. White areas represent states where no spin pattern with a significant probability was found.

Trends dictated by non-zero Γ', J_3 and negative $\Gamma < 0$

The large number of model parameters makes it difficult to properly map the whole phase diagram. Our approach is to map out the trends induced by Γ' and J_3 terms and to supply them by the interpretation founded on hidden symmetries and classical trends. As will be demonstrated, these are sufficient to understand the basic evolution of the phase diagram slices. A fuller range of phase diagram maps have been included in the Appendix of Ref. [12].

We shall begin with the effect of $\Gamma' < 0$, captured in the phase diagram slice in Fig. 2.15(a). The left side of the panel shows the probability map, whereas at the right side, we plot the angle of ordered moment with the honeycomb plane. The probabilities show that zigzag and vortex phases expand significantly at the expense of neighboring phases. Tracing the $\Gamma' < 0$ evolution further, we confirm that this trend continues and is connected to points of hidden symmetry that are associated with zigzag and vortex phases. First is the hidden $\mathcal{T}_1\mathcal{T}_4$ $SU(2)$ point which we regard as the source for the middle zigzag phase, where the moment direction is between x and y axes (compatible with experimental data [99]). Second, the vortex phase expands in the proximity of the AF compass point, which is located at $\Gamma' \approx -0.6$ in our parametrization. Further, negative Γ' influences the AF and FM phases in the form of the anisotropic contribution to classical energy $\pm(\Gamma + 2\Gamma')(n_x^2 + n_y^2 + n_z^2)$ – see discussion in Sec. 2.2.3. In the case of FM, sufficiently large negative Γ' can overcome the moment localization to the honeycomb plane due to $\Gamma > 0$ and lift the moment to the Z-direction. The transition is sharp and can be spotted on the probability map as well – the Γ'-enforced moment localization reduces quantum fluctuations

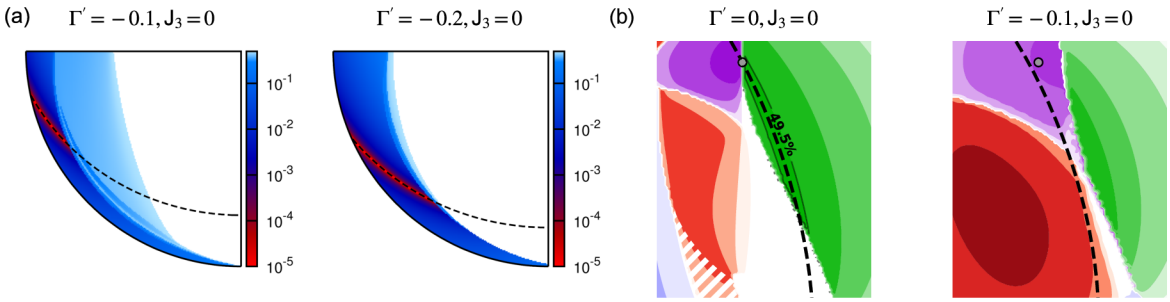

Figure 2.16: (a) FM phase displayed in the lower left quadrant of the phase diagram for two negative values of Γ'. The color plot shows the difference $1/2 - P$ between the probability P of the classical FM state in the ground state and its maximum value $1/2$. The maximum probability is reached at the intersection of the dashed line given by $K + 2\Gamma - 2\Gamma' = 0$ with the FM subphase that features moments polarized perpendicular to the honeycomb plane. (b) The probability of Néel ordering peaking at $1/2$ at the dashed line $3J + K - \Gamma - 2\Gamma' = 0$, indicating the presence of classical AF Ising states. The line crosses the hidden vortex point (gray •) for $\Gamma' = 0$, but negative $\Gamma' < 0$ leads to a shift such that the line no longer intersects the AF phase.

compared to the relative freedom that the moment experiences in the honeycomb plane, creating a notable difference in probabilities between said regions. In the case of AF, the effect is the opposite: $\Gamma' < 0$ now works against Γ to confine the moment to the honeycomb plane. The circular shape of the transition boundary between the two AF regimes demonstrates that it is entirely driven by the balance of Γ and Γ', regardless of J, K.

The direction of ordered moment in FM and AF phases was important in relation to the fluctuation-free Z-polarized states that we introduced in Sec. 2.1.4. In this regard the $\Gamma' = -0.1, J_3 = 0$ phase diagram slice represents an opportunity to observe the FM Ising phase for the first time, since the FM phases contain areas where the moment points in the Z-direction. Panel (a) of Fig. 2.16 shows the relevant quadrant of FM phase for two negative Γ' values, plotting $1/2 - P$. The parameter line $K + 2\Gamma - 2\Gamma' = 0$ where all fluctuation terms in the Hamiltonian cancel out is clearly visible in the portions of the FM phase where $\Gamma' < 0$ is strong enough to align the moment with the Z-direction. On the other hand, the AF Ising states are visible already at the $\Gamma' = J_3 = 0$ phase diagram slice (panel (b) of Fig. 2.16). Negative Γ' leads to a shift of the $3J + K - \Gamma - 2\Gamma' = 0$ parameter line in such a way that the intersection with the AF phase is avoided. The opposing effects in FM and AF cases make it so that both FM and AF Ising states without fluctuations are almost never observed in a single phase diagram Γ'-slice.

Coming back to Fig. 2.15, we advance to panel (b) showing a phase diagram portion at $\Gamma' = +0.1$. The effect of positive Γ' can be summed up as unifying. Zigzag, vortex, and stripy phases are suppressed, and eventually, only AF, FM, and some possibly disordered regions survive. The fixation of moment direction in both the AF and FM phases is strengthened, leading to a smaller amount of quantum fluctuations, making the phase diagram closer to the classical one. The quantum fluctuations are non-existent at the Ising point occurring at $\Gamma' = +0.707$ and on the fluctuation-free parameter line, crossing it and rising only modestly away from it.

The effect of J_3 on the phase diagram is understood simply on an intuitive level – ferromagnetic J_3 supports stripy and FM at the expense of zigzag and AF, and antiferromagnetic J_3 acts in the opposite way. Considering the J_3 interaction is isotropic, it is not surprising that robust features regarding the moment direction (such as the moment localization in FM and AF

phases discussed above) are unaffected. The most notable is the expansion of the zigzag phase seen in the panel Fig. 2.15 panel (d), where $J_3 = 0.1$ is sufficient to merge both zigzag regions into one. It is interesting to follow the evolution of the ordered moment direction: the limiting cases are the z cubic direction (in the top zigzag region) and the direction between x and y cubic axes (central zigzag region). At the boundary, the moments are pushed to the honeycomb plane, smoothly connecting both limits. Here, the quantum fluctuations are significantly suppressed, as can be observed in the elevated probability values.

Based on experiments measuring the lattice distortions of Na_2IrO_3 [101, 76], the expected parameter regime for this compound is $\Gamma' < 0$ [52]. We found that model parameters with these signs strongly support the middle zigzag phase, where the moment is between x and y cubic axes. By translating the experimental moment direction from Ref. [99] to a pseudospin direction, it is possible to estimate the parameter window for Na_2IrO_3 as one with a dominant ferromagnetic K and comparable $J > 0, \Gamma > 0, \Gamma' < 0$ and $J_3 > 0$. This result is in agreement with previous numerical [10] and *ab-initio* [5] works, and was confirmed by the interpretation of RIXS spectra [177].

After thoroughly discussing the $\Gamma > 0$ subspace, we now turn to address the $\Gamma < 0$ case. Our interpretation is led by contrast and analogy with the $\Gamma > 0$ case, again supplemented by hidden symmetries and trends dictated by classical energy. First, we refer the reader to Fig. 2.7 which highlights the fact that each hidden $SU(2)$ point in the $\Gamma > 0$ subspace has a $\Gamma < 0$ partner of opposite FM/AF nature. Moreover, we should keep in mind the classical symmetry connecting $\Gamma \leftrightarrow -\Gamma$ phase diagram slices, which maps $(\Gamma > 0, \Gamma', J_3)$ phase diagram cuts to $(\Gamma < 0, -\Gamma', -J_3)$ cuts by applying mirror symmetry around the center and flipping every other spin in the spin arrangement (see Sec. 2.2.3 for details). These insights will be sufficient to explain most similarities and differences between $\Gamma > 0$ and $\Gamma < 0$ phase diagrams.

The phase diagram slices for $\Gamma' = J_3 = 0$ as well as those with nonzero Γ', J_3 are plotted in Fig. 2.17. At first sight, it looks qualitatively similar to the $\Gamma > 0$ case, with some differences that we can understand based on the symmetries of the model. The spin-flip associated with classical $\Gamma \leftrightarrow -\Gamma$ symmetry connects zigzag and stripy phases, thus classically zigzag and stripy phases can be seen as $\Gamma \leftrightarrow -\Gamma$ partners. Indeed, the most notable difference in the phase diagram compared to $\Gamma > 0$ is the role reversal of zigzag and stripy phases – the central region of the phase diagram now contains a second stripy phase associated with the FM $\mathcal{T}_1\mathcal{T}_4$ $SU(2)$ point. Connected with the other stripy phase by the $\mathcal{T}_1$ rotation, it features moments polarized between x and y axes. The analogy with the central zigzag phase of $\Gamma > 0$ runs further: the central stripy phase expands in the presence of negative J_3, accompanied by a suppression of the zigzag phase. Again, the magnetic moment evolution between the two stripy regions is smooth, with the moments pushed to the honeycomb plane at the boundary. On the other hand, positive J_3 wipes out the stripy phase, supporting zigzag.

The vortex phase can be understood in the same way as before, by noting the presence of hidden exact points. The $\mathcal{T}_6$ $SU(2)$ point of AF origin is at the boundary of the vortex and FM phases. The other two relevant points are compass points, one located at $-J = K = \Gamma < 0$ and the other occurring for positive $\Gamma' \approx 0.6$ as part of the Ising-Kitaev-compass continuum of states. Once more, we find vortex-a and vortex-b patterns to be most probable throughout the phase, with the additional difference that every other spin in the ordering is flipped (due to AF origin of the vortex phase). Because of the AF nature, the vortex phase also carries larger quantum fluctuations compared to the $\Gamma > 0$ case, which is manifested by lower $P_{\max}$ probabilities.

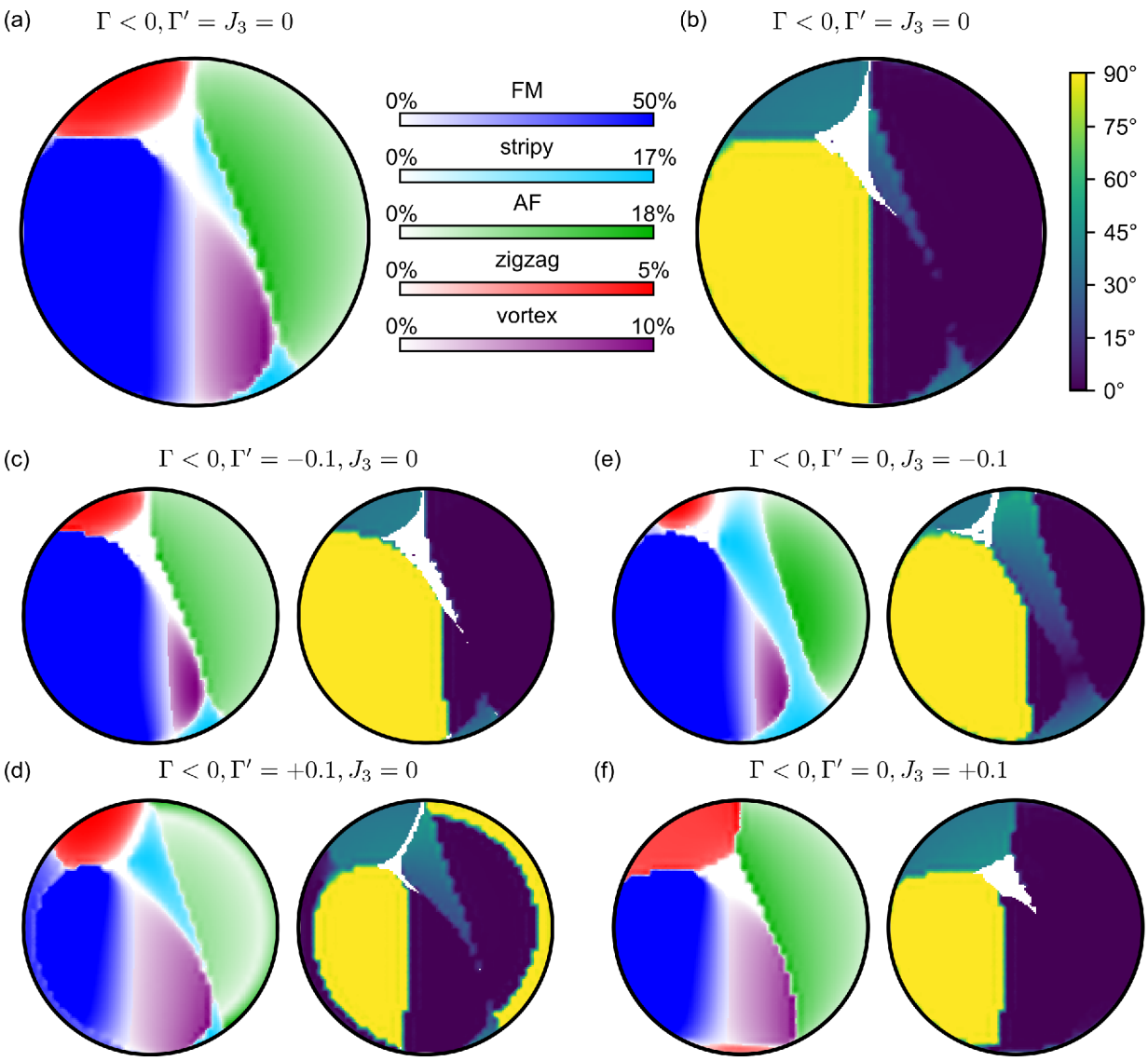

Figure 2.17: Phase diagram of the EKH model in the $\Gamma < 0$ parameter subspace. (a) Probability map of the $\Gamma' = J_3 = 0$ cut – darker color corresponds to higher probability. (b) The angle of the ordered moment with the honeycomb plane for the $\Gamma' = J_3 = 0$ slice. Panels (c)-(f) show both the probability map and the moment direction map for different Γ', J_3 values. In all plots, white areas represent states where long-range order was not detected.

The key effect of non-zero Γ' on AF and FM phases can be once more explained classically. The prefactor in the anisotropic energy term is $\pm(\Gamma + 2\Gamma')$, and therefore it is the $\Gamma/2\Gamma'$ balance that dictates the direction of the ordered moment. In the absence of Γ', $\Gamma < 0$ confines the moment in the FM phase to the Z direction and keeps it in the honeycomb plane in the AF phase. Negative Γ' (see Fig. 2.17(c)) further supports the confinement, turning the phases more classical, similarly to the previously discussed $\Gamma > 0, \Gamma' > 0$ case. The FM phase in particular features very small quantum fluctuations, becoming fluctuation-free in the FM Ising point which occurs at large negative Γ', as well as on the line given by $K + 2\Gamma - 2\Gamma' = 0$. Positive Γ' leads to a richer phase diagram (see panel (d)), supporting the central stripy phase as well as the

vortex, which expands due to the proximity to the "compass" point. In the context of moment direction in AF and FM phases, $\Gamma' > 0$ acts against Γ, creating AF and FM subphases with complementary directions of ordered moment, in analogy to the $\Gamma > 0, \Gamma' < 0$ situation (cf. Fig. 2.15(a)).

To summarize, qualitative trends in the $\Gamma < 0$ phase diagram are consistent with the expectations based on the classical $\Gamma \leftrightarrow -\Gamma$ symmetry. The main deviations from this symmetry are rooted in the fact that quantum AF- and FM-type states are fundamentally distinct on a quantum level, though classically connected by a simple spin flip on one sublattice. Thus, even though the phase diagrams in $\Gamma > 0$ and $\Gamma < 0$ cases may seem similar, the ground states of corresponding phases may have a different internal structure (cf. discussion of vortex phase above).

Ising-Kitaev-compass model

At the end of the numerical part of this chapter, we take a closer look at the Ising-Kitaev-compass line of states introduced in Sec. 2.1.3. To recapitulate, we have found a mapping that connects a parameter subspace of the four-parameter extended Kitaev-Heisenberg model to a single-parameter model characterized by a single interacting spin component (interaction axis). We dubbed this model the Ising-Kitaev-compass model:

$$\mathcal{H}_{IKc} = \sum_{\langle ij \rangle \in NN} \tilde{K} (\mathbf{n}_\xi \cdot \mathbf{S}_i)(\mathbf{n}_\xi \cdot \mathbf{S}_j), \tag{2.95}$$

where $\tilde{K}$ is the interaction strength and $\mathbf{n}_\xi$ specifies the interaction axis

$$\mathbf{n}_\xi = (\sin\vartheta\cos\varphi, \sin\vartheta\sin\varphi, \cos\vartheta), \tag{2.96}$$

valid in the rotating reference frame $\tilde{x}\tilde{y}\tilde{z}$ (see Fig. 2.1(c)). This type of model has been studied before [148] using tensor networks, although with the axis in the $\tilde{x}\tilde{z}$ plane and not in connection with the EKH model. Here we analyze it using exact diagonalization with the spin-$\frac{1}{2}$ coherent states method combined with the calculation of spin correlation functions.

Figure 2.18(a) shows the resulting phase diagram of the Ising-Kitaev-compass (IKc) model plotted as a function of $|\vartheta|$. Since the physical properties do not depend on φ, it is sufficient to focus on the ϑ-dependence. Moreover, the phase diagram for negative ϑ is identical, even though it corresponds to a different parameter manifold in the EKH model's phase diagram. We plot the trace of the spin structure factor defined as $S(\mathbf{q}) = \sum_\alpha \langle S^\alpha_{-\mathbf{q}} S^\alpha_{\mathbf{q}} \rangle$ at five symmetric points in reciprocal space, in effect measuring the intensity of peaks at candidate ordering wavevectors.

In the order of increasing ϑ, the model encompasses Ising model ($\vartheta = 0$), Kitaev model ($\vartheta = \arccos\left(1/\sqrt{3}\right), \varphi = \pi/2$) and "compass model" ($\vartheta = \pi/2, \varphi = \pi/2$). Starting at the Ising point, the model's phase diagram contains an AF Ising phase, in which the moments are pointing in the Z-direction, i.e. perpendicular to the honeycomb plane – see panels (b),(e). At the Ising point, there are no quantum fluctuations and the ground state is classical; these pick up in strength as ϑ increases. The increasing amount of quantum fluctuations can be observed directly as a sharp drop of Γ'-point AF correlations.

Around $|\vartheta| \approx 49.5^\circ$ occurs a transition to a spin-liquid phase associated with the π-rotated Kitaev point at $|\vartheta| \approx 54.7^\circ$. Further at approximately 62° the spin liquid state breaks down and an ordered state emerges. Here, the ground state initially displays peaks at the Γ' and X points

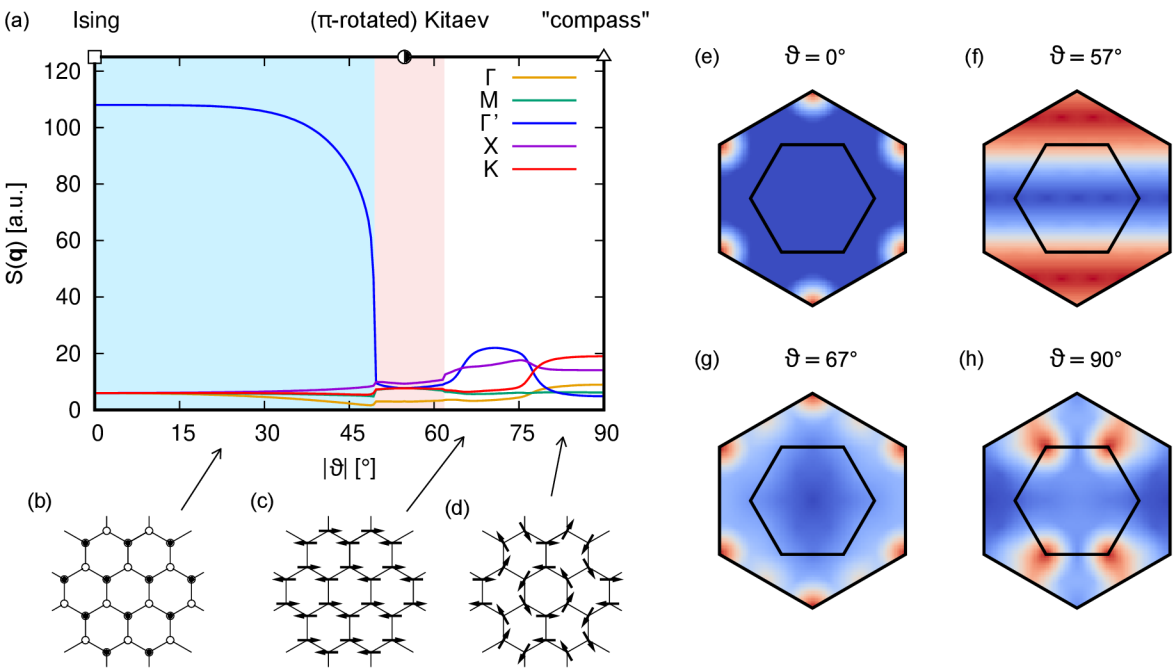

Figure 2.18: (a) Trace of the spin structure factor $S(\mathbf{q}) = \sum_\alpha \langle S^\alpha_{-\mathbf{q}} S^\alpha_{\mathbf{q}} \rangle$ at five symmetric points in reciprocal space as a function of angle ϑ between the interaction axis and the $\tilde{z} = Z$ axis. The model contains several distinct phases – in the order of increasing $|\vartheta|$, these are: (b) Z-polarized AF Ising phase, Kitaev spin liquid, (c) a Néel phase and (d) a vortex-a phase. (e)-(h) Maps of the spin structure factor for four distinct regions in the phase diagram.

(see panel (g)) – the highest probability spin configuration is a Néel state with a slight tilt from the honeycomb plane. The amount of quantum fluctuations in this region is comparable with the ground state of the AF Heisenberg model.

Increasing ϑ further, the correlations at Γ' drop and the K point becomes dominant (this happens around 77°) as shown in the spin correlations map in panel (h). This final region is associated with the compass point at $\vartheta = 90°$ that has been studied before, though with conflicting conclusions pertaining to the ground state of this model. Suggested has been a Néel state [147], a dimer pattern [178], superposition of dimer coverings [146] or a quantum spin liquid state [179]. Our analysis yields the vortex-a pattern as the most probable one throughout the phase, with the probability around 3%. This value is significantly smaller than what we observed earlier for the vortex phase (around 15%), which suggests that this phase might be disordered, as claimed by previous studies.

Notably, the presence of two distinct ordered phases between the π-rotated Kitaev and "compass" limits is in disagreement with the conclusions of Ref. [148] where authors found the whole interval filled with a dimer phase. The reason for this disagreement is unclear to us; additional calculations using 32-site clusters confirmed the presence of the Néel phase. In general, we find the compass limits of the model to be most complex, and worth further study to fully establish their ground state properties.

Chapter 3

Soft spins in d^4 ruthenates

In this chapter, we depart from the d^5 frustrated physics and consider a specific class of d^4 systems. As we have seen in Section 1.3, in some cases, the electronic structure of d^4 transition metal ions involves spin-orbit coupled $J = 0$ singlet and $J = 1$ triplet states, which get mixed by superexchange interactions. As a consequence of the exchange-induced mixing, magnetic moments are not of fixed length as in rigid spin systems, but fluctuate both in orientation and amplitude, which is why they are sometimes referred to as "soft spins" [21].

The motivation to study such systems is supported by unusual physics observed in calcium ruthenate Ca_2RuO_4. It is a Mott insulator and becomes antiferromagnetic below 110K [123, 126, 127]. The magnetic Ru^{4+} ions are arranged into a square lattice in RuO_2 planes weakly bound along the c-axis and host magnetic moments lying inside the planes. The balance of the tetragonal crystal field and spin-orbit coupling strength is such that low-energy states form the basis of a singlet-triplet model, which we focus on in this chapter.

We study the effective magnetic model for Ca_2RuO_4 by parts, first considering a simplified model containing only triplet energy cost E_T derived from spin-orbit coupling λ and an exchange term J. By tuning the balance of J and E_T, we address the condensation of triplet excitations (triplons) using a variational procedure. The elementary excitations of the bosonic condensate involve a gapless magnon as well as a gapped amplitude mode - the Higgs mode [133], which we study on a harmonic level, along with the effects of the additional Hamiltonian terms on the mode dispersions.

Next, we go beyond the harmonic approximation and consider the effects of the hard-core nature of bosons carrying excitations in our model. We provide a two-fold approach – we (i) solve the model fully numerically and (ii) implement an analytic method that captures the hard-core effects approximately. The numerical solution is based on the Quantum Monte Carlo Stochastic Series Expansion (QMC-SSE) technique [157], which allows for efficient and unbiased access to equilibrium properties of spin systems. The favorable scaling of computation time with system size permits the use of large clusters, which we use to study the quantum critical point of the model, as well as to obtain dynamical spin susceptibility spectra with high resolution in momentum space. We compare and contrast the full numerical solution with a mean-field approximation based on a theory by Gopalan, Rice, and Sigrist [180]. We find that this analytical approach, which essentially extends the harmonic approximation by screening of interactions and a chemical potential, is sufficient to capture the hard-core effects with good qualitative fidelity while preserving technical simplicity.

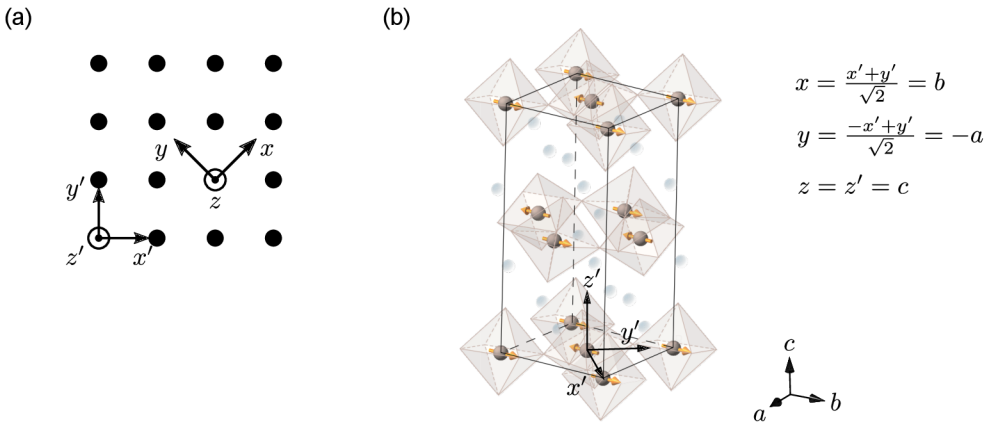

Figure 3.1: (a) Square lattice and two possible coordinate reference frames. We use the (xyz) reference frame in the rest of the chapter. (b) Crystal structure of Ca_2RuO_4. It is a quasi-two-dimensional structure where the RuO_2 planes are stacked on top of each other along the c axis. Ruthenium Ru^{4+} ions are shown in grey, and around them are oxygen octahedra (oxygen atoms are not shown for clarity). Calcium ions are shown in light blue. Experimentally established magnetic order is antiferromagnetic with magnetic moments lying in-plane along the b axis, moments shown in yellow. Adapted from [18].

3.1 Singlet-doublet model in the harmonic approximation

3.1.1 Definition of the model and used reference frames

We start by formally introducing the effective magnetic model and the coordinate reference frames used in the rest of the chapter. As we have discussed in Chapter 1.3, the local basis in the present case is composed of quasi-degenerate $J = 0$ and $J = 1$ levels, which can be naturally described by using singlet and triplet operators (s, T_x, T_y, T_z) defined in (1.30),(1.31). From the triplet set, only the (T_x, T_y) doublet is used henceforth, because a large tetragonal splitting pushes the T_z member of the triplet higher in energy. The singlet-doublet basis can be mapped to pseudospin-1 using the relations (1.37):

$$\begin{aligned} S^x &= -i(s^\dagger T_x - T_x^\dagger s), \\ S^y &= -i(s^\dagger T_y - T_y^\dagger s), \\ S^z &= -i(T_x^\dagger T_y - T_y^\dagger T_x). \end{aligned} \tag{3.1}$$

This mapping enables us to formulate the effective Hamiltonian using both a pseudospin-1 basis and the singlet-doublet basis.

The Hamiltonian is formulated as a sum of a local part and an interaction term between nearest neighbors on the square lattice:

$$\mathcal{H}^{\text{eff}} = \sum_i \mathcal{H}_i^{\text{loc}} + \sum_{\langle ij \rangle \in \text{NN}} \mathcal{H}_{ij}^{(\xi)}. \tag{3.2}$$

The two-dimensional square lattice corresponds to RuO_2 planes of Ca_2RuO_4, where each lattice point is a Ru^{4+} ion – see Fig. 3.1 panel (b). Using (x', y', z') axes, where x', y' point to the nearest

lattice points and z' points out of the plane, the local Hamiltonian is

$$\mathcal{H}_i^{\text{loc}} = E_T \left(S_i^{z'}\right)^2 - \tfrac{1}{2}\Delta' \left(S^{x'} S^{y'} + S^{y'} S^{x'}\right)_i, \tag{3.3}$$

and the nearest-neighbor interaction term reads as

$$\mathcal{H}_{ij}^{(\xi)} = (J + A_\xi) S_i^{x'} S_j^{x'} + (J - A_\xi) S_i^{y'} S_j^{y'} + J_z S_i^{z'} S_j^{z'} \tag{3.4}$$

with bond-dependent A_ξ:

$$A_\xi = \begin{cases} A & \text{if } \xi = x', \\ -A & \text{if } \xi = y'. \end{cases} \tag{3.5}$$

Because of orthorhombic crystal field Δ' due to the deformation of oxygen octahedra around the ruthenium ions, there is a preferential direction for the magnetic moment in the RuO_2 plane along the crystallographic b axis. We can, therefore, rotate the local coordinate system by 45° to (x, y, z), so that x coincides with the preferential b direction. The local Hamiltonian term then reads

$$\mathcal{H}_i^{\text{loc}} = E_T \left(S_i^z\right)^2 + \tfrac{1}{2}\Delta' \left(S_y^2 - S_x^2\right)_i, \tag{3.6}$$

where the role of Δ' term choosing x over y is nicely highlighted. The interaction term remains in a simple form:

$$\mathcal{H}_{ij}^{(\xi)} = J \left(S_i^x S_j^x + S_i^y S_j^y\right) - A_\xi \left(S_i^x S_j^y + S_i^y S_j^x\right) + J_z S_i^z S_j^z. \tag{3.7}$$

To translate the Hamiltonian into the singlet-doublet basis, we start with the local terms:

$$\begin{aligned} (S_i^x)^2 &= (s^\dagger s + T_x^\dagger T_x)_i, \\ (S_i^y)^2 &= (s^\dagger s + T_y^\dagger T_y)_i, \\ (S_i^z)^2 &= (T_x^\dagger T_x + T_y^\dagger T_y)_i. \end{aligned} \tag{3.8}$$

Plugging these relations into the expression (3.6), we obtain a transparent form of the local Hamiltonian, which allows an intuitive interpretation of the E_T term as a triplet excitation cost and the Δ' term as a preference of one triplon kind over the other:

$$\mathcal{H}_i^{\text{loc}} = E_T (n_T)_i + \tfrac{1}{2}\Delta' (n_{T_y} - n_{T_x})_i. \tag{3.9}$$

The bond interaction terms are more involved. The isotropic exchange J translates to two interaction processes between nearest neighbors: triplon hopping and triplon pair creation/annihilation

$$S_i^x S_j^x + S_i^y S_j^y = \sum_{\alpha=x,y} \Big[\underbrace{(T_\alpha^\dagger s)_i (s^\dagger T_\alpha)_j}_{\text{hopping}} - \underbrace{(s^\dagger T_\alpha)_i (s^\dagger T_\alpha)_j}_{\text{pair annihilation}} + \text{h.c.} \Big]. \tag{3.10}$$

The bond-dependent A-term corresponds to triplon hopping with a "color-flip" ($x \leftrightarrow y$) and xy-pair creation/annihilation

$$S_i^x S_j^y + S_i^y S_j^x = \underbrace{(T_x^\dagger s)_i (s^\dagger T_y)_j + (T_y^\dagger s)_i (s^\dagger T_x)_j}_{\text{hopping with a color flip}} - \underbrace{(s^\dagger T_x)_i (s^\dagger T_y)_j - (s^\dagger T_y)_i (s^\dagger T_x)_j}_{xy\text{-pair annihilation}} + \text{h.c.} \tag{3.11}$$

Finally, the interaction between the z-components of the pseudospin is rewritten purely in terms of T_x, T_y operators as the exchange of $T_i^x T_j^y \leftrightarrow T_i^y T_j^x$ on a bond and a conversion between $T_i^x T_j^x$ and $T_i^y T_j^y$ pairs on a bond:

$$S_i^z S_j^z = \underbrace{(T_y^\dagger T_x)_i (T_x^\dagger T_y)_j + (T_x^\dagger T_y)_i (T_y^\dagger T_x)_j}_{\text{exchange of } T_x, T_y} - \underbrace{(T_x^\dagger T_y)_i (T_x^\dagger T_y)_j - (T_y^\dagger T_x)_i (T_y^\dagger T_x)_j}_{xx \leftrightarrow yy \text{ pair conversion}}. \tag{3.12}$$

Altogether, the bond interaction is expressed as

$$\begin{aligned}\mathcal{H}_{ij}^{(\xi)} = &+ J\left[(T_x^\dagger s)_i (s^\dagger T_x)_j + (T_y^\dagger s)_i (s^\dagger T_y)_j - (T_x^\dagger s)_i (T_x^\dagger s)_j - (T_y^\dagger s)_i (T_y^\dagger s)_j + \text{h.c.}\right] - \\ &- A_\xi \left[(T_x^\dagger s)_i (s^\dagger T_y)_j + (T_y^\dagger s)_i (s^\dagger T_x)_j - (s^\dagger T_x)_i (s^\dagger T_y)_j - (s^\dagger T_y)_i (s^\dagger T_x)_j + \text{h.c.}\right] + \\ &+ J_z \left[(T_y^\dagger T_x)_i (T_x^\dagger T_y)_j + (T_x^\dagger T_y)_i (T_y^\dagger T_x)_j - (T_x^\dagger T_y)_i (T_x^\dagger T_y)_j - (T_y^\dagger T_x)_i (T_y^\dagger T_x)_j\right].\end{aligned} \tag{3.13}$$

3.1.2 Variational magnetic ground state

As the first step when approaching the model solution, we will focus on the simplified version of the model introduced above that includes only triplet energy cost E_T and interaction J:

$$\mathcal{H} = \sum_i \mathcal{H}_i^{\text{loc}} + \sum_{\langle ij\rangle \in \text{NN}} \mathcal{H}_{ij} = E_T \sum_i n_{Ti} + J \sum_{\langle ij\rangle} \sum_{\alpha=x,y} \left[(T_\alpha^\dagger s)_i (s^\dagger T_\alpha)_j - (T_\alpha^\dagger s)_i (T_\alpha^\dagger s)_j + \text{h.c.}\right]. \tag{3.14}$$

Our goal is to understand the model's behavior in both limits of high and low triplet energy cost, specifically focusing on the emergence of magnetic order. Intuitively, the high triplet energy cost limit $E_T \gg J$ should result in a singlet ground state with isolated triplet excitations, which we call triplons. If, on the other hand, triplon cost is negligible, the interaction term leads to the formation of a magnetic state in the form of a condensate of triplons. We can employ the following variational wavefunction that supports both limits:

$$|\Psi\rangle = \prod_{\mathbf{R}} \left(\cos\theta s_{\mathbf{R}}^\dagger + \sin\theta \sum_{\alpha=x,y} d_{\alpha\mathbf{R}}^* T_{\alpha\mathbf{R}}^\dagger\right) |\text{vac}\rangle. \tag{3.15}$$

Here, angle θ encodes the balance between E_T and J: the $E_T \gg J$ limit is characterized by $\theta = 0$ whereas the condensate is captured by nonzero θ. The complex vector $\mathbf{d}_{\mathbf{R}}$ describes the spatial distribution of triplets $T_{x\mathbf{R}}, T_{y\mathbf{R}}$ on the lattice, and therefore also characterizes the magnetic order in the condensed phase. We can calculate singlet and triplet occupation averages to see the role of θ and $\mathbf{d}_{\mathbf{R}}$ explicitly:

$$\begin{aligned}\langle n_s\rangle_{\mathbf{R}} &= \langle\Psi|n_s|\Psi\rangle_{\mathbf{R}} = \cos^2\theta, \\ \langle n_{Tx}\rangle_{\mathbf{R}} &= \langle\Psi|n_{Tx}|\Psi\rangle_{\mathbf{R}} = \sin^2\theta |d_{x\mathbf{R}}|^2, \\ \langle n_{Ty}\rangle_{\mathbf{R}} &= \langle\Psi|n_{Ty}|\Psi\rangle_{\mathbf{R}} = \sin^2\theta |d_{y\mathbf{R}}|^2.\end{aligned} \tag{3.16}$$

The variational procedure consists of minimizing the variational energy with respect to free parameters θ and $\mathbf{d}_{\mathbf{R}}$. The individual constituents of the energy to be minimized are

$$\langle\Psi|\mathcal{H}_{\mathbf{R}}^{\text{loc}}|\Psi\rangle = E_T \langle\Psi|n_T|\Psi\rangle_{\mathbf{R}} = E_T \rho,$$

$$\begin{aligned}
\langle\Psi|(T_\alpha^\dagger s)_i(s^\dagger T_\alpha)_j|\Psi\rangle &= \rho(1-\rho)d_{\alpha i}^* d_{\alpha j},\\
\langle\Psi|(s^\dagger T_\alpha)_i(s^\dagger T_\alpha)_j|\Psi\rangle &= \rho(1-\rho)d_{\alpha i} d_{\alpha j},\\
\langle\Psi|\mathcal{H}_{ij}|\Psi\rangle &= \rho(1-\rho)(d_{\alpha i}^* d_{\alpha j} + d_{\alpha i} d_{\alpha j}^* - d_{\alpha i} d_{\alpha j} - d_{\alpha i}^* d_{\alpha j}^*),
\end{aligned} \tag{3.17}$$

where we introduced condensate density $\rho \equiv \langle\Psi|n_T|\Psi\rangle_{\mathbf{R}} = \sin^2\theta$. It is also convenient to separate $\mathbf{d_R}$ into real and imaginary parts $(\mathbf{u}+i\mathbf{v})_{\mathbf{R}}$ with the constraint $|\mathbf{u}|^2 + |\mathbf{v}|^2 = 1$ given by normalization of the variational wavefunction $\langle\Psi|\Psi\rangle = 1$. With these simplifications of notation, we obtain the variational energy in the form:

$$E_{\text{var}} = \langle\Psi|\mathcal{H}|\Psi\rangle = E_T\rho N_{\text{site}} + J\sum_{\langle ij\rangle} 4\rho(1-\rho)\mathbf{v}_i\cdot\mathbf{v}_j. \tag{3.18}$$

The local term $E_T\rho N_{\text{site}}$ is always positive, while the interaction term can lower the energy. When triplon cost E_T dominates, the minimum value of energy is zero with $\rho = 0$. At some critical J_{crit}, the second term outweighs the triplon cost, and the condensate emerges. We can already deduce something about the resulting magnetic order: to lower the energy, the product $\mathbf{v}_i\cdot\mathbf{v}_j$ must be negative. It turns out that the magnetic moment is linearly proportional to $\mathbf{v_R}$:

$$\begin{aligned}
\langle\Psi|M_x|\Psi\rangle &= g_{xy}\langle\Psi|(-i)(s^\dagger T_x - T_x^\dagger s)|\Psi\rangle = -2g_{xy}v_{x\mathbf{R}}\sqrt{\rho(1-\rho)},\\
\langle\Psi|M_y|\Psi\rangle &= g_{xy}\langle\Psi|(-i)(s^\dagger T_y - T_y^\dagger s)|\Psi\rangle = -2g_{xy}v_{y\mathbf{R}}\sqrt{\rho(1-\rho)},\\
\langle\Psi|M_z|\Psi\rangle &= g_z\langle\Psi|(-i)(T_x^\dagger T_y - T_y^\dagger T_x)|\Psi\rangle = 0.
\end{aligned} \tag{3.19}$$

Therefore, a negative dot product $\mathbf{v}_i\cdot\mathbf{v}_j$ translates into a staggered in-plane magnetic order. Since the product is isotropic, the ordered moment can lie in any direction in the xy-plane (a side note: in the next section, we will observe that as a consequence of such freedom of orientation, the excitation spectrum of the condensate includes a gapless magnon). We can choose a specific form of $\mathbf{v_R}$ that leads to a compact expression for the variational wavefunction Ψ, which will be useful in the following section devoted to harmonic excitations. A simple choice is to pick x as the ordered moment direction; the staggered in-plane ordering is then represented by $\mathbf{v_R}$ in the form:

$$v_{x\mathbf{R}} = -e^{i\mathbf{Q}\cdot\mathbf{R}}, \quad v_{y\mathbf{R}} = 0, \quad \mathbf{Q} = (\pi,\pi), \tag{3.20}$$

with $\mathbf{Q}$ labeling the ordering wavevector. The magnetic moment then reads as:

$$M_x = 2g_{xy}\sqrt{\rho(1-\rho)}e^{i\mathbf{Q}\cdot\mathbf{R}}, \quad M_y = M_z = 0. \tag{3.21}$$

Finally, we can find the critical J_{crit} at which the condensate starts to form. The variational energy per site for antiferromagnetic $\mathbf{v} \sim e^{-i\mathbf{Q}\cdot\mathbf{R}}$ is

$$\frac{E_{\text{var}}}{N_{\text{site}}} = E_T\rho - 8J\rho(1-\rho), \tag{3.22}$$

which has a minimum at

$$\rho = \frac{1}{2}\left(1 - \frac{E_T}{8J}\right), \tag{3.23}$$

determining the critical ratio J/E_T where condensation occurs:

$$(J/E_T)_{\text{crit}} = \frac{1}{8}. \tag{3.24}$$

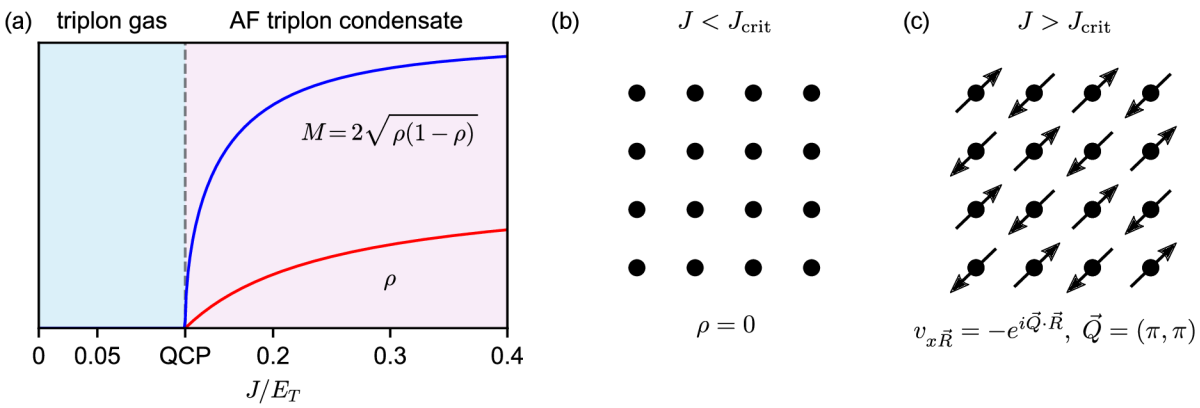

Figure 3.2: (a) Variational phase diagram of the J, E_T model consisting of a non-magnetic singlet phase and an antiferromagnetic triplon condensate. Condensate density serves as an order parameter. The figure also shows the magnitude of staggered magnetization featuring a familiar shape. (b) Non-magnetic singlet state, without local magnetic moments. Each site is occupied by singlet s. (c) Antiferromagnetic ordering on a square lattice, with ordered moment direction $v_{x\mathbf{R}}$ chosen arbitrarily to lie in the x-direction – the model is isotropic in xy-plane. The ordered moment direction gets locked to the x-axis upon adding orthorhombic splitting Δ'.

The above variational analysis yields a phase diagram of the singlet-doublet model, shown in Fig. 3.2 panel (a), with two phases – a non-magnetic singlet and an antiferromagnetic triplon condensate. It is worth noting, that the quantum critical point (QCP) position is shifted significantly once we include the hard-core nature of $s, \mathbf{T}$ bosons. Before that, though, we will stick to a lower level of approximation and study the harmonic excitations in both of these phases.

3.1.3 Harmonic excitations

To find out about the harmonic modes of our model, consider first the non-condensed phase – as we saw in the previous section, the ground state is a sea of singlets with triplon excitations embodied directly by the T_x, T_y operators. However, there is a mixing of s and $\mathbf{T}$ bosons when condensation occurs, which is clear from the form of the variational wavefunction (3.15):

$$|\Psi\rangle = \prod_{\mathbf{R}} \left(\cos\theta s^\dagger_{\mathbf{R}} + ie^{i\mathbf{QR}} \sin\theta T^\dagger_{x\mathbf{R}} \right) |\mathrm{vac}\rangle \,. \tag{3.25}$$

To obtain the harmonic modes in the whole parameter range of the model, we need to expand around $|\Psi\rangle$ using a new set of bosonic operators. First, we introduce boson c such that $|\Psi\rangle = \prod_{\mathbf{R}} c^\dagger_{\mathbf{R}} |\mathrm{vac}\rangle$, thus

$$c^\dagger_{\mathbf{R}} = \cos\theta s^\dagger_{\mathbf{R}} + \sin\theta i e^{i\mathbf{QR}} T^\dagger_{x\mathbf{R}}. \tag{3.26}$$

The T_y boson is not mixed with s and T_x, which means we can keep it and only relabel it to b. What remains is to choose a form for boson a complementary to c. We are guided by two conditions it should fulfill: i) we want to preserve continuity between (s, T_x, T_y) and (c, a, b) at the phase transition, and ii) the bosonic commutation relations must, of course, hold also for the new set of bosons. An appropriate choice is

$$ie^{i\mathbf{QR}} a^\dagger_{\mathbf{R}} = -\sin\theta s^\dagger_{\mathbf{R}} + \cos\theta i e^{i\mathbf{QR}} T^\dagger_{x\mathbf{R}}. \tag{3.27}$$

Bosons c, a in this form are a result of a θ-rotation of original s, T_x bosons, thus the bosonic commutation relations are obeyed. The extra $ie^{i\mathbf{QR}}$ factor takes care of continuity at the phase transition, i.e. $a = T_x$ for $\theta = 0$. The transformation from the original to the new set of bosons is:

$$\begin{pmatrix} s \\ T_x \\ T_y \end{pmatrix}_{\mathbf{R}} = \begin{pmatrix} \cos\theta & ie^{i\mathbf{QR}}\sin\theta & 0 \\ ie^{i\mathbf{QR}}\sin\theta & \cos\theta & 0 \\ 0 & 0 & 1 \end{pmatrix} \begin{pmatrix} c \\ a \\ b \end{pmatrix}_{\mathbf{R}} . \tag{3.28}$$

To continue, we need to deal with the hard-core boson constraint $n_s + n_{T_x} + n_{T_y} = n_c + n_a + n_b = 1$. We adopt the approach used in flavor-wave expansion methods [181, 182, 183, 184, 115], meaning we replace $c, c^\dagger$ operators with an operator $\sqrt{1 - n_a + n_b}$ and expand the square root, keeping only terms up to quadratic order. The harmonic Hamiltonian then has the following structure: constant terms corresponding to the classical energy, linear terms in a, b, and quadratic terms that embody the harmonic excitations.

$$\begin{aligned} \mathcal{H}_{\text{harm}} = & \underbrace{\sum_i H_i^{(0)} + \sum_{\langle ij \rangle} H_{ij}^{(0)}}_{\text{classical energy}} + \underbrace{\sum_i H_i^{(1)} + \sum_{\langle ij \rangle} H_{ij}^{(1)}}_{\text{linear in } a,b} + \\ & \underbrace{+ \sum_i \left[H_i^{(2)} - n_i H_i^{(0)} \right] + \sum_{\langle ij \rangle} \left[H_{ij}^{(2)} - (n_i + n_j) H_{ij}^{(0)} \right]}_{\text{harmonic excitations}} . \end{aligned} \tag{3.29}$$

Writing out the individual terms:

$$\begin{aligned} H_i^{(0)} &= E_T \sin^2\theta, \\ H_i^{(1)} &= \frac{E_T}{2} ie^{i\mathbf{Q}R_i} \sin 2\theta (a_{\mathbf{R}_i}^\dagger - a_{\mathbf{R}_i}), \\ H_i^{(2)} &= E_T (\cos^2\theta a_i^\dagger a_i + b_i^\dagger b_i), \\ H_{ij}^{(0)} &= -J \sin^2 2\theta, \\ H_{ij}^{(1)} &= -J \sin 2\theta \cos 2\theta \left[ie^{i\mathbf{QR}_i} (a_i^\dagger - a_i) + ie^{i\mathbf{QR}_j} (a_j^\dagger - a_j) \right], \\ H_{ij}^{(2)} &= J \sin^2 2\theta (a_i^\dagger a_i + a_j^\dagger a_j) + J \cos^2 2\theta (a_i^\dagger a_j + a_i a_j^\dagger - a_i a_j - a_i^\dagger a_j^\dagger) + \\ & + J \cos^2\theta (b_i^\dagger b_j + b_i b_j^\dagger - b_i b_j - b_i^\dagger b_j^\dagger). \end{aligned} \tag{3.30}$$

We easily find the minimum of the classical energy

$$\frac{\partial E_{\text{class}}}{\partial \theta} = \frac{\partial (E_T N_{\text{site}} \sin^2\theta - 2J N_{\text{site}} \sin^2 2\theta)}{\partial \theta} = 0, \tag{3.31}$$

which can be rearranged to

$$\sin 2\theta (E_T - 8J \cos 2\theta) = 0. \tag{3.32}$$

This expression tells us that there are two solutions that minimize the classical energy: $\theta = 0$ (triplon gas phase) and $\cos 2\theta = E_T / 8J$ that is relevant in the condensed phase and is consistent

with the condition (3.23) we obtained using the variational procedure in the previous section. At the minimum the linear terms in $\mathcal{H}_{\text{harm}}$ vanish:

$$\sum_i H_i^{(1)} + \sum_{\langle ij \rangle} H_{ij}^{(1)} = \sum_i 2ie^{i\mathbf{QR}_i}(a_i^\dagger - a_i)\sin 2\theta(E_T - 8J\cos 2\theta) = \\ = \frac{1}{N_{\text{site}}}\sum_i 2ie^{i\mathbf{QR}_i}(a_i^\dagger - a_i)\frac{\partial E_{\text{class}}}{\partial \theta}. \tag{3.33}$$

What remains is a Hamiltonian containing constant and quadratic terms in a, b:

$$\mathcal{H}_{\text{harm}} = E_{\text{class}} + \sum_i \left[E_T \cos 2\theta + 8J\sin^2 2\theta\right] a_i^\dagger a_i + \sum_i \left[E_T \cos^2\theta + 4J\sin^2 2\theta\right] b_i^\dagger b_i + \\ + J\sum_{\langle ij \rangle} \cos^2 2\theta (a_i^\dagger a_j + a_i a_j^\dagger - a_i a_j - a_i^\dagger a_j^\dagger) + J\sum_{\langle ij \rangle} \cos^2\theta (b_i^\dagger b_j + b_i b_j^\dagger - b_i b_j - b_i^\dagger b_j^\dagger). \tag{3.34}$$

From the form of the interaction, we see that we are dealing with two independent modes carried by the a, b bosons. The solution follows a standard procedure. First, we rewrite the Hamiltonian in Fourier-space

$$\mathcal{H}_{\text{harm}} = \sum_{\alpha=a,b}\sum_{\mathbf{q}} A_{\alpha\mathbf{q}}\alpha_{\mathbf{q}}^\dagger\alpha_{\mathbf{q}} - \frac{1}{2}B_{\alpha\mathbf{q}}(\alpha_{\mathbf{q}}\alpha_{-\mathbf{q}} + \alpha_{\mathbf{q}}^\dagger\alpha_{-\mathbf{q}}^\dagger) \tag{3.35}$$

with

$$A_{a\mathbf{q}} = E_T\cos 2\theta + 8J\sin^2 2\theta + 4J\cos^2 2\theta\gamma_{\mathbf{q}}, \qquad B_{a\mathbf{q}} = 4J\cos^2 2\theta\gamma_{\mathbf{q}}, \tag{3.36}$$

$$A_{b\mathbf{q}} = E_T\cos^2\theta + 4J\sin^2 2\theta + 4J\cos^2\theta\gamma_{\mathbf{q}}, \qquad B_{b\mathbf{q}} = 4J\cos^2\theta\gamma_{\mathbf{q}}. \tag{3.37}$$

The momentum-dependent factor $\gamma_{\mathbf{q}}$ is a sum over the nearest neighbors on the square lattice, denoted by the vector δ:

$$\gamma_{\mathbf{q}} = \frac{1}{z}\sum_\delta e^{i\mathbf{q}\cdot\delta} = \frac{1}{2}(\cos q_{x'} + \cos q_{y'}). \tag{3.38}$$

Subsequently, we diagonalize the Hamiltonian by a Bogoliubov transformation, which yields the dispersions of the two harmonic modes

$$\omega_{\alpha\mathbf{q}} = \sqrt{A_{\alpha\mathbf{q}}^2 - B_{\alpha\mathbf{q}}^2}, \quad \alpha = a, b. \tag{3.39}$$

We plot these for several J/E_T values in Fig. 3.3.

In the triplon gas phase, the two modes coincide, representing triplon excitations in the homogeneous sea of singlets – see Fig. 3.3 panel (a). The small dispersion that we see there disappears in the limit $J \to 0$, leaving flat degenerate bands with energy E_T corresponding to purely local, non-interacting triplon excitations. Gradually, as J/E_T increases, the dispersion arises and softens at (π, π), touching zero at the quantum critical point $J = \frac{1}{8}E_T$. Upon condensation, the degeneracy between modes is lifted, and the excitations carried by a- and b-bosons

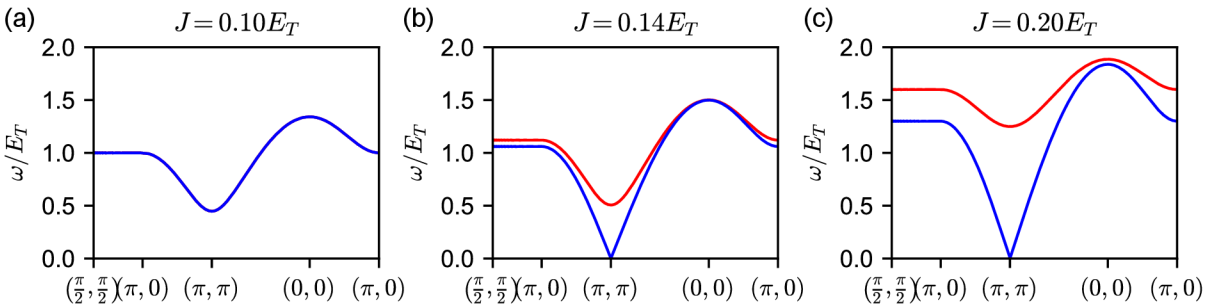

Figure 3.3: Harmonic modes of the simplified E_T, J model plotted along a line in the first Brillouin zone of the square lattice. (a) Degenerate modes in the triplon gas phase corresponding to triplon excitations in the homogeneous sea of singlets. (b) Non-degenerate modes in the condensed phase close to the QCP. Gapless magnon (blue) is carried by the b-boson and gapful amplitude mode by the a-boson. Minima of both excitation branches lie at the ordering wavevector $\mathbf{Q} = (\pi, \pi)$. (c) Deeper into the ordered phase, the magnon remains gapless, and the amplitude mode hardens as the condensate density increases.

become distinct. The b-boson branch is gapless at ordering wavevector $\mathbf{Q} = (\pi, \pi)$, due to a compensation of A and B for that $\mathbf{q}$:

$$\omega_{b\mathbf{Q}} = 0 \Leftrightarrow |A_{b\mathbf{Q}}| = |B_{b\mathbf{Q}}|, \tag{3.40}$$

which reduces to a familiar relation

$$\sin^2\theta = \frac{1}{2}\left(1 - \frac{E_T}{8J}\right) \tag{3.41}$$

that holds throughout the condensed phase. The excitation carried by boson b is a magnon, corresponding to an in-plane rotation of magnetization, which does not cost energy – the classical energy is isotropic in the xy-plane. The second mode that develops at QCP is carried by the a boson, which, according to the bosonic transformation we performed, is a particular mix of s and T_x bosons modulated by the mixing angle θ, which also determines the condensate density via $\rho = \sin^2\theta$. We can thus understand the a-mode as amplitude oscillations of the condensate density (also sometimes referred to as the Higgs mode [133]). The energy of the system is proportional to the condensate density, therefore density modulations cost energy, and the mode is always gapped. As we can see in Fig. 3.3 panels (b)-(c), the energy cost increases with J/E_T. Intuitively, such an evolution makes sense since as J/E_T increases, the condensate develops ($\rho \to \frac{1}{2}$), the magnetic moment saturates ($M \to 1$) – see Fig. 3.2 – and is thus more resistant to amplitude changes.

Effect of secondary Hamiltonian terms Δ', J_z, A

Apart from triplet energy cost E_T and symmetric exchange J, the full Hamiltonian contains also terms corresponding to orthorhombic crystal field Δ', exchange anisotropy J_z and bond-selective A-term. In this section, we show how their inclusion affects the harmonic excitations.

The orthorhombic term Δ' introduces a local shift of triplon energies in the Hamiltonian

$$\mathcal{H} = \frac{\Delta'}{2}\left(n_{T_y} - n_{T_x}\right) = \frac{\Delta'}{2}\left(T_y^\dagger T_y - T_x^\dagger T_x\right). \tag{3.42}$$

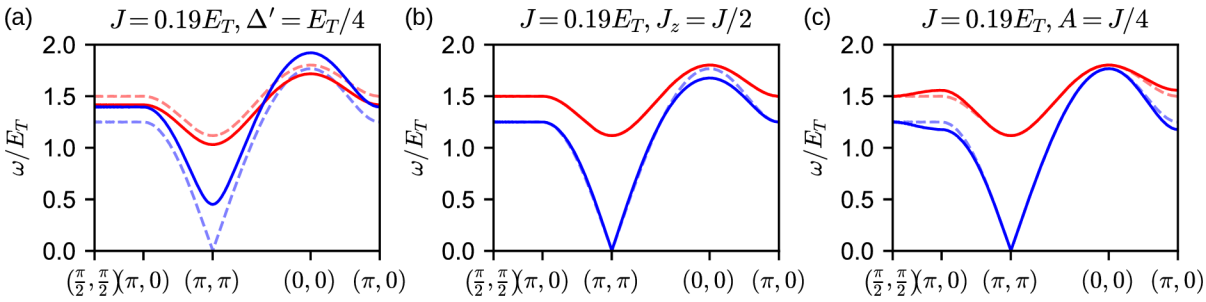

Figure 3.4: Harmonic excitations in the triplon condensate including (a) Δ', (b) J_z and (c) A interaction terms. Dashed lines indicate reference dispersions for the model including only E_T, J terms. While the inclusion of J_z and A terms only leads to small changes in the shape of the harmonic modes, orthorhombic splitting Δ' introduces a magnon gap $\sqrt{\Delta'(\Delta' + 8J\cos^2\theta)}$ in the b mode.

Translating this expression using the bosonic rotation (3.28), we obtain the following local interaction terms

$$H_i^{(0)} = -\frac{\Delta'}{2}\sin^2\theta,$$
$$H_i^{(2)} = -\frac{\Delta'}{2}\cos^2\theta a_i^\dagger a_i + \frac{\Delta'}{2} b_i^\dagger b_i \tag{3.43}$$

that modify the diagonal terms of the total harmonic Hamiltonian in Fourier space as follows:

$$A_{a\mathbf{q}} = \left(E_T - \frac{\Delta'}{2}\right)\cos 2\theta + 8J\sin^2 2\theta + 4J\cos^2 2\theta\gamma_{\mathbf{q}}, \qquad B_{a\mathbf{q}} = 4J\cos^2 2\theta\gamma_{\mathbf{q}}, \tag{3.44}$$

$$A_{b\mathbf{q}} = (E_T - \frac{\Delta'}{2})\cos^2\theta + \Delta' + 4J\sin^2 2\theta + 4J\cos^2\theta\gamma_{\mathbf{q}}, \qquad B_{b\mathbf{q}} = 4J\cos^2\theta\gamma_{\mathbf{q}}, \tag{3.45}$$

where the extra terms are highlighted in red. The effect of orthorhombic splitting Δ' on the excitation spectra differs between the triplon gas phase and the condensate. In the disordered phase, Δ' leads to a splitting of the a and b modes, which are no longer degenerate. The changes in the condensed phase can be seen in Fig. 3.4 panel (a). The longitudinal a-mode is shifted down in energy by $-\frac{\Delta'}{2}\cos 2\theta$, which is a relatively small effect compared to the mode bandwidth. Much more qualitatively important is the shift in b-mode brought about by the addition of Δ': the previously gapless magnon in the condensed phase now becomes gapped with the gap size

$$\sqrt{\Delta'(\Delta' + 8J\cos^2\theta)}, \tag{3.46}$$

i.e. the gap goes as $\sqrt{\Delta'}$ for $8J \gg \Delta'$. Additionally, the shift in local energy means a shifted QCP position to be obtained from:

$$\frac{J}{E_T - \Delta'/2} = \frac{1}{8} \tag{3.47}$$

instead of (3.24).

Let's step into the shoes of an experimental physicist who wishes to better understand their material and has measured the spin excitation spectrum. The simple model discussed above is sufficient to explain the essential features of the excitations, i.e., the presence of amplitude

and magnon modes, the mechanism driving the phase transition, and non-Heisenberg magnon dispersion shape with the minimum at $\mathbf{Q} = (\pi, \pi)$ and maximum at $\mathbf{Q} = (0,0)$. The overall balance of E_T and J can be easily inferred from the measured spectra since E_T gives the overall energy scale and J is given by the bandwidth (the specific value is $4zJ$ in the limit $E_T \gg J$ and the bands get flatter with increasing J/E_T). Finally, the size of a gap at (π, π) in the ordered phase is directly tied to the magnitude of orthorhombic splitting Δ'.

Understanding the role each Hamiltonian term plays helps the experimentalist to interpret the measured spectra. More refined fitting procedures uncover further deviations from harmonic-mode dispersions that cannot be explained by the simplified E_T, J, Δ' model. The full version of the effective model for ruthenates (3.2) introduced at the beginning of this chapter includes also the interaction of the out-of-plane pseudospin components J_z and a bond-dependent term A which both arise in real materials. These lead to the following extra terms in the harmonic Hamiltonian:

$$\begin{aligned} H_{ij}^{(2)} = &- J_z \sin^2\theta (b_i^\dagger b_j + b_i b_j^\dagger + b_i^\dagger b_j^\dagger + b_i b_j) - A_\xi \sin^2\theta \cos\theta (a_i^\dagger b_i + a_i b_i^\dagger + a_j^\dagger b_j + a_j b_j^\dagger) \\ &- A_\xi \cos^3\theta (a_i^\dagger b_j + a_i b_j^\dagger + b_i^\dagger a_j + b_i a_j^\dagger - a_i^\dagger b_j^\dagger - b_i^\dagger a_j^\dagger - a_i b_j - b_i a_j). \end{aligned} \tag{3.48}$$

No change in classical energy arises due to either of the above interaction terms. The J_z interaction is manifested on the harmonic level by a small change of the b-magnon dispersion and takes effect only in the ordered phase. Fig. 3.4 panel (b) shows calculated dispersions for a substantial value of $J_z = J/2$ (in ruthenates the fitted value is $0.85J$ [18] compared to dispersions without J_z, showing that the only visible effect is a slight flattening of the magnon mode at (π, π).

The bond-dependent A-interaction takes effect both in the ordered and the normal phase, as an interaction between the a-mode and the b-mode. The most visible effects can be seen at $(\pi, 0)$, see Fig. 3.4 panel (c). The calculation whose results are visible in the figure are performed in the ordered phase; in the triplon gas phase, the A-term splits the a- and b- modes, with the largest shift occurring again at $(\pi, 0)$.

For completeness, we briefly comment on the Fourier forms of the J_z- and A-interactions. The J_z Hamiltonian component contains quadratic terms in b-operators:

$$\mathcal{H}_{\text{harm}} = \sum_{\mathbf{q}} A_{b\mathbf{q}} b_{\mathbf{q}}^\dagger b_{\mathbf{q}} - \frac{1}{2} B_{b\mathbf{q}} (b_{\mathbf{q}} b_{-\mathbf{q}} + b_{\mathbf{q}}^\dagger b_{-\mathbf{q}}^\dagger), \tag{3.49}$$

where

$$A_{b\mathbf{q}} = -4J_z \sin^2\theta \gamma_{\mathbf{q}}, \qquad B_{b\mathbf{q}} = 4J_z \sin^2\theta \gamma_{\mathbf{q}}. \tag{3.50}$$

The A-type interaction, on the other hand, contains off-diagonal quadratic terms

$$\mathcal{H}_{\text{harm}} = -\sum_{\mathbf{q}} 4A\cos^3\theta \eta_{\mathbf{q}} \left[a_{\mathbf{q}}^\dagger b_{\mathbf{q}} + b_{\mathbf{q}}^\dagger a_{\mathbf{q}} - \frac{1}{2}(a_{-\mathbf{q}} b_{\mathbf{q}} + b_{-\mathbf{q}} a_{\mathbf{q}} + a_{\mathbf{q}}^\dagger b_{-\mathbf{q}}^\dagger + b_{\mathbf{q}}^\dagger a_{-\mathbf{q}}^\dagger) \right], \tag{3.51}$$

where the interaction's bond-dependence is hidden into the factor $\eta_{\mathbf{q}}$

$$\eta_{\mathbf{q}} = \frac{1}{z} \sum_{\delta} (\pm) e^{i\mathbf{q}\cdot\delta} = \frac{1}{2}(\cos q_{x'} - \cos q_{y'}). \tag{3.52}$$

Such off-diagonal Hamiltonian terms require numerical diagonalization of the full Bogoliubov matrix; see Appendix D.

3.2 Beyond the harmonic approximation: mean-field and quantum Monte Carlo

So far, we have presented an approximate analytical solution based on the variational wavefunction. Though simplified, it qualitatively captures the phase transition between triplon gas and antiferromagnetic triplon condensate phases. Applying a bosonic rotation enabled a unified description of the whole J/E_T parametric range, where the condensate solution is smoothly connected to the triplon gas phase through the quantum critical point, as described by the bosonic angle θ. Further, we added quantum fluctuations around the variational ground state on a harmonic level, obtaining dispersion relations of the magnon and amplitude (Higgs) modes, together with their evolution through the QCP.

In this section, we go beyond the above approximate analytical description and try to include further quantum effects. We approach this problem using two methods: a generalized mean-field procedure and a numerical quantum Monte Carlo method. First, we perform a general mean-field procedure that enforces the hard-core boson condition on average. Here, the hard-core effect is implemented by an increase of local triplon cost by a chemical potential λ, as well as by a triplon interaction screening by a factor $(1-n_T)$ corresponding to a probability that triplon hopping (or triplon creation/annihilation) is blocked by a presence of another boson. Such changes are manifested by a substantial shift of the quantum critical point as well as the renormalization of harmonic modes.

The mean-field procedure is still approximate since only quadratic bosonic terms are kept in the interaction. Therefore, the second approach we take is a fully quantum numerical treatment, using the quantum Monte Carlo stochastic series expansion (QMC SSE) technique [185, 186, 187, 157]. Its advantage over direct diagonalization methods is the possibility to use large lattice clusters and therefore get good **q**-resolution in calculated excitation spectra. As a bonus, it naturally includes temperature dependence in the model. The main drawback, as will be seen, is the necessity of analytical continuation to obtain dynamical properties, which is numerically difficult and requires careful handling of the Monte Carlo statistics.

Looking at the model through different levels of approximation, we hope to judge the relative importance of various quantum effects and the fidelity with which the mean-field procedure captures the hard-core boson condition. The motivation is to see whether it's possible to use such approximate procedures for modeling and fitting experimental RIXS/neutron diffraction spectra instead of relying on numerics.

3.2.1 Quantum Monte Carlo: Stochastic Series Expansion (SSE) method

Strongly correlated systems are often analytically untractable and, for this reason, have been a driver for the development of numerical methods. One of the most widely used classes of methods is Quantum Monte Carlo (QMC) [188] due to its key combination of unbiased, exact solutions together with polynomial dependence of calculation time on system size. These key features make it possible to simulate large systems, which is important when studying boson/spin dynamics or critical properties near quantum phase transitions. The main limitations of the QMC approach lie in its inefficiency when dealing with frustrated boson and spin systems and fermionic systems with a sign problem – in such cases, the statistical errors can rise exponentially with lowering temperature/increasing system size [189].

In this section, we briefly describe the Stochastic Series expansion (SSE) [185, 186, 187, 157] variant of QMC methods, which is especially suitable for spin systems on bipartite lattices, such as the one we are studying. More details on the technical implementation can be found in Appendix C.

The method is formulated using a statistical description of the system using the partition function Z

$$Z = \mathrm{Tr}\left\{e^{-\beta\mathcal{H}}\right\}. \tag{3.53}$$

For lattice spin systems with a discrete set of basis states $|\alpha\rangle = \left|S_1^z, S_2^z, \ldots, S_N^z\right\rangle$, we form a high-temperature expansion of the partition function in powers of $(-\beta\mathcal{H})$:

$$Z = \sum_\alpha \langle\alpha|e^{-\beta\mathcal{H}}|\alpha\rangle = \sum_\alpha \sum_n \frac{\beta^n}{n!} \langle\alpha|(-\mathcal{H})^n|\alpha\rangle\,, \tag{3.54}$$

where the trace is written as a sum over the diagonal elements of the basis $\{|\alpha\rangle\}$. In lattice models, the Hamiltonian is typically in the form of a sum of bond-interaction terms

$$\mathcal{H} = \sum_{\langle ij\rangle} H_{ij} = \sum_b -H_b, \tag{3.55}$$

where b is the bond index running through all bonds on the lattice, i.e. $b \in \{1, 2, \ldots, N_{\text{bond}}\}$, $N_{\text{bond}} = 2N_{\text{site}}$ for the square lattice. For instance, the Ising interaction between spins on lattice sites (i, j) is $H_{b(i,j)} = S_i^z S_j^z$. Using this decomposition of the Hamiltonian into bond operators, we can rewrite the product $(-\mathcal{H})^n$ as a sum over sequences of bond operators $S_n = \{b_1, b_2, \ldots, b_n\}$ of length n:

$$(-\mathcal{H})^n = \left(-\sum_b -H_b\right)^n = \sum_{S_n} \prod_{i=1}^n H_{b_i}. \tag{3.56}$$

Notice that the extra minus sign introduced in the Hamiltonian decomposition into bond operators is now canceled out. Plugging back into into the expression for the partition function, we obtain:

$$Z = \sum_n \frac{\beta^n}{n!} \sum_{S_n} \sum_\alpha \langle\alpha|\prod_{i=1}^n H_{b_i}|\alpha\rangle\,. \tag{3.57}$$

For many spin models, each bond interaction term H_b transforms a basis state $|\alpha\rangle$ into a single different state $|\beta\rangle$, as opposed to a general scenario where a general superposition of states could arise:

$$H_b|\alpha\rangle = \langle\beta|H_b|\alpha\rangle\,|\beta\rangle\,. \tag{3.58}$$

This is the case for the spin Hamiltonians containing terms $S_i^\alpha S_j^\alpha, (S^z)_i^2$, which are present in the effective spin model for Ca_2RuO_4. It is useful to introduce a notation for the normalized state $|\alpha(p)\rangle$ resulting after the application of the first p bond operators in the operator sequence S_n:

$$|\alpha(p)\rangle \propto \prod_{i=1}^p H_{b_i}|\alpha\rangle\,. \tag{3.59}$$

Finally, the partition function can be written as a sum over weight factors for a given operator sequence S_n and spin state α:

$$Z_{\mathrm{SSE}} = \sum_{n} \sum_{S_n} \sum_{\{\alpha\}} W(\alpha, S_n), \tag{3.60}$$

$$W(\alpha, S_n) = \frac{\beta^n}{n!} \prod_{p=1}^{n} \langle \alpha(p) | H_{b_p} | \alpha(p-1) \rangle . \tag{3.61}$$

We can think of the state $|\alpha\rangle \equiv |\alpha(0)\rangle$ as an initial state in a sequence, being propagated by the action of bond operators H_{b_p}, resulting in propagated states $|\alpha(p)\rangle$. In analogy with the path integral formulation of statistical mechanics [190], the propagation direction is imaginary time. The whole sequence of propagated states forms a configuration, whose statistical weight is given by $W(\alpha, S_n)$. In the case of a two-dimensional spin-lattice system, such a configuration would be represented by layers of up/down spins stacked on top of each other along the imaginary time dimension, with a single bond operator connecting every two successive layers. The partition function is an infinite sum over such $(D+1)$-dimensional configurations.

In practice, the vast majority of such configurations will not contribute to the partition function. Instead, the standard practice is to perform an importance sampling of these configurations with carefully chosen update procedures that fulfill the requirements of ergodicity and detailed balance. It is then relatively straightforward to calculate static physical quantities such as ground state energy or spin-spin correlation functions such as

$$\langle S^{\mu}_{-\mathbf{q}} S^{\nu}_{\mathbf{q}} \rangle = \sum_{ij} e^{i\mathbf{q}\cdot(\mathbf{R}_i - \mathbf{R}_j)} \langle S^{\mu}_i S^{\nu}_j \rangle . \tag{3.62}$$

Dynamical quantities are often of most interest as they provide the richest information about the system, as well as mediate a link with data from scattering experiments. Time-resolved spin-spin correlation function can be written in the Heisenberg picture as

$$\langle S^{\mu}_i(t) S^{\nu}_j(0) \rangle = \frac{1}{Z} \mathrm{Tr} \left[e^{it\mathcal{H}} S^{\mu}_i e^{-it\mathcal{H}} S^{\nu}_j e^{-\beta\mathcal{H}} \right], \quad \mu\nu \in x, y, z. \tag{3.63}$$

The oscillating character of $e^{it\mathcal{H}}$ poses problems for a Taylor expansion – the standard solution is the perform a Wick rotation and work in imaginary time:

$$e^{it\mathcal{H}} \to e^{\tau\mathcal{H}}, \quad \tau = it. \tag{3.64}$$

We perform the expansion in imaginary time, obtaining

$$\langle S^{\mu}_i(\tau) S^{\nu}_j(0) \rangle = \frac{1}{Z} \sum_{m_1=0}^{\infty} \sum_{m_2=0}^{\infty} \sum_{\{\alpha\}} \frac{(\beta-\tau)^{m_1}}{m_1!} \frac{\tau^{m_2}}{m_2!} \left\langle \alpha \middle| (-\mathcal{H})^{m_1} S^{\mu}_i (-\mathcal{H})^{m_2} S^{\nu}_j | \alpha \right\rangle . \tag{3.65}$$

Finally, we implement the operator sequence S_n of total length n by relabeling the sums and after some algebra, we obtain the final expression:

$$\begin{aligned} \langle S^{\mu}_i(\tau) S^{\nu}_j(0) \rangle = & \frac{1}{Z} \sum_{n=0}^{\infty} \sum_{\{\alpha\}} \sum_{S_n} \sum_{m=0}^{n} W_{nm}(\tau) \times \\ & \times \langle \alpha | H_{b_n} | \alpha(n-1) \rangle \ldots \left\langle \alpha(m+1) \middle| H_{b_{m+1}} S^{\mu}_i | \alpha(m) \right\rangle \ldots \left\langle \alpha(1) \middle| H_{b_1} S^{\nu}_j | \alpha \right\rangle , \end{aligned} \tag{3.66}$$

where the weights W_{nm} read

$$W_{nm}(\tau) = \frac{\beta^n}{n!}\binom{n}{m}\left(\frac{\tau}{\beta}\right)^m\left(1-\frac{\tau}{\beta}\right)^{n-m}. \tag{3.67}$$

We notice that in the SSE scheme, two spin operators separated in imaginary time by τ correspond to configurations containing these two operators separated by m α-levels, and the distribution of m is binomial around the maximum given by $\frac{\tau}{\beta}$. The above calculation shows that we may interpret the additional dimension of the configuration space as discrete imaginary time slices τ_i. As a result of the cyclical property of the trace, the imaginary time dimension is periodic with the period β:

$$W_{nm}(\tau) = W_{n,n-m}(\beta-\tau). \tag{3.68}$$

Ultimately, we want to access the dynamical susceptibility $\langle S^\mu_{\mathbf{q}} S^\nu_{\mathbf{q}}\rangle(\omega)$, hence we need to "un-do" the Wick rotation. First, we move to the Matsubara representation

$$S^{\mu\nu}(i\omega_n,\mathbf{q}) = \langle S^\mu_{\mathbf{q}} S^\nu_{\mathbf{q}}\rangle(i\omega_n) = \int_0^\beta d\tau \sum_{ij} e^{-i(\omega_n\tau-\mathbf{q}\cdot(\mathbf{R}_i-\mathbf{R}_j))}\langle S^\mu_i(\tau)S^\nu_j(0)\rangle, \tag{3.69}$$

and then use the fluctuation-dissipation theorem along with the Kramers-Kronig relations to obtain the connection to dynamical susceptibility:

$$S^{\mu\nu}(i\omega_n,\mathbf{q}) = \int_0^\infty d\omega \frac{\omega}{\pi}\frac{1-e^{-\beta\omega}}{\omega^2+\omega_n^2}S^{\mu\nu}(\omega,\mathbf{q}). \tag{3.70}$$

Inverting the above expression is called analytical continuation. It is a difficult problem since inverting the kernel is numerically ill-posed. Additionally, QMC adds errors to the imaginary-time data, which may lead to high-frequency noise that does not carry information about the real frequency spectrum. The maximum entropy method [191] has been specifically formulated to tackle this problem, and we will use it in the last section of this chapter to calculate the spin dynamical susceptibility.

3.2.2 Mean-field treatment of the hard-core bosonic Hamiltonian

In this section, we describe an analytical treatment of our Hamiltonian that goes beyond the harmonic approximation of the previous section. We start with a general consideration of the problem we face. Our model involves three bosons s, T_x, T_y participating in local and nearest-neighbor bond interactions. These bosons are constrained by the hard-core condition, i.e. there can be only one boson per site:

$$s^\dagger s + T_x^\dagger T_x + T_y^\dagger T_y = 1. \tag{3.71}$$

Introducing a bosonic rotation angle θ allows for a consistent description in the whole parameter range, where the c boson condenses – the hard-core condition translates to $c^\dagger c + a^\dagger a + b^\dagger b = 1$. Previously, the approximations we introduced were replacing $c, c^\dagger$ by a number $\sqrt{1-n}$, expanding the square root and leaving only terms up to second order in the number of bosons. Here, we propose an improvement following a similar approach by Gopalan, Rice, and Sigrist developed to deal with spin ladders [180]. It amounts to replacing $c, c^\dagger$ by a number κ and

adding a chemical potential λ in the form of a Lagrange multiplier. The Hamiltonian then has the following form:

$$\mathcal{H}_{\mathrm{MF}} = \sum_i \left[(1-n)H_i^{(0)} + H_i^{(2)}\right] + \sum_{\langle ij\rangle} \left(\kappa^4 H_{ij}^{(0)} + \kappa^2 H_{ij}^{(2)}\right) + \lambda \sum_i \left(n_i + \kappa^2 - 1\right), \tag{3.72}$$

where $H^{(k)}$ is an interaction term of $k-$th order in bosons a, b and $n_i = a_i^\dagger a_i + b_i^\dagger b_i$. We still consider only terms up to quadratic order in boson number, the improvement of the description lies in the additional λ-term. The Lagrange multiplier enforces the hard-core constraint $c^\dagger c + a^\dagger a + b^\dagger b = 1$, but not exactly at every site, but only on average through a single chemical potential. The numbers κ and λ are determined by the condition that the mean-field energy is stationary

$$\frac{\partial \mathcal{H}_{\mathrm{MF}}}{\partial \lambda} = 0, \quad \frac{\partial \mathcal{H}_{\mathrm{MF}}}{\partial \kappa} = 0. \tag{3.73}$$

Applying these, we get

$$\begin{aligned} \kappa^2 &= 1 - \langle n\rangle, \\ \lambda &= -\frac{1}{N_{\mathrm{bond}}} \sum_{\langle ij\rangle} \left[4\kappa^2 H_{ij}^{(0)} + 2\langle H_{ij}^{(2)}\rangle\right]. \end{aligned} \tag{3.74}$$

Using these relations for λ, κ, the Hamiltonian can be rewritten as:

$$\begin{aligned} \mathcal{H}_{\mathrm{MF}} = &\sum_i H_i^{(0)} + (1-\langle n\rangle^2) \sum_{\langle ij\rangle} H_{ij}^{(0)} + \sum_i \left[H_i^{(2)} - n_i H_i^{(0)}\right] + \\ &+ (1-\langle n\rangle) \sum_{\langle ij\rangle} \left[H_{ij}^{(2)} - (n_i + n_j) H_{ij}^{(0)}\right] - \sum_{\langle ij\rangle} \left\langle H_{ij}^{(2)} \right\rangle \left(\frac{n_i + n_j}{2} - \langle n\rangle\right). \end{aligned} \tag{3.75}$$

The Hamiltonian is similar to the harmonic one, with some extra multiplicative and additive terms (in red). The multiplicative terms of the form $(1-\langle n\rangle)$ screen the bond interaction, whereas the additive terms play the role of chemical potential. The mean-field Hamiltonian has to be solved self-consistently with the equations for $\langle n\rangle, \left\langle H_{ij}^{(2)}\right\rangle$. The mean-field energy is

$$E_{\mathrm{MF}} \equiv \langle \mathcal{H}_{\mathrm{MF}}\rangle = \sum_i \left[(1-\langle n\rangle) H_i^{(0)} + \left\langle H_i^{(2)}\right\rangle\right] + (1-\langle n\rangle) \sum_{\langle ij\rangle} \left[\left\langle H_{ij}^{(2)}\right\rangle + (1-\langle n\rangle) H_{ij}^{(0)}\right], \tag{3.76}$$

where the black terms represent classical energy and red terms indicate mean-field corrections.

After a general exposition, we apply the above procedure to the singlet-doublet model and show how to use the method in practice. In addition to J and E_T, we also include orthorhombic splitting Δ', since this is qualitatively important for the gap in excitation spectra at the ordering wavevector. The bond-dependent term A and J_z interaction are skipped for simplicity, as they bring only marginal differences. The mean-field interaction terms read:

$$H_i^{(0)} = \left(E_T - \frac{\Delta'}{2}\right) \sin^2\theta,$$

$$
\begin{aligned}
H_i^{(2)} &= \left(E_T - \frac{\Delta'}{2}\right)\cos^2\theta a_i^\dagger a_i + \left(E_T + \frac{\Delta'}{2}\right) b_i^\dagger b_i, \\
H_{ij}^{(0)} &= -J\sin^2 2\theta, \\
H_{ij}^{(2)} &= J\sin^2 2\theta(a_i^\dagger a_i + a_j^\dagger a_j) + J\cos^2 2\theta(a_i^\dagger a_j + a_i a_j^\dagger - a_i a_j - a_i^\dagger a_j^\dagger) + \\
&\quad + J\cos^2\theta(b_i^\dagger b_j + b_i b_j^\dagger - b_i b_j - b_i^\dagger b_j^\dagger).
\end{aligned} \tag{3.77}
$$

Our solution strategy follows a similar recipe as previously: perform the Bologiubov transformation on the model expressed in Fourier space. The resulting coefficients $A_{\alpha\mathbf{q}}, B_{\alpha\mathbf{q}}, \alpha \in a,b$ read:

$$
\begin{aligned}
A_{a\mathbf{q}} &= \left(E_T - \frac{\Delta'}{2}\right)\cos 2\theta + 8J(1-\langle n\rangle)\sin^2 2\theta + 4J\gamma_{\mathbf{q}}(1-\langle n\rangle)\cos^2 2\theta + \tilde{\lambda}, \\
B_{a\mathbf{q}} &= 4J\gamma_{\mathbf{q}}(1-\langle n\rangle)\cos^2 2\theta, \\
A_{b\mathbf{q}} &= E_T\cos^2\theta + \frac{\Delta'}{2}(1+\sin^2\theta) + 4J(1-\langle n\rangle)\sin^2 2\theta + 4J\gamma_{\mathbf{q}}(1-\langle n\rangle)\cos^2\theta + \tilde{\lambda}, \\
B_{b\mathbf{q}} &= 4J\gamma_{\mathbf{q}}(1-\langle n\rangle)\cos^2\theta,
\end{aligned} \tag{3.78}
$$

where

$$
\gamma_{\mathbf{q}} = \frac{1}{z}\sum_{\delta} e^{i\mathbf{q}\cdot\delta} = \frac{1}{2}(\cos q_{x'} + \cos q_{y'}), \tag{3.79}
$$

$$
\tilde{\lambda} = -\frac{1}{N_{\text{bond}}}\sum_{\langle ij\rangle} 2\left\langle H_{ij}^{(2)}\right\rangle. \tag{3.80}
$$

After the diagonalization, dispersions ω_a, ω_b of a,b modes are easily obtained, as are the other averages $\left\langle a_{\mathbf{q}}^\dagger a_{\mathbf{q}}\right\rangle, \langle a_{-\mathbf{q}} a_{\mathbf{q}}\rangle, \langle a_{\mathbf{q}}^\dagger a_{-\mathbf{q}}^\dagger\rangle, \left\langle b_{\mathbf{q}}^\dagger b_{\mathbf{q}}\right\rangle, \langle b_{-\mathbf{q}} b_{\mathbf{q}}\rangle, \langle b_{\mathbf{q}}^\dagger b_{-\mathbf{q}}^\dagger\rangle$. However, these expressions still contain the two parameters $\langle n\rangle, \tilde{\lambda}$ for which two equations have to hold:

$$
\langle n\rangle = \frac{1}{N_{\text{site}}}\sum_{\mathbf{q}}\left[\left\langle a_{\mathbf{q}}^\dagger a_{\mathbf{q}}\right\rangle + \left\langle b_{\mathbf{q}}^\dagger b_{\mathbf{q}}\right\rangle\right], \tag{3.81}
$$

and

$$
\begin{aligned}
\tilde{\lambda} = -\frac{4J}{N}\sum_{\mathbf{q}}\gamma_{\mathbf{q}}\Bigg\{&\sin^2 2\theta\left\langle a_{\mathbf{q}}^\dagger a_{\mathbf{q}}\right\rangle + \cos^2 2\theta\left[\left\langle a_{\mathbf{q}}^\dagger a_{\mathbf{q}}\right\rangle - \frac{1}{2}\left(\langle a_{-\mathbf{q}} a_{\mathbf{q}}\rangle + \langle a_{\mathbf{q}}^\dagger a_{-\mathbf{q}}^\dagger\rangle\right)\right] + \\
&+ \cos^2\theta\left[\left\langle b_{\mathbf{q}}^\dagger b_{\mathbf{q}}\right\rangle - \frac{1}{2}\left(\langle b_{-\mathbf{q}} b_{\mathbf{q}}\rangle + \langle b_{\mathbf{q}}^\dagger b_{-\mathbf{q}}^\dagger\rangle\right)\right]\Bigg\}.
\end{aligned} \tag{3.82}
$$

These expressions, in turn, depend on the mean-field averages. The way to solve the problem is, therefore, to iteratively solve for $\langle n\rangle, \tilde{\lambda}$, and the mean-field averages to obtain a self-consistent solution. Such a self-consistent loop is performed separately for each possible $\theta \in (0, \pi/2)$, and subsequently the θ-value corresponding to the ground state is identified by the minimum of mean-field energy. More details on the technical implementation of the self-consistent loop can be found in Appendix E.

3.2.3 Quantitative analysis of the effects beyond the harmonic approximation

In this section, we look at the phase diagram of our model obtained using the methods of 3.2.1 and 3.2.2, i.e. with the inclusion of hard-core boson effects beyond the harmonic approximation. We are especially interested in the renormalized position of the quantum critical point, and also, more generally, at the model's properties, both static (spin-spin correlation functions, triplon occupation) and dynamic (spin susceptibility) at the fully quantum level that can be reached numerically using quantum Monte Carlo simulations. These are then taken as a reference for analytical calculations using the mean-field approximation. One of the main goals of this section is to assess to what extent are the hard-core boson effects captured by the mean-field approximation. The hope is, that if the main renormalization effects are well observed, it may suffice as an adequate description without resorting to technically demanding numerical simulations.

QMC phase diagram

We start this result section with a discussion of numerical QMC calculations. We implemented the singlet-doublet model in the spin-1 representation (3.2), but without the bond-directional A-term because of the sign problem [192]. The QMC SSE method allows for a calculation (often called "measurement") of various static ground state properties (ground state energy, specific heat, spin-spin correlation function, magnetization, total spin, etc.) as well as dynamical quantities such as dynamical susceptibility. Off-diagonal spin components (other than the component in the direction of the quantization axis) are more difficult to measure in the considered scheme, thus we perform the calculation several times for the model expressed in suitably rotated coordinate frames. The numerical correctness of the implemented scheme was checked by a careful comparison with exact diagonalization on a small 4×4-site cluster. For the interested reader, we leave the technical details of the method – the chosen Monte Carlo update procedure, handling of statistical errors, etc. – for the Appendix C.

Figure 3.5 shows the $J/E_T - T$ phase diagram of the ruthenate model in the form of spin-spin correlations at the ordering wavevector $\mathbf{Q} = (\pi, \pi)$. The triplon cost E_T and temperature T are calculated in a meaningful range whereas the values for the other interaction parameters are fit to experiment following Ref. [18]: $J = 5.8$ meV, $\alpha = 1 - J_z/J = 0.15$, $\Delta' = 4.0$ meV. The spin correlations are scaled by the number of lattice sites N to get rid of the linear dependence in the ordered phase. The scaling also allows us to judge the amount of fluctuations by the departure of the magnitude of spin correlations from the fully saturated value 1. Panel (a) shows the component of the spin-spin correlation function that is parallel to the ordered moment direction x and plays the role of an order parameter. Panel (b) shows the perpendicular component for comparison.

We see the order parameter taking on finite values in a region representing the ordered antiferromagnetic triplon condensate. At very low temperatures, the system is close to the ground state, and the evolution with the J/E_T parameter is similar to what we obtained using the variational solution – cf. Fig. 3.2 panel (a). At low J/E_T, the energy cost of triplet excitations is very high, and the system is in a triplon gas phase. The transition to the ordered phase is marked by the quantum critical point at zero temperature. Increasing temperature at this point – directly above QCP in the phase diagram Fig. 3.5 panel (a) – destroys the fragile order.

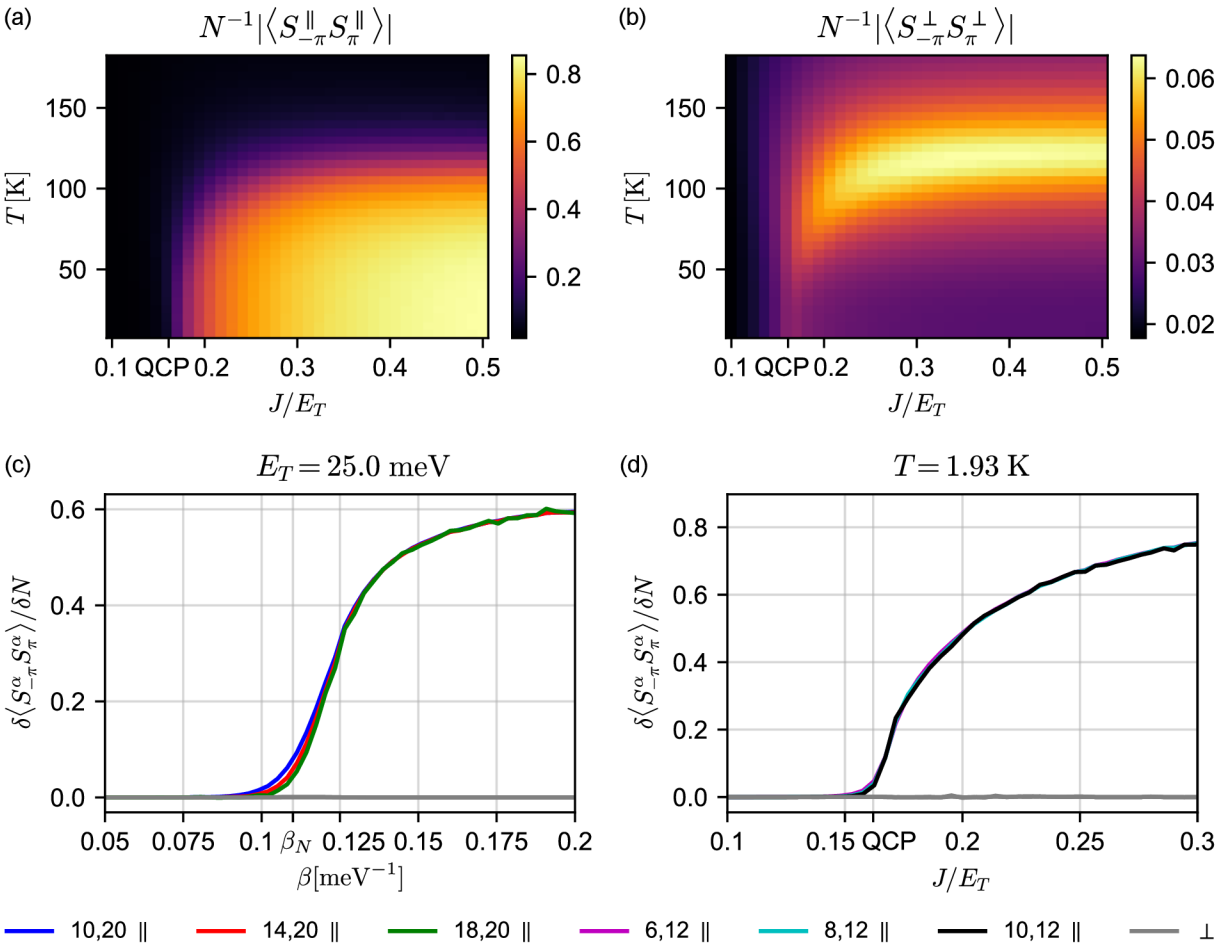

Figure 3.5: Phase diagram of the singlet-doublet model obtained by quantum Monte Carlo. The figure shows components of static spin-spin correlations at the ordering wavevector $\mathbf{Q} = (\pi, \pi)$ scaled by the number of lattice sites $1/N$. (a) The diagonal component in the direction of the ordered moment (xx) and (b) the sum of diagonal components perpendicular to the ordered moment ($yy + zz$). The calculation was performed for a 10×10 cluster with periodic boundary conditions. (c) Finite-size scaling: J/E_T-cut through the phase diagram for various cluster sizes using experimental values of interaction parameters following Ref. [18]. Differences of spin-spin correlations for various pairs of cluster sizes are shown, with the clusters' linear dimensions indicated in the legend. The Néel transition temperature is $\beta_N = 0.11$ meV^{-1}, which translates to $T_N = 106$ K. (d) Finite-size scaling: constant-β cut through the phase diagram for a large β value, well-representative of the ground-state behavior. The QCP is shown at $J/E_T = 0.162$. The three curves overlap almost completely, showing that at such low temperatures, the ground state is developed well even for cluster sizes around 10×10 lattice sites.

As the condensate develops with increasing J/E_T, the transition temperature rapidly increases, eventually reaching a plateau. The border line separating the ordered condensate phase from the disordered phase can also be observed in the plot of the perpendicular component of spin-spin correlations at $\mathbf{Q}$, shown in Fig. 3.5 panel (b). The perpendicular component does not scale with the number of lattice sites and, therefore, tends to zero as $N_{\text{site}} \to \infty$, but the largest fluctuations occur at the transition.

After the brief above discussion of the phase diagram, we now focus on pinpointing the position of the transition at two specific cuts through the diagram. Locating the transition using

numerical data on a finite cluster requires extra analysis since the transition points evolve with cluster size. We choose to locate the transition using spin-spin correlation functions at ordering wavevector $\mathbf{Q} = (\pi, \pi)$ calculated numerically for various cluster sizes. Considering multiple cluster sizes is used as an attempt to extrapolate to infinite lattice values. We base our simplified finite-size scaling analysis on the fact that the component of spin-spin correlations parallel to the magnetic moment scales linearly with the number of lattice sites since each lattice site hosts a spin that contributes to the function average. Formally, we can write:

$$\langle S^{\parallel}_{-\pi} S^{\parallel}_{\pi} \rangle (N) = S_{\parallel}(\infty) N + \mathcal{O}(1), \tag{3.83}$$

where $S^{\parallel}(\infty)$ is part of the average associated with the ordering, for infinite lattice size. We can obtain this quantity by combining two different cluster sizes since this allows us to get rid of the constant component:

$$S_{\parallel}(\infty) = \frac{\langle S^{\parallel}_{-\pi} S^{\parallel}_{\pi} \rangle (N_2) - \langle S^{\parallel}_{-\pi} S^{\parallel}_{\pi} \rangle (N_1)}{N_2 - N_1} = \frac{\delta \langle S^{\parallel}_{-\pi} S^{\parallel}_{\pi} \rangle (N)}{\delta N}. \tag{3.84}$$

Using progressively larger lattices N_1, N_2, we find that the above quantity indeed quickly converges towards a size-independent profile.

Figure 3.5 panel (c) shows the inverse temperature evolution of scaled spin-spin correlations for a fixed $E_T = 25$ meV ($J/E_T = 0.232$), which corresponds to the experimental value found for Ca_2RuO_4. The clusters we used were $N_2 = 20 \times 20$ and $N_1 = 10 \times 10, 14 \times 14, 18 \times 18$. The plot still shows some evolution for the largest clusters we considered, thus even larger clusters would be necessary if high precision in inverse Néel temperature β_N is required. The value we found is $\beta_N = 0.11$ meV^{-1}, which can be converted to Kelvin using a simple relation

$$T[\mathrm{K}] = \frac{e}{k} \times \beta^{-1}[\mathrm{eV}] \doteq 11.6 \times \beta^{-1}[\mathrm{meV}], \tag{3.85}$$

yielding $T_N \doteq 106$ K. This result is remarkably close to the experimental value of the Néel temperature for Ca_2RuO_4 measured as $T_{\mathrm{crit}} = 110$ K [127, 193], which provides additional evidence towards the model's consistency with the physics of the real material.

Let us now apply the same procedure to find the position of the quantum critical point from the numerical data. Ideally, we would want a cut through the phase diagram at exactly zero temperature to access the ground state, but because the QMC simulation time scales linearly with inverse temperature β, we can only access states for a small finite value of T. Since we are dealing with a two-dimensional system, there is always a finite-size gap (Mermin-Wagner theorem [160, 161, 162]). Therefore, we have to consider a temperature that is much smaller than such a gap dependent on the number of lattice sites. For the 10×10 cluster a temperature value $T = 1/6$ meV ≈ 2 K is sufficient (one can make sure of this by lowering the temperature further and checking that the physical quantities do not differ outside of statistical errors). A T-cut through the phase diagram is shown in Fig. 3.5 panel (d). Again, we consider several cluster sizes, specifically $N_2 = 12 \times 12$ and $N_1 = 6 \times 6, 8 \times 8, 10 \times 10$. Even though these are quite a bit smaller than the clusters we chose for finding the transition temperature, the plot shows that the scaled spin correlations are already well-converged. The resulting QCP position is

$$(J/E_T)_{\mathrm{crit}} \doteq 0.162. \tag{3.86}$$

This value differs substantially from the classical value 0.125 obtained by the variational method 3.1.2. Such a discrepancy is often encountered in similar bosonic systems, and thus, a numerical QMC calculation with a finite-size scaling analysis is frequently used to find the QCP [194]. The question we will answer next is what improvement to the QCP estimate can be reached by accounting for the hard-core boson effects by a mean-field procedure described earlier.

Mean-field solution

We used the general mean-field procedure as introduced in Sec. 3.2.2 for the model in bosonic singlet-triplet notation that includes E_T, J, and Δ' interaction terms. Adding J_z and A interactions lead to numerical difficulties, and, since these do not influence the QCP position and have only a small effect on the shapes of excitation spectra (cf. Fig. 3.4) we decided to omit them from the analytical calculation. As described earlier 3.2.2, the mean-field calculation requires a numerical solution of the self-consistent equations separately for each bosonic rotation angle θ, and afterward the physical solution is found at the minimum of mean-field energy $E_{\mathrm{MF}}(\theta)$. The condensation happens at such J/E_T where optimum θ becomes non-zero. As a further consistency check, one can also check that this point coincides with the closing of a spin gap $\omega_{a\mathbf{Q}} = \omega_{b\mathbf{Q}}$ at the ordering wavevector $\mathbf{Q}$ in the case without orthorhombic splitting Δ' (for $\Delta' > 0$ the spectrum is always gapped).

Performing the mean-field minimization over the interesting J/E_T range, we find that the condensation point occurs at

$$(J/E_T)_{\mathrm{crit}} \doteq 0.164, \tag{3.87}$$

which is around 1% off compared to the value 0.162 extracted by finite-size scaling of QMC data. We thus find that the approximate implementation of the bosons' hard-core character through the inclusion of interaction screening κ and on-site energy shift λ accounts completely for the difference in QCP position between the classical value of 0.125 and the fully quantum value 0.162.

Aside from the QCP position, we can also obtain various ground-state properties using the mean-field solution. We first look at static ground-state quantities, namely triplon occupation n_T and spin-spin correlation functions $\langle S^\alpha_{-\mathbf{q}} S^\alpha_{\mathbf{q}} \rangle$. Triplon occupation is easily calculated from the mean-field averages:

$$n_T = (1 - n_a - n_b)\sin^2\theta + n_a \cos\theta + n_b, \tag{3.88}$$

where

$$n_a = \frac{1}{N}\sum_{\mathbf{R}} \langle a^\dagger_{\mathbf{R}} a_{\mathbf{R}} \rangle, \quad n_b = \frac{1}{N}\sum_{\mathbf{R}} \langle b^\dagger_{\mathbf{R}} b_{\mathbf{R}} \rangle. \tag{3.89}$$

We compare the n_T evolution with the triplon energy E_T on the top left panel (a) of Fig. 3.6, which shows the quantity calculated at all levels of approximation considered in this thesis – harmonic, mean-field, and QMC – for the simplified J, E_T model. As we have shown, the condensation point determined by the harmonic approximation is quite inaccurate. To better highlight differences other than this QCP shift, we plot each data series against J/E_T scaled relative to the QCP position calculated by the corresponding method

$$(J/E_T)_{\mathrm{rel}} \equiv \frac{(J/E_T)}{(J/E_T)_{\mathrm{crit}}}. \tag{3.90}$$

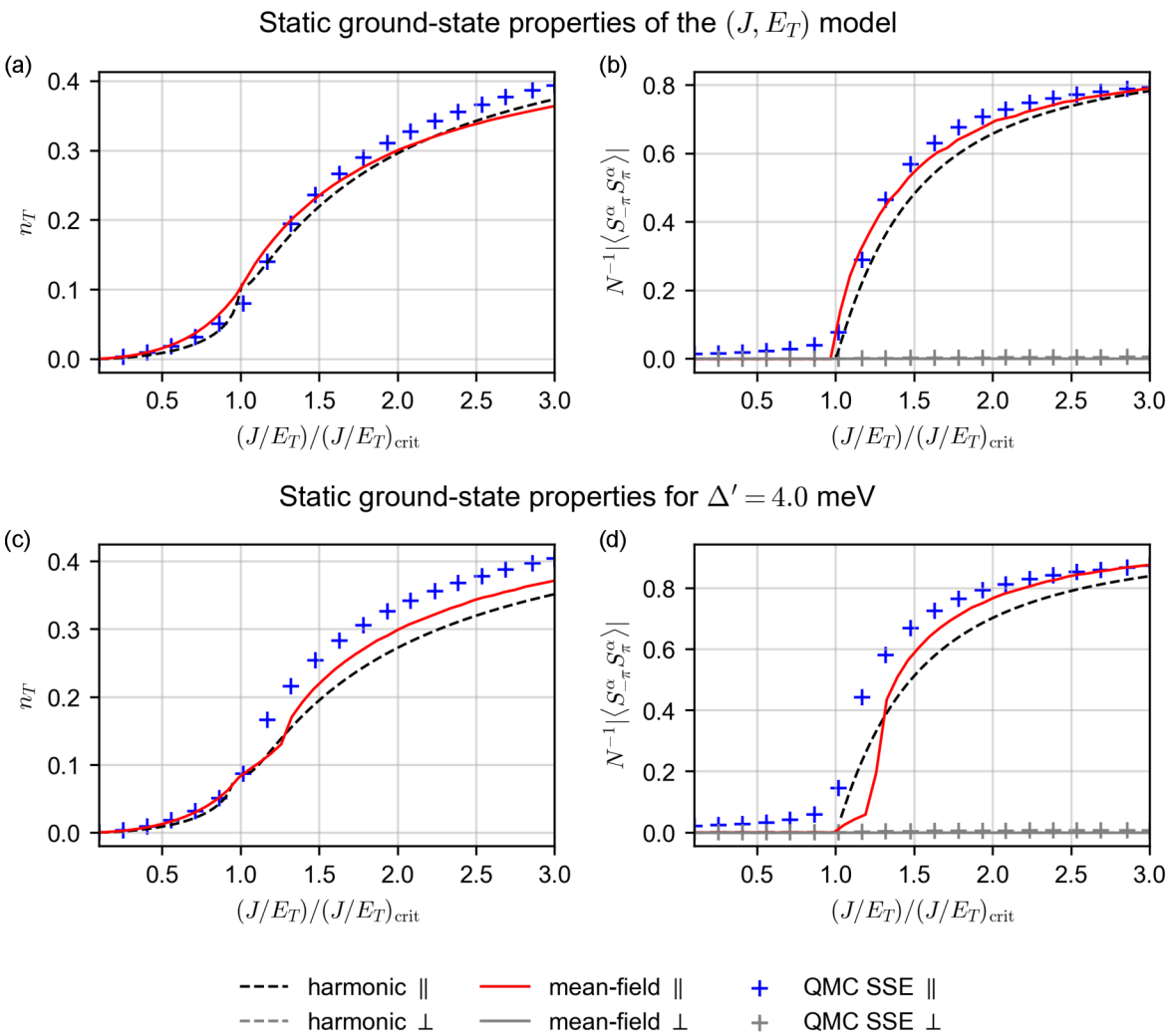

Figure 3.6: (a),(c) Triplon occupation and (b),(d) spin-spin correlation functions at the ordering wavevector $\mathbf{Q}$ scaled by the number of lattice sites N. The dashed curves were obtained using harmonic approximation, full red lines correspond to the analytical mean-field solution, and blue crosses were extracted from QMC SSE simulations using a 12×12 square lattice cluster. On the x-axis is J/E_T scaled with respect to QCP position $(J/E_T)_{\mathrm{crit}}$ obtained separately by each of the methods, thus highlighting effects other than the QCP position renormalization. The top row (a),(b) was obtained using a simplified model containing only E_T, J terms, while the bottom row (c),(d) also includes orthorhombic splitting term Δ'.

The figure reveals that both the harmonic solution as well as the mean field procedure produces curves that fit quite well to the fully quantum solution with only minor deviations.

A similar comparison can be done for the spin-spin correlation function at the ordering wavevector, which we used to produce a QMC phase diagram at the beginning of this section. The mean-field solution is based on the singlet-triplet formulation, meaning it is necessary to convert between the bosonic operators a, b and spins S^x, S^y, S^z to obtain expressions for spin correlations in terms of mean-field averages:

$$\langle S^x_i S^x_j \rangle = -\sin^2 2\theta (1-n)^2 e^{i\mathbf{Q}\cdot\mathbf{R}_i} e^{i\mathbf{Q}\cdot\mathbf{R}_j} + \sin^2 2\theta (1-n) e^{i\mathbf{Q}\cdot\mathbf{R}_i} e^{i\mathbf{Q}\cdot\mathbf{R}_j} (\langle a^\dagger_i a_i \rangle + \langle a^\dagger_j a_j \rangle) +$$

$$
\begin{aligned}
&+\cos^2 2\theta(1-n)(\langle a_i^\dagger a_j\rangle + \langle a_i a_j^\dagger\rangle - \langle a_i a_j\rangle - \langle a_i^\dagger a_j^\dagger\rangle),\\
\langle S_i^y S_j^y\rangle =& \cos^2\theta(1-n)e^{i\mathbf{Q}\cdot\mathbf{R}_i}e^{i\mathbf{Q}\cdot\mathbf{R}_j}(\langle b_i^\dagger b_j\rangle + \langle b_i b_j^\dagger\rangle - \langle b_i b_j\rangle - \langle b_i^\dagger b_j^\dagger\rangle)\\
\langle S_i^z S_j^z\rangle =& -\sin^2\theta(1-n)e^{i\mathbf{Q}\cdot\mathbf{R}_i}e^{i\mathbf{Q}\cdot\mathbf{R}_j}(\langle b_i^\dagger b_j\rangle + \langle b_i b_j^\dagger\rangle + \langle b_i b_j\rangle + \langle b_i^\dagger b_j^\dagger\rangle).
\end{aligned}
\tag{3.91}
$$

Focusing on the Fourier component of the spin correlations at the ordering wavevector $\mathbf{Q}$, we find that the *yy*- and *zz*- components (perpendicular to the magnetic moment direction) are constant with respect to lattice size, whereas the *xx*-component scales linearly with the number of sites N. In other words:

$$
\begin{aligned}
N^{-1}\langle S^x_{-\mathbf{Q}} S^x_{\mathbf{Q}}\rangle &= -\sin^2 2\theta(1-n)^2 + 2\sin^2 2\theta(1-n)n_a + \mathcal{O}(N^{-1}),\\
N^{-1}\langle S^y_{-\mathbf{Q}} S^y_{\mathbf{Q}}\rangle &= \mathcal{O}(N^{-1}),\\
N^{-1}\langle S^z_{-\mathbf{Q}} S^z_{\mathbf{Q}}\rangle &= \mathcal{O}(N^{-1}).
\end{aligned}
\tag{3.92}
$$

The top right panel (b) of Fig. 3.6 shows the components of spin-spin correlations relative to the QCP position, similarly as was done for n_T. Again, we get a reasonably good qualitative agreement between the harmonic and QMC values, while the mean-field corrections lead to an even better match. We may conclude that when only J, E_T interaction terms are considered, the harmonic approximation provides qualitatively accurate results, as long as the parameters J/E_T are properly scaled with respect to the QCP position.

However, this positive picture slightly changes with the inclusion of Δ'. We decided to include $\Delta' = 4.0$ meV following the experimental values for Ca_2RuO_4 as in the preceding section, varying E_T to cover the plotted J/E_T range. Panels (c),(d) of Fig. 3.6 show that, in this case, the mean-field curves contain an unphysical step between relative J/E_T 1.0 and 1.3, which is not seen in either the numerical data nor the harmonic solution. In this interval, the numerical optimization step used to solve the self-consistent equations failed to converge at a physical solution and got stuck in a different mode.

To investigate this problem, we inspected the excitation modes for a, b bosons. We recollect that for $\Delta' = 0$, the b-mode corresponding to a magnon touches zero at $\mathbf{Q}$ upon condensation and stays gapless throughout the condensed phase, whereas the a amplitude mode goes up in energy as the condensate develops. This situation can be seen in Fig. 3.7 panel (a), which shows harmonic modes in the ordered phase close to the transition. The inclusion of positive Δ' leads to a crucial difference, which is the creation of a gap in the spectrum of the b magnon – see panel (b). This gap, whose relation to Δ' is captured by (3.46), if large enough, leads to mode reversal at $\mathbf{Q}$. This means, that at some point in the J/E_T parameter range that falls in the condensate region, the a and b modes cross – while at large J/E_T, the amplitude mode is higher in energy, near the transition, it falls below the b magnon's dispersion; this situation is shown in Fig. 3.7 panel (c). We think that such a mode reversal may be the reason for the numerical problems happening near the transition. If we inspect the evolution of the mean-field amplitude mode starting deep in the condensed phase and moving towards QCP, we observe that the amplitude mode softens until we hit relative $J/E_T \approx 1.3$, where the numerical problems begin. Since that point, the mean-field amplitude mode stays fixed, until we reach the transition where it lies below the magnon. The mode crossing is therefore not smoothly captured by the mean-field solution. Additionally, we calculated the triplon occupation n_T and spin-spin correlations for a lower value of $\Delta' = 1.0$, for which a modest gap in b mode develops but without a mode crossing

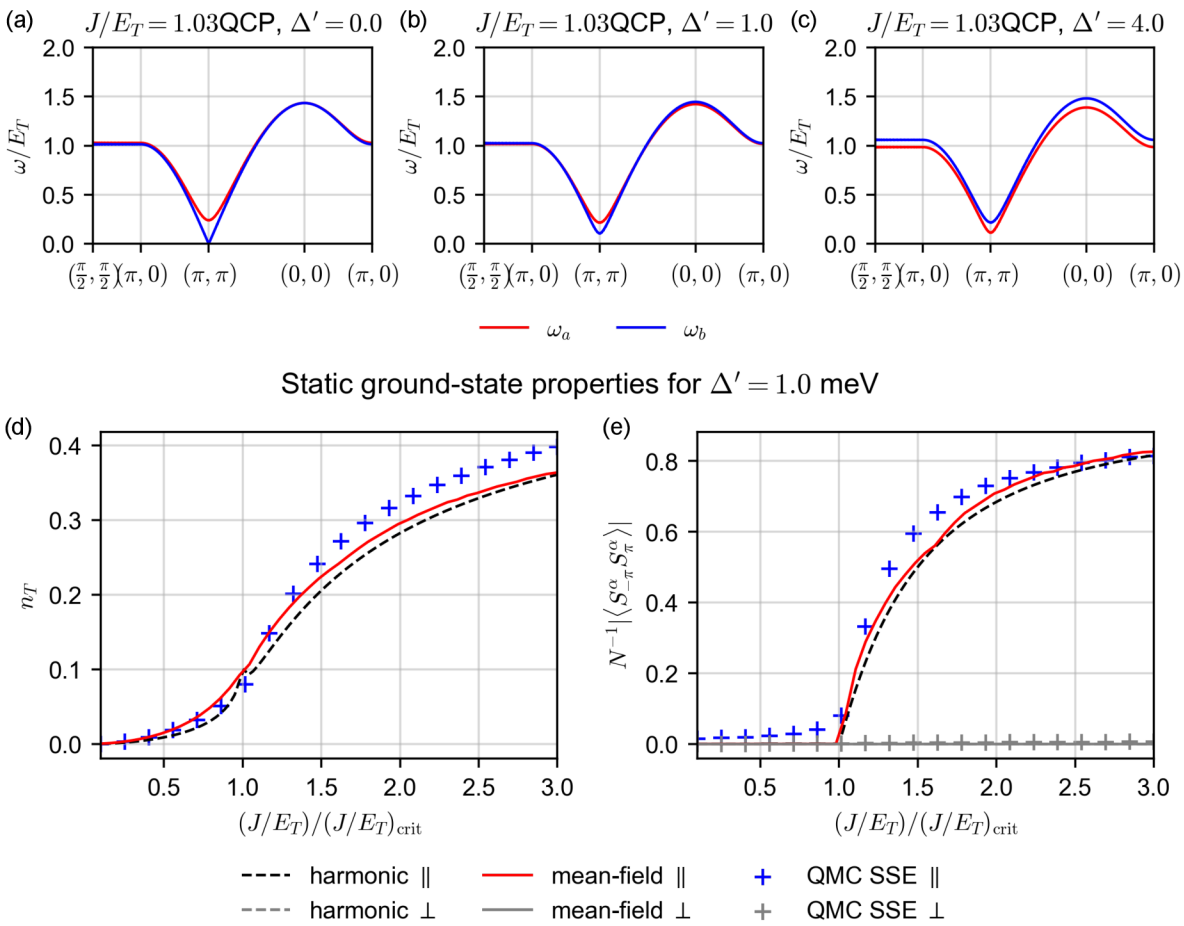

Figure 3.7: (a)-(c) Harmonic dispersions of bosonic a, b modes in the condensed phase near the transition. The panels demonstrate that the inclusion of Δ' causes a gap in the b mode that, for sufficiently large Δ', leads to a mode reversal at $\mathbf{Q} = (\pi, \pi)$. (d) Triplon occupation and (e) spin-spin correlation functions at the ordering wavevector $\mathbf{Q}$ scaled by the number of lattice sites N. The displayed quantities are the same as in panels (c) and (d) of the preceding Figure 3.6, but for a lower value of $\Delta' = 1.0$ meV. In contrast to the $\Delta' = 4.0$ meV case, numerical artifacts within the mean-field solution near the transition do not occur.

– see Fig. 3.7 (d), (e). Consistently with expectations, the numerical artifacts in the mean-field solution do not arise in this case.

The general conclusion that we draw from the above comparisons is, that the mean-field inclusion of hard-core boson effects leads to a very good agreement with QMC results, both in the position of the quantum critical point and in the evolution of static quantities describing the condensate. The QCP shift seems to be the most important effect captured by the mean-field corrections – when this is accounted for by an appropriate scaling, even the harmonic approximation gives a good quantitative description of the triplon condensate. Care must be taken, however, when a gap is created by including the orthorhombic Δ' term, which can lead to instabilities in the mean-field procedure in the condensed phase close to the transition. Next, we look at the comparison of the dynamical correlations.

Dynamical susceptibility and magnetic excitations in Ca_2RuO_4

The nature of a magnetic ground state is typically fingerprinted in great detail in the dynamical magnetic susceptibility, reflecting the excitations on top of the ground state. As we have already mentioned in section 3.2.1, a quantum Monte Carlo procedure called Stochastic series expansion can be used to calculate the dynamical susceptibility as well. The estimator is, however, formulated in imaginary Matsubara frequencies $i\omega_n$, because the procedure works as an expansion in imaginary time. An extra step of analytic continuation is thus needed to transform the imaginary Matsubara frequencies into real frequency data.

The main advantage of quantum Monte Carlo techniques in these kinds of calculations is an approximately linear scaling of the required computer resources with cluster size. In our calculations, we used a 20×20 site square lattice cluster with periodic boundary conditions. To access the ground state, a sufficiently high value of inverse temperature β must be chosen to overcome the finite size gap. We found that the value $\beta = 6$ meV^{-1} which corresponds to $T \doteq 2$ K works well for the 20×20 cluster. For the analytical continuation step, we used a procedure [195] based on the maximum entropy approach [191]. In order to resolve the main spectral features, one needs to consider a sufficient number n of Matsubara frequencies $i\omega_n = i2\pi n/\beta$. It can be technically demanding to obtain high-quality imaginary data for high n with good statistics, therefore a reasonable cutoff is chosen – in our case, we stopped at $n = 100$.

Before we comment on the calculated susceptibilities, we first discuss the connection to harmonic and mean-field dispersions discussed in previous sections. To properly interpret the spin susceptibility, a conversion must be made to elementary excitations carried by a and b bosons. We can do so in a simplified way, by transforming the components of magnetic moment, proportional to spin components, to the a and b bosons using equations (3.1) and (3.28). Keeping only terms up to quadratic order, we get:

$$\begin{aligned} S^x &\approx e^{i\mathbf{Q}\cdot\mathbf{R}} \sin 2\theta - i\cos 2\theta (a - a^\dagger), \\ S^y &\approx -i\cos\theta (b - b^\dagger), \\ S^z &\approx -e^{i\mathbf{Q}\cdot\mathbf{R}} \sin\theta (b + b^\dagger), \end{aligned} \tag{3.93}$$

revealing the connection between a, b bosonic excitations and components of spin susceptibility. We see that the excitations carried by the a mode are included in the diagonal x component of the spin susceptibility. This is a longitudinal mode since, according to our choice of the reference frame, the magnetic mode lies in the x direction. The yy and zz susceptibility components corresponding to transverse oscillations of the magnetic moments are linked to the b magnon. The chief qualitative difference between S^y and S^z lies in an extra $e^{i\mathbf{Q}\cdot\mathbf{R}}$ factor, which mathematically translates to a mere shift in momentum space by $\mathbf{Q} = (\pi, \pi)$. Other than this shift, the main features of the transverse magnetic modes are identical.

Figure 3.8 shows dynamical spin susceptibility calculated using the QMC SSE method. For brevity, only xx and yy components of the susceptibility are shown. The observed evolution of longitudinal xx and transverse yy, zz modes through the J/E_T parameter range is consistent with our description of harmonic modes given in Sec. 3.1. In the triplon gas phase, the longitudinal and transverse modes are approximately degenerate (degeneracy is lifted in the presence of Δ') and soften towards the quantum critical point – see panels (a),(d). Beyond the transition, the longitudinal mode goes up in energy, while the transverse magnetic modes evolve only very slightly – the gap size is chiefly determined by Δ', cf. panels (b)-(c), (e)-(f).

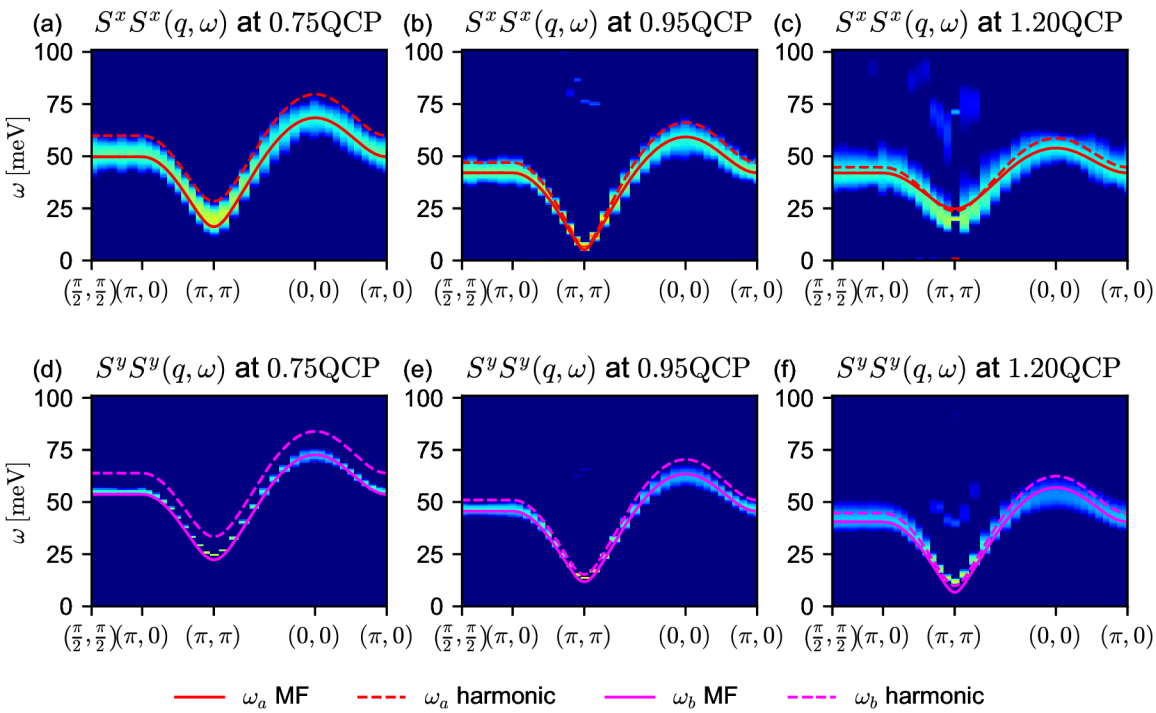

Figure 3.8: Dynamical spin susceptibility calculated numerically by QMC SSE method including J, E_T and Δ' Hamiltonian terms. The panels show an evolution through the parameter range J/E_T from (a),(d) the triplon gas phase, through (b),(e) a point close to the transition, to (c),(f) the well-developed condensate. The top row (a)-(c) contains the diagonal *xx*-component of the spin susceptibility, and the bottom row (d)-(f) shows the *yy* component. Additionally, each panel contains red or pink curves corresponding to harmonic (dashed lines) and mean-field (full lines) dispersions of the amplitude a mode and the b magnon. The comparison is made for parameter points relative to the QCP position calculated by each respective method. The *x*-component of spin susceptibility is connected to the amplitude a mode and the *y* susceptibility component to the b mode, as described in the text. The QMC calculation was performed for $J = 5.8$ meV, $\Delta' = 4.0$ meV and E_T varied from 48 meV in (a),(d) to 30 meV in (c),(f).

Since we made an explicit connection between bosonic excitations and spin susceptibility components, we may also compare the approximate analytic dispersions obtained by the harmonic approximation and the mean-field method. Same as in the previous section, we perform the comparison for parameter values J/E_T relative to QCP positions determined by each respective method (0.125 for the harmonic approximation, 0.164 for QMC and 0.162 for mean-field). This is intended to correct the large QCP position error of the harmonic solution. What we observe is similar to the comparison of static quantities in the previous section: after the QCP position correction, both analytic methods represent the mode dispersions qualitatively correctly. Notably, we find that in the simple triplon gas phase (panels (a),(d)), the mean-field dispersions fit the QMC spectra almost perfectly. In the condensate, we encounter the same mode-crossing issue we described in the previous section, i.e. the longitudinal *xx* mode falls below the transverse *yy* mode in energy close to the transition, which brings about numerical difficulties in the self-consistent solution of the mean-field Hamiltonian. Outside this problematic region, deeper into the condensate, the main inconsistency between the analytical and QMC dispersions is the overestimation of longitudinal mode gap size.

Let us comment on how the simplified theoretical picture described above fits the experimental studies of Ca_2RuO_4. The dynamical spin susceptibility is directly proportional to the intensities of channels in polarized inelastic neutron scattering (INS) experiments, opening the door for direct theory-experiment comparison. Experimental studies [18] have found that INS spectra of Ca_2RuO_4 can be successfully fitted using the considered spin model with the parameter values $J = 5.8$ meV, $E_T = 25$ meV, $\Delta' = 4$ meV, $J_z = 0.85J$ and $A = 2.3$ meV. The panel (c) of Fig. 3.8 contains calculated spectra for parameters close to the experimental situation in [18]. The overall shapes of the spectra are well-reproduced by our calculations: the maxima are at $(0,0)$, minima at ordering wavevector (π,π), the S^zS^z-response is the same as S^yS^y apart from a (π,π)-shift, and also the size of the gap in the transverse response fits quite well. The comparison is worse when we focus on the longitudinal response. Experimentally, the INS longitudinal response is hard to resolve near $\mathbf{Q} = (\pi,\pi)$ due to a strong decay of the mode stemming from the interaction with a two-magnon continuum. The high-energy continuum of composite excitations is not well developed in the QMC spectra. This might be caused by too large QMC errorbars for high Matsubara frequencies, leading to a failure of the analytical continuation procedure.

Conclusion

In this thesis, we presented a theoretical study of magnetism in spin-orbit entangled transition metal oxides, which may possess unconventional magnetic properties. A common feature of these materials is the presence of strong spin-orbit coupling, which plays a prominent role especially in the heavier transition metal oxides. One class of such systems are those that feature frustration due to bond-selective interactions, possibly leading to exotic magnetic states such as a spin liquid. Another example is the physics of soft spin systems, where the spins undergo amplitude fluctuations as a consequence of the quasi-degeneracy of nonmagnetic $J = 0$ and triplet $J = 1$ energy levels.

In the first chapter, we described how the combination of spin-orbit coupling, lattice symmetry, and inter-ionic hopping gives rise to an effective spin model. The spin-orbit coupling plays a crucial role here: it entangles the spin and orbital degrees of freedom, imprinting the spatial symmetry of orbitals into the local pseudospin degrees of freedom. This may give rise to the anisotropy of interactions such as the bond-selective Kitaev interaction. The latter part of the chapter presented an experimental overview of some prototype materials that host the physics discussed later in the thesis: Na_2IrO_3 and Ca_2RuO_4. Sodium iridate Na_2IrO_3 is one of the most studied candidate Kitaev materials. Even though the magnetic state is the long-range ordered zigzag state and not the Kitaev spin liquid, the interpretation of x-ray scattering studies clearly shows a strong influence of Kitaev interaction on the direction of magnetic moment and spectrum of magnetic excitations. Calcium ruthenate Ca_2RuO_4 has been shown to host excitonic Van Vleck magnetism. The most solid evidence of it is given by the spectra of magnetic excitations measured by inelastic neutron scattering (INS) methods. Moreover, Raman scattering experiments uncover the Higgs mode, which is otherwise difficult to resolve in INS due to the interaction with a two-magnon continuum.

The second chapter was devoted to the study of the extended Kitaev-Heisenberg (EKH) model, which is the effective spin model originally devised to characterize the magnetism of honeycomb compounds Na_2IrO_3 and α-Li_2IrO_3, but since then has been found relevant to a large number of different materials and lattices. The goal of the study was to provide a global analysis of the phase diagram throughout its parameter space. To understand the trends present in the phase diagram, we employed a combined analysis of the model's symmetries and numerically obtained magnetic phases. Numerical ground states obtained by exact diagonalization were analyzed by the spin-$\frac{1}{2}$ coherent states method, which enabled us to extract the direction of ordered magnetic moment, creating an important link of theory to an experimentally accessible quantity. We extended the spin-$\frac{1}{2}$ coherent states method to non-collinear spin orderings and provided efficient numerical implementations. We highlight two original results of our analysis of the phase diagram: i) we found fluctuation-free ground states as parts of the FM and AF phases, present along a phase-space continuum. These states emerge due to a surprising cancel-

lation of interaction terms for the particular spin patterns. ii) The EKH model includes, e.g., the Heisenberg and Kitaev models as subparts of its parameter space. However, we found another type of models connected to the parts of EKH phase space: this type of models characterized by a single interaction axis includes the Ising model, Kitaev model, and also the so-called compass model. Since the mechanism of how EKH interaction arises in real materials is well understood [39], such a mapping could create a different avenue to find experimental realizations of the single-interaction models. We believe that the presented symmetry-aided numerical study can also serve as a methodological template for future works, applied to other spin models containing bond-dependent spin interactions as a result of strong spin-orbit coupling.

The third and final chapter addressed the singlet-triplet bosonic model describing Van Vleck magnetism in d^4 transition metal oxides with t_{2g}^4 valence configuration such as Ca_2RuO_4. Same as before, the main emphasis was put on the solution of the effective model. Starting with a simple variational method, we showed how the bosonic excitations (triplons) between nonmagnetic $J = 0$ ground state levels and magnetic $J = 1$ excited levels can condense and create a long-range ordered magnetic state. We provided harmonic spectra of spin excitations, highlighting the main differences with standard Heisenberg magnets: the existence of Higgs mode as a manifestation of "soft" spins. To go beyond the harmonic approximation, we first employed a numerical Quantum Monte Carlo (QMC) method called Stochastic Series Expansion (SSE), which allowed us to obtain the phase diagram based on static physical quantities, as well as dynamical magnetic susceptibility. The QMC method allows the use of large clusters, thanks to which we were able to obtain a better estimate of critical ratio $(J/E_T)_{\text{crit}}$ where bosonic condensation occurs, i.e. the position of the quantum critical point (QCP). Further, we extracted the QMC value of Neél temperature $T_N = 106$ K, which agrees very well with the experimental value 110 K. To understand the role of the hard-core nature of bosons in the model, we employed a mean-field (MF) analytical method, which includes the two main consequences of the hard-core nature: increase of local triplon energy cost and interaction screening due to triplon hopping being blocked by the presence of another boson. Interestingly, we found that incorporating the above two effects is enough to account for the large shift in the QCP position between the harmonic value and the QMC value. The quantitative agreement between QMC and MF spectra is also remarkably good. The main conclusion is that the shift in QCP position is the biggest qualitative change induced by the hard-core bosonic nature; we demonstrate this by comparing bosonic occupation and spin-spin correlation functions plotted with respect to the relative distance from the QCP, obtaining good agreement between the harmonic approximation, mean-field method, and QMC. Thus, by accounting for the inaccuracy of the harmonic QCP position value, it is possible to obtain a quantitatively correct phase diagram and dispersions of magnetic excitations even on the harmonic level. The presented mean-field approach could be employed in other lattice systems featuring hard-core bosons as a relatively simple method of obtaining dispersions of spin excitation modes. Since the approximation involves an expansion in the number of bosons, it is likely to work even better for models with a larger number of bosons than the two in our case.

Appendix A

Derivation of the Kitaev-Heisenberg model

The following derivation of the effective Kitaev-Heisenberg model follows [21] including the labeling conventions. The starting point of the calculation are t_{2g} orbitals in the convention by Tanabe and Sugano [19]:

$$\begin{aligned} |\xi\rangle &= \frac{i}{\sqrt{2}}(|d_{+1}\rangle + |d_{-1}\rangle), \\ |\eta\rangle &= -\frac{1}{\sqrt{2}}(|d_{+1}\rangle - |d_{-1}\rangle), \\ |\zeta\rangle &= -\frac{i}{\sqrt{2}}(|d_{+2}\rangle - |d_{-2}\rangle). \end{aligned} \tag{A.1}$$

The t_{2g}^5 configuration is conveniently handled in a hole picture, where it is represented by a single hole in the t_{2g} subspace. The hole operators $a^\dagger, b^\dagger, c^\dagger$ create such a single hole with orbital momentum $L_z^{\text{eff}} = +1, 0, -1$. Choosing z as the quantization axis, the definition of a, b, c operators in terms of Tanabe-Sugano ξ, η, ζ operators which remove electrons from corresponding orbitals is:

$$\begin{aligned} a_\sigma^\dagger &= (+\sigma)(i\eta_{-\sigma} + \xi_{-\sigma})/\sqrt{2}, \\ b_\sigma^\dagger &= (-\sigma)\zeta_{-\sigma}, \\ c_\sigma^\dagger &= (+\sigma)(i\eta_{-\sigma} - \xi_{-\sigma})/\sqrt{2}. \end{aligned} \tag{A.2}$$

As was elaborated in Sec. 1.1.2, the t_{2g}^5 multiplet structure resulting from effects of crystal field, local Coulomb interactions and spin-orbit coupling is formed by a $J = \frac{1}{2}$ Kramers doublet and a $J = \frac{3}{2}$ quintuplet. The low-energy doublet carrying $J = \frac{1}{2}$ moment can therefore play a role of pseudospin-$\frac{1}{2}$ basis:

$$|\tilde{\uparrow}\rangle = \left(\sqrt{\tfrac{2}{3}}\, a_\downarrow^\dagger - \sqrt{\tfrac{1}{3}}\, b_\uparrow^\dagger\right), \qquad |\tilde{\downarrow}\rangle = \left(\sqrt{\tfrac{1}{3}}\, b_\downarrow^\dagger - \sqrt{\tfrac{2}{3}}\, c_\uparrow^\dagger\right). \tag{A.3}$$

The orbitals are superimposed in the pseudospin states, which has consequences for the electronic hopping between neighboring ions. More specifically, let us consider the situation displayed in Fig. A.1(a) and single-out a square plaquette containing two metallic and two ligand atoms, forming two 90° *d-p-d* bonds. This can be done in three different directions corresponding to three bond types; we opt for the plaquette perpendicular to the cubic z axis. On such a plaquette, two t_{2g} orbitals are active in p-mediated hopping, namely $\xi \sim yz$ and $\eta \sim zx$, while

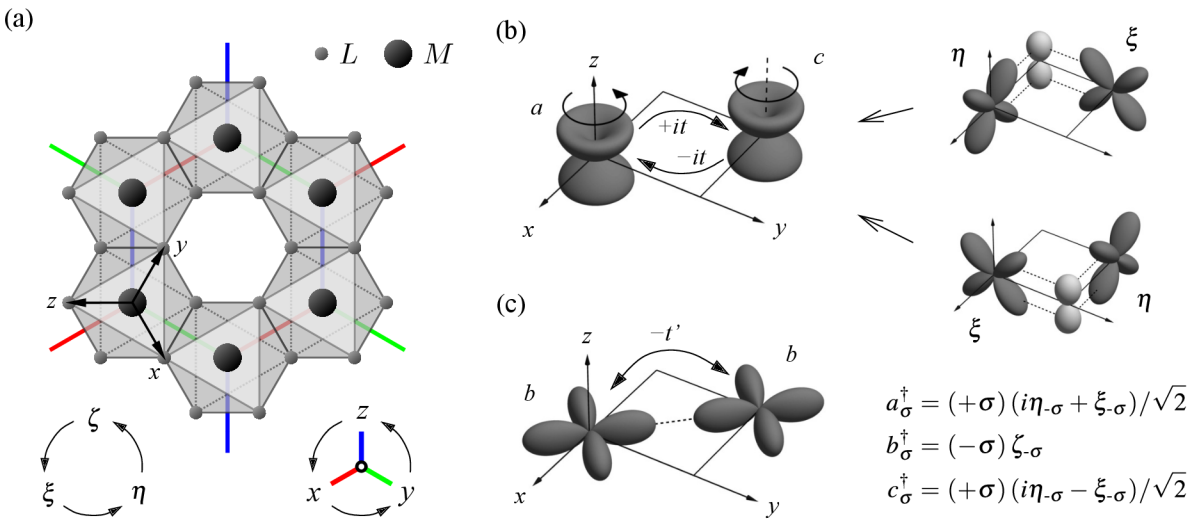

Figure A.1: (a) Atomic structure of a layered honeycomb transition metal oxide, such as α-$RuCl_3$ or Na_2IrO_3. Magnetic atoms M form a two-dimensional honeycomb net with each atom M surrounded by an octahedral cage out of ligand atoms L (typically oxygen). The C_3 symmetry is manifested by tying together bond directions specified by cubic axes x,y,z to the orbitals ξ,η,ζ active in the hopping processes – permutation among x,y,z is accompanied by a concurrent permutation among ξ,η,ζ. (b) The edge-sharing octahedra form a 90° *M-L-M* bonding geometry. The picture shows an elementary hopping process on a square perpendicular to the z axis, where two possible hopping routes between ξ and η orbitals merge into a single imaginary hopping between a and c orbitals with opposite L_z^{eff}. (c) Direct hopping between b orbitals is significant due to the large spatial extent of the orbitals and their compatible orientation. The hopping processes for the other two bond directions can be obtained by permuting ξ,η,ζ in the definition of a,b,c orbitals. Figure partially adopted from Ref. [21].

ζ is disconnected by symmetry. One can observe this is the case by considering the possible arrangements of *d-p-d* orbitals on the square and eliminating the cases where orbital overlaps amount to zero. Fig. A.1(b) shows the two active bonding routes, expressed mathematically as

$$\mathcal{H}_t = t\sum_\sigma (\xi^\dagger_{i\sigma}\eta_{j\sigma} + \eta^\dagger_{i\sigma}\xi_{j\sigma}) + \text{h.c.}, \tag{A.4}$$

where $t = t^2_{pd\pi}/\Delta_{pd}$. Moreover, because of the considerable spatial extent of d orbitals, sizeable direct overlaps among compatible orbitals contribute to the bonding. The strongest among direct bonding geometries is the $dd\sigma$ bonding [27], which in this case connects two $b \sim xy$ orbitals, see Fig. A.1(c). The corresponding hopping Hamiltonian is very simple:

$$\mathcal{H}_{t'} = -t'\sum_\sigma \zeta^\dagger_{i\sigma}\zeta_{j\sigma} + \text{h.c.}, \tag{A.5}$$

with $t' = (3t_{dd\sigma} + t_{dd\delta})/4$. For convenience, we may switch to the hole operators a,b,c using (A.2), obtaining for the combined hopping $\mathcal{H}_{tt'} = \mathcal{H}_t + \mathcal{H}_{t'}$:

$$\mathcal{H}_{tt'} = \sum_\sigma \left[-it(a^\dagger_{i\sigma}c_{j\sigma} - c^\dagger_{i\sigma}a_{j\sigma}) + t' b^\dagger_{i\sigma}b_{j\sigma}\right] + \text{h.c.} \tag{A.6}$$

The two *d-p-d* hopping routes are thus represented by a single imaginary hopping between hole orbitals a,c with opposite L_z^{eff} (see panel (b) of Fig. A.1). Another advantage of this form of

hopping is that it can be used universally for all three bond types, provided one performs a cyclic permutation of ξ,η,ζ orbitals in the definition of hole operators a,b,c (A.2) together with the change of the $\mathbf{L}$ quantization axis.

We treat the hopping $\mathcal{H}_{tt'}$ as a perturbation acting on the bond represented by two neighboring $J=\frac{1}{2}$ pseudospin moments. The perturbation generates a d^4-d^6 excited state which is left by the second application of the hopping, restoring the low-energy configuration. As usual, the energy of the second-order process is obtained by the product of two hopping matrix elements divided by the negatively taken excitation energy, as we outlined in Sec. 1.1.3. Let us first consider the oxygen-mediated hopping $\mathcal{H}_t$ in the direction $j\to i$: the excited state reads

$$\mathcal{H}_t^{j\to i}\left(|\tilde{\uparrow}\rangle_i\otimes|\tilde{\uparrow}\rangle_j\right)=\frac{2}{3}it\left(-c_{i\downarrow}^\dagger a_{i\downarrow}^\dagger+\frac{\sqrt{2}}{2}c_{i\downarrow}^\dagger b_{i\uparrow}^\dagger\right)\left|t^6\right\rangle_i\otimes\left|t^6\right\rangle_j. \tag{A.7}$$

Using Clebsch-Gordan coefficients, we decompose the state with two holes at site i into angular momentum eigenstates $|j_1,j_2;J,J_z\rangle$, obtaining

$$\mathcal{H}_t^{j\to i}\left(|\tilde{\uparrow}\rangle_i\otimes|\tilde{\uparrow}\rangle_j\right)=\frac{it}{\sqrt{2}}\left(\left|\frac{3}{2},\frac{1}{2};1,-1\right\rangle_i-\frac{1}{\sqrt{3}}\left|\frac{3}{2},\frac{1}{2},2,-1\right\rangle_i\right)\otimes\left|t^6\right\rangle_j. \tag{A.8}$$

In a similar way, we may obtain expressions for the intermediate states generated from the other three pairs of pseudospins $\tilde{\uparrow}\tilde{\downarrow},\tilde{\downarrow}\tilde{\uparrow},\tilde{\downarrow}\tilde{\downarrow}$:

$$\begin{aligned}
\mathcal{H}_t^{j\to i}\left(|\tilde{\downarrow}\rangle_i\otimes|\tilde{\downarrow}\rangle_j\right)&=-\frac{it}{\sqrt{2}}\left(\left|\frac{3}{2},\frac{1}{2};1,+1\right\rangle_i+\frac{1}{\sqrt{3}}\left|\frac{3}{2},\frac{1}{2},2,+1\right\rangle_i\right)\otimes\left|t^6\right\rangle_j,\\
\mathcal{H}_t^{j\to i}\left(|\tilde{\uparrow}\rangle_i\otimes|\tilde{\downarrow}\rangle_j\right)&=-it\sqrt{\frac{2}{3}}\left|\frac{3}{2},\frac{1}{2};2,+2\right\rangle_i\otimes\left|t^6\right\rangle_j,\\
\mathcal{H}_t^{j\to i}\left(|\tilde{\downarrow}\rangle_i\otimes|\tilde{\uparrow}\rangle_j\right)&=-it\sqrt{\frac{2}{3}}\left|\frac{3}{2},\frac{1}{2};2,-2\right\rangle_i\otimes\left|t^6\right\rangle_j.
\end{aligned} \tag{A.9}$$

The equations above reveal an important finding: the intermediate states generated by t-hopping are completely disconnected, such that the application of second hopping merely restores the original pseudospin pair. Such a second order process can be described effectively by an Ising term $S_i^zS_j^z$, valid for the z-bond in consideration. By symmetry, the term valid for the x-bond is $S_i^xS_j^x$ and $S_i^yS_j^y$ for the y-bond, which is exactly the Kitaev interaction. The remarkable phenomenon here is a complete absence of an isotropic contribution of Heisenberg-type $\mathbf{S}_i\cdot\mathbf{S}_j$ to the effective interaction. The isotropic contribution vanishes because of the destructive interference of two bonding paths shown in Fig. A.1(b), similar to the situation of e_g orbital exchange in the 90° geometry, where e_g orbitals cannot form d-p-d bonding [2]. We may gain more insight by noting that the t-hopping term $\mathcal{H}_t$ (A.4) does not conserve L_z, but rather changes it by ±2, since it interchanges orbitals $a\leftrightarrow c$. However, the maximum momentum transfer between pseudospin-$\frac{1}{2}$ states is $|\Delta J_z|=1$, therefore the hopping $\mathcal{H}_t$ cannot connect them. Since the conventional superexchange pathway leading to an antiferromagnetic $4t^2/U$ interaction term is blocked, the Kitaev interaction arises due to a higher order process: Hund's coupling between holes in the excited $J=\frac{3}{2}$ virtual states. Because first Hund's rule favors aligned spins, the resulting coupling is ferromagnetic and of order $\propto t^2J_H/U^2$, i.e. weaker by a factor J_H/U.

The situation changes significantly when considering the direct hopping between b-orbitals contained in $\mathcal{H}_{t'}$. The hopping Hamiltonian (A.5) conserves spin as well as orbital momentum and consequently must lead to an isotropic effective interaction between pseudospins. The intermediate states generated by the t'-hopping are:

$$\begin{aligned}
\mathcal{H}_{t'}^{j\to i}\left(|\tilde{\uparrow}\rangle_i \otimes |\tilde{\uparrow}\rangle_j\right) &= \frac{t'}{\sqrt{2}}\left(-\frac{1}{3}\left|\frac{3}{2},\frac{1}{2};1,+1\right\rangle_i + \frac{1}{\sqrt{3}}\left|\frac{3}{2},\frac{1}{2},2,+1\right\rangle_i\right)\otimes\left|t^6\right\rangle_j,\\
\mathcal{H}_{t'}^{j\to i}\left(|\tilde{\downarrow}\rangle_i \otimes |\tilde{\downarrow}\rangle_j\right) &= -\frac{t'}{\sqrt{2}}\left(\frac{1}{3}\left|\frac{3}{2},\frac{1}{2};1,-1\right\rangle_i + \frac{1}{\sqrt{3}}\left|\frac{3}{2},\frac{1}{2},2,-1\right\rangle_i\right)\otimes\left|t^6\right\rangle_j,\\
\mathcal{H}_{t'}^{j\to i}\left(|\tilde{\uparrow}\rangle_i \otimes |\tilde{\downarrow}\rangle_j\right) &= \frac{t'}{3}\left(\left|\frac{3}{2},\frac{1}{2};1,0\right\rangle_i + \left|\frac{1}{2},\frac{1}{2},0,0\right\rangle_i - \left|\frac{3}{2},\frac{1}{2},2,0\right\rangle_i\right)\otimes\left|t^6\right\rangle_j,\\
\mathcal{H}_{t'}^{j\to i}\left(|\tilde{\downarrow}\rangle_i \otimes |\tilde{\uparrow}\rangle_j\right) &= \frac{t'}{3}\left(\left|\frac{3}{2},\frac{1}{2};1,0\right\rangle_i - \left|\frac{1}{2},\frac{1}{2},0,0\right\rangle_i + \left|\frac{3}{2},\frac{1}{2},2,0\right\rangle_i\right)\otimes\left|t^6\right\rangle_j.
\end{aligned} \tag{A.10}$$

The connection between $\uparrow\downarrow$ and $\downarrow\uparrow$ configurations is clearly visible, leading to $S^+S^- + S^-S^+$ terms in the effective Hamiltonian. Additionally, $\uparrow\uparrow$ and $\downarrow\downarrow$ pseudospin states are connected when considering both t- and t'-hopping at once.

To obtain the resulting effective Hamiltonian, we ought to calculate the energies of excited states, which amounts to the diagonalization of Hund's exchange in the j-j coupling scheme. The detailed calculation can be found in Ref. [21], we merely state the result:

$$\mathcal{H}_{ij}^z = J\mathbf{S}_i\cdot\mathbf{S}_j + KS_i^zS_j^z + \Gamma(S_i^xS_j^y + S_i^yS_j^x), \tag{A.11}$$

where S^α are pseudospin-$\frac{1}{2}$ operators. The expressions for x- and y-bonds can be obtained by cyclic permutation in the x,y,z components of pseudospin operators. The interaction parameters J,K,Γ are functions of microscopic quantities t,t',U,J_H:

$$\begin{aligned}
J &= \frac{4}{9}\frac{t'^2}{U-3J_H}\left[1-\frac{5}{3}\frac{J_H}{U+2J_H}-\frac{4}{3}\frac{J_H}{U-J_H}\right],\\
K &= \frac{8}{9}J_H\left[\frac{t'^2-3t^2}{(U-3J_H)(U-J_H)}\right],\\
\Gamma &= \frac{16}{9}J_H\left[\frac{tt'}{(U-3J_H)(U-J_H)}\right].
\end{aligned} \tag{A.12}$$

The SOC strength λ does not enter the expressions, because the derivation was performed in the limit $U,J_H \gg \lambda \gg t,t'$, and therefore only Hund's coupling in virtual states was considered. The strong coupling expansion can be considered also in the limit $U,\lambda \gg J_H \gg t,t'$, yielding similar expressions to (A.12) but with λ involved in the energies of the excited states instead of J_H [51, 52]. The only conventional AF exchange term $\propto t'^2/U$ occurs in J coupling, originating from direct hopping between b orbitals. All other exchange contributions come from the mixing with higher energy $J=\frac{3}{2}$ states.

Appendix B

The method of spin-$\frac{1}{2}$ coherent states

Calculation of the weight $P(\theta,\phi)$ in a degenerate ground state

As we have discussed before in Section 2.1.2, the EKH model possesses hidden symmetries; among other factors, these can lead to a degeneracy of the ground state even for a finite cluster (one example would be the Ising point discussed in 2.1.3 with a doubly degenerate ground state). To be able to tackle such cases with the method of spin-$\frac{1}{2}$ coherent states, we must make some adjustments to the calculation of $P(\theta,\phi)$.

Assume the degree of degeneracy D and the ground state vectors $|\mathrm{GS}_i\rangle$ that have been orthonormalized by a Gramm-Schmidt process:

$$|\mathrm{GS}\rangle = \sum_{j=1}^{D} d_j \left|\mathrm{GS}_j\right\rangle, \quad \sum_{j=1}^{D} \left|d_j\right|^2 = 1. \tag{B.1}$$

The overlap of the ground state with the (θ,ϕ)-polarized cluster state $|\Psi\rangle_{\theta\phi}$ is

$$\left\langle \Psi_{\theta\phi} \middle| \mathrm{GS} \right\rangle = \sum_{j=1}^{D} d_j \left\langle \Psi_{\theta\phi} \middle| \mathrm{GS}_j \right\rangle \tag{B.2}$$

and the absolute square of the overlap reads

$$\left|\left\langle \Psi_{\theta\phi} \middle| \mathrm{GS} \right\rangle\right|^2 = \sum_{j=1}^{D}\sum_{k=1}^{D} d_j^* d_k \left\langle \mathrm{GS}_j \middle| \Psi_{\theta\phi} \right\rangle \left\langle \Psi_{\theta\phi} \middle| \mathrm{GS}_k \right\rangle = \mathbf{d}^\dagger \hat{O} \mathbf{d}, \tag{B.3}$$

where $\hat{O}$ with elements $O_{jk} = \left\langle \mathrm{GS}_j \middle| \Psi_{\theta\phi} \right\rangle \left\langle \Psi_{\theta\phi} \middle| \mathrm{GS}_k \right\rangle$ is the overlap matrix of shape $D \times D$. We can immediately see that this matrix is hermitian and hence has an eigendecomposition

$$\hat{O} = \sum_{j=1}^{D} \lambda_j \mathbf{u}_j \mathbf{u}_j^\dagger, \tag{B.4}$$

where λ_j are the (real) eigenvalues and $\mathbf{u}_j$ are the (orthonormal) eigenvectors of matrix $\hat{O}$. Inserting the eigendecomposition into the expression for the absolute square of the overlap, we

get

$$\left|\left\langle \Psi_{\theta\phi} \middle| \mathrm{GS} \right\rangle\right|^2 = \sum_{j=1}^{D} \mathbf{d}^\dagger \mathbf{u}_j \lambda_j \mathbf{u}_j^\dagger \mathbf{d} = \sum_{j=1}^{D} \left|\mathbf{d}^\dagger \mathbf{u}_j\right|^2 \lambda_j. \tag{B.5}$$

Since $\mathbf{d}^\dagger \mathbf{d} = 1$ and the set $\{\mathbf{u}_j\}$ is orthonormal, it also holds that

$$\sum_{j=1}^{D} \left|\mathbf{d}^\dagger \mathbf{u}_j\right|^2 = 1, \tag{B.6}$$

and, therefore, the maximum of $\left|\left\langle \Psi_{\theta\phi} \middle| \mathrm{GS} \right\rangle\right|^2$ equals the largest eigenvalue λ of the overlap matrix $\hat{O}$:

$$\max\{P(\theta,\phi)\} = \max_{j=1\ldots D}\{\lambda_j\}. \tag{B.7}$$

This result is very natural and could have perhaps been guessed before performing the calculation.

To sum up, the method of spin-$\frac{1}{2}$ coherent states can handle degenerate ground states without any problems, provided that the ground state vectors have been orthogonalized beforehand.

Custom global optimization algorithm for general non-collinear phases

We choose $|\Psi\rangle_{00}$ as a Z-polarized FM state, meaning that θ_j for each site j is measured from this axis. We choose the initial values of $\{\theta_j,\phi_j\}_{j=1}^{N}$ parameters randomly, which corresponds to choosing a random classical spin configuration $|\Psi\rangle$. We perform the optimization of probability $P(\{\theta_j,\phi_j\})$ iteratively, where each iteration consists of the following steps:

- randomly pick $n < N$ cluster sites out of the total N,
- use a standard local constrained optimization algorithm (e.g. limited memory BFGS [196]) to find the maximum of P with only the $2\times n$ variables corresponding to the n chosen sites active, while the other $2\times(N-n)$ are kept constant.

When optimizing the direction of only a subset of chosen spins on the cluster, the algorithm is looking for a maximum in the environment of fixed (initially) random spins. In this limited parameter space there is a high chance that only one prominent maximum occurs, corresponding to the optimized spins pointing in the "correct" directions, and therefore a fast local solver can find it. The appropriate number of optimized sites n is a result of a compromise. If set too low, the optimization algorithm will have trouble finding the correct sub-pattern of the most probable spin configuration. On the other hand, if n is chosen too large, one may end in a local maximum that is different from the global one. For example, in our case of a 24-site honeycomb cluster and the EKH model, experimentation led us to the optimal $n = 8$.

The main advantage of the above procedure compared to a global optimization algorithm applied to the full N-site problem is speed, which comes from two sources. First, local optimization algorithms are generally faster than global ones. However, most of the speed gain comes from a faster evaluation of the merit function P: since $N-n$ spins are fixed and the contribution of each site j to the overlap $\langle\Psi|\mathrm{GS}\rangle$ is in the form of a multiplicative coefficient $\alpha^{\xi_i\chi_j}$,

we can factor out these constant contributions. For a fixed cluster size N the computational effort scales as $\mathcal{O}\left(2^N N\right)$, and thus the evaluation is faster by a factor of $2^{N-n}N/n$.

We tested the suggested optimization procedure on a set of phase diagram points representative of all the phases of the EKH model. We used a 24-site honeycomb cluster with $n = 8$ of them being optimized in each iteration step and $N - n = 16$ fixed. We ran the algorithm several times over to see whether it arrives at the same solution consistently, and we also compared the results with the moment direction obtained by a traditional method of diagonalizing the correlation matrix $\left\langle S^{\mu}_{-\mathbf{q}} S^{\nu}_{\mathbf{q}} \right\rangle$. The results were very satisfying – the procedure almost always arrives at a solution consistent with the benchmark on the first try. Moreover, the convergence was relatively fast, with no more than 100 iterations needed to reach the desired relative accuracy of 10^{-3}. Each iteration contains a whole optimization cycle, but because of the speed gains in quantifying the merit function, it only takes a few seconds.

Efficient method of calculating $P(\theta,\phi)$ for collinear phases

It is often the case that one has prior information about the phase of a particular ground state, and is specifically interested in the precise ordered moment direction and/or the strength of quantum fluctuations. The prior knowledge can come, for example, from a classical phase diagram (see section 2.1.5), the correlation matrix $\left\langle S^{\mu}_{-\mathbf{q}} S^{\nu}_{\mathbf{q}} \right\rangle$, the general variant of spin-$\frac{1}{2}$ coherent states method, etc. If this is the case and the probed spin states are collinear, we can use a very efficient algorithm for finding the most probable moment direction.

In case of a collinear spin pattern, all possible moment directions are described by only two angular parameters θ,ϕ, i.e., the probability $P(\theta,\phi)$ is a function of two variables. Finding a global maximum is, naturally, far easier than in the fully general case of $2N$ variables. In fact, one can consider using a "brute-force" method of evaluating $P(\theta,\phi)$ on a regular two-dimensional grid instead of using global optimization. If such an approach is feasible, it is the most preferred solution, since we obtain the full profile of P. Consider the elements that make up P: first, we have the ground state vector expressed in the standard cluster basis $|i\rangle$:

$$|\mathrm{GS}\rangle = \sum_{i=0}^{2^N-1} c_i \, |i\rangle \, . \tag{B.8}$$

Second, the rotated cluster state $|\Psi\rangle_{\theta\phi}$ is likewise expressed as a linear combination of the basis states $|i\rangle$

$$\left|\Psi_{\theta\phi}\right\rangle = \sum_{i=0}^{2^N-1} \Lambda_i(\theta,\phi)\,|i\rangle = \sum_{i=0}^{2^N-1} \prod_{j=1}^{N} \alpha^{\chi_j \xi_i}(\theta,\phi)\,|i\rangle \, , \tag{B.9}$$

where the initially chosen spin pattern $|\Psi\rangle_{00}$ is encoded in this expression by χ_j. Each coefficient of this linear combination $\Lambda_i(\theta,\phi)$ is a product of terms $\alpha^{\chi_j \xi_i}(\theta,\phi)$ which are all functions of the *same* angles θ,ϕ. For each value of (θ,ϕ), there are only four possible α terms $(\alpha^{\uparrow\uparrow}, \alpha^{\uparrow\downarrow}, \alpha^{\downarrow\uparrow}, \alpha^{\downarrow\downarrow})$, and therefore the products can be written:

$$\sum_{i=0}^{2^N-1} \prod_{j=1}^{N} \alpha^{\chi_j \xi_i}(\theta,\phi)\,|i\rangle = \sum_{i=0}^{2^N-1} (\alpha^{\uparrow\uparrow})^{n_1} (\alpha^{\uparrow\downarrow})^{n_2} (\alpha^{\downarrow\uparrow})^{n_3} (\alpha^{\downarrow\downarrow})^{n_4}\,|i\rangle \, , \tag{B.10}$$

where the powers n_1, n_2, n_3, n_4 depend on i and $|\Psi\rangle_{00}$, but their sum is fixed $n_1+n_2+n_3+n_4 = N$. The number of unique products of α's (and therefore the number of unique coefficients Λ_i) is given by the number of unique combinations N_{comb} of n_1, n_2, n_3, n_4 which turns out to be

$$N_{\text{comb}} \equiv \sum_{n_1=0}^{N}\sum_{n_2=0}^{N}\sum_{n_3=0}^{N}\sum_{n_4=0}^{N}\delta(N-n_1-n_2-n_3-n_4) = \frac{1}{6}(N+1)(N+2)(N+3). \tag{B.11}$$

This number scales as the cube of the number of sites N^3, while the number of basis states $|i\rangle$ is exponential in N

$$\dim\mathcal{H} = 2^N, \tag{B.12}$$

and so

$$N_{\text{comb}} \ll \dim\mathcal{H}. \tag{B.13}$$

For this reason, each unique combination (n_1, n_2, n_3, n_4) is common for a large number of basis states $|i\rangle$. We can create one such group $i \in \mathcal{I}$ for each (n_1, n_2, n_3, n_4) and write

$$\left|\Psi_{\theta\phi}\right\rangle = \sum_{\substack{n_1,n_2,n_3,n_4\\ n_1+n_2+n_3+n_4=N}} (\alpha^{\uparrow\uparrow})^{n_1}(\alpha^{\uparrow\downarrow})^{n_2}(\alpha^{\downarrow\uparrow})^{n_3}(\alpha^{\downarrow\downarrow})^{n_4}\sum_{i\in\mathcal{I}}|i\rangle\,. \tag{B.14}$$

The grouping of i in $\mathcal{I}$ depends only on the initial spin pattern $|\Psi\rangle_{00}$ and it is therefore enough to calculate it once. This greatly speeds up the calculation of $|\Psi\rangle_{\theta\phi}$, since for each (θ,ϕ) we only need to enumerate $\approx N^3$ coefficients instead of 2^N. The probability P of a given direction (θ,ϕ) is then

$$\begin{aligned} P(\theta,\phi) = \left|\left\langle\Psi_{\theta\phi}\middle|\text{GS}\right\rangle\right|^2 &= \left|\sum_{\substack{n_1,n_2,n_3,n_4\\ n_1+n_2+n_3+n_4=N}} \left[(\alpha^{\uparrow\uparrow})^{n_1}(\alpha^{\uparrow\downarrow})^{n_2}(\alpha^{\downarrow\uparrow})^{n_3}(\alpha^{\downarrow\downarrow})^{n_4}\right]^*\sum_{i\in\mathcal{I}}c_i\right|^2 = \\ &= \left|\sum_{k=0}^{N_{\text{comb}}}\Lambda_k^*(\theta,\phi)C_k\right|^2, \end{aligned} \tag{B.15}$$

where the index k enumerates the unique combinations (n_1, n_2, n_3, n_4) and C_k is a sum of ground state coefficients c_i corresponding to basis states $|i\rangle$ from one group $\mathcal{I}(k)$. To provide some specific numbers, we again turn to the 24-site honeycomb cluster. The Hilbert space dimension is $2^{24} = 16777216$ and the number N_{comb} of coefficients Λ_k is $N_{\text{comb}} = 2925$, therefore we gain a factor of 10^3 in speed. We evaluate $P(\theta,\phi)$ on a finite grid of $N_\theta \times N_\phi$ points – the total number of points on this grid determines the accuracy of the ordered moment direction. For a desired accuracy of 0.5° in both the polar and azimuthal directions, it takes less than one minute to evaluate the whole profile of $P(\theta,\phi)$ on a standard desktop machine. The memory requirements are only limited by the space to store the ground-state vector, and the problem is embarrassingly parallel; thus, depending on the desired accuracy, it is easily feasible to obtain $P(\theta,\phi)$ for one ground state in a matter of seconds.

Appendix C

Stochastic Series Expansion

The Stochastic Series Expansion (SSE) is a well-known Quantum Monte Carlo (QMC) method, suitable for treating spin and bosonic systems on finite lattices. Several educational texts are available [157, 187, 197] providing a general overview of the method. In this Appendix, we focus on some specific aspects of the SSE technique that are relevant to the effective spin model for Ca_2RuO_4, as well as some technical details of the implementation.

Application to the pseudospin-1 model for Ca_2RuO_4

In Section 3.1 we have introduced the effective model for Ca_2RuO_4 formulated in terms of singlet and triplet operators (3.9),(3.13), as well as in a pseudospin-1 formulation (3.6),(3.7). Since one of our goals is to calculate spin susceptibility, we choose to continue with the pseudospin-1 version of the model. Our basis for the lattice cluster states is given by S^z eigenstates:

$$|\alpha\rangle = \left|S_1^z, S_2^z, \ldots, S_N^z\right\rangle. \tag{C.1}$$

The SSE-form of the partition function is obtained by a power expansion, and thus involves powers of the Hamiltonian. These can be written as products of bond operators summed over operator sequences S_n:

$$(-\mathcal{H})^n = \left(-\sum_b -H_b\right)^n = \sum_{S_n}\prod_{i=p}^{n} H_{b_p}, \tag{C.2}$$

where S_n is a sequence of single-bond operators H_{b_i} of length n:

$$S_n = [a_1, b_1], [a_2, b_2], \ldots, [a_n, b_n]. \tag{C.3}$$

In the above expression, a labels the type of operator (1=diagonal, 2=offdiagonal) and b labels the bonds. As we have shown in Section 3.2.1, the partition function is a weighted sum over all basis states $|\alpha\rangle$, operator sequences S_n and expansion orders n:

$$Z_{\mathrm{SSE}} = \sum_n \sum_{S_n} \sum_{\{\alpha\}} W(\alpha, S_n), \tag{C.4}$$

where the weights are products of matrix elements of Hamiltonian bond operators

$$W(\alpha, S_n) = \frac{\beta^n}{n!}\prod_{p=1}^{n} \langle\alpha(p)|H_{b_p}|\alpha(p-1)\rangle. \tag{C.5}$$

Here we use a notation for the normalized *propagated states* $|\alpha(p)\rangle$, which are a result of the application of p Hamiltonian bond operators:

$$|\alpha(p)\rangle \propto \prod_{i=1}^{p} H_{b_i} |\alpha\rangle . \tag{C.6}$$

All propagated states are also basis states, and states at successive propagation levels $|\alpha(p)\rangle$, $|\alpha(p+1)\rangle$ are either the same or differ only at a single bond. Due to the cyclic property of the trace, there is periodicity in the propagation direction, i.e. $|\alpha(n)\rangle = |\alpha(0)\rangle$.

Not all powers n contribute to the partition function equally. It can be shown [198, 199] that the average expansion order n is centered around

$$\langle n \rangle \propto \beta N_b, \tag{C.7}$$

and the distribution has a width of approximately $\sqrt{\langle n \rangle}$. Therefore, we can truncate the expansion at expansion order $M > n$ and insert $M - n$ identity operators into each operator sequence. Accounting for $(M-n)!$ ways in which this insertion can be done, the partition function becomes

$$Z_{\mathrm{SSE}} = \sum_{S_M} \sum_{\{\alpha\}} \frac{\beta^n (M-n)!}{M!} \prod_{p=1}^{M} \langle \alpha(p) | H_{b_p} | \alpha(p-1) \rangle . \tag{C.8}$$

In practice, one starts with some given M and an empty operator sequence of length S_M. A Monte Carlo updating procedure (to be specified in the following paragraphs) which can add or remove diagonal bond operators $H_{1,b}$ is repeatedly applied during the equilibration phase of the algorithm, thus sampling the expansion order n. During the sampling, M is adjusted to be sufficiently larger than the maximum reached n, and thus any truncation errors are avoided.

To continue, we need to calculate the configuration weights $W(\alpha, S_M)$, which include matrix elements of the bond Hamiltonian operators. The full pseudospin-1 Hamiltonian reads as:

$$\mathcal{H} = \sum_i \mathcal{H}_i^{\mathrm{loc}} + \sum_{\langle ij \rangle \in \mathrm{NN}} \mathcal{H}_{ij}^{(\xi)}, \tag{C.9}$$

$$\mathcal{H}_i^{\mathrm{loc}} = E_T \left(S_i^z\right)^2 + \tfrac{1}{2}\Delta' \left(S_y^2 - S_x^2\right)_i, \tag{C.10}$$

$$\mathcal{H}_{ij}^{(\xi)} = J \left(S_i^x S_j^x + S_i^y S_j^y\right) - A_\xi \left(S_i^x S_j^y + S_i^y S_j^x\right) + J_z S_i^z S_j^z. \tag{C.11}$$

We express it as the sum of diagonal $H_{1,b}$ and off-diagonal $H_{2,b}$ bond operators:

$$\mathcal{H} = -J \sum_{b=1}^{N_b} (H_{1,b} + H_{2,b}). \tag{C.12}$$

The factor J taken out of the sum plays the role of a common energy scale and is typically absorbed into the variable β. We rewrite the interaction terms using ladder operators S^+, S^-:

$$S_i^x S_j^x + S_i^y S_j^y = \frac{1}{2}(S_i^+ S_j^- + S_i^- S_j^+), \tag{C.13}$$

$$S_i^x S_i^x - S_i^y S_i^y = \frac{1}{2}(S_i^+ S_i^+ + S_i^- S_i^-), \tag{C.14}$$

$$S_i^x S_j^y + S_i^y S_j^x = -\frac{i}{2}(S_i^+ S_j^+ - S_i^- S_j^-). \tag{C.15}$$

We obtain the diagonal part of the interaction on a bond b:

$$H_{1,b} = C - J_z S_i^z S_j^z - \frac{E_T}{zJ}(S_i^z S_i^z + S_j^z S_j^z), \tag{C.16}$$

where C is a number added to ensure that the term $H_{1,b}$ is always positive, which is necessary to avoid sampling with negative weights. We choose $C = C_0 + \varepsilon$, with $C_0 = J_z - \frac{4E_T}{3zJ}$ and a free parameter $\varepsilon > 0$ whose value can be adjusted to improve the convergence of the algorithm. A factor $z \equiv 2N_b/N_{\text{site}}$ arises due to the rewriting of the on-site interaction term $\mathcal{H}_{\text{loc}}$ to a bond interaction form. The off-diagonal part of the bond Hamiltonian reads as

$$H_{2,b} = -\frac{1}{2}(S_i^+ S_j^- + S_i^- S_j^+) + \frac{iA_\xi}{2J}(S_i^- S_j^- - S_i^+ S_j^+) + \frac{\Delta'}{4zJ}(S_i^+ S_i^+ + S_i^- S_i^- + S_j^+ S_j^+ + S_j^- S_j^-). \tag{C.17}$$

First, we notice that the first term yields a negative matrix element. This problem can easily be mended by dividing the square lattice into two sublattices, such that neighboring sites belong to different sublattices, and introducing a π-rotation around S^z for spins on one sublattice. After such a rotation, the matrix element is positive and on-site terms $S_i^\mu S_i^\nu$ are unaffected. As a consequence of this sublattice rotation, reciprocal-space observables will be shifted in $\mathbf{q}$ by (π, π), which has to be manually corrected after the simulation.

A more serious issue is due to the imaginary matrix element of the bond-dependent A_ξ-term. Since there is no guarantee of how many $S_i^- S_j^- + S_i^+ S_j^+$ operators are present in each sampled operator sequence S_M, the inclusion of such a term could lead to negative or complex weights. For this reason we decided to omit this term from the SSE simulations. As we have discussed in Section 3.1.3, the dispersion shapes are given mainly by (E_T, J, Δ') terms, whereas the effects of the J_z and A_ξ terms are relatively small.

Monte Carlo updating procedure

An updating procedure is at the heart of any QMC scheme. To sample new configurations S_M, we need an algorithm that produces updates $[a_i, b_i] \leftrightarrow [a_i', b_i']$. Any such algorithm needs to first of all fulfill the conditions of *ergodicity* and *detailed balance*, which means that the whole configuration space can be reached and that the flow of probability is locally balanced [197].

For the discussion of the specific updating procedures, it is useful to introduce a visual representation of the SSE configurations. Each configuration is represented by the spin state $|\alpha(0)\rangle$ and an operator sequence $S_M = [a_1, b_1], [a_2, b_2], \ldots, [a_M, b_M]$. In our case, $|\alpha(0)\rangle$ is a 2D cluster state of $S = 1$ spins on a square lattice, and S_M is a sequence of n bond operators H_b together with $M - n$ identity operators. The bond operators act on a bond represented by two neighboring lattice sites i, j and possibly change their spin states. In this way, bond operators propagate the states – they connect neighboring spins $|\alpha_i(p-1)\rangle, |\alpha_j(p-1)\rangle$ with $|\alpha_i(p)\rangle, |\alpha_j(p)\rangle$, incrementing the propagation level p. Together, the four spin states (also called *legs*) form a *vertex*, depicted in Figure C.1(a). Placing the propagation direction as orthogonal to the lattice dimensions, we obtain a visual representation of a SSE configuration as M layers of $|\alpha(p)\rangle$ states stacked on top of each other and n vertices, with two successive layers connected by at most a single vertex. As was mentioned earlier, the SSE configuration is periodic in the propagation

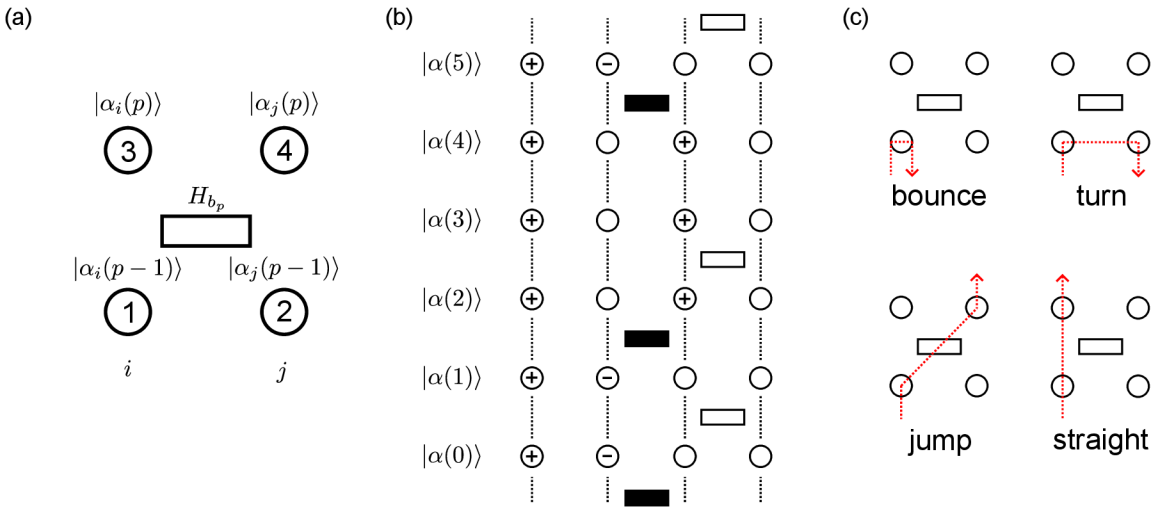

Figure C.1: (a) A vertex consists of four spin states connected by a bond operator: two neighboring spins on a bond $|\alpha_i(p-1)\rangle, |\alpha_j(p-1)\rangle$ are acted upon by an operator H_{b_p}, incrementing the propagation level from $(p-1)$ to p and, in case of an off-diagonal operator, also changing the spin states. (b) Example of a SSE configuration of four $S=1$ spins, $n=4$ vertices and $M=5$ propagation levels. The spin states are labeled by their S^z-eigenvalue m: "+" labels $m=+1$, "−" labels $m=-1$ and an empty circle corresponds to $m=0$. The dashed lines show the propagation direction. The boundary in propagation direction is periodic. (c) Possible paths of an operator head (dashed red line) through a vertex during the directed loop update. The sum of the four path weights equals to the vertex weight of the original vertex before the changes to the spin states.

direction: $|\alpha(M)\rangle = |\alpha(0)\rangle$. An example is shown in Figure C.1 panel (b) with four spins and $M=5$.

We carry out two types of updates during a SSE computation:

(i) *Diagonal update*: updates of the form $[0,0] \leftrightarrow [1,b]$, changing the total number of non-identity operators n (=number of vertices),

(ii) *Off-diagonal update*: updates of the type $[1,b] \leftrightarrow [2,b]$ changing the operator type from diagonal to off-diagonal or vice versa, and also changing the spin states at the affected vertex. The total number of vertices n stays unchanged.

Performing a diagonal update is quite straightforward. Starting from the initial state $|\alpha(0)\rangle$, we pick a bond randomly and insert/remove a diagonal operator $H_{1,b}$ with a certain probability. To satisfy detailed balance, we choose the Metropolis-Hastings probabilities [200, 201]:

$$P([0,0]_p \to [1,b]_p) = \min\left(1, \frac{N_b \beta \langle\alpha(p)|H_{1,b}|\alpha(p)\rangle}{M-n}\right), \tag{C.18}$$

$$P([1,b]_p \to [0,0]_p) = \min\left(1, \frac{M-n+1}{N_b \beta \langle\alpha(p)|H_{1,b}|\alpha(p)\rangle}\right). \tag{C.19}$$

The procedure is then repeated successively at each propagation direction. Note, that the probability of inserting an operator (and consequently also the number of vertices n) rises linearly with system size N_b and inverse temperature β, which is generally an important advantage of QMC methods.

The goal of an off-diagonal updating procedure is to make substitutions $[1,b]_p \leftrightarrow [2,b]_p$, that is, to change diagonal operators into off-diagonal ones (and vice versa), and also to change the spin states on the bond b, thus sampling different spin configurations. The formulation of an off-diagonal updating scheme is considerably more involved compared to the diagonal update. The reason is that local updating schemes become increasingly inefficient at sampling relevant configurations near phase transitions, where the correlation length is very large and fluctuations are present on all scales: a phenomenon known as critical slowing down [202]. The solution is to rather use cluster algorithms, which change many states in the configuration at once; one of the first examples of such algorithms are the well-known Swendsen-Wang [203] and Wolff [204] cluster algorithms.

For the off-diagonal updating scheme, we use the directed-loop algorithm [187, 157, 205]. The algorithm provides a way to build a loop in the configuration space, changing operator types and spin states of all affected vertices. The loop starts by (uniformly randomly) inserting a pair of operators which change the local spin states; in our case of a spin-1 system, the pair consists of and S^+ and S^- operator. One of these operators remains static (the *tail*) and the other can move (the *head*) through the configuration space. The operator head acts on the spin state and then moves to the next vertex in the propagation direction. Upon hitting the vertex, it can continue in four possible ways connected to the four legs of each vertex. Each of these moves, depicted in Figure C.1 (c), happens with a specified probability (to be determined). The passage of the head changes the spin states of the entrance and exit legs, and consequently also the operator type connecting the legs of the vertex. In this way, the head continues its motion through the configuration space, until encountering the tail, at which point the loop closes. The result is a new spin configuration $|\alpha\rangle$ and a new operator sequence S_M.

The probabilities connected with the passage of the operator head need to preserve detailed balance. The insertion of the S^+ operator at a spin state with S^z-eigenvalue m must therefore happen with the same probability as an insertion of the S^- operator at a spin state with S^z-eigenvalue $(m+1)$:

$$P_{\text{ins}}(S^+,m) = P_{\text{ins}}(S^-,m+1). \tag{C.20}$$

This is simple to achieve: we choose $P(S^-,+1) = P(S^+,0) = P(S^-,0) = P(S^+,-1) = \frac{1}{2}$, $P(S^-,-1) = P(S^+,+1) = 0$.

A more difficult problem is to find the probabilities for the four ways of passing a vertex. For a given entrance leg l, exit leg l' and vertex v, we start with weights $a_{l'l}(v)$ for each of the possible paths through the vertex. For these weights, it must hold that the sum over all exit legs l' equals the vertex weight $W(v)$ given by the matrix element of the bond operator H_{b_p} before the spins have been changed:

$$\sum_{l'} a_{l'l}(v) = W(v) = \left\langle \alpha_i(p)\alpha_j(p) \middle| H_{b_p} \middle| \alpha_i(p-1)\alpha_j(p-1) \right\rangle. \tag{C.21}$$

The individual path probabilities are given by the path weights a divided by the vertex weight: $P_{l'l}(v) = a_{l'l}(v)/W(v)$. The process of the operator head traversing a vertex must respect detailed balance, meaning that the process must have the same weight as its reverse:

$$W(v)P_{l'l}(v) = W(v')P_{l'l}(v') \quad \Rightarrow \quad a_{l'l}(v) = a_{ll'}(v'). \tag{C.22}$$

This condition, together with the condition for the sum of path weights over exit legs, constitutes the directed-loop equations for path weights a.

Typically, there are more unknowns a than equations, meaning that an infinity of solutions exist. For example, four possible entrance and exit legs mean $4 \times 4 = 16$ unknowns $a_{l'l}$, but there are only four equations (C.21). The number of unknowns is reduced to 10 by applying (C.22), but the equation set remains largely underdetermined. Since the probabilities meaningfully affect the efficiency of the directed loop update procedure, it is worth trying to find advantageous solutions. One heuristic [205] is to minimize the so-called bounce process (see Figure C.1 (c)) which reverses the direction of the operator head, undoing the loop. We achieve this by employing a linear programming minimization routine. Often, minimizing the bounce process still leaves infinite solutions for the other vertex paths. Then, the minimized bounce weight value can be added to the equation set as another constraint and one can continue with further optimizations. For our simulations, we measured the efficiency of six further optimization goals after the bounce process has been minimized: minimize/maximize turn weight, minimize/maximize jump weight, minimize/maximize straight weight (see Figure C.1 (c) for a visualization of these paths). We obtained the best results when maximizing the weight of the jump process, although the differences were relatively small and depended on the model parameters.

Measurement of observables

In the SSE scheme, observables are measured during runtime and their statistical errors are determined using the jackknife or bootstrap technique [197]. The estimators of various quantitiess can be obtained with varying difficulty depending on the observable and the model; in the following paragraphs we comment on the spin susceptibility and equal-time spin-spin correlation functions, which were computed for the soft-spin model in Section 3.2.3.

As we have discussed in Section 3.2.1, the propagation direction in SSE can be mapped to imaginary time τ, allowing us to obtain dynamical observables such as the dynamical magnetic susceptibility. Let us take the specific example of the $S^{\mu}(\tau)S^{\nu}(0)$ estimator, where the operators S^{μ}, S^{ν} are diagonal in the chosen basis, i.e. $S^{\mu} = S^{\nu} = S^{z}$. Then, we have:

$$S^{zz}(i\omega_m) = \int_0^{\beta} d\tau e^{-i\omega_m \tau} \langle S^z(\tau) S^z(0) \rangle. \tag{C.23}$$

Following the approach in [206], we use the periodicity of the imaginary time axis $\tau + \beta = \tau$ and replace the S^z operators by their eigenvalues $s_\tau, s_{\tau'}$:

$$S^{zz}(i\omega_m) = \frac{1}{\beta} \int_0^{\beta} d\tau \int_0^{\beta} d\tau' e^{-i\omega_m(\tau-\tau')} \langle s_\tau s_{\tau'} \rangle. \tag{C.24}$$

Since s_τ is constant between imaginary time slices τ_{p+1} and τ_p, the integral can be calculated piecewise, resulting in the final expression:

$$S^{zz}(i\omega_m) = \frac{1}{\omega_m^2 \beta} \left\langle \left(\sum_{p=0}^{n} s_p \left[e^{-i\omega_m \tau_{p+1}} - e^{-i\omega_m \tau_p} \right] \right) \left(\sum_{p=0}^{n} s_p \left[e^{i\omega_m \tau_{p+1}} - e^{i\omega_m \tau_p} \right] \right) \right\rangle, \tag{C.25}$$

where n is the number of non-identity operators in the operator string S_M. The special case of equal-time correlator $S^{zz}(i\omega_m = 0)$ is given by:

$$S^{zz}(i\omega_m = 0) = \frac{1}{\beta} \left\langle \left(\sum_{p=0}^{n} s_p [\tau_{p+1} - \tau_p] \right)^2 \right\rangle. \tag{C.26}$$

The above estimators can be efficiently sampled during diagonal updates of the Monte Carlo configurations, as the formulas merely require reading S^z-eigenvalues s_p at different propagation levels p. A more challenging task is met when off-diagonal estimators such as $S^{xx}(i\omega_n), S^{yy}(i\omega_n)$ are desired. The application of off-diagonal spin operators changes the spin states, thereby exiting the configuration space of valid configurations (α, S_M). However, local changes in spin states are introduced during the directed loop update that introduces the S^+ and S^- operators into the SSE configuration and ensures that they traverse the configuration space in an ergodic way. As the operator head S^+ moves through the configuration and the tail S^- is stationary at propagation level p, the estimator $S^+(p+q)S^-(p)$ can be measured [207]:

$$S_i^+(p+q)S_j^-(p) = \left\langle \alpha_i'(p+q) \middle| S_i^+ \middle| \alpha_i(p+q) \right\rangle \left\langle \alpha_j'(p) \middle| S_j^- \middle| \alpha_j(p) \right\rangle . \tag{C.27}$$

The transformation from propagation level to imaginary time is then performed according to (3.66).

The measurement of off-diagonal dynamical observables is quite computationally intensive: it slows-down the loop update and adds additional overhead due to repetitive integration of binomial coefficients in (3.66). As an alternative, we propose a way to obtain at least some of the off-diagonal estimators by formulating the spin model in a rotated coordinate frame XYZ, in which the newly introduced Z-direction corresponds to the original x or y axis. In this way, the off-diagonal quantity S^{xx} or S^{yy} can be calculated by a diagonal estimator S^{ZZ}. For the pseudospin-1 model of Chapter 3, we introduce the coordinate reference frame XYZ such that $X = y, Y = z, Z = x$, so that $\langle S^x S^x \rangle \equiv \langle S^Z S^Z \rangle$. The Hamiltonian expressed in the XYZ coordinate frame reads:

$$\mathcal{H}_i^{\text{loc}} = E_T S_i^Y S_i^Y + \tfrac{1}{2}\Delta' \left(S_X^2 - S_Z^2\right)_i, \tag{C.28}$$

$$\mathcal{H}_{ij}^{(\xi)} = J\left(S_i^Z S_j^Z + S_i^X S_j^X\right) - A_\xi \left(S_i^X S_j^Z + S_i^Z S_j^X\right) + J_z S_i^Y S_j^Y . \tag{C.29}$$

$$\tag{C.30}$$

Rewriting the interaction into the form of bond Hamiltonian terms $H_{1,b}, H_{2,b}$, we confirm that the matrix elements are positive (after applying a sublattice rotation as previously) in the range of parameters where $E_T > \Delta'/2$, which holds for the most interesting part of the phase diagram:

$$H_{1,b} = C - S_i^Z S_j^Z - \frac{1}{zJ}\left(E_T + \frac{\Delta'}{2}\right) S(S+1) + \frac{1}{2zJ}\left(E_T + \frac{3\Delta'}{2}\right)(S_i^Z S_i^Z + S_j^Z S_j^Z), \tag{C.31}$$

$$H_{2,b} = -\left(\frac{1}{2} + \frac{1-J_z}{4}\right)(S_i^+ S_j^- + S_i^- S_j^+) - \frac{1-J_z}{4}(S_i^+ S_j^+ + S_i^- S_j^-) + \tag{C.32}$$

$$+ \frac{1}{4zJ}\left(E_T - \frac{\Delta'}{2}\right)(S_i^+ S_i^+ + S_i^- S_i^- + S_j^+ S_j^+ + S_j^- S_j^-). \tag{C.33}$$

The above expressions can be used to construct a SSE calculation that efficiently produces $\langle S^x S^x \rangle$. A similar approach to obtaining $\langle S^y S^y \rangle$ from $\langle S^Z S^Z \rangle$ fails, as the matrix elements turn out to be negative in that case.

Appendix D

Bogoliubov transformation by numerical diagonalization

The Bogoliubov transformation [208] is a linear mapping between sets of bosonic or fermionic operators which can used to diagonalize bilinear Hamiltonians. It was developed in the context of the BCS theory of superconductivity but can be used more generally, as in our case of antiferromagnets. Here we provide a general matrix formulation that can be used for numerical diagonalization of Bogoliubov matrices in cases that are not easily solved analytically. Afterwards, we provide an example relevant to the text, namely the diagonalization of a harmonic singlet-doublet Hamiltonian for Ca_2RuO_4 including J_z and A terms.

General matrix formulation

We aim to diagonalize a bosonic bilinear Hamiltonian in the form

$$H^{(2)} = H^{(0)} + \sum_{\mathbf{q}} \Psi^\dagger_{\mathbf{q}} K \Psi_{\mathbf{q}}, \tag{D.1}$$

where

$$\Psi_{\mathbf{q}} = \begin{pmatrix} a_{+\mathbf{q}} \\ a^\dagger_{-\mathbf{q}} \end{pmatrix}. \tag{D.2}$$

To do that, we apply a linear transformation T, obtaining a different set of creation/annihilation operators $\tilde{\Psi}_{\mathbf{q}} = T^{-1}\Psi_{\mathbf{q}}$, such that the transformation diagonalizes the interaction matrix:

$$\sum_{\mathbf{q}} \Psi^\dagger_{\mathbf{q}} K \Psi_{\mathbf{q}} = \sum_{\mathbf{q}} \tilde{\Psi}^\dagger_{\mathbf{q}} \underbrace{T^\dagger K T}_{\tilde{K}\text{ diagonal}} \tilde{\Psi}_{\mathbf{q}}. \tag{D.3}$$

Apart from linearity, the condition for transformation T is that it must preserve bosonic commutation relations, which can be expressed using the Pauli matrix σ_3

$$\left[\Psi_{\mathbf{q}i}, \Psi^\dagger_{\mathbf{k}j}\right] = \delta_{\mathbf{q},\mathbf{k}} \begin{pmatrix} 1 & 0 \\ 0 & -1 \end{pmatrix}_{ij} = \delta_{\mathbf{q},\mathbf{k}} (\sigma_3)_{ij}. \tag{D.4}$$

We calculate the commutator for the new operator set $\tilde{\Psi}_{\mathbf{q}}$:

$$\begin{aligned} \left[\tilde{\Psi}_i, \tilde{\Psi}^\dagger_j\right] &= \tilde{\Psi}_i \tilde{\Psi}^\dagger_j - \tilde{\Psi}^\dagger_j \tilde{\Psi}_i = T^{-1}_{ik} T^{-1\dagger}_{lj} \Psi_k \Psi^\dagger_l - T^{-1}_{ik} T^{-1\dagger}_{lj} \Psi^\dagger_l \Psi_k = \\ &= T^{-1}_{ik} T^{-1\dagger}_{lj} \left[\Psi_k, \Psi^\dagger_l\right] = T^{-1} \sigma_3 T^{-1\dagger}. \end{aligned} \tag{D.5}$$

To preserve the bosonic commutation relations, this expression must equal σ_3. Together with the unitarity of T (to preserve the norm of Ψ), this gives an expression

$$T^\dagger \sigma_3 T = \sigma_3 \quad \Rightarrow \quad \sigma_3 T^\dagger \sigma_3 = T^{-1}. \tag{D.6}$$

The final trick is to multiply the diagonal matrix of Hamiltonian coefficients $\tilde{K}$ by σ_3 from the left, and use the identity $\sigma_3\sigma_3 = 1$:

$$\sigma_3 \tilde{K} = \sigma_3 T^\dagger K T = \underbrace{\sigma_3 T^\dagger \sigma_3}_{T^{-1}} \sigma_3 K T = T^{-1}(\sigma_3 K) T. \tag{D.7}$$

We have obtained a similarity transformation for $\sigma_3 K$ employing the T, T^{-1} matrices. This means that T is a matrix of eigenvectors of the matrix $\sigma_3 K$, and $\sigma_3 \tilde{K}$ contains the eigenvalues. Therefore, obtaining the Bogoliubov transformation matrix T and with it the new basis $\tilde{\Psi}$ reduces to a diagonalization of the matrix $\sigma_3 K$.

Let us add some practical remarks. The eigenvectors and eigenvalues can be obtained by a general numerical diagonalization procedure, such as `DGEEV` from the LAPACK software library. There are specific numerical algorithms for the diagonalization of hermitian matrices, which, however, are not applicable in this case – while K is hermitian, $\sigma_3 K$ is not. Generally, the matrix of transformation T does not consist of normalized column vectors, but many numerical diagonalization procedures shuffle the eigenvectors and normalize them. The proper order can be reestablished by ordering the eigenvalues such that $\tilde{K}$ contains positive diagonal elements, which is the case for bosonic Hamiltonians:

$$\sigma_3 \tilde{K} = \begin{pmatrix} +\lambda & 0 \\ 0 & -\lambda \end{pmatrix}, \quad \lambda > 0. \tag{D.8}$$

Finally, we can recover the full unnormed T matrix. Let's label Z the normed version of T, as produced by numerical diagonalization, and C the diagonal matrix of eigenvector magnitudes:

$$T = CZ. \tag{D.9}$$

To recover the norms C, we use the relations connecting $\tilde{K}$ to T and $\tilde{K}$ to Z separately:

$$\tilde{K} = T^\dagger \sigma_3 T \qquad \& \qquad \sigma_3 \tilde{K} = Z^{-1}(\sigma_3 K) Z, \tag{D.10}$$

which, after a few simple manipulations, yield the expressions for eigenvector magnitudes C:

$$|C|^2_{ii} = \frac{(Z^\dagger K Z)_{ii}}{\tilde{K}_{ii}}. \tag{D.11}$$

Singlet-doublet model in a harmonic approximation

We encountered a situation where the above formalism can be used in Section 3.1, obtaining the harmonic excitation modes of the singlet-doublet model. After the bosonic rotation to the basis containing two bosons a, b the model reads

$$\begin{aligned} H^{(2)} = \sum_{\mathbf{q}} \Big[& A_{1\mathbf{q}} a^\dagger_{\mathbf{q}} a_{\mathbf{q}} + A_{2\mathbf{q}} b^\dagger_{\mathbf{q}} b_{\mathbf{q}} - \frac{1}{2} B_{1\mathbf{q}} \left(a_{-\mathbf{q}} a_{\mathbf{q}} + a^\dagger_{\mathbf{q}} a^\dagger_{-\mathbf{q}} \right) - \frac{1}{2} B_{2\mathbf{q}} \left(b_{-\mathbf{q}} b_{\mathbf{q}} + b^\dagger_{\mathbf{q}} b^\dagger_{-\mathbf{q}} \right) + \\ & + C_{\mathbf{q}} \left(a^\dagger_{\mathbf{q}} b_{\mathbf{q}} + b^\dagger_{\mathbf{q}} a_{\mathbf{q}} \right) - \frac{1}{2} C_{\mathbf{q}} \left(a_{-\mathbf{q}} b_{\mathbf{q}} + a^\dagger_{\mathbf{q}} b^\dagger_{-\mathbf{q}} + b_{-\mathbf{q}} a_{\mathbf{q}} + b^\dagger_{\mathbf{q}} a^\dagger_{-\mathbf{q}} \right) \Big]. \end{aligned} \tag{D.12}$$

The Hamiltonian terms are:

$$\begin{aligned} A_{1\mathbf{q}} &= E_T - \Delta'/2 + Jz\gamma_{\mathbf{q}}, \\ A_{2\mathbf{q}} &= E_T + \Delta'/2 + Jz\gamma_{\mathbf{q}}, \\ B_{1\mathbf{q}} &= Jz\gamma_{\mathbf{q}}, \\ B_{2\mathbf{q}} &= Jz\gamma_{\mathbf{q}} + 4J_z \sin^2\theta\gamma_{\mathbf{q}}, \\ C_{\mathbf{q}} &= -Az\cos^3\theta\eta_{\mathbf{q}}, \end{aligned} \tag{D.13}$$

where E_T, J, Δ', A, J_z are model parameters, $z = 4$ is the coordination number of the lattice, and $\gamma_{\mathbf{q}}, \eta_{\mathbf{q}}$ are lattice sums

$$\begin{aligned} \gamma_{\mathbf{q}} &= \frac{1}{z}\sum_{\delta} e^{i\mathbf{q}\cdot\delta} = \frac{1}{2}(\cos q_x + \cos q_y), \\ \eta_{\mathbf{q}} &= \frac{1}{z}\sum_{\delta} \mathrm{sign}(\delta) e^{i\mathbf{q}\cdot\delta} = \frac{1}{2}(\cos q_x - \cos q_y), \end{aligned} \tag{D.14}$$

with the sign of lattice vector δ positive for the x direction and negative for the y direction. We turn the Hamiltonian into a matrix form:

$$H^{(2)} = \sum_{\mathbf{q}} \left[\frac{1}{2}\Psi_{\mathbf{q}}^{\dagger} H_{\mathbf{q}} \Psi_{\mathbf{q}} - \frac{1}{2}\left(A_{1\mathbf{q}} + A_{2\mathbf{q}}\right) \right], \tag{D.15}$$

with the basis vectors containing four bosonic operators

$$\Psi_{\mathbf{q}} = \begin{pmatrix} a_{\mathbf{q}} \\ b_{\mathbf{q}} \\ a_{-\mathbf{q}}^{\dagger} \\ b_{-\mathbf{q}}^{\dagger} \end{pmatrix}, \tag{D.16}$$

and the Hamiltonian represented by a 4×4 matrix of coefficients

$$H_{\mathbf{q}} = \begin{pmatrix} A_{1\mathbf{q}} & -B_{1\mathbf{q}} & C_{\mathbf{q}} & -C_{\mathbf{q}} \\ -B_{1\mathbf{q}} & A_{1\mathbf{q}} & -C_{\mathbf{q}} & C_{\mathbf{q}} \\ C_{\mathbf{q}} & -C_{\mathbf{q}} & A_{2\mathbf{q}} & -B_{2\mathbf{q}} \\ -C_{\mathbf{q}} & C_{\mathbf{q}} & -B_{2\mathbf{q}} & A_{2\mathbf{q}} \end{pmatrix}. \tag{D.17}$$

Numerical Bogoliubov diagonalization of $\sigma_3 H_{\mathbf{q}}$ for each $\mathbf{q}$ yields the transformation matrices $T_{\mathbf{q}}$ and eigenvalues $\omega_{1\mathbf{q}}$ and $\omega_{2\mathbf{q}}$ corresponding to the harmonic excitation modes. Explicitly

$$\tilde{\Psi}_{\mathbf{q}} = T_{\mathbf{q}}^{-1}\Psi_{\mathbf{q}} = \begin{pmatrix} \alpha_{\mathbf{q}} \\ \beta_{\mathbf{q}} \\ \alpha_{-\mathbf{q}}^{\dagger} \\ \beta_{-\mathbf{q}}^{\dagger} \end{pmatrix} \quad \text{and} \quad \tilde{H}_{\mathbf{q}} = \left(T^{\dagger} H T\right)_{\mathbf{q}} = \begin{pmatrix} \omega_{1\mathbf{q}} & 0 & 0 & 0 \\ 0 & \omega_{2\mathbf{q}} & 0 & 0 \\ 0 & 0 & \omega_{1\mathbf{q}} & 0 \\ 0 & 0 & 0 & \omega_{2\mathbf{q}} \end{pmatrix}. \tag{D.18}$$

The Hamiltonian is diagonal in the Bogoliubov bosons $\alpha_{\mathbf{q}}, \beta_{\mathbf{q}}$ and has the form of two independent sets of harmonic oscillators

$$H^{(2)} = \sum_{\mathbf{q}} \left[\omega_{1\mathbf{q}} \left(\alpha_{\mathbf{q}}^{\dagger}\alpha_{\mathbf{q}} + \frac{1}{2} \right) + \omega_{2\mathbf{q}} \left(\beta_{\mathbf{q}}^{\dagger}\beta_{\mathbf{q}} + \frac{1}{2} \right) \right] - E_T N. \tag{D.19}$$

Along with the dispersions $\omega_{1\mathbf{q}}, \omega_{2\mathbf{q}}$, we can also obtain the averages containing original a, b bosonic operators, such as $\left\langle a^\dagger_{\mathbf{q}} a_{\mathbf{q}} \right\rangle, \left\langle b^\dagger_{\mathbf{q}} b_{\mathbf{q}} \right\rangle, \langle a_{-\mathbf{q}} a_{\mathbf{q}} \rangle$, etc. from the transformation matrices $T_{\mathbf{q}}$. For example:

$$\begin{aligned}\left\langle a^\dagger_{\mathbf{q}} a_{\mathbf{q}} \right\rangle &= \left\langle a^\dagger_{-\mathbf{q}} a_{-\mathbf{q}} \right\rangle = \left\langle \left(\Psi_{\mathbf{q}} \Psi^\dagger_{\mathbf{q}} \right)_{33} \right\rangle = \\ &= |T_{31}|^2_{\mathbf{q}} \left\langle \alpha_{\mathbf{q}} \alpha^\dagger_{\mathbf{q}} \right\rangle + |T_{32}|^2_{\mathbf{q}} \left\langle \beta_{\mathbf{q}} \beta^\dagger_{\mathbf{q}} \right\rangle + |T_{33}|^2_{\mathbf{q}} \left\langle \alpha^\dagger_{-\mathbf{q}} \alpha_{-\mathbf{q}} \right\rangle + |T_{34}|^2_{\mathbf{q}} \left\langle \beta^\dagger_{-\mathbf{q}} \beta_{-\mathbf{q}} \right\rangle = \\ &= |T_{31}|^2_{\mathbf{q}} + |T_{32}|^2_{\mathbf{q}}.\end{aligned} \tag{D.20}$$

All the other averages can be calculated in a similar way, leading to the expressions:

$$\begin{aligned}\left\langle a^\dagger_{\mathbf{q}} a_{\mathbf{q}} \right\rangle &= \left\langle a^\dagger_{-\mathbf{q}} a_{-\mathbf{q}} \right\rangle = |T_{31}|^2_{\mathbf{q}} + |T_{32}|^2_{\mathbf{q}}, \\ \left\langle b^\dagger_{\mathbf{q}} b_{\mathbf{q}} \right\rangle &= \left\langle b^\dagger_{-\mathbf{q}} b_{-\mathbf{q}} \right\rangle = |T_{41}|^2_{\mathbf{q}} + |T_{42}|^2_{\mathbf{q}}, \\ \langle a_{-\mathbf{q}} a_{\mathbf{q}} \rangle &= \langle a_{\mathbf{q}} a_{-\mathbf{q}} \rangle = T_{11\mathbf{q}} T^*_{31\mathbf{q}} + T_{12\mathbf{q}} T^*_{32\mathbf{q}}, \\ \langle b_{-\mathbf{q}} b_{\mathbf{q}} \rangle &= \langle b_{\mathbf{q}} b_{-\mathbf{q}} \rangle = T_{21\mathbf{q}} T^*_{41\mathbf{q}} + T_{22\mathbf{q}} T^*_{42\mathbf{q}}, \\ \left\langle a^\dagger_{\mathbf{q}} a^\dagger_{-\mathbf{q}} \right\rangle &= \left\langle a^\dagger_{-\mathbf{q}} a^\dagger_{\mathbf{q}} \right\rangle = T_{31\mathbf{q}} T^*_{11\mathbf{q}} + T_{32\mathbf{q}} T^*_{12\mathbf{q}}, \\ \left\langle b^\dagger_{\mathbf{q}} b^\dagger_{-\mathbf{q}} \right\rangle &= \left\langle b^\dagger_{-\mathbf{q}} b^\dagger_{\mathbf{q}} \right\rangle = T_{41\mathbf{q}} T^*_{21\mathbf{q}} + T_{42\mathbf{q}} T^*_{22\mathbf{q}}.\end{aligned} \tag{D.21}$$

Appendix E

Self-consistent solution of the mean-field bosonic Hamiltonian

We start by formulating the mean-field method for a system of $(N+1)$ hard-core bosons; a specific solution is later given for the case $N=2$ corresponding to the singlet-doublet bosonic model for Ca_2RuO_4. The bosonic Hamiltonian consisting of a local part and a pair-wise interaction between $(N+1)$ hard-core bosons on a lattice reads:

$$\mathcal{H}_{\text{bos}} = \sum_i H^{\text{loc}}_{\alpha\beta} \psi^\dagger_{\alpha i} \psi_{\beta i} + \sum_{\langle ij \rangle} H^{ij}_{\alpha\beta\alpha'\beta'} \psi^\dagger_{\alpha i} \psi^\dagger_{\beta j} \psi_{\alpha' i} \psi_{\beta' j}, \tag{E.1}$$

where $\psi^\dagger$ is a vector of $(N+1)$ bosons

$$\psi^\dagger = \begin{pmatrix} s \\ T_1 \\ T_2 \\ \vdots \\ T_N \end{pmatrix}. \tag{E.2}$$

We perform a bosonic rotation from the set of bosons $(s, T_1, \ldots, T_N)$ to a set of rotated bosons $(\alpha, \beta, \gamma, \ldots)$ such that the boson α condenses. After condensation, operators $\alpha, \alpha^\dagger$ can be replaced by a number κ. The hard-core boson constraint $\psi_i^\dagger \psi_i = 1$ which holds locally at every site i can then be rewritten to

$$\kappa^2 + n_i = 1, \tag{E.3}$$

where $n_i = \beta_i^\dagger \beta_i + \gamma_i^\dagger \gamma_i + \ldots$. Next, we split the Hamiltonian into a polynomial in powers of κ:

$$\begin{aligned} H^{\text{loc}} &= H_i^{(2)} + \kappa H_i^{(1)} + \kappa^2 H_i^{(0)}, \\ H^{ij} &= H_{ij}^{(4)} + \kappa H_{ij}^{(3)} + \kappa^2 H_{ij}^{(2)} + \kappa^3 H_{ij}^{(1)} + \kappa^4 H_{ij}^{(0)}. \end{aligned} \tag{E.4}$$

The present method relies on the following two approximations to the bond interaction term introduced at this juncture (the local term is kept exact):

1. we discard Hamiltonian terms $H_{ij}^{(n)}$ of higher than second order in bosonic operators $(\beta, \gamma, \ldots)$,

2. we implement the hard-core boson condition only on average throughout the lattice, not strictly at every site.

As a result of these approximations, we obtain a mean-field Hamiltonian containing constant terms and interaction terms quadratic in the number of bosons, since linear terms drop at the stationary point. The hard-core condition is enforced on average by a common Lagrange multiplier λ:

$$\mathcal{H}_{\mathrm{MF}} = \sum_i \left[(1-n_i)H_i^{(0)} + H_i^{(2)}\right] + \sum_{\langle ij\rangle} \left(\kappa^4 H_{ij}^{(0)} + \kappa^2 H_{ij}^{(2)}\right) + \lambda \sum_i (n_i + \kappa^2 - 1). \tag{E.5}$$

Variables κ and λ are determined by the saddle-point equations

$$\frac{\partial \langle \mathcal{H}_{\mathrm{MF}}\rangle}{\partial \kappa^2} = 0, \qquad \frac{\partial \langle \mathcal{H}_{\mathrm{MF}}\rangle}{\partial \lambda} = 0, \tag{E.6}$$

which can be rearranged to

$$\begin{aligned} \kappa^2 &= 1 - \langle n\rangle, \\ \lambda &= -\frac{1}{N}\sum_{\langle ij\rangle}\left(2\kappa^2 H_{ij}^{(0)} + \langle H_{ij}^{(2)}\rangle\right). \end{aligned} \tag{E.7}$$

Plugging these back into the expression for the Hamiltonian, we get

$$\begin{aligned} \mathcal{H}_{\mathrm{MF}} = &\sum_i \left[(1-n_i)H^{(0)} + H_i^{(2)}\right] + \sum_{\langle ij\rangle}\left(1-\langle n\rangle^2\right)H_{ij}^{(0)} + (1-\langle n\rangle)\sum_{\langle ij\rangle}\left[H_{ij}^{(2)} - (n_i+n_j)H_{ij}^{(0)}\right] \\ &- \sum_{\langle ij\rangle}\langle H_{ij}^{(2)}\rangle\left(\frac{n_i+n_j}{2} - \langle n\rangle\right). \end{aligned} \tag{E.8}$$

To be more specific, we apply the above approximation and decomposition to the singlet-doublet bosonic model for Ca_2RuO_4 consisting of the E_T, J, Δ' interaction terms. In this case, the interaction terms read

$$\begin{aligned} H_i^{(0)} &= \left(E_T - \frac{\Delta'}{2}\right)\sin^2\theta, \\ H_i^{(2)} &= \left(E_T - \frac{\Delta'}{2}\right)\cos^2\theta\, a_i^\dagger a_i + \left(E_T + \frac{\Delta'}{2}\right) b_i^\dagger b_i, \\ H_{ij}^{(0)} &= -J\sin^2 2\theta, \\ H_{ij}^{(2)} &= J\sin^2 2\theta(a_i^\dagger a_i + a_j^\dagger a_j) + J\cos^2 2\theta(a_i^\dagger a_j + a_i a_j^\dagger - a_i a_j - a_i^\dagger a_j^\dagger) + \\ &\quad + J\cos^2\theta(b_i^\dagger b_j + b_i b_j^\dagger - b_i b_j - b_i^\dagger b_j^\dagger), \end{aligned} \tag{E.9}$$

where θ is the bosonic rotation angle. We want to find the minimum of mean-field energy per

site, which is calculated as the average of the mean-field Hamiltonian:

$$\begin{aligned}\frac{E_{\mathrm{MF}}}{N} \equiv \frac{\langle H_{\mathrm{MF}}\rangle}{N} = \; & (1-n)\sin^2\theta\left(E_T - \frac{\Delta'}{2}\right) - 2J(1-n)^2\sin^2 2\theta + \\ & + \frac{E_T - \Delta'/2}{N}\sum_i \cos^2\theta\langle a_i^\dagger a_i\rangle + \frac{E_T + \Delta'/2}{N}\sum_i \langle b_i^\dagger b_i\rangle + \\ & + \frac{1}{N}(1-n)J\sin^2 2\theta \sum_{\langle ij\rangle}(a_i^\dagger a_i + a_j^\dagger a_j) + \\ & + \frac{1}{N}(1-n)J\cos^2 2\theta \sum_{\langle ij\rangle}(a_i^\dagger a_j + a_i a_j^\dagger - a_i a_j - a_i^\dagger a_j^\dagger) + \\ & + \frac{1}{N}(1-n)J\cos^2\theta \sum_{\langle ij\rangle}(b_i^\dagger b_j + b_i b_j^\dagger - b_i b_j - b_i^\dagger b_j^\dagger).\end{aligned} \tag{E.10}$$

To find the proper value $\theta_{\min}$ corresponding to the minimum of mean-field energy, E_{MF} must be calculated for each possible $\theta \in [0, \pi/2]$. Such a calculation consists of a self-consistent loop because the unknown variables κ, λ depend on the bosonic averages $\langle a_i^\dagger a_i\rangle, \langle b_i^\dagger, b_i\rangle, \ldots$ and those, in turn, are calculated from a Hamiltonian containing κ, λ.

The first step in constructing the self-consistent loop is to Fourier transform the mean-field Hamiltonian. In the case of the single-doublet model, this results in

$$H_{\mathrm{MF}} = \sum_{\mathbf{q}}\left[A_{1\mathbf{q}} a_{\mathbf{q}}^\dagger a_{\mathbf{q}} + A_{2\mathbf{q}} b_{\mathbf{q}}^\dagger b_{\mathbf{q}} - \frac{1}{2}B_{1\mathbf{q}}(a_{\mathbf{q}} a_{-\mathbf{q}} + a_{-\mathbf{q}}^\dagger a_{\mathbf{q}}^\dagger) - \frac{1}{2}B_{2\mathbf{q}}(b_{\mathbf{q}} b_{-\mathbf{q}} + b_{-\mathbf{q}}^\dagger b_{\mathbf{q}}^\dagger)\right], \tag{E.11}$$

where the interaction terms in Fourier space are

$$\begin{aligned} A_{a\mathbf{q}} &= \left(E_T - \frac{\Delta'}{2}\right)\cos 2\theta + 8J(1-\langle n\rangle)\sin^2 2\theta + 4J\gamma_{\mathbf{q}}(1-\langle n\rangle)\cos^2 2\theta + \tilde{\lambda}, \\ B_{a\mathbf{q}} &= 4J\gamma_{\mathbf{q}}(1-\langle n\rangle)\cos^2 2\theta, \\ A_{b\mathbf{q}} &= E_T\cos^2\theta + \frac{\Delta'}{2}(1+\sin^2\theta) + 4J(1-\langle n\rangle)\sin^2 2\theta + 4J\gamma_{\mathbf{q}}(1-\langle n\rangle)\cos^2\theta + \tilde{\lambda}, \\ B_{b\mathbf{q}} &= 4J\gamma_{\mathbf{q}}(1-\langle n\rangle)\cos^2\theta \end{aligned}$$

with the notation

$$\gamma_{\mathbf{q}} = \frac{1}{z}\sum_{\delta} e^{i\mathbf{q}\cdot\delta} = \frac{1}{2}(\cos q_{x'} + \cos q_{y'}), \tag{E.12}$$

$$\tilde{\lambda} = -\frac{1}{N_{\mathrm{bond}}}\sum_{\langle ij\rangle} 2\left\langle H_{ij}^{(2)}\right\rangle. \tag{E.13}$$

The above quadratic Hamiltonian is readily diagonalized by the Bogoliubov transformation (see Appendix D). As a result, we obtain two eigenmodes $\omega_{1\mathbf{q}}, \omega_{2\mathbf{q}}$

$$\omega_{\alpha\mathbf{q}} = \sqrt{A_{\alpha\mathbf{q}}^2 - B_{\alpha\mathbf{q}}^2}, \qquad \alpha = 1,2 \tag{E.14}$$

and the bosonic averages

$$\begin{aligned}
\langle a_{\mathbf{q}}^{\dagger} a_{\mathbf{q}} \rangle &= \frac{1}{2}\left(\frac{A_{1\mathbf{q}}}{\omega_{1\mathbf{q}}} - 1\right), \\
\langle a_{\mathbf{q}} a_{-\mathbf{q}} \rangle = \langle a_{-\mathbf{q}}^{\dagger} a_{\mathbf{q}}^{\dagger} \rangle &= \frac{1}{2}\frac{B_{1\mathbf{q}}}{\omega_{1\mathbf{q}}}, \\
\langle b_{\mathbf{q}}^{\dagger} b_{\mathbf{q}} \rangle &= \frac{1}{2}\left(\frac{A_{2\mathbf{q}}}{\omega_{2\mathbf{q}}} - 1\right), \\
\langle b_{\mathbf{q}} b_{-\mathbf{q}} \rangle = \langle b_{-\mathbf{q}}^{\dagger} b_{\mathbf{q}}^{\dagger} \rangle &= \frac{1}{2}\frac{B_{2\mathbf{q}}}{\omega_{2\mathbf{q}}}.
\end{aligned} \tag{E.15}$$

We notice that the $\mathbf{q}$-dependence in expressions for $A_{\alpha\mathbf{q}}, B_{\alpha\mathbf{q}}$ is common to both terms. To simplify the calculation, we can isolate the $\mathbf{q}$-dependent part and choose a common energy scale A_α for each boson:

$$\begin{aligned}
\omega_{\alpha\mathbf{q}} &= A_\alpha \sqrt{(1+\chi_\alpha\gamma_{\mathbf{q}})^2 - (\chi_\alpha\gamma_{\mathbf{q}})^2}, \\
A_{\alpha\mathbf{q}} &= A_\alpha(1+\chi_\alpha\gamma_{\mathbf{q}}), \\
B_{\alpha\mathbf{q}} &= A_\alpha\chi_\alpha\gamma_{\mathbf{q}},
\end{aligned} \tag{E.16}$$

where

$$\begin{aligned}
A_1 &= \left(E_T - \frac{\Delta'}{2}\right)\cos 2\theta + 8J(1-\langle n\rangle)\sin^2 2\theta + \tilde{\lambda}, \\
A_2 &= E_T\cos^2\theta + \frac{\Delta'}{2}(1+\sin^2\theta) + 4J(1-\langle n\rangle)\sin^2 2\theta + \tilde{\lambda}, \\
B_1 &= 4J(1-\langle n\rangle)\cos^2 2\theta, \\
B_2 &= 4J(1-\langle n\rangle)\cos^2\theta.
\end{aligned} \tag{E.17}$$

After this simplification, we are left with a $\mathbf{q}$-independent set of two equations for the numbers χ_1, χ_2:

$$A_\alpha\chi_\alpha - B_\alpha = 0. \tag{E.18}$$

The bosonic averages in real space can be easily obtained from χ_1, χ_2 by a $\mathbf{q}$-sum through the first Brillouin zone:

$$\begin{aligned}
\langle a_i^{\dagger} a_i \rangle &= \frac{1}{N}\sum_{\mathbf{q}}\frac{1}{2}\left[\frac{1+\chi_1\gamma_{\mathbf{q}}}{\sqrt{(1+\chi_1\gamma_{\mathbf{q}})^2 - (\chi_1\gamma_{\mathbf{q}})^2}} - 1\right] = n_a, \\
\langle a_i^{\dagger} a_j \rangle &= \frac{1}{N}\sum_{\mathbf{q}}\frac{1}{2}\left[\left(\frac{1+\chi_1\gamma_{\mathbf{q}}}{\sqrt{(1+\chi_1\gamma_{\mathbf{q}})^2 - (\chi_1\gamma_{\mathbf{q}})^2}} - 1\right)\gamma_{\mathbf{q}}\right], \\
\langle a_j a_j \rangle &= \frac{1}{N}\sum_{\mathbf{q}}\frac{1}{2}\left[\frac{\chi_1\gamma_{\mathbf{q}}}{\sqrt{(1+\chi_1\gamma_{\mathbf{q}})^2 - (\chi_1\gamma_{\mathbf{q}})^2}}\gamma_{\mathbf{q}}\right],
\end{aligned} \tag{E.19}$$

and analogously for the boson averages containing boson b. Finally, the relationship between the quantities κ, λ and the bosonic averages is given by the two equations

$$\kappa^2 = 1 - \langle n\rangle = 1 - \frac{1}{N}\sum_i\left(\langle a_i^{\dagger} a_i\rangle + \langle b_i^{\dagger} b_i\rangle\right) = 1 - \langle a_i^{\dagger} a_i\rangle - \langle b_i^{\dagger} b_i\rangle, \tag{E.20}$$

$$\begin{aligned}\lambda = -\frac{J}{N}\sum_{\langle ij\rangle}\sin^2 2\theta(\langle a_i^\dagger a_i\rangle + \langle a_j^\dagger a_j\rangle) + \cos^2 2\theta(\langle a_i^\dagger a_j\rangle + \langle a_i a_j^\dagger\rangle - \langle a_i a_j\rangle - \langle a_i^\dagger a_j^\dagger\rangle) \\ + \cos^2\theta(\langle b_i^\dagger b_j\rangle + \langle b_i b_j^\dagger\rangle - \langle b_i b_j\rangle - \langle b_i^\dagger b_j^\dagger\rangle) = \\ = -4J\sin^2 2\theta\langle a_i^\dagger a_i\rangle - 4J\cos^2 2\theta(\langle a_i^\dagger a_j\rangle - \langle a_i a_j\rangle) - 4J\cos^2\theta(\langle b_i^\dagger b_j\rangle - \langle b_i b_j\rangle).\end{aligned} \tag{E.21}$$

We are now fully equipped to formulate the self-consistent loop, which must be performed separately for each possible θ:

1. Starting with a reasonable estimate for κ and λ, calculate χ_1, χ_2 using expressions for $A_{1\mathbf{q}}, B_{1\mathbf{q}}, A_{2\mathbf{q}}, B_{2\mathbf{q}}$ and equations $A_1\chi_1 - B_1 = 0$, $A_2\chi_2 - B_2 = 0$.

2. Using χ_1, χ_2, calculate the bosonic averages $\langle a_i^\dagger a_i\rangle, \langle a_i^\dagger a_j\rangle, \langle a_i a_j\rangle, \langle b_i^\dagger b_i\rangle, \langle b_i^\dagger b_j\rangle, \langle b_i b_j\rangle$ as $\mathbf{q}$-summations over first Brillouin zone.

3. Minimize the expression:

$$\begin{aligned}&\left|\kappa^2 - 1 + \langle a_i^\dagger a_i\rangle + \langle b_i^\dagger b_i\rangle\right| + \\ &\left|\lambda + 4J\sin^2 2\theta\langle a_i^\dagger a_i\rangle + 4J\cos^2 2\theta(\langle a_i^\dagger a_j\rangle - \langle a_i a_j\rangle) + 4J\cos^2\theta(\langle b_i^\dagger b_j\rangle - \langle b_i b_j\rangle)\right|\end{aligned}$$

   using a numerical minimization procedure such as the simplex method.

4. Use the newly calculated values of κ, λ as input to step 1, forming a loop.

5. Repeat until change in κ and λ between subsequent loop runs is lower than an accepted error ε.

Published articles

Dorota Gotfryd, Juraj Rusnačko, Krzysztof Wohlfeld, George Jackeli, Jiří Chaloupka, and Andrzej M. Oleś,
Phase diagram and spin correlations of the Kitaev-Heisenberg model: Importance of quantum effects,
Phys. Rev. B **95**, 024426 (2017).
Author's contribution:
JR conducted the exact diagonalization and Luttinger-Tisza calculations and derived the second-order perturbation theory results. JR also contributed the figures showing these results. The Luttinger-Tisza and second-order perturbation theory calculations were carried out as part of JR's diploma thesis, while the exact diagonalization calculations were finalized during JR's PhD studies.

—

Juraj Rusnačko, Dorota Gotfryd, and Jiří Chaloupka,
Kitaev-like honeycomb magnets: Global phase behavior and emergent effective models,
Phys. Rev. B **99**, 064425 (2019).
Author's contribution:
JR performed the exact diagonalization calculations, as well as the analytical derivations, under the guidance of JC. JR co-wrote the manuscript with JC, which was complemented by DG's contribution of the CMFT part.

Bibliography

[1] H. Takagi, T. Takayama, G. Jackeli, G. Khaliullin, and S. E. Nagler, Nat. Rev. Phys. **1**, 264-280 (2019).

[2] T. Takayama, J. Chaloupka, A. Smerald, G. Khaliullin, and H. Takagi, J. Phys. Soc. Jpn. **90**, 062001 (2021).

[3] H. Liu and G. Khaliullin, Phys. Rev. B **97**, 014407 (2018).

[4] A. Kitaev, Annals of Physics **321**, 2-111 (2006).

[5] S. M. Winter, A. A. Tsirlin, M. Daghofer, J. van den Brink, Y. Singh, P. Gegenwart, and R. Valentí, J. Phys.: Condens. Matter **29**, 493002 (2017).

[6] S. M. Winter, Y. Li, H. O. Jeschke, and R. Valentí, Phys. Rev. B **93**, 214431 (2016).

[7] J. Lou, L. Liang, Y. Yu, and Y. Chen, ArXiv e-prints (2015), arXiv:1501.06990 [cond-mat.str-el].

[8] K. Shinjo, S. Sota, and T. Tohyama, Phys. Rev. B **91**, 054401 (2015).

[9] S. Nishimoto, V. M. Katukuri, V. Yushankhai, H. Stoll, U. K. Rössler, L. Hozoi, I. Rousochatzakis, and J. van den Brink, Nat. Comm. **7**, 10273 (2016).

[10] J. Chaloupka and G. Khaliullin, Phys. Rev. B **94**, 064435 (2016).

[11] J. Chaloupka and G. Khaliullin, Phys. Rev. B **92**, 024413 (2015).

[12] J. Rusnačko, D. Gotfryd, and J. Chaloupka, Phys. Rev. B **99**, 064425 (2019).

[13] M. Imada, A. Fujimori, and Y. Tokura, Rev. Mod. Phys. **70**, 1039 (1998).

[14] W. Witczak-Krempa, G. Chen, Y. B. Kim, and L. Balents, Annu. Rev. Condens. Matter Phys. **5**, 57-82 (2014).

[15] L. Savary and L. Balents, Rep. Prog. Phys. **80**, 016502 (2017).

[16] J. Hubbard, Proc. R. Soc. Lond. A **276**, 238-257 (1963).

[17] D. Khomskii, *Transition Metal Compounds* (Cambridge University Press, Cambridge, 2014).

[18] A. Jain, M. Krautloher, J. Porras, G. H. Ryu, D. P. Chen, D. L. Abernathy, J. T. Park, A. Ivanov, J. Chaloupka, G. Khaliullin, B. Keimer, and B. J. Kim, Nat. Phys. **13**, 633-637 (2017).

[19] Y. Tanabe and S. Sugano, J. Phys. Soc. Jpn. **9**, 753-766 (1954).

[20] H. Y. Kee, Presentation at the COR.S.O summer school in Corsica (2015).

[21] J. Chaloupka, habilitation thesis, Masaryk University (2021).

[22] L. D. Landau and L. M. Lifshitz, *Quantum Mechanics: Non-Relativistic Theory, Third Edition* (Pergamon Press, Oxford, 1977).

[23] C. G. Fatuzzo, M. Dantz, S. Fatale, P. Olalde-Velasco, N. E. Shaik, B. Dalla Piazza, S. Toth, J. Pelliciari, R. Fittipaldi, A. Vecchione, N. Kikugawa, J. S. Brooks, H. M. Rønnow, M. Grioni, Ch. Rüegg, T. Schmitt, and J. Chang, Phys. Rev. B **91**, 155104 (2015).

[24] A. Abragam and B. Bleaney, *Electron Paramagnetic Resonance of Transition Ions* (Oxford University Press, New York, 1970).

[25] J. Kanamori, Prog. Theor. Phys. **30**, 275-289 (1963).

[26] S. Sugano, Y. Tanabe and H. Kamimura, Multiplets of Transition-Metal Ions in Crystals, Academic Press (1970).

[27] J. C. Slater and G. F. Koster, Phys. Rev. **94**, 1498 (1954).

[28] J. Zaanen, G. A. Sawatzky, and J. W. Allen, Phys. Rev. Lett. **55**, 418 (1985).

[29] J. Zaanen and G. A. Sawatzky, J. Solid State Chem. **88**, 8-27 (1990).

[30] P. W. Anderson, Phys. Rev. **79**, 350 (1950).

[31] P. W. Anderson, Phys. Rev. **115**, 2 (1959).

[32] N. F. Mott, Proc. Phys. Soc. A **62**, 416 (1949).

[33] W. Heisenberg, Z. Physik **49**, 619-636 (1928).

[34] P. A. M. Dirac, Proc. R. Soc. Lond. A **123**, 714-733 (1929).

[35] P. W. Anderson, Mater. Res. Bull. **8**, 153-160 (1973).

[36] M. G. Yamada, H. Fujita, and M. Oshikawa, Phys. Rev. Lett. **119**, 057202 (2017).

[37] M. G. Yamada, V. Dwivedi, and M. Hermanns, Phys. Rev. B **96**, 155107 (2017).

[38] J. Q. You, X.-F. Shi, X. Hu, and F. Nori, Phys. Rev. B **81**, 014505 (2010).

[39] G. Jackeli and G. Khaliullin, Phys. Rev. Lett. **102**, 017205 (2009).

[40] J. Knolle, D. L. Kovrizhin, J. T. Chalker, and R. Moessner, Phys. Rev. Lett. **112**, 207203 (2014).

[41] J. Knolle, G. W. Chern, D. L. Kovrizhin, R. Moessner, and N. B. Perkins, Phys. Rev. Lett. **113**, 187201 (2014).

[42] J. Nasu, J. Knolle, D. L. Kovrizhin, Y. Motome, and R. Moessner, Nat. Phys. **12**, 912-915 (2016).

[43] J. Nasu, M. Udagawa, and Y. Motome, Phys. Rev. B **92**, 115122 (2015).

[44] S. Trebst, ArXiv e-prints (2017), arXiv:1701.07056 [cond-mat.str-el].

[45] M. Hermanns, I. Kimchi, and J. Knolle, Annu. Rev. Condens. Matter Phys. **9**, 17-33 (2018).

[46] Y. Motome and J. Nasu, J. Phys. Soc. Jpn. **89**, 012002 (2020).

[47] K. I. Kugel and D. I. Khomskii, Sov. Phys. Usp. **25**, 231 (1982).

[48] G. Khaliullin, Prog. Theor. Phys. Suppl. **160**, 155-202 (2005).

[49] R. Yadav, N. A. Bogdanov, V. M. Katukuri, S. Nishimoto, J. van den Brink, and L. Hozoi, Sci. Rep. **6**, 37925 (2016).

[50] H.-S. Kim, V. Vijay Shankar, A. Catuneanu, and H. Y. Kee, Phys. Rev. B **91**, 241110(R) (2015).

[51] J. G. Rau, E. Kin-Ho Lee, and H.-Y. Kee, Phys. Rev. Lett. **112**, 077204 (2014).

[52] J. G. Rau and H.-Y. Kee, ArXiv e-prints (2014), arXiv:1408.4811 [cond-mat.str-el].

[53] M. Becker, M. Hermanns, B. Bauer, M. Garst, and S. Trebst, Phys. Rev. B **91**, 155135 (2015).

[54] I. Rousochatzakis, U. K. Rössler, J. van den Brink, and M. Daghofer, Phys. Rev. B **93**, 104417 (2016).

[55] K. Li, S.-L. Yu, and J.-X. Li, New J. Phys **17**, 043032 (2015).

[56] A. Catuneanu, J. G. Rau, H.-S. Kim, and H.-Y. Kee, Phys. Rev. B **92**, 165108 (2015).

[57] K. Morita, M. Kishimoto, and T. Tohyama, Phys. Rev. B. **98**, 134437 (2018).

[58] T. Takayama, A. Kato, R. Dinnebier, J. Nuss, H. Kono, L. S. I. Veiga, F. Fabbris, D. Haskel, and H. Takagi, Phys. Rev. Lett. **114**, 077202 (2015).

[59] E. K-H. Lee and Y. B. Kim, Phys. Rev. B **91**, 064407 (2015).

[60] H.-S. Kim, E. K.-H. Lee, and Y. B. Kim, EPL **112**, 67004 (2015).

[61] E. K.-H. Lee, J. G. Rau, and Y. B. Kim, Phys. Rev. B **93**, 184420 (2016).

[62] V. M. Katukuri, R. Yadav, L. Hozoi, S. Nishimoto, and J. van den Brink, Sci. Rep. **6**, 29585 (2016).

[63] K. A. Modic, T. E. Smidt, I. Kimchi, N. P. Breznay, A. Biffin, S. Choi, R. D. Johnson, R. Coldea, P. Watkins-Curry, G. T. McCandless, J. Y. Chan, F. Gandara, Z. Islam, A. Vishwanath, A. Shekhter, R. D. McDonald, and J. G. Analytis, Nat. Comm. **5**, 4203 (2014).

[64] A. Biffin, R. D. Johnson, I. Kimchi, R. Morris, A. Bombardi, J. G. Analytis, A. Vishwanath, and R. Coldea, Phys. Rev. Lett. **113**, 197201 (2014).

[65] I. Kimchi, J. G. Analytis, and A. Vishwanath, Phys. Rev. B **90**, 205126 (2014).

[66] Y. Okamoto, M. Nohara, H. Aruga-Katori, and H. Takagi, Phys. Rev. Lett. **99**, 137207 (2007).

[67] G. Chen and L. Balents, Phys. Rev. B **78**, 094403 (2008).

[68] G. Cao, A. Subedi, S. Calder, J.-Q. Yan, J. Yi, Z. Gai, L. Poudel, D. J. Singh, M. D. Lumsden, A. D. Christianson, B. C. Sales, and D. Mandrus, Phys. Rev. B **87**, 155136 (2013).

[69] A. M. Cook, S. Matern, C. Hickey, A. A. Aczel, and A. Paramekanti, Phys. Rev. B **92**, 020417(R) (2015).

[70] A. A. Aczel, A. M. Cook, T. J. Williams, S. Calder, A. D. Christianson, G.-X. Cao, D. Mandrus, Y.-B. Kim, and A. Paramekanti, Phys. Rev. B **93**, 214426 (2016).

[71] H. Kuriyama, J. Matsuno, S. Niitaka, M. Uchida, D. Hashizume, A. Nakao, K. Sugimoto, H. Ohsumi, M. Takata, and H. Takagi, Appl. Phys. Lett. **96**, 182103 (2010).

[72] I. Kimchi and A. Vishwanath, Phys. Rev. B **89**, 014414 (2014).

[73] M. Hermanns and S. Trebst, Phys. Rev. B **89**, 235102 (2014).

[74] Y. Singh and P. Gegenwart, Phys. Rev. B **82**, 064412 (2010).

[75] X. Liu, T. Berlijn, W.-G. Yin, W. Ku, A. Tsvelik, Y.-J. Kim, H. Gretarsson, Y. Singh, P. Gegenwart, and J. P. Hill, Phys. Rev. B **83**, 220403(R) (2011).

[76] F. Ye, S. Chi, H. Cao, B. C. Chakoumakos, J. A. Fernandez-Baca, R. Custelcean, T. F. Qi, O. B. Korneta, and G. Cao, Phys. Rev. B **85**, 180403(R) (2012).

[77] J. Kim, J. Chaloupka, Y. Singh, J. W. Kim, B. J. Kim, D. Casa, A. Said, X. Huang, and T. Gog, Phys. Rev. X **10**, 021034 (2020).

[78] M. Abramchuk, C. Ozsoy-Keskinbora, J. W. Krizan, K. R. Metz, D. C. Bell, and F. Tafti, J. Am. Chem. Soc. **139**, 15371-15376 (2017).

[79] Y. Singh, S. Manni, J. Reuther, T. Berlijn, R. Thomale, W. Ku, S. Trebst, and P. Gegenwart, Phys. Rev. Lett. **108**, 127203 (2012).

[80] F. Freund, S. C. Williams, R. D. Johnson, R. Coldea, P. Gegenwart, and A. Jesche, Sci. Rep. **6**, 35362 (2016).

[81] S. C. Williams, R. D. Johnson, F. Freund, S. Choi, A. Jesche, I. Kimchi, S. Manni, A. Bombardi, P. Manuel, P. Gegenwart, and R. Coldea, Phys. Rev. B **93**, 195158 (2016).

[82] A. Ruiz, A. Frano, N. P. Breznay, I. Kimchi, T. Helm, I. Oswald, J. Y. Chan, R. J. Birgeneau, Z. Islam, and J. G. Analytis, Nat. Comm. **8**, 961 (2017).

[83] T. Takayama, A. Krajewska, A. S. Gibbs, A. N. Yaresko, H. Ishii, H. Yamaoka, K. Ishii, N. Hiraoka, N. P. Funnell, C. L. Bull, and H. Takagi, Phys. Rev. B **99**, 125127 (2019).

[84] K. Kitagawa, T. Takayama, Y. Matsumoto, A. Kato, R. Takano, Y. Kishimoto, S. Bette, R. Dinnebier, G. Jackeli, and H. Takagi, Nature **554**, 341-345 (2018).

[85] J. H. Roudebush, K. A. Ross, and R. J. Cava, Dalton Trans. **45**, 8783-8789 (2016).

[86] V. Todorova, A. Leineweber, L. Kienle, V. Duppel, and M. Jansen, J. Soc. Chem **184**, 1112-1119 (2011).

[87] H. B. Cao, A. Banerjee, J.-Q. Yan, C. A. Bridges, M. D. Lumsden, D. G. Mandrus, D. A. Tennant, B. C. Chakoumakos, and S. E. Nagler, Phys. Rev. B **93**, 134423 (2016).

[88] R. D. Johnson, S. C. Williams, A. A. Haghighirad, J. Singleton, V. Zapf, P. Manuel, I. I. Mazin, Y. Li, H. O. Jeschke, R. Valentí, and R. Coldea, Phys. Rev. B **92**, 235119 (2015).

[89] P. Lampen-Kelley, S. Rachel, J. Reuther, J.-Q. Yan, A. Banerjee, C. A. Bridges, H. B. Cao, S. E. Nagler, and D. Mandrus, Phys. Rev. B **98**, 100403(R) (2018).

[90] J. A. Sears, M. Songvilay, K. W. Plumb, J. P. Clancy, Y. Qiu, Y. Zhao, D. Parshall, and Y.-J. Kim, Phys. Rev. B **91**, 144420 (2015).

[91] H. Suzuki, H. Liu, J. Bertinshaw, K. Ueda, H. Kim, S. Laha, D. Weber, Z. Yang, L. Wang, H. Takahashi, K. Fürsich, M. Minola, B. V. Lotsch, B. J. Kim, H. Yavaş, M. Daghofer, J. Chaloupka, G. Khaliullin, H. Gretarsson, and B. Keimer, ArXiv e-prints (2020), arXiv:2008.02037v2 [cond-mat.str-el].

[92] Y. Imai, K. Nawa, Y. Shimizu, W. Yamada, H. Fujihara, T. Aoyama, R. Takahashi, D. Okuyama, T. Ohashi, M. Hagihala, S. Torii, D. Morikawa, M. Terauchi, T. Kawamata, M. Kato, H. Gotou, M. Itoh, T. J. Sato, K. Ohgushi, Phys. Rev. B **105**, L041112 (2022).

[93] R. Sano, Y. Kato, and Y. Motome, Phys. Rev. B **97**, 014408 (2018).

[94] H. Liu, Int. J. Mod. Phys. B **35**, 2130006 (2021).

[95] M. Songvilay, J. Robert, S. Petit, J. A. Rodriguez-Rivera, W. D. Ratcliff, F. Damay, V. Balédent, M. Jiménez-Ruiz, P. Lejay, E. Pachoud, A. Hadj-Azzem, V. Simonet, and C. Stock, Phys. Rev. B **102**, 224429 (2020).

[96] H. K. Vivanco, B. A. Trump, C. M. Brown, and T. M. McQueen, Phys. Rev. B **102**, 224411 (2020).

[97] J.-Q. Yan, S. Okamoto, Y. Wu, Q. Zheng, H. D. Zhou, H. B. Cao, and M. A. McGuire, Phys. Rev. Materials **3**, 074405 (2020).

[98] E. A. Zvereva, M. I. Stratan, A. V. Ushakov, V. B. Nalbandyan, I. L. Shukaev, A. V. Silhanek, M. Abdel-Hafiez, S. V. Streltsov, and A. N. Vasiliev, Dalton Trans. **45**, 7373-7384 (2016).

[99] S. H. Chun, J.-W. Kim, J. Kim, H. Zheng, C. C. Stoumpos, C. D. Malliakas, J. F. Mitchell, K. Mehlawat, Y. Singh, Y. Choi, T. Gog, A. Al-Zein, M. Moretti Sala, M. Krisch, J. Chaloupka, G. Jackeli, G. Khaliullin, and B. J. Kim, Nat. Phys. **11**, 462-466 (2015).

[100] A. Shitade, H. Katsura, J. Kuneš, X.-L. Qi, S.-C. Zhang, and N. Nagaosa, Phys. Rev. Lett. **102**, 256403 (2009).

[101] S. K. Choi, R. Coldea, A. N. Kolmogorov, T. Lancaster, I. I. Mazin, S. J. Blundell, P. G. Radaelli, Y. Singh, P. Gegenwart, K. R. Choi, S.-W. Cheong, P. J. Baker, C. Stock, and J. Taylor, Phys. Rev. Lett. **108**, 127204 (2012).

[102] R. Comin, G. Levy, B. Ludbrook, Z.-H. Zhu, C. N. Veenstra, J. A. Rosen, Y. Singh, P. Gegenwart, D. Stricker, J. N. Hancock, D. van der Marel, I. S. Elfimov, and A. Damascelli, Phys. Rev. Lett. **109**, 266406 (2012).

[103] S. J. Moon, H. Jin, K. W. Kim, W. S. Choi, Y. S. Lee, J. Yu, G. Cao, A. Sumi, H. Funakubo, C. Bernhard, and T. W. Noh, Phys. Rev. Lett. **101**, 226402 (2008).

[104] H. Gretarsson, J. P. Clancy, Y. Singh, P. Gegenwart, J. P. Hill, J. Kim, M. H. Upton, A. H. Said, D. Casa, T. Gog, and Y.-J. Kim, Phys. Rev. B **87**, 220407(R) (2013).

[105] B. H. Kim, G. Khaliullin, and B. I. Min, Phys. Rev. B **89**, 081109(R) (2014).

[106] V. M. Katukuri, S. Nishimoto, V. Yushankhai, A. Stoyanova, H. Kandpal, S. Choi, R. Coldea, I. Rousochatzakis, L. Hozoi, and J. van den Brink, New J. Phys. **16**, 013056 (2014).

[107] Y. Yamaji, Y. Nomura, M. Kurita, R. Arita, and M. Imada, Phys. Rev. Lett. **113**, 107201 (2014).

[108] Y. Li, S. M. Winter, D. A. S. Kaib, K. Riedl, and R. Valentí, Phys. Rev. B **103**, L220408 (2021).

[109] J. Chaloupka, G. Jackeli, and G. Khaliullin, Phys. Rev. Lett. **110**, 097204 (2013).

[110] J. H. Van Vleck, Phys. Rev. **31**, 587 (1928).

[111] G. Khaliullin, Phys. Rev. Lett. **111**, 197201 (2013).

[112] J. Chaloupka and G. Khaliullin, Phys. Rev. B **100**, 224413 (2019).

[113] M. Matsumoto, B. Normand, T. M. Rice, and M. Sigrist, Phys. Rev. B **69**, 054423 (2004).

[114] Y. Kulik and O. P. Sushkov, Phys. Rev. B **84**, 134418 (2011).

[115] T. Sommer, M. Vojta, and K. W. Becker, Eur. Phys. J. B **23**, 329-339 (2001).

[116] M. Vallone, Phys. Status Solidi B **257**, 1900443 (2020).

[117] Y. Nambu, Phys. Rev. **117**, 648 (1960).

[118] J. Goldstone, Nuovo Cim **19**, 154-164 (1961).

[119] P. W. Higgs, Phys. Rev. Lett. **13**, 508 (1964).

[120] P. W. Anderson, Phys. Rev. **130**, 439 (1963).

[121] M. Z. Hasan and C. L. Kane, Rev. Mod. Phys. **82**, 3045 (2010).

[122] K. I. Kugel' and D. I. Khomskii, Sov. Phys. JETP **37**, 725 (1973).

[123] S. Nakatsuji, S. Ikeda, and Y. Maeno, J. Phys. Soc. Jpn. **66**, 1868-1871 (1997).

[124] S. Nakatsuji and Y. Maeno, Phys. Rev. Lett. **84**, 2666 (2000).

[125] C. S. Alexander, G. Cao, V. Dobrosavljevic, S. McCall, J. E. Crow, E. Lochner, and R. P. Guertin, Phys. Rev. B **60**, R8422(R) (1999).

[126] G. Cao, S. McCall, M. Sheppard, J. E. Crow, and R. P. Guertin, Phys. Rev. B **56**, R2916 (1997).

[127] M. Braden, G. André, S. Nakatsuji, and Y. Maeno, Phys. Rev. B **58**, 847 (1998).

[128] V. I. Anisimov, I. A. Nekrasov, D. E. Kondakov, T. M. Rice, and M. Sigrist, Eur. Phys. J. B **25**, 191-201 (2002).

[129] E. Gorelov, M. Karolak, T. O. Wehling, F. Lechermann, A. I. Lichtenstein, and E. Pavarini, Phys. Rev. Lett. **104**, 226401 (2010).

[130] T. Mizokawa, L. H. Tjeng, G. A. Sawatzky, G. Ghiringhelli, O. Tjernberg, N. B. Brookes, H. Fukazawa, S. Nakatsuji, and Y. Maeno, Phys. Rev. Lett. **87**, 077202 (2001).

[131] H. Gretarsson, H. Suzuki, Hoon Kim, K. Ueda, M. Krautloher, B. J. Kim, H. Yavaş, G. Khaliullin, and B. Keimer, Phys. Rev. B **100**, 045123 (2019).

[132] S.-M. Souliou, J. Chaloupka, G. Khaliullin, G. Ryu, A. Jain, B. J. Kim, M. Le Tacon, and B. Keimer, Phys. Rev. Lett. **119**, 067201 (2017).

[133] D. Pekker and C. M. Varma, Annu. Rev. Condens. Matter Phys. **6**, 269-297 (2015).

[134] D. Podolsky, A. Auerbach, and D. P. Arovas, Phys. Rev. B **84**, 174522 (2011).

[135] R. J. Baxter, *Exactly Solved Models in Statistical Mechanics* (Academic Press, London, 1985).

[136] E. Ising, Z. Physik **31**, 253–258 (1925).

[137] Lars Onsager, Phys. Rev. **65**, 117 (1944).

[138] G. H. Wannier, Phys. Rev. **79**, 357 (1950).

[139] H. Bethe, Z. Physik **71**, 205-226 (1931).

[140] E. Lieb, T. Schultz, and D. Mattis, Annals of Physics **16**, 407-466 (1961).

[141] P. A. Maksimov and A. L. Chernyshev, Phys. Rev. Research **2**, 033011 (2020).

[142] J. Goldstone, A. Salam, and S. Weinberg, Phys. Rev. **127**, 965 (1962).

[143] J. Chaloupka, G. Jackeli, and G. Khaliullin, Phys. Rev. Lett. **105**, 027204 (2010).

[144] E. Quinn, S. Bhattacharjee, and R. Moessner, Phys. Rev. B **91**, 134419 (2015).

[145] R. M. F. Houtappel, Physica **16**, 425-455 (1950).

[146] J. Nasu, A. Nagano, M. Naka, and S. Ishihara, Phys. Rev. B **78**, 024416 (2008).

[147] E. Zhao and W. V. Liu, Phys. Rev. Lett. **100**, 160403 (2008).

[148] H. Zou, B. Liu, E. Zhao, and W. V. Liu, New J. Phys. **18**, 053040 (2016).

[149] Z. Nussinov and J. van den Brink, Rev. Mod. Phys. **87**, 1 (2015).

[150] P. P. Stavropoulos, A. Catuneanu, and H.-Y. Kee, Phys. Rev. B **98**, 104401 (2018).

[151] P. A. Maksimov, Z. Zhu, S. R. White, and A. L. Chernyshev, Phys. Rev. X **9**, 021017 (2019).

[152] K. Ran, J. Wang, W. Wang, Zhao-Yang Dong, X. Ren, S. Bao, S. Li, Z. Ma, Y. Gan, Y. Zhang, J. T. Park, G. Deng, S. Danilkin, Shun-Li Yu, Jian-Xin Li, and J. Wen, Phys. Rev. Lett. **118**, 107293 (2017).

[153] A. Banerjee, P. Lampen-Kelley, J. Knolle, Ch. Balz, A. A. Aczel, B. Winn, Y. Liu, D. Pajerowski, J. Yan, C. A. Bridges, A. T. Savici, B. C. Chakoumakos, M. D. Lumsden, D. A. Tennant, R. Moessner, D. G. Mandrus, and S. E. Nagler, npj Quan. Mater. **3**, 8 (2018).

[154] Y. Sizyuk, C. Price, P. Wölfle, and N. B. Perkins, Phys. Rev. B **90**, 155126 (2014).

[155] L. Janssen, E. C. Andrade, and M. Vojta, Phys. Rev. B **96**, 064430 (2017).

[156] H. Fehske, R. Schneider, and A. Weiße, *Computational Many-Particle Physics* (Springer, Berlin Heidelberg, 2008).

[157] A. W. Sandvik, AIP Conf. Proc. **1297**, 135-338 (2010).

[158] C. Lacroix, P. Mendels, and F. Mila, *Introduction to Frustrated Magnetism: Materials, Experiments, Theory* (Springer, Berlin Heidelberg, 2011).

[159] R. M. Noack and S. Manmana, AIP Conf. Proc. **789**, 93-163 (2005).

[160] P. C. Hohenberg, Phys. Rev. **158**, 383 (1967).

[161] N. D. Mermin, J. Math. Phys **8**, 1061-1064 (1967).

[162] N. D. Mermin and H. Wagner, Phys. Rev. Lett. **17**, 1133 (1966); erratum: **17**, 1307 (1966).

[163] J. H. Wilkinson, *The Algebraic Eigenvalue Problem* (Clarendon Press, Oxford, 1988).

[164] C. Lanczos, J. Res. Nat. Bur. Stand. **45**, 255 (1950).

[165] E. Anderson, Z. Bai, C. Bischof, S. Blackford, J. Demmel, J. Dongarra, J. Du Croz, A. Greenbaum, S. Hammarling, A. McKenney, and D. Sorensen, *LAPACK Users' Guide, Third Edition* (Society For Industrial and Applied Mathematics, Piladelphia, 1999).

[166] A. F. Albuquerque, D. Schwandt, B. Hetényi, S. Capponi, M. Mambrini, and A. M. Läuchli, Phys. Rev. B **84**, 024406 (2011).

[167] A. Auerbach, *Interacting Electrons and Quantum Magnetism* (Springer, New York, 1994).

[168] P. J. van Laarhoven and E. H. Aarts, *Simulated Annealing: Theory and Applications* (Springer, Dordrecht, 1987).

[169] D. E. Goldberg, *Genetic Algorithms in Search, Optimization and Machine Learning* (Addison-Wesley Longman Publishing, Boston, 1989).

[170] J. Mockus, W. Eddy, G. Reklaitis, *Bayesian Heuristic Approach to Discrete and Global Optimization* (Springer, Dordrecht, 1997).

[171] J. M. Luttinger and L. Tisza, Phys. Rev. **70**, 954 (1946).

[172] Z. Friedman and J. Felsteiner, Phil. Mag. **29**, 957 (1973).

[173] G. Jackeli and A. Avella, Phys. Rev. B **92**, 184416 (2015).

[174] M. Gohlke, G. Wachtel, Y. Yamaji, F. Pollmann, and Y. B. Kim, Phys. Rev. B **97**, 075126 (2018).

[175] J. Wang, B. Normand, and Z.-X. Liu, Phys. Rev. Lett. **123**, 197201 (2019).

[176] D. Gotfryd, J. Rusnačko, K. Wohlfeld, G. Jackeli, J. Chaloupka, and A. M. Oleś, Phys. Rev. B **95**, 024426 (2017).

[177] J. Kim, J. Chaloupka, Y. Singh, J. W. Kim, B. J. Kim, D. Casa, A. Said, X. Huang, and T. Gog, Phys. Rev. X **10**, 021034 (2020).

[178] C. Wu, Phys. Rev. Lett. **100**, 200406 (2008).

[179] C.-C. Chen, L. Muechler, R. Car, T. Neupert, and J. Maciejko, Phys. Rev. Lett. **117**, 096405 (2016).

[180] S. Gopalan, T. M. Rice, and M. Sigrist, Phys. Rev. B **49**, 8901 (1994).

[181] N. Papanicolaou, Nucl. Phys. B **240**, 281-311 (1984).

[182] N. Papanicolaou, Nucl. Phys. B **305**, 367-395 (1988).

[183] A. V. Chubukov J. Phys.: Condens. Matter **2**, 1593 (1990).

[184] A. Joshi, M. Ma, F. Mila, D. N. Shi, and F. C. Zhang, Phys. Rev. B **60**, 6584 (1999).

[185] A. W. Sandvik, J. Phys. A: Math. Gen. **25**, 3667 (1992).

[186] A. W. Sandvik, Phys. Rev. B **59**, R14157(R) (1999).

[187] O. F. Syljuåsen, Phys. Rev. E **67**, 046701 (2003).

[188] A. Avella and F. Mancini, *Strongly Correlated Systems – Numerical Methods* (Springer Berlin, Heidelberg, 2013).

[189] E. Y. Loh, Jr., J. E. Gubernatis, R. T. Scalettar, S. R. White, D. J. Scalapino, and R. L. Sugar, Phys. Rev. B **41**, 9301 (1990).

[190] J. W. Negele and H. Orland, *Quantum Many-Particle systems* (CRC Press, Boca Raton, 1998).

[191] M. Jarrell and J. E. Gubernatis, Phys. Rep. **269**, 133-195 (1996).

[192] P. Henelius and A. W. Sandvik, Phys. Rev. B **62**, 1102 (2000).

[193] I. Zegkinoglou, J. Strempfer, C. S. Nelson, J. P. Hill, J. Chakhalian, C. Bernhard, J. C. Lang, G. Srajer, H. Fukazawa, S. Nakatsuji, Y. Maeno, and B. Keimer, Phys. Rev. Lett. **95**, 136401 (2005).

[194] L. Wang, K. S. D. Beach, and A W. Sandvik, Phys. Rev. B **73**, 014431 (2006).

[195] J. Kaufmann and K. Held, ArXiv e-prints (2021), arXiv:2105.11211 [cond-mat.str-el].

[196] D. C. Liu and J. Nocedal, Math. Programming **45**, 503-528 (1989).

[197] J. Gubernatis, N. Kawashima, and P. Werner, *Quantum Monte Carlo Methods: Algorithms for Lattice Models* (Cambridge University Press, Cambridge, 2016).

[198] A. W. Sandvik and J. Kurkijärvi, Phys. Rev. B **43**, 5950 (1991).

[199] D. C. Handscomb, Proc. Cambridge Philos. Soc. **58**, 594 (1962); **60** 115 (1964).

[200] N. Metropolis, A. W. Rosenbluth, M. N. Rosenbluth, A. H. Teller, and E. Teller, J. Chem. Phys. **21**, 1087-1092 (1953).

[201] W. K. Hastings, Biometrika **57**, 97-109 (1970).

[202] U. Wolff, Nucl. Phys. B **17**, 93-102 (1990).

[203] R. H. Swendsen and J.-S. Wang, Phys. Rev. Lett. **58**, 86 (1987).

[204] U. Wolff, Phys. Rev. Lett. **62**, 361 (1989).

[205] F. Alet, S, Wessel, and M. Troyer, Phys. Rev. E **71**, 036706 (2005).

[206] S. Humeniuk, dissertation thesis, Universität Stuttgart, 2018.

[207] S. Grossjohann, dissertation thesis, Technische Universität Braunschweig, 2010.

[208] N. N. Bogoliubov, J. Exptl. Theoret. Phys. **34**, 58-65 (1958).